Detection and Study of Galactic Cosmic Rays with the DAMPE and HERD space missions

Dimitrios Kyratzis

Advisor: Prof. I. De Mitri Co-advisor: Dr. F.C.T. Barbato

Department of Astroparticle Physics
Gran Sasso Science Institute

This dissertation is submitted for the degree of
PhD in Astroparticle Physics

March 2023

Acknowledgements

I would like to sincerely thank all the people that assisted towards the realization of this thesis. I'm glad to say that they're quite a few and their support is greatly appreciated.

I'm thankful to my advisor, Prof. Ivan De Mitri, for displaying a unique combination of scientific excellence and exemplary mentoring skills, throughout the course of this PhD. He followed the work tirelessly, provided insightful suggestions (one after the other...) while being patient enough to sustain my numerous questions and (short) comments. Additionally, he has been a charismatic leader for the expanding GSSI Space Group, a group of which I'm proud to be a part of since its inception. Ivan, thank you for being present in both good and bad times. Your sense of direction has been fundamental in providing a clearer perspective for personal and scientific matters, alike.

I would also like to thank my co-advisor, Dr. Felicia Carla Tiziana Barbato. Her inherent virtues (just like her names) are countless. She has been very supportive throughout the years, helping to solve a plethora of problems, by utilizing a synergy of solid scientific knowledge and pure determination. Feli, I'm grateful for having the chance to work side-by-side with you in many occasions as well as for being able to call you and Gennaro "family" through ups and downs.

A big thanks goes to the whole GSSI Space Group for the assistance (and good times!) in all these years. I'm grateful to be collaborating with such an engaging group of individuals working towards a multitude of diverse objectives. At that point I would like to give credit to Francesca Alemanno, Leandro Silveri and Andrea Parenti. Through numerous meetings conversing over endless blocks of code, we managed to solve common issues pertaining (but not limited) to various aspects of our respective DAMPE analyses. Consequently, part of this thesis wouldn't have been made possible without their indispensable contribution and continuous support.

Furthermore, I'm grateful for the assistance and kindness of Attanasio Candela, Massimiliano De Deo and Marco D'Incecco from the Electronics' lab at LNGS. Their valuable aid from the beginning of this PhD is really appreciated.

I would also like to thank Dr. David Droz for his continuous help and support on DAMPE-related aspects and arising problems during his time in the University of Geneva. He has been a brilliant colleague and above all, a valuable friend.

Moreover, I would like to express my appreciation to Assoc. Prof. Carmelo Evoli (internal referee) along with Profs. Fausto Guarino, Roberta Sparvoli and Andrii Tykhonov (external referees) for taking the time to carefully review this thesis and provide insightful comments. Additionally, I would like to commend Prof. Elisabetta Baracchini for precisely coordinating the efforts regarding the PhD submission, defense and related procedures.

This paragraph is dedicated to people I have in high regard, who managed to make such an adventure worthwhile. These could be people mentioned previously and people not mentioned yet. These might be GSSI alumni and current members. These could easily be people working in the historical center and people playing basketball in via Strinella or Paganica. These are people living in L'Aquila and people living in Thessaloniki. The list is extensive, although I'm quite sure they know. It has been without a doubt, a great pleasure getting to share such experiences with them.

Before closing this section, I would like to thank my family for the immense support throughout the years, especially when times were challenging.

Abstract

The Cosmos[1] and our (somehow limited) knowledge of it, can be divided -for the sake of simplicity- in two categories: the macrocosm and microcosm. The former comprises immense structures like stars, planets, galaxies, clusters, the Interstellar Medium, etc, while the latter focuses on the building blocks constituting the aforementioned structures, such as subatomic particles, radiation and heavier elements, covering a vast energy range. A prominent part of the microcosm is manifested through Cosmic Rays (CRs) in the Universe.

These can be elements such as protons, helium, carbon, oxygen (all the way up to iron, nickel and beyond) nuclei, electrons/positrons, antiprotons, gamma-rays and neutrinos. Understanding their (inherently complex) origin, acceleration and propagation mechanisms in the Universe is of paramount importance to Astroparticle Physics. As a consequence to the above-stated questions, a multitude of theoretical models have been introduced, along with an impressive number of sophisticated experiments focusing on CR detection in a broad energy range. Such experiments are devoted either to direct or indirect CR detection, with the former including space or balloon-borne instruments and the latter corresponding to ground-based experiments. This work focuses on the study and direct detection of highly energetic Galactic Cosmic Rays with space-borne detectors, specifically oriented towards the Dark Matter Particle Explorer (DAMPE) and High Energy cosmic-Radiation Detector (HERD) experiments.

DAMPE, is a space-borne detector designed for direct CR and gamma ray studies along with indirect searches for Dark Matter (DM). The instrument is operative since December 2015, comprising a plastic scintillator detector, a silicon tracker, a deep calorimeter and a neutron detector. Such a configuration allows for precise measurements of electrons/positrons and gamma rays in the energy range of 5 GeV to 10 TeV, as well as protons and heavier nuclei spanning from 50 GeV to hundreds of TeV.

[1] a word introduced by Pythagoras to describe the Universe and everything it constitutes

An important part of this thesis is dedicated to spectral measurements pertaining to the BCNO nucleonic group, focusing mainly on carbon and oxygen fluxes along with complimentary insights on flux ratios such as C/O, B/C and B/O. DAMPE is able to provide precise measurements of the aforementioned nuclei in the multi-TeV/n region, for the first time, thus exhibiting a novelty amongst direct measurements. The fluxes of carbon and oxygen are precisely measured in the energy range of 10 GeV/n (energy per nucleon) to approximately 20 TeV/n and 10 TeV/n respectively, with the flux ratios reaching up to a few TeV/n. Pertaining to the fluxes, the main objective will be to validate features detected previously as well as extending current spectral measurements in the multi-TeV region for the first time, with unprecedented precision. In this region, a softening feature could be evident for carbon and oxygen, as in recent measurements of DAMPE proton and helium fluxes, where the aforementioned spectral feature was detected approximately at 15 TV. Regarding the C/O, B/C and B/O flux ratios, nuclei such as carbon and oxygen are of primary origin while boron originates from the spallation of heavier primaries with Interstellar Medium particles. Extending the prevailing knowledge on CR nucleonic spectra up to multi-TeV/n energies, while understanding the nature of CR propagation in the Galaxy via secondary-to-primary ratios (such as B/C and B/O), will be an important part of this work.

Benefiting from the successful and long-standing experience of DAMPE in orbit, along with the experience gained from the various challenges that accompany a space mission, an additional part of this work is dedicated to the development and realization of a novel CR detector. HERD or, the High Energy cosmic-Radiation Detection facility is a future space-borne payload proposed to be installed onboard the China Space Station (CSS). Due to its unique geometrical design and deep calorimeter (55 X_0) HERD will be detecting incoming particles from both its top and four lateral sides, thus leading to an increase of more that an order of magnitude in acceptance, while maintaining manageable payload dimensions for a space mission.

Main goal of this activity pertains to the optimal configuration of the Plastic Scintillator Detector (PSD), an instrument aiming to provide gamma-ray and charged particle trigger signals, together with an essential charge measurement for particle identification purposes. This work is based on the preparation, construction and validation of various configurations regarding plastic scintillator bars' readout by silicon photomultipliers (SiPMs). Each setup is thoroughly

examined in order to provide high detection efficiency, large dynamic range and satisfactory energy resolution. The entirety of all aforementioned configurations were tested both in Gran Sasso Science Institute (GSSI) and National Laboratories of Gran Sasso (LNGS) as well as in CERN Super Proton Synchrotron (SPS) and Proton Synchrotron (PS) facilities, verified via a multitude of particles, ranging from: electrons, CR muons, pions and protons in a wide energy range (from a few MeV to a few hundred GeV). The thesis is structured as follows:

1. The **first** chapter will provide a general introduction to Cosmic Rays, starting from a brief historical overview, moving on to a description of the cosmic ray spectrum along with a concise examination of the acceleration and propagation mechanisms of CRs in the Galaxy. Then, an illustration of previous and current generation space-borne experiments will be presented, followed by the main motivations of this work.

2. The **second** chapter will present the DAMPE experiment. A detailed look on its main sub-detectors, scientific objectives and performance figures will be provided, alongside few of its main CR results.

3. The **third** chapter will illustrate the entire analysis procedure concerning carbon and oxygen nuclei (being the main objective of this work), starting from the respective data samples, moving on to the various selection cuts, detailed background estimation and efficiency calculations.

4. The **fourth** chapter will showcase spectral measurements of carbon and oxygen nuclei, corresponding to 6 years of DAMPE flight data, in addition to complimentary flux ratio results for C/O, B/C and B/O. An estimation of statistical and systematic uncertainties is presented, along with a detailed interpretation of all presented results in this analysis.

5. The **fifth** chapter will introduce the HERD space mission along with its novel design, scientific goals and expected results.

6. The **sixth** chapter will focus on R&D activities concerning the HERD PSD. Scintillator bars of various sizes and geometries are examined, readout by SiPMs. An important part of this work focuses on the design, preparation and performance assessment of various configurations, in a wide range of energies.

Since we cannot change reality, let us change the eyes which see reality.
–Nikos Kazantzakis

Table of contents

List of figures

List of tables

Chapter 1

Introduction to Cosmic Rays

Cosmic ray (CR) studies comprise a significant part of rigorous research activities, with fundamental open questions concerning their origin, acceleration and propagation mechanisms in the Galaxy. Substantial insight arises from the investigation of CRs; originating from violent stellar phenomena, then accelerated to high energies with their subsequent propagation in the Universe, these cosmic messengers provide a unique opportunity for understanding the microscopic world with its intrinsic interactions, as well as the macroscopic world from the perspective of astrophysics/cosmology at the largest scales.

1.1 Brief historic overview

One of the first possible hints regarding the onset of CR detection could date back to 1785, when Coulomb detected spontaneous electrical discharges from insulated electroscopes. More than a century later, in 1896, Henri Becquerel [1] was astonished by a number of spontaneous processes that occurred when potassium uranyl sulfate compounds were applied onto photographic plates. Such processes could produce ionizations and took place (partially) due to the emission of X-rays by uranium, a phenomenon that led to the discovery of radioactivity (as coined by Marie Curie later on).

In the beginning of the 20th century, Wilson, Elster and Geitel devised a novel method for insulating electroscopes within an enclosed container, which resulted in an enhanced sensitivity. Nevertheless, discharges were still observed even in the absence of radioactive substances inside the electroscope shielding, leading to a postulation that the radiation responsible for the discharge was of terrestrial origin, although without a robust experimental confirmation.

Then in 1909, Wulf [2] used an improved electroscope with the aim of measuring the ionization rate at the summit of the Eiffel Tower, located 300 meters above ground level. Based on prevailing hypotheses attributing most radiation to a terrestrial source, it was expected that the ionization rate would be lower at the top of the tower than at ground level. The measured ionization rate was found to be smaller than the rate recorded at ground level, larger than was expected when taking into account the absorption properties of radiation. Additionally, Domenico Pacini [3] carried out ionization measurements underwater (3 meters below the surface), observing a 20% reduction in the rate when comparing these results with the analogous rate at sea level.

Figure 1.1: Historical photograph depicting Viktor Hess in one of his various balloon flights. From [4, 5].

The definitive answer was given by Victor Hess, using various balloon-borne pressurized ionization chambers in a series of flights between 1911 and 1912 [4, 5]. Firstly, a slight diminution of ionization was observed while the balloon ascended, followed by a fast increase in ionizing radiation that persisted up to an altitude of 5200 m, as seen in Figure 1.2. Hess concluded that this elevation-dependent augmentation of ionization was due to radiation emanating from outer space. He also observed the absence of diurnal variations, hence, he ruled out the sun as the immediate origin of this postulated penetrating radiation. The results of Hess's

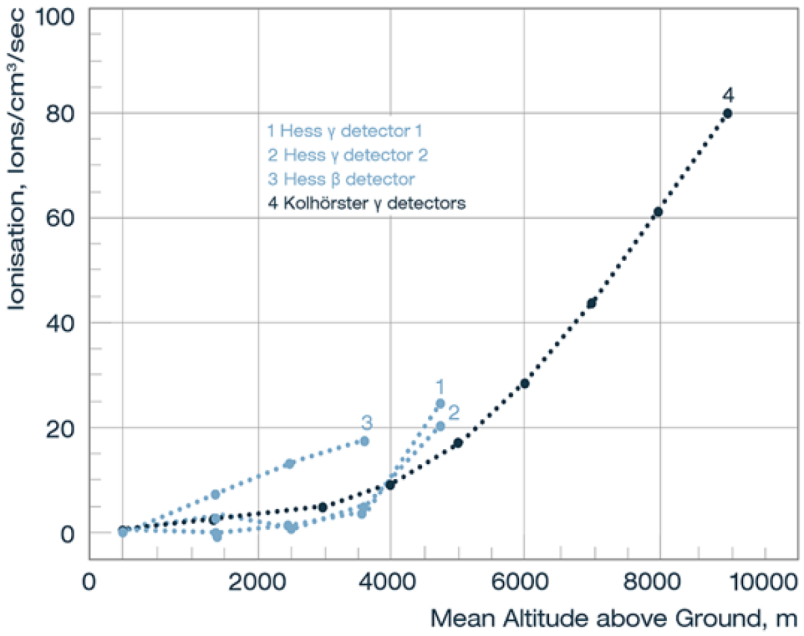

Figure 1.2: Measurements of the discharge rate with respect to the altitude, coming from the various flights performed by Viktor Hess (adapted from [4]) along with the flight of Kolhorster in 1914 (average of his two detectors). The increasing discharge rates imply an extraterrestrial origin of said radiation. From [5].

experiment were later confirmed by Kolholster, who reached an altitude of 9200 meters (as in Fig. 1.2). Consequently, in 1936, Hess was awarded the Nobel Prize in Physics for the discovery of cosmic rays.

Cosmic radiation was commonly believed to be composed of gamma-rays due to their strong permeation effects. A fundamental experiment conducted to examine the nature of cosmic rays, pertained to the variance of count intensity with geomagnetic latitude. In 1927 and 1928, the Dutch physicist Clay [6] conducted said measurements and discovered that ionization rose with latitude. This result was confirmed by an extensive survey directed by Compton [7], which illustrated that cosmic rays were influenced by the geomagnetic field and were primarily composed of charged particles. In 1933, Alvarez and Compton [8], Johnson [9], and Rossi [10] performed three independent experiments that discovered increased fluxes of cosmic rays originating from the West rather than the East, near the equator. This phenomenon, caused by interactions of cosmic rays with the geomagnetic field, indicated that such particles were positively charged and most probably protons; a hypothesis which was verified later on.

The discovery of cosmic rays established a new field of fundamental particle physics, more than 40 years prior to the advent of high–energy particle accel-

erators (established around the late 1950s). Nowadays, man-made accelerators reach center of mass energies up to $\sqrt{s} \sim 14$ TeV following great technological advancements while providing important scientific breakthroughs. Nevertheless, CR particles accelerated at the highest energies in distant galaxies throughout the Universe, surpass such energies by orders of magnitude and give rise to a multitude of open questions. These questions motivate the search on novel and insightful phenomena deep in the Cosmos, leading to the development of complex detectors, experiments and theoretical CR models employed towards their clarification.

1.2 The CR Energy Spectrum

After more than a century of investigations, cosmic rays have been the subject of intense study, both with ground-based detectors as well as with space-borne telescopes. CRs can be classified as primary or secondary, with charged particles produced and accelerated at astrophysical sources representing the bulk of such primaries. In that sense, the majority of CRs are identified as protons with a smaller percentage attributed to heavier nuclei, then electrons/positrons, antiprotons, gamma-rays and neutrinos. Following the acceleration at the sources, CR radiation propagates through the Interstellar Medium (ISM), eventually reaching the top of the Earth's atmosphere.

At that point, CRs can either be measured with space-borne instruments (direct detection) or interact with atmospheric nuclei, thus giving rise to extensive air showers (EAS) of secondary particles. Such energetic secondaries can be probed with ground-based experiments (indirect detection). Both direct and indirect CR detection approaches remain in the forefront of intense activities, represented by a multitude of sophisticated experiments aiming at the clarification of their origin, acceleration and propagation mechanisms in the Universe, in a very broad range of energies (from a few GeV to 10^{20} eV) [11–14].

A general view of the differential intensity of CRs with respect to the energy is presented in Fig. 1.3, where a vast selection of contributions from ground and space-base experiments is evident across the spectrum. The CR yield in various energies across the spectrum can be represented by integral fluxes above a given energy threshold, as denoted by shaded bands in Fig. 1.3:

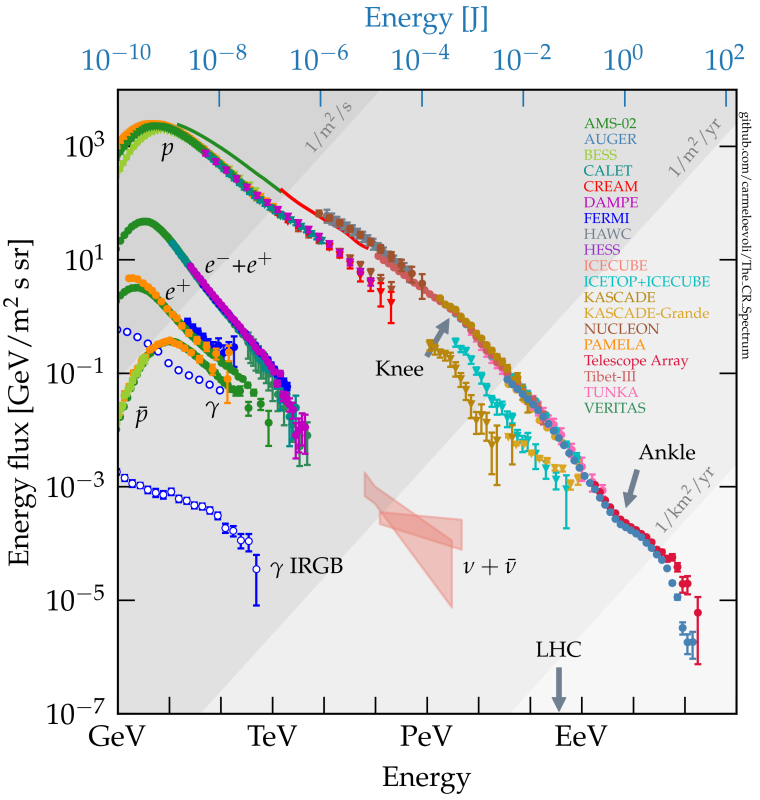

Figure 1.3: A recent view of the Cosmic Ray energy spectrum. From [15].

$$
\begin{aligned}
F\left(>10^{9}\mathrm{eV}\right) &\simeq 1000 \text{ particles/s m}^2 \\
F\left(>10^{15}\mathrm{eV}\right) &\simeq 1 \text{ particle/year m}^2 \\
F\left(>10^{20}\mathrm{eV}\right) &\simeq 1 \text{ particle/century km}^2
\end{aligned}
\tag{1.1}
$$

At a first glance, the all-particle component of the CR spectrum corresponds to a seemingly featureless power-law, apart from the spectral part below 30 GeV which is primarily attributed to solar modulation since the Sun's magnetic field partially shields the Earth from CRs. Consequently, for energies larger than a few GeV the all-particle spectrum could be described by

$$
\Phi(E) = K\left(\frac{E}{E_0}\right)^{-\alpha} \quad \frac{\text{particles}}{\text{cm}^2 \ \text{ s sr GeV}} \tag{1.2}
$$

where α is the differential spectral index of the CR flux and K is the normalization factor. The aforementioned power-law is characterized by (at least) two notable spectral breaks, the first detected at energies of a few PeV ($\sim$ 3-5$\times 10^{15}$ eV) [16] and commonly known as the "knee" while the other is found around $5 \times 10^{18} eV$, and is referred to as the "ankle". The former corresponds to a

spectral steepening from $E^{-2.7}$ to approximately $E^{-3.1}$, which appears to be accompanied by a change in mass composition, with heavier nuclei becoming increasingly more abundant. Cosmic rays detected up to this energy range are customarily attributed to particles produced and accelerated within sources of violent supernovae explosions within the Galaxy. This knee feature could signal the upper energy limit of such cosmic accelerators, for singly-charged particles, such as protons. So far, this aspect has been studied indirectly (with ground-based observations), making the prospect of direct observations (via space-borne experiments) critical in validating previous results and ultimately, establishing the origin of such a feature with great precision.

From the interpretation of current data, the knee feature could be explained by a rigidity[1]-dependent mechanism of CR acceleration in the Galaxy, foreseeing a maximum energy attainable energy by protons around $1 - 3 \times 10^{15}$ eV. In that sense, heavier nuclei would be able to reach larger energies, proportional to their charge number (i.e., iron nuclei with Z = 26 could reach energies approximately 26 times larger than protons).

The knee is believed to signal the upper energy limit in which galactic sources can accelerate protons, with the general consensus favoring a picture of galactic CRs accelerated by diffusive shock acceleration (DSA) in the proximity of strong supernova remnant (SNR) shocks, subsequently injected into the ISM before leaving the Galaxy [12, 17]. A detailed view on the acceleration and propagation mechanisms of CRs in the Galaxy will be provided in the following sections. Finally, the "ankle" feature could mark the transition region between cosmic rays of galactic and extragalactic origin [12]. This transition could arise due to limitations in the maximum energy attainable by cosmic ray accelerators within the Galaxy for heavier nuclei or due to CR energies exceeding the galactic confinement limit, leading to leakage into the ISM.

The CR spectrum is largely dominated by protons with a decreased contribution from helium, carbon and oxygen nuclei, up to iron. Individual contributions of CR primaries at lower energies, are shown in Fig. 1.4. Among the other fluxes, electrons comprise a percentage corresponding to 10^{-2} - 10^{-3} of the proton flux, with positrons and antiprotons corresponding to 10^{-4} (depending on the energy). Finally, the integrated contribution of gamma-rays in the CR spectrum amount

[1]The rigidity term R, is defined as the ratio between the momentum (p) and the charge (Z, measured in units of electron charge) of the particle: $R = \frac{pc}{Ze}$

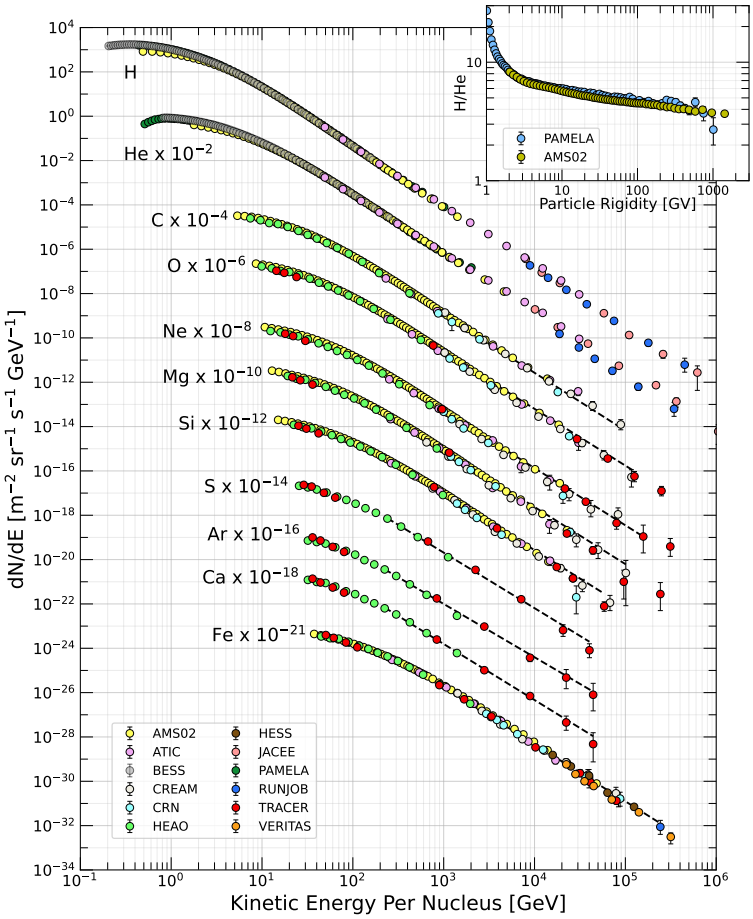

Figure 1.4: Fluxes of primary CR nuclei with respect to the kinetic energy per nucleus. The inset shows the H/He ratio as a function of rigidity. From [18].

to 10^{-4} - 10^{-5} with respect to the proton flux, showing a strong dependence on the energy.

Celestial gamma-rays above 1 GeV are tightly connected to cosmic rays since they are partially[2] produced by interactions of the latter with the interstellar gas along with magnetic and radiation fields during propagation, an example of which is illustrated in the following formula. Such interactions result in a galactic diffuse gamma-ray emission, an effect evidently brighter in the galactic plane and specifically towards the center.

$$\begin{aligned} p + \text{gas} &\rightarrow \pi^0 + \text{anything} \\ &\hookrightarrow \gamma + \gamma \end{aligned} \tag{1.3}$$

[2]High-energy gamma rays can also be produced by Inverse Compton (IC) scattering of high energy cosmic electrons on ambient thermal photons.

1.3 Composition of Cosmic Rays

Following a general overview on the CR spectral characteristics, the discussion will be shifted towards the study of CR elemental abundances along with fluxes of individual nuclei. Fig. 1.5, illustrates the relative abundance of nuclei produced from solar activity and cosmic rays.

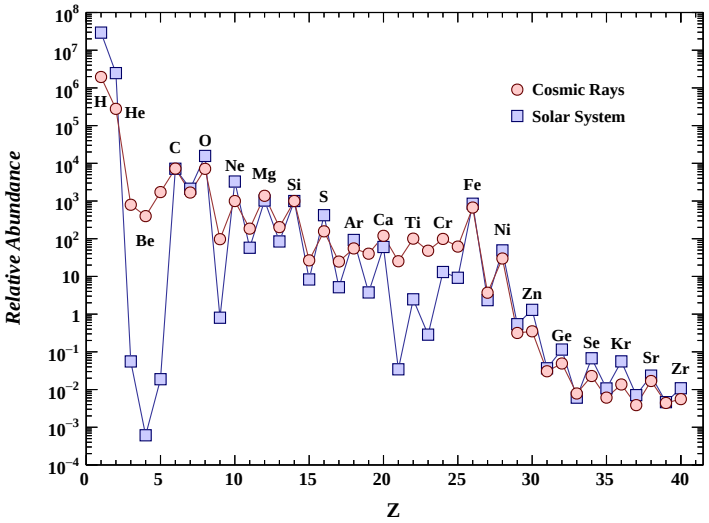

Figure 1.5: Relative elemental abundances from cosmic rays compared to contributions stemming from the solar system at low energies (0.2 GeV/n). Abundances are normalized to Si=10^3. From [18].

A large divergence between the relative abundances of Li, Be, B and Sc, Ti, V, Cr, Mn is evident, when comparing cosmic ray and solar system contributions at low energies (0.2 GeV/n). These elements differ by orders of magnitude in the latter case, since they are absent during stellar nucleosynthesis. On the other hand, they are readily available as products of spallation interactions involving (heavier) CR primaries with the ISM. The ISM is made up mostly of hydrogen and comprises a 5 - 10% of the total galactic mass with an average density of [19]:

$$n_{\mathrm{ISM}} \sim 1 \text{ proton/cm}^3 = 1.67 \times 10^{-24} \text{ g/cm}^3 \tag{1.4}$$

For example, heavier nuclei such as carbon, oxygen and iron, give rise to fluxes of CR secondaries when propagating through the ISM. Consequently, one can determine the amount of matter that is traversed by CRs, assuming a certain knowledge on the spallation cross sections in order to produce the aforementioned nuclei.

Taking into account the galactic disk density, ρ_N ($\sim$ 1 proton/cm^3) along with the grammage[3] traversed by the bulk of cosmic rays during propagation ($X = 5\ g/cm^2$ on average), the thickness of material corresponds to:

$$\ell = X/\left(m_p \rho_N\right) = 3 \cdot 10^{24}\ \text{cm} \approx 1000\ \text{kpc} \tag{1.5}$$

Given that cosmic rays potentially reside within the less dense galactic halo, this factor establishes a minimal threshold for the distance traversed. In any case, the thickness of the galactic disk is quite small in comparison to the average distance covered by CRs. This suggests that the confinement of cosmic rays is a diffusive mechanism where particles undergo significant dispersing motion before ultimately escaping in the intergalactic space. These effects will be discussed in following sections, focusing on the CR acceleration and propagation mechanisms.

1.4 Carbon and oxygen production in stellar environments

A brief overview of the various aspects characterizing the production of medium-mass elements (i.e., CNO group) in stellar environments, will be presented. Stellar nucleosynthesis is fundamental in shaping the elemental composition through a multitude of thermonuclear reactions. The main equation describing the energy production rate within a stellar environment is given by:

$$\frac{dL}{dr} = 4\pi r^2 \rho \varepsilon, \tag{1.6}$$

where, L is the rate of energy flow over a spherical surface of radius r, ρ is the density of the stellar material and ε is the energy generation rate per unit mass. For stars similar to the Sun (in mass), hydrogen and helium are the most common elements in abundance, with carbon, oxygen and iron comprising a lower percentage (1 - 2%) with respect to hydrogen [20]. The main process of energy production in the Sun is determined by the fusion of protons to helium with a subsequent emission of energy, summarized as follows [21]:

[3]The grammage is defined as the average material density traversed by a CR particle, multiplied by its path length.

$$4p \rightarrow {}^{4}\mathrm{He} + 2\mathrm{e}^{+} + 2v_e + 26.73 \text{ MeV} \tag{1.7}$$

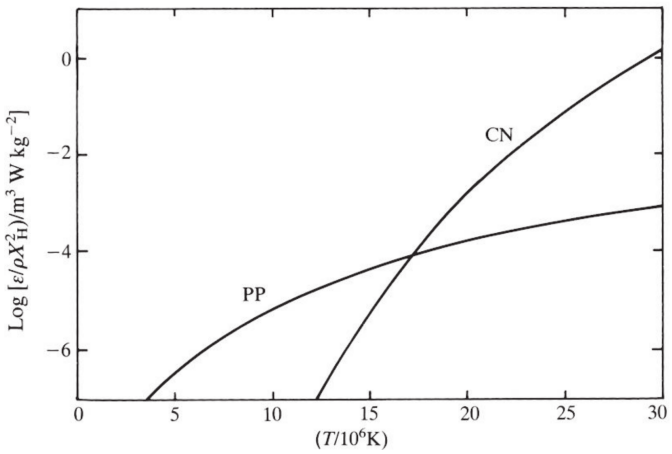

Figure 1.6: Nuclear energy production for the $p-p$ chain and CNO cycle with respect to the temperature. From [22].

This general process takes place in several stages and is customarily known as the proton-proton $(p-p)$ cycle or chain. In that case, the energy production rate for the $p-p$ cycle can be described by $\varepsilon \propto \rho T^4$. If the stellar core temperature is found to be less than approximately 1.7×10^7 K, the aforementioned chain corresponds to the main primary energy source in a star. For temperatures larger than 1.7×10^7 K, the Carbon-Nitrogen-Oxygen (CNO) cycle is dominating the energy production process (as shown in Fig. 1.6). This reaction chain takes place when protons are progressively added into heavier nuclei, which leads to instabilities due to their increasing mass, thus resulting to the production of helium by emission of α-particles. In this cycle, carbon serves as a catalyst[4] for the production of helium, coupled by two $\beta+$ decays occurring during the second and fifth interactions, as seen below:

$$\begin{aligned} &{}^{12}\mathrm{C} + \mathrm{p} \rightarrow {}^{13}\mathrm{N} + \gamma;\ {}^{13}\mathrm{N} \rightarrow {}^{13}\mathrm{C} + \mathrm{e}^{+} + v_{\mathrm{e}};\ {}^{13}\mathrm{C} + \mathrm{p} \rightarrow {}^{14}\mathrm{N} + \gamma \\ &{}^{14}\mathrm{N} + \mathrm{p} \rightarrow {}^{15}\mathrm{O} + \gamma;\ {}^{15}\mathrm{O} \rightarrow {}^{15}\mathrm{N} + \mathrm{e}^{+} + v_{\mathrm{e}};\ {}^{15}\mathrm{N} + \mathrm{p} \rightarrow {}^{4}\mathrm{He} + {}^{12}\mathrm{C}. \end{aligned} \tag{1.8}$$

Finally, the energy production rate for the CNO cycle can be described by $\varepsilon \propto \rho T^{17}$. When the majority of protons in the stellar core are consumed, the energy production mechanism will proceed with helium nuclei as primary source

[4] as opposed to the proton-proton cycle which consumes all its constituents.

of fuel, leading to a simultaneous increase in shell mass and density. The core temperature is increased (above 10^8 K) in order to facilitate the "burning" of helium, consequently leading to an intricate chain of events manifested by triple-alpha reactions [23]. Said reactions are represented (in a simplified manner) by the conversion of three helium nuclei to carbon. From that point onward, oxygen nuclei are produced via radiative alpha-particle capture, as seen below:

$$^4\mathrm{He} + {}^{12}\mathrm{C} \longrightarrow {}^{16}\mathrm{O} + \gamma \tag{1.9}$$

These stellar processes give rise to the production of carbon and oxygen nuclei, being the most abundant primaries after proton and helium in the Universe (as well as elements of interest in this thesis). Following their emission in supernovae explosions, such CR particles are accelerated at their respective sources and subsequently propagate in the ISM. Detailed insights on the CR acceleration and propagation mechanisms will be provided in Sections 1.5 and 1.6.

1.5 Acceleration mechanism of CRs

Two aspects play an important role in defining the cosmic ray acceleration process: the source of power for CR particles and the acceleration mechanism. Both features will be discussed in the following.

1.5.1 Power requirements

The local cosmic ray density amounts to $\rho \simeq 1$ eV/cm^3. The luminosity L_{CR} of galactic CR sources can be determined, taking into account a residence time of CRs, $\tau^{\mathrm{esc}} \sim 10^7$ yr in a galactic disk with a volume of:

$$V_D = \pi R^2 h \sim 4 \times 10^{66} \ \ \mathrm{cm}^3 \tag{1.10}$$

where the galactic disk radius and height correspond to R = 15 kpc and h = 200pc, respectively. In that case the estimated power requirement for cosmic rays, taking into account an energy-dependent CR escape time while assuming a uniform distribution of sources in the galactic disk, is [13]:

$$L_{\mathrm{CR}} = \frac{V_D \cdot \rho_{CR}}{\tau^{esc}} \sim 6 \times 10^{40} \ \mathrm{erg/s} \tag{1.11}$$

This requirement is suggesting supernovae explosions as a possible candidate of CR acceleration. Focusing on the core-collapse supernova paradigm, where the average energy output is close to $E_{SN} \sim 10^{51}$ erg, while taking into account one galactic supernova explosion every 30 years [13], a small percentage efficiency of the aforementioned power would be enough for such explosions to energize all galactic cosmic rays.

1.5.2 Fermi acceleration mechanism

The evidence for supernova explosions as the primary source of cosmic rays (mentioned before) is reinforced by the fact that strong shocks operating through first-order Fermi acceleration naturally generate a cosmic ray spectrum that closely matches the observed one. Initially, Fermi [24, 25] introduced a mechanism to clarify the energy transfer from magnetized clouds to individual particles[5], involving energetic particle scattering off magnetic anomalies, with a change in the particle's motion when encountering magnetized clouds. This effect resulted in energy gains or losses, depending on the nature of the collision. Following numerous interactions between particles and magnetized cloud, the process leads to a net energy gain (averaging over many particle-cloud interactions) of:

$$\frac{\Delta E}{E} = \frac{4\ V^2}{3\ c^2} \tag{1.12}$$

where V denotes the cloud velocity and c represents the speed of light. In this formulation, the acceleration is quite slow since the cloud velocity is generally way smaller than the speed of light.

When the aforementioned process is analyzed in the context of a shock, the scenario changes dramatically. The fluid velocity on both sides of the shock is exceedingly larger than the magnetic anomalies. A particle moving from upstream to downstream (or the other way around) always perceives the fluid on the other side of the shock as approaching (as seen in Fig. 1.7).

Consequently, each time an energetic particle crosses the shock front, its energy gain is considerably faster, it can be shown that:

[5] later named as the second-order Fermi mechanism.

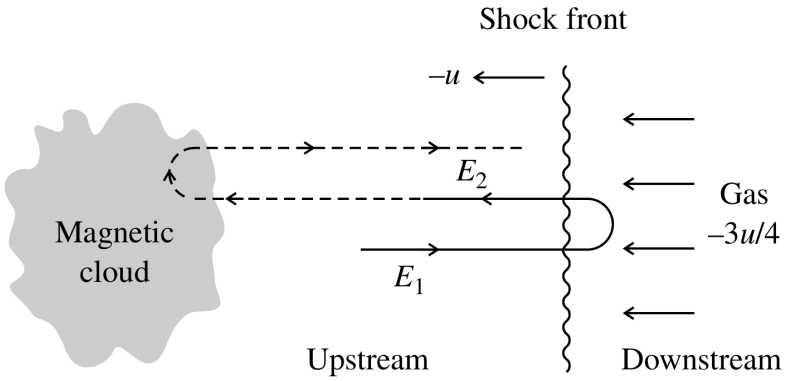

Figure 1.7: Acceleration at a plane shock front. From [20].

$$\frac{\Delta E}{E} = \frac{V_S}{c} \tag{1.13}$$

where V_S represents the shock velocity. The spectrum of particles accelerated at the shock front is provided by $N(p) \propto p^{-\gamma_p}$, where $N(p)$ is the number of particles per unit momentum interval and:

$$\gamma_p = 3\,\frac{\frac{u_1}{u_2}}{\frac{u_1}{u_2} - 1} \tag{1.14}$$

where u_1 and u_2 correspond to the fluid velocities upstream and downstream of the shock, respectively. Additionally the $\frac{u_1}{u_2}$ ratio (commonly known as compression ratio) depends only on the Mach number M_s, thus leading to:

$$\frac{u_1}{u_2} = \frac{4M_s^2}{3 + M_s^2} \tag{1.15}$$

In the case of very strong shocks, i.e., $M_s \gg 1$, the compression ratio is equal to $\simeq 4$ and for the case of relativistic particles, the slope in momentum is equal to a slope in energy thus leading to $\gamma_\mathrm{e} = 2$, which is an exact requirement on the spectral index of accelerated CRs below the knee. It should be noted that particles returning to the shock front are unaffected by scattering, although the maximal number of crossings a particle can sustain (thus affecting the maximum particle energy) depends on the aforementioned scattering. Consequently, in the diffusive regime the time needed for a given particle to perform a full cycle around the shock front is given by [26]:

$$t_{\mathrm{acc}} = \frac{3}{u_1 - u_2}\left[\frac{D_1}{u_1} + \frac{D_2}{u_2}\right] \tag{1.16}$$

with D_1 and D_2 corresponding to the diffusion coefficients upstream and downstream of the shock. Finally, the maximum energies achieved from the acceleration process are delineated by a condition where the acceleration time is less than the age of the system and timescale for losses, as summarized below:

$$t_{\mathrm{acc}}\left(E_{\mathrm{Max}}\right) = \min\left(t_{\mathrm{age}}, t_{\mathrm{loss}}\right) \tag{1.17}$$

In conclusion, if the acceleration process of galactic CRs up to the knee is caused by SNR shocks, it must be due to the substantial amplification of the magnetic field in their vicinity, compared to the ISM average. Alternatively, if supernova remnants are the primary sources of galactic CRs, then they must convert about 10% of the blast wave's kinetic energy into accelerated particles. This implies that the test-particle description of the shock acceleration process might be inadequate and the dynamical particle feedback on the accelerators must be considered [17]. Thus, a full description of the acceleration process can be achieved through the Non-Linear Diffusive Shock Acceleration (NLDSA) framework coupled with Magnetic Field Amplification (MFA). A few considerations on non-linear acceleration effects are briefly summarized in the following [12]:

- Supernova shocks generate CR particles that impact the acceleration process and shock dynamics via two effects: precursor creation from slowed down upstream plasma due to pressure from accelerated particles, and radiative-like shocks from the escape of high-energy particles. These effects lead to a modified particle acceleration spectrum, that no longer corresponds to a perfect power law.

- Magnetic field amplification at the shock surface is required to account for most cosmic rays up to 10^6 GV. The resulting non-linear diffusion coefficient is responsible for narrow X-ray rims observed in young SNRs and is determined by the distribution function of accelerated particles.

- Magnetic pressure, while only a fraction of the ram pressure, can affect the compression factor at the shock, leading to a modified spectrum of accelerated particles, and thus impact the level of magnetic field amplification, another non-linear aspect of Diffusive Shock Acceleration.

1.6 Propagation of CRs

The CR spectrum discussed previously, results from the synergy of injection and propagation effects. During propagation, particles might experience interactions with the ISM, convection by galactic winds, energy losses or gains (due to reaccelerations), or radioactive decays, before reaching Earth or escaping the Galaxy (as seen in Fig. 1.8). These processes have to be "translated" in differential transport equations including the number density N_i, atomic and mass numbers Z_i, A_i of every cosmic ray species as a function of the position, energy and time. Synthesizing all of the above contributions, lead to [13]:

$$\begin{aligned}\frac{\partial N_i}{\partial t} = C_i + \nabla \cdot (D\nabla N_i - \mathbf{V}N_i) + \frac{\partial}{\partial E}\left(b(E)N_i\right) + \\ - \left(n\beta_i c\sigma_i^{\text{spall}} + \frac{1}{\gamma_i \tau_i^{\text{decay}}} + \frac{1}{\hat{\tau}_i^{\text{esc}}}\right) N_i + \\ + \sum_{j>i} \left(n\beta_j c\sigma_{ji}^{\text{spall}} + \frac{1}{\gamma_j \tau_{ji}^{\text{decay}}}\right) N_j\end{aligned} \tag{1.18}$$

where:

1. The first term, C_i, corresponds to the injection spectrum.
2. The second term accounts for diffusion and convection, where D corresponds to the diffusion coefficient and $\mathbf{V}$ to the flow velocity.
3. The third term represents changes in the energy spectrum due to energy losses or reacceleration, at a rate of $dE/dt = -b(E)$.
4. The fourth term quantifies the losses due to spallation, radioactive decays as well as the probability of escaping the Galaxy, where n constitutes the number density of the ISM.
5. The fifth term corresponds to the gains due to spallation or decays of heavier nuclei.

This equation includes all physical processes and its possible solutions can be obtained in a semi-analytical or numerical approaches, with the latter involving the usage of sophisticated frameworks. A more simple solution to the CR propagation can be obtained via the so-called leaky box model. Essentially, the fundamental form of the leaky box model is characterized by a specific volume (i.e., a cylinder)

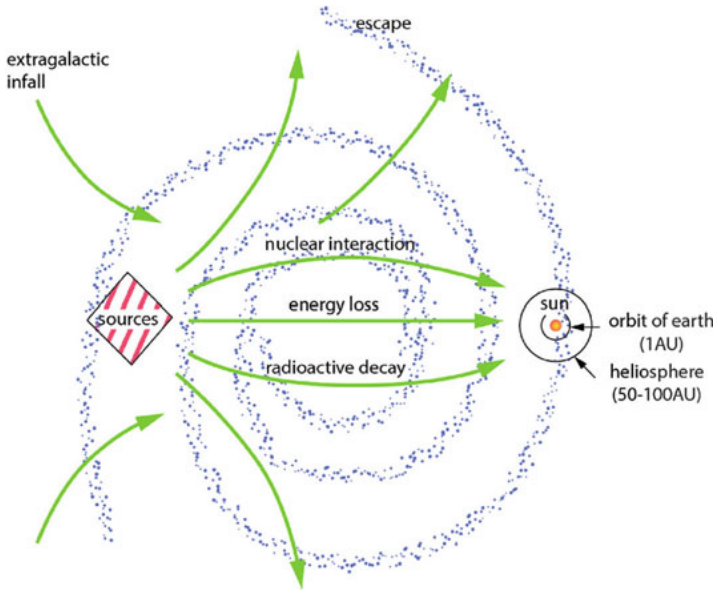

Figure 1.8: Schematic view of the CR propagation mechanism in the Galaxy From [11].

of a given radius and height, analogous to the Galactic disk size. In this volume, sources are evenly distributed and cosmic rays are permitted to propagate freely within, with a given escape probability including diffusion and convection effects. Thus, the equation is written as:

$$0 \simeq C_i - N_i \left(n\beta_i c\sigma_i^{\text{spall}} + \frac{1}{\gamma_i \tau_i^{\text{decay}}} + \frac{1}{\tau_i^{\text{esc}}} \right) + \sum_{j>i} N_j \left(n\beta_j c\sigma_{ji}^{\text{spall}} + \frac{1}{\gamma_j \tau_{ji}^{\text{decay}}} \right). \tag{1.19}$$

In that case, the first term corresponds to the contribution of sources, while the second and third refer to energy losses (spallation, decays, escape) and gains (spallation or decays), respectively. The escape time in this instance depends on the particle energy and charge by the following: $\tau_i^{\text{esc}} \propto E^{-\delta}/Z_i$, where the δ index if found to be $\delta \sim 0.6$ when taking into account the Milky Way size and related magnetic fields.

The previous equation can be simplified further when examining primary or secondary CRs. Therefore, spallation contributions from heavier nuclei in the case of primary CRs, along with an assumption involving negligible production of secondaries at the sources, can be excluded from this paradigm. In that case, defining a primary CR nucleus P, with energy E and speed β, leads to the following equation:

$$\frac{N_P(E)}{\tau^{\text{esc}}(E)} \simeq C_P(E) - \frac{\beta c \rho_H N_P(E)}{\lambda_P(E)} \Longrightarrow N_P(E) \simeq \frac{C_P(E)}{1/\tau^{\text{esc}}(E) + \beta c \rho_H / \lambda_P(E)} \quad (1.20)$$

where $\rho_H = n m_H$ is the target density and λ_P the interaction length (in g/cm^2). Finally, in the case of highly energetic primaries with interaction lengths considerably larger than the escape length, the equation can be be written as follows:

$$N_p(E) \simeq C_p(E) \tau^{\text{esc}}(E) \quad (1.21)$$

Considering that $C_P(E) \propto E^{-2}$, which results from CR accelerated at the sources, the expected spectrum would be:

$$N_p(E) \propto E^{-2.6} \quad (1.22)$$

Secondary-over-primary ratios such as B/C and B/O show a strong energy dependence especially at higher energies, stemming from an increased escape probability, while ratios of primary nuclei such as C/O, do not show such a dependence. By measuring both types of ratios with respect to the energy, great insight on propagation and diffusion properties of CRs can be inferred.

1.7 Detection of Cosmic Rays

In previous sections, an introduction to the CR spectrum has been provided, highlighting its main features and aspects, in addition to an illustration of the prevailing acceleration and propagation mechanisms in the Galaxy. This section will emphasize on one of the most decisive and challenging steps, which pertains to the precise detection of said CRs reaching Earth. Results previously shown in Figs. 1.3 and 1.4 culminate from the rigorous efforts represented by a multitude of space-borne and ground-based experiments over a span of numerous years.

CRs arriving at Earth can be detected above the atmosphere with space- or balloon-borne detectors, or by ground-experiments located at various altitudes. Detection of energetic particles from space is regarded as *direct* CR detection, while *indirect* detection refers to observations with ground-based instruments (Fig. 1.9). The difference between direct and indirect CR detection is found in the presence of Earth's atmosphere, which promotes the production of extensive

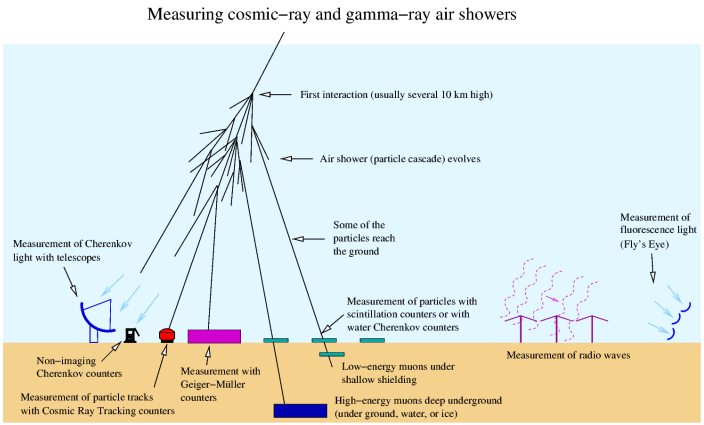

Figure 1.9: Detection of CR showers, by a variety of ground-based detectors. From Max Plank Institut.

air showers (EAS) when an energetic cosmic ray impinges on its top. Secondary particles originating from EAS are detected by ground-based experiments with the aim of reconstructing the primary CR energy, while in the case of space-borne instruments, the primary CR is directly interacting with the detector's sensitive surface(s).

Both detection techniques show advantages and disadvantages. Space detectors are naturally limited in size, weight and power budget due to strict requirements necessitated by their respective missions, while ground based detectors are not affected by such prerequisites. For that reason, due to very low fluxes, highly–energetic particles (above "knee" energies in the CR spectrum) were customarily detected only via indirect CR experiments, although with fundamental difficulties in making composition studies without large systematic uncertainties. On the other hand, direct CR experiments provide very precise energy and charge measurements of incident particles with smaller systematics. Crucial information has been well-received from extended observations of ground and space based experiments alike, although there is an imminent need to explore distinct features in CR energy spectra (and mass composition) at increasingly higher energies, by means of direct measurements.

This thesis is emphasizing on direct measurements of galactic CRs with space-borne detectors in a range of hundreds of GeV to hundreds of TeV, hence a brief presentation of the various instruments is deemed relevant for the completeness of this introduction. The basic characteristics concerning a selection of previous, current and future generation instruments will be illustrated in the following.

1.7.1 Examples of space-borne instruments

ATIC

The Advanced Thin Ionization Calorimeter (ATIC) was a balloon-borne experiment dedicated to the measurement of energy and composition of cosmic rays (shown in Fig. 1.10a). It comprised a bismuth germanate (BGO) calorimeter consisting of eight-layers, in addition to a matrix of silicon sensors in order to measure the trajectory and charge of impinging particles [27]. The mission was launched from Antarctica and performed three successful flights.

CREAM

Cosmic Ray Energetics And Mass (CREAM) [28] was a balloon-borne experiment designed to investigate high energy cosmic rays from protons up to iron nuclei, in the multi-TeV energy range. CREAM (as viewed in Fig. 1.10b), comprises a series of detectors, including a silicon charge detector, a sampling calorimeter featuring a tungsten absorber, a transition radiation detector, and a time-of-flight system. It provided two independent measurements of the particle energy and four independent measurements of the electric charge. The mission was launched from Antarctica and performed seven flights, from 2004 to 2016.

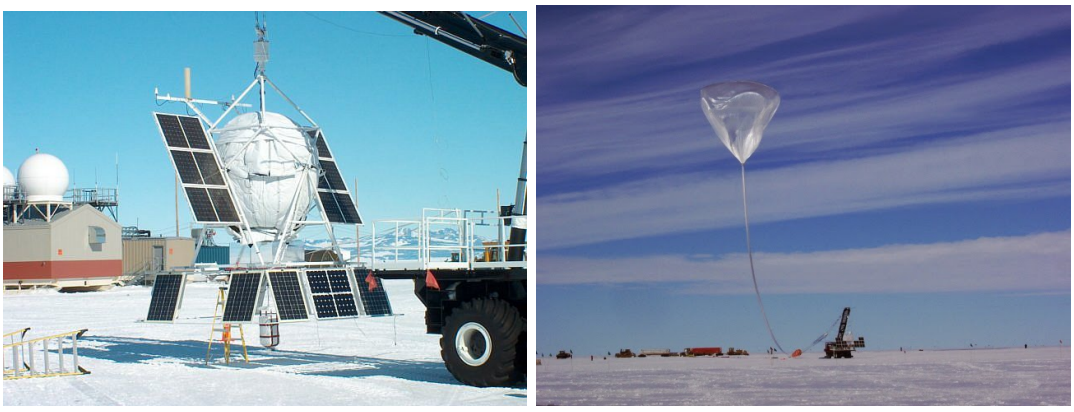

(a) ATIC **(b)** CREAM

Figure 1.10: (a) ATIC and (b) CREAM balloon detectors before flight. From ATIC and CREAM experiment web pages.

PAMELA

The Payload for Antimatter-Matter Exploration and Light-nuclei Astrophysics (PAMELA) [29] was attached to the Resurs-DK1 Earth observation satellite and launched by a Soyuz-FG rocket in 2006. It collected CRs until 2016, where the host satellite operations ended. PAMELA consists of several sub-detectors, including a magnetic spectrometer, a silicon-tungsten calorimeter, a time-of-flight system, and an anticoincidence detector. The main scientific objective of PAMELA was to study the CR antiproton and positron fluxes, as well as measuring the spectra of protons, electrons, and light nuclei in the energy range from 100 MeV to several hundred GeV.

Fermi-LAT

The Fermi Gamma-ray Space Telescope was initially designed as a gamma-ray telescope but provided great insights in charged CRs, as well. The payload was launched by a Delta-II rocket in 2008 and comprised two instruments: the Large Area Telescope (LAT) [30], consisting of a segmented tracker, a calorimeter, and an anticoincidence detector that allow for a precise measurement of the photon energy and direction[6] along with a Gamma-ray Burst Monitor (GBM), an array of scintillators on the side of the spacecraft for detection of Gamma Ray Bursts. The main scientific objective of Fermi is to study the gamma-ray emission from sources such as pulsars, supernova remnants, and active galactic nuclei in the energy range from 20 MeV to over 300 GeV and lower energies with the GBM.

AMS-02

The Alpha Magnetic Spectrometer (AMS-02) [31] is a large CR detector (presented in Fig. 1.12a), installed in 2011 onboard the International Space Station (ISS) by one of the very last missions of the Space Shuttle (Shuttle Endeavour, mission STS-134). The payload amounts to a 7-ton instrument, consisting of a permanent magnet, a silicon tracker, a transition radiation detector (TRD), four time-of-flight detectors (TOF), a ring-imaging Cherenkov detector (RICH) and an electromagnetic calorimeter (ECAL). It remains in stable operations, having collected more than 218 billion CR events, with its main scientific objectives revolving around the precise spectral measurement of CR particles up to TeV

[6] following a conversion into electron-positron pairs within the LAT system

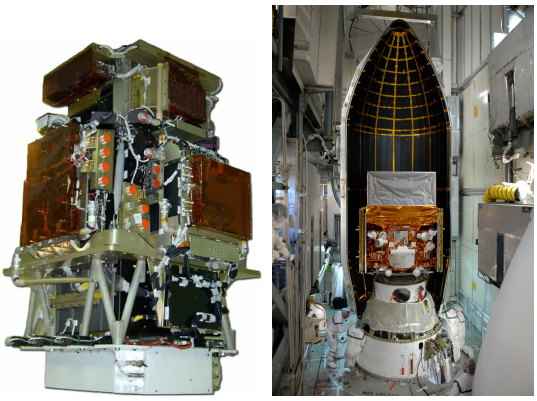

(a) PAMELA **(b)** FERMI

Figure 1.11: Layout of (a) the complete PAMELA detector and (b) preparatory procedure for the Fermi Gamma-Ray Telescope launch (not to scale). From PAMELA and NASA/Fermi experiment web pages.

energies, while searching for antimatter particles and signatures of dark matter in CRs.

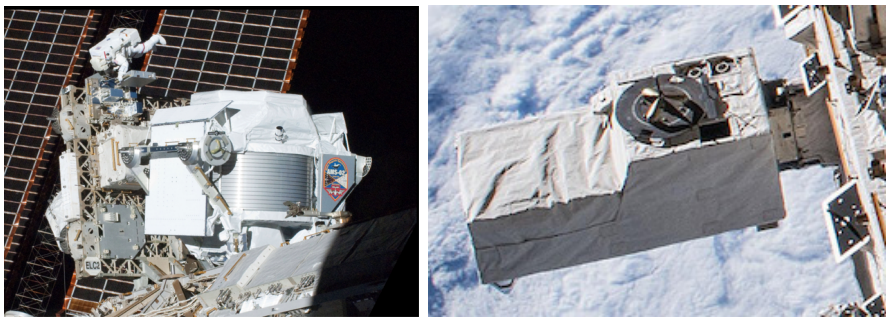

(a) AMS-02 **(b)** CALET

Figure 1.12: Layouts of (a) AMS-02 and (b) CALET payloads installed on the ISS. From AMS-02 and CALET mission web pages.

CALET

The CALorimetric Electron Telescope (CALET) [32, 33] is an additional CR observatory onboard the ISS, as illustrated in Fig. 1.12b. It was successfully launched by the JAXA mission HTV-5 in 2015 and has been acquiring data ever since, with its main scientific goals focusing on the study of cosmic electrons and nuclei up to 20 and 100 TeV, respectively. The payload comprises two layers of segmented plastic scintillators for charge identification, a tungsten-scintillating fiber imaging telescope with a depth of 3 radiations lengths (X_0) and a lead-tungsten calorimeter with 27 X_0 thickness.

Finally, Fig. 1.13 presents a comparison between a sample of previous and current generation CR detectors, scaled according to their original dimensions. Only the respective sub-detectors are shown, without the PaMeLa and AMS-02 magnets. The illustrated subsystems correspond to: Fermi-LAT; anti-coincidence detector (ACD), tracker (TKR) and calorimeter (CAL), AMS-02; transition radiation detector (TRD), time of flight (TOF), tracker layers, electromagnetic calorimeter (ECAL) and ring imaging Cherenkov detector (RICH), CREAM-II; timing charge detector (TCD), Cherenkov detector (CD), silicon charge detector (SCD) and calorimeter (CAL), PaMeLa; time of flight scintillators (S1–S3), tracker (TKR), calorimeter (CAL) and neutron detector.

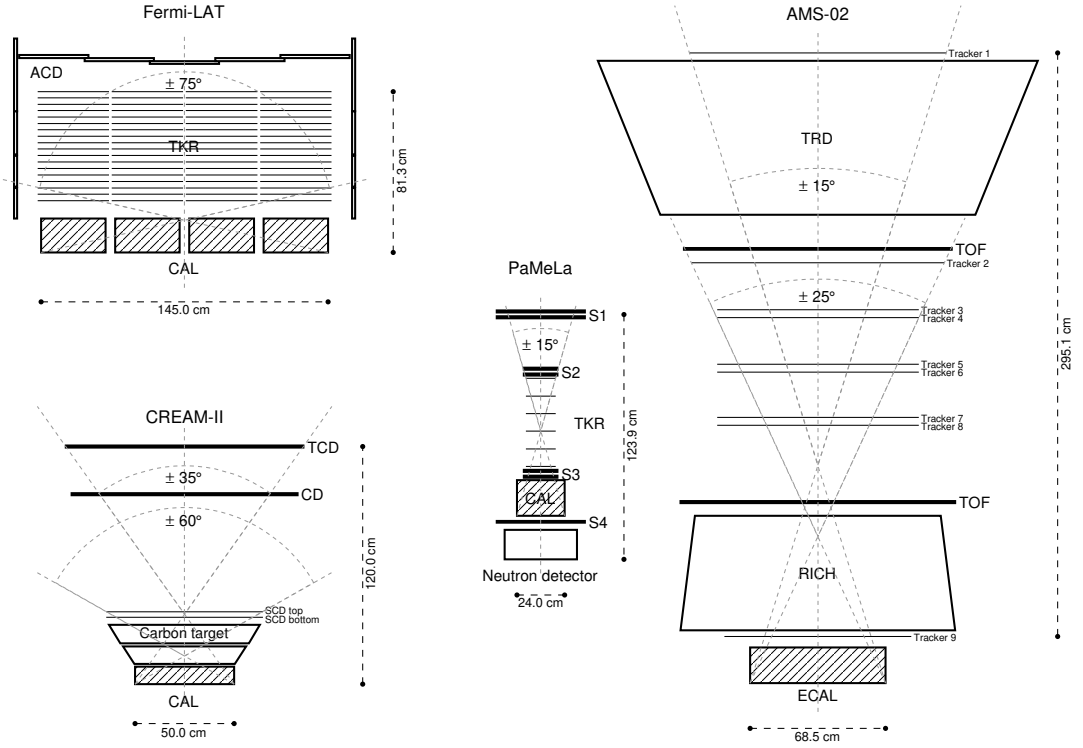

Figure 1.13: Schematic view regarding some of the previous and current space- or balloon-borne cosmic-ray detectors (all dimensions are meant to be in scale). Only the detector subsystems are shown (PaMeLa and AMS-02 magnets are not represented). From [11].

DAMPE

The Dark Matter Particle Explorer (DAMPE), is a space–borne detector designed for precise galactic CR studies in a wide energy range (up to hundreds of TeV), along with detailed measurements of high–energy gamma–rays and indirect searches of Dark Matter (DM) annihilation/decay to detectable particles. The satellite was launched into a sun–synchronous orbit at 500 km, on December 17th 2015 and has been successfully acquiring data ever since. DAMPE has been an important part of this thesis and will be thoroughly introduced, in Chapter 2.

HERD

The High Energy cosmic-Radiation Detection (HERD) facility is one of the leading projects among future space-borne instruments to be installed on - board the China Space Station (CSS), around 2027. Its main scientific goals include: accurate measurements of CR energy spectra up to the highest achievable energies in space ($\sim$ few PeV), gamma-ray astronomy and transient studies, along with indirect searches for Dark Matter (DM). HERD is uniquely configured to accept particles from both its top and four lateral sides. Due to its novel design, an order of magnitude increase in geometric acceptance is foreseen, compared to current generation experiments.

HERD is configured around a highly-segmented (55 X_0, 3 λ_I) 3D calorimeter (CALO). A Fiber Tracker (FIT) is installed on all active sides, with a Plastic Scintillator Detector (PSD) covering both instruments. Finally, a Silicon Charge Detector (SCD) envelops the aforementioned sub-detectors, while a Transition Radiation Detector (TRD) is situated on one of the lateral sides, for energy calibration in the TeV range. Since an important part of this thesis is dedicated to the realization of HERD, a detailed detector overview will be provided in Chapter 5.

1.8 Main results on intermediate mass CR nuclei

DAMPE

The main focus of this dissertation is to provide spectral measurements related to CR carbon and oxygen nuclei, along with additional insights on flux ratios such as C/O, B/C, and B/O, with the DAMPE space mission. In Fig. 1.14, published results on CR carbon and oxygen fluxes are presented in the energy range of 10 GeV/n to a few TeV/n. An interesting feature has been detected in both spectra, represented by a hardening, evident at energies of approximately 300 GeV/n (for carbon and oxygen), the shape of which is consistent with observations from previous and current CR experiments.

The existence of this feature rejects the idea pertaining to a universal injection spectrum at the sources and a single, featureless power-law spectrum extending up to PeV energies, as introduced in the beginning of this chapter. Such a feature is visible only with current generation direct measurements and challenges the validity of prevalent CR models. In conjunction to this feature, some disagreement can be noted (at lower energies), between carbon and oxygen spectra of AMS-02 with respect to the majority of experiments, regardless of instrument nature (magnetic spectrometers or calorimetric experiments). Such a variation might be attributed to differences in the energy scale, although a more focused work is definitely needed and more measurements are welcome.

This thesis aims to clarify the picture regarding both fluxes at lower energies (below 100 GeV/n), provide a possible confirmation on the novel hardening feature, with an ultimate goal of extending current spectral measurements in the multi-TeV region for the first time, with precise measurements. In this region, a softening feature could be evident for carbon and oxygen, as in recent measurements of DAMPE proton and helium fluxes, where the aforementioned spectral feature was detected approximately at 15 TV [34, 35].

An additional aspect of this work is associated to flux ratios such as carbon-over-oxygen ratio, as well as secondary-over-primary ratios like boron-over-carbon and boron-over-oxygen. As mentioned before, these ratios are valuable probes in comprehending various features of the CR diffusion and propagation mechanism in the Galaxy. Fig. 1.15, illustrates the current landscape of measurements, manifested by a plethora of balloon- and space-borne experiments. The main message coming from the C/O ratio is an overall balance between the two contributions across the spectrum, although with an increasing trend towards

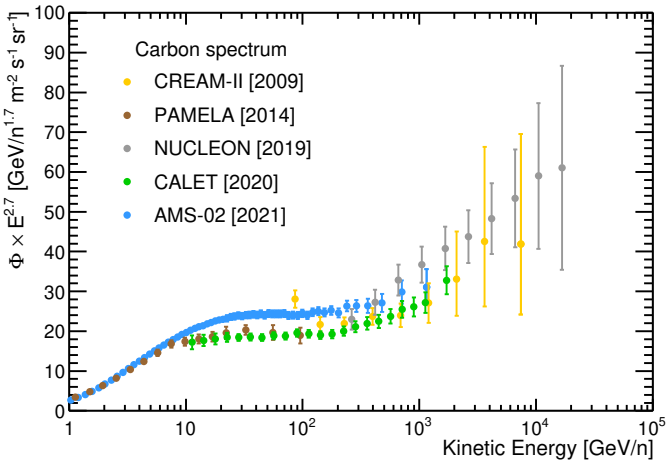

(a) Carbon flux

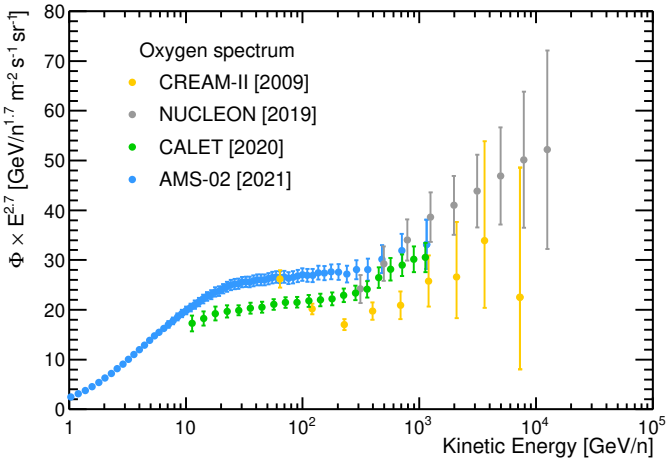

(b) Oxygen flux

Figure 1.14: Published results on (a) carbon and (b) oxygen fluxes. The various data-sets correspond to CREAM [36], PAMELA (for carbon) [37], NUCLEON [38], CALET [39] and AMS-02 [40] experiments.

the TeV/n region. Such a behavior would be interesting to probe with more precise measurements and lower uncertainties. Regarding the B/C and B/O ratios, an overall agreement is achieved between the various measurements, although additional measurements are needed in the multi-TeV/n region, since most experiments conclude their results around 1 TeV/n. A hint of a spectral break could be seen but no robust results can confirm a possible variation from a single power-law which reproduces both flux ratios up to now.

Summarizing, very insightful results have been obtained with direct CR measurements in recent years, which unveiled inherent characteristics in a variety

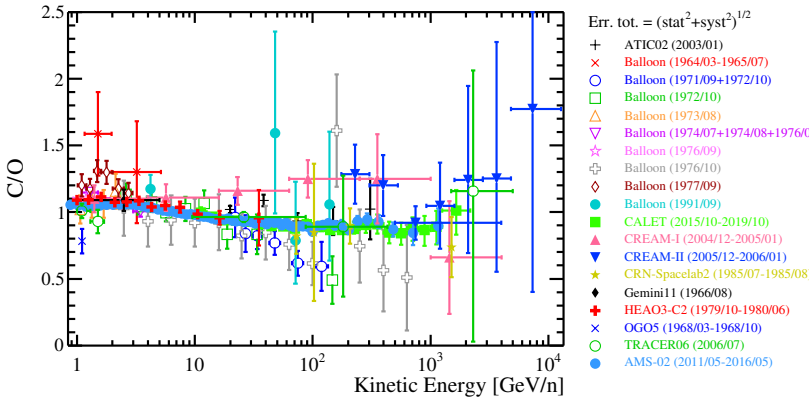

(a) C/O ratio

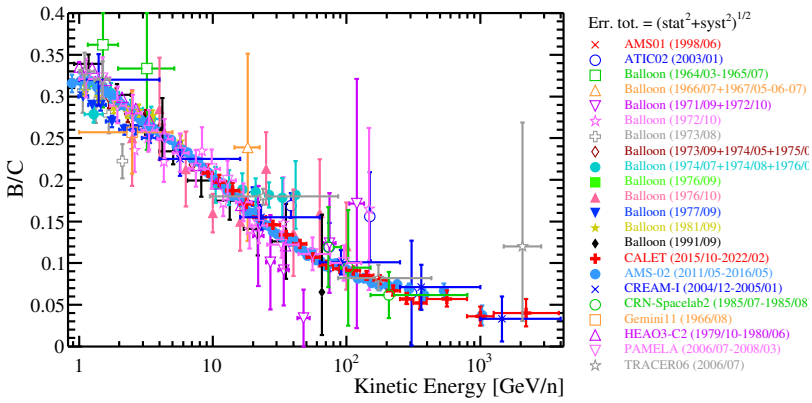

(b) B/C ratio

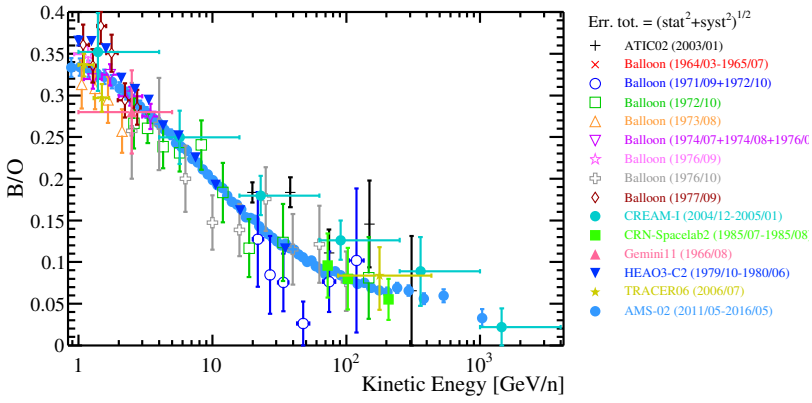

(c) B/O ratio

Figure 1.15: Published results on (a) carbon-over-oxygen, (b) boron-over-carbon and (c) boron-over-oxygen flux ratios. Datasets correspond to [41–52] for balloon experiments and [53–59] for space-borne detectors. Converted from [60].

of nucleonic spectra, especially for carbon and oxygen. The same goes for primary-primary and secondary-primary ratios, which can help clarify the diffusion and propagation mechanisms. These goals can be attained with very precise results extending to the multi-TeV range, being a major scientific objective of DAMPE and a great part of this thesis. Chapters 2,3 and 4 are dedicated to DAMPE, starting from a detailed introduction, moving on to the analysis procedure, all the way up to novel measurements concerning the entirety of scientific objectives discussed above.

1.9 Future space-borne experiments

HERD

As discussed previously, highly–energetic particles were customarily detected only via indirect CR experiments, although with large systematic uncertainties. At the same time direct CR experiments provide precise measurements both in energy and charge with small systematics. Keeping in mind that space detectors have a smaller overall exposure than ground-based experiments along with a lower power and mass budget, optimized solutions are sought in order to reach higher energies.

Consequently, forthcoming space–borne experiments should combine an increased geometric factor (> 1 m^{2}sr), with extended mission duration ($\geq$10 yr), along with high discrimination power in separating different cosmic radiation components. Therefore, an overall enhancement in detector exposure should be attained, allowing for a deeper understanding of distinctive structures in CR spectra up to the highest achievable energies. Merging all of the above–stated properties will lead to a great enhancement in the instrument's exposure, hence allowing for an advanced understanding of the intricate features and distinctive structures in CR spectra covering a broad energy range.

Taking into account the fruitful and long-standing experience of DAMPE in orbit, coupled with the experience gained from the various challenges that always accompany a space mission, an additional part of this work is dedicated to the development and realization of a novel CR detector.

HERD is designed to satisfy all of the requirements presented above. Specifically, the payload is optimally designed to be a precise probe of various CR nuclei up to the PeV energy range, while also providing insights on various topics

concerning gamma ray astronomy and dark matter searches. Chapters 5 and 6 are dedicated to a brief detector introduction and specific results regarding the Plastic Scintillator Detector (PSD), being one of its main instruments, aiming to provide gamma-ray and charged particle trigger signals, together with an essential charge measurement for particle identification purposes.

1.10 Summary

This chapter served as a general introduction to CRs, emphasizing mainly on highly-energetic particles originating in the Galaxy. Particular attention has been given to the intricate acceleration and propagation mechanisms, aspects which govern the final CR spectra of primary and secondary CRs arriving at Earth. These particles travel the intergalactic space and are detected by state-of-the-art detectors located at ground level or in space.

This thesis will focus on space-borne detectors, especially oriented towards precise spectral measurements of carbon and oxygen nuclei, along with their respective flux ratios i.e., C/O, B/C and B/O, from a few GeV/n up to the multi-TeV/n region, with DAMPE. These activities will be presented in Chapters 2, 3 and 4. A supplementary part of this work is dedicated to the realization and optimization of HERD, a future space-borne detector. Main goal of this activity pertains to the optimal configuration regarding one of its main sub-systems. These activities will be highlighted in Chapters 5 and 6.

Chapter 2

The Dark Matter Particle Explorer

Following the introduction on the origin, acceleration and propagation mechanisms of CRs in the Galaxy, this chapter will focus on introducing one of the main representatives pertaining to direct observations of Galactic CRs (GCRs) and a major aspect of this thesis. The Dark Matter Particle Explorer (DAMPE)[61], or *Wukong*[1] (as nicknamed in China) is a space-borne detector designed for direct detection of GCRs, while providing insights on gamma rays and possible indirect signatures of Dark Matter (DM).

2.1 The mission

DAMPE was initially installed on a Long March 2D rocket and subsequently launched on December 17th, 2015 from the Jiuquan Satellite Launch Center (Gobi desert, China), as seen in Fig. 2.1.

The payload was successfully injected in a sun-synchronous, Low-Earth Orbit (LEO), at an altitude of 500 km, with an inclination angle of 97.4 degrees and orbital period of 95 minutes. Following the complete range of consistent ground and on-orbit calibrations [62], the detector is operating in a stable manner throughout its lifetime, thus allowing for high quality data collection.

An international collaboration is formed around the DAMPE initiative, involving numerous universities, institutes and laboratories from China, Italy and Switzerland. The experiment aims to address open questions and assist in current efforts concerning: (1) a deeper understanding of the acceleration mechanism of particles in stellar environments, while realizing the nature of propagation of CRs

[1] In Chinese mythology, Wukong stands for the legendary Monkey King, a trickster god whose name represents the journey from ignorance towards spiritual ascension or enlightenment.

in the Interstellar Medium, (2) detecting gamma ray signatures of galactic and extragalactic origin and (3) probing the essence of Dark Matter by its annihilation/decay in observable particles. The DAMPE instrument is able to detect electrons, positrons and gamma rays in the energy range of approximately 5 GeV to 10 TeV and protons with heavier nuclei spanning from few tens of GeV to few hundreds of TeV.

Figure 2.1: Launching of the Long March 2D rocket containing the DAMPE payload.

2.2 Detector overview

The DAMPE payload (highlighted in Fig. 2.2) consists of four sub-detectors (starting from the top): a Plastic Scintillator Detector (PSD), a Silicon-Tungsten tracKer-converter (STK), a deep Bismuth Germanium Oxide (BGO) calorimeter (32 X_0 and 1.6 λ_I), along with a NeUtron Detector (NUD).

A highly-energetic particle impinging on DAMPE should deposit energy within the PSD, which is configured to precisely measure the charge as well as providing an effective veto in the case of gamma rays. Subsequently, the particle should traverse the STK, which accurately reconstructs its track and converts incoming gamma-rays into electron-positron pairs (due to the inclusion of tungsten layers), while also providing an additional charge measurement. Afterwards, the propagating particle should deposit its energy inside the BGO calorimeter, by means of electromagnetic or hadronic cascades, therefore yielding valuable information regarding its overall identification. Finally, an additional level of electron-hadron discrimination from showers initiated in the BGO is achieved with the NUD. The above-stated sub-detectors were precisely configured and thoroughly tested in order to achieve optimal detection efficiency and overall structural robustness over an extended period of time. All sub-detectors were

combined in a single prototype - the DAMPE Engineering Qualification Model - which was subsequently subjected to a multitude of particle beams of various energies, at the facilities of the European Organization for Nuclear Research (CERN). The selected beams included electrons (500 MeV - 250 GeV), gamma rays (500 MeV - 250 GeV), muons (150 GeV), pions (π^+: 10 - 100 GeV, π^-: 3 - 10 GeV), protons (3.5 - 400 GeV) and heavier nuclei produced from the fragmentation of argon (30 - 75 GeV/n) and lead (30 GeV/n) [61].

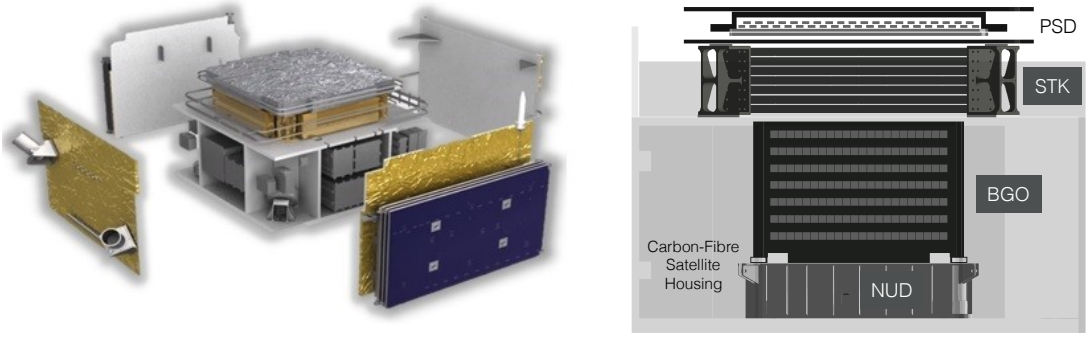

(a) **(b)**

Figure 2.2: The complete DAMPE payload in its (a) exploded view along with (b) a cross-section illustrating its various sub-detectors. From [63].

2.2.1 Plastic Scintillator Detector (PSD)

The Plastic Scintillator Detector (PSD) [61, 64] is the first sub-detector an impinging particle will encounter and is designed to accurately measure the electric charge Z, while providing an effective way of discriminating gamma-rays from charged particles. The PSD is configured as follows (Figure 2.3): two double-layered planes, orthogonally interleaved in X and Y axes (where the Z axis points towards the nadir), readout by two PhotoMultiplier Tubes (PMTs) on each side.

The full PSD consists of 82 plastic scintillator bars manufactured by Eljen Technology (EJ-200) [65], while the readout PMTs were provided by Hamamatsu Photonics (R4443) [66]. Each bar measures $88.4 \times 2.8 \times 1.0$ cm^3, leading to an integrated area of 82.5×82.5 cm^2. The instrument is designed to cover a wide dynamic range, from protons ($Z = 1$) all the way up to iron nuclei ($Z = 26$), thus good energy resolution, high detection efficiency and broad dynamic range are primary objectives towards its realization. Each PMT covers a range of 0.1 to

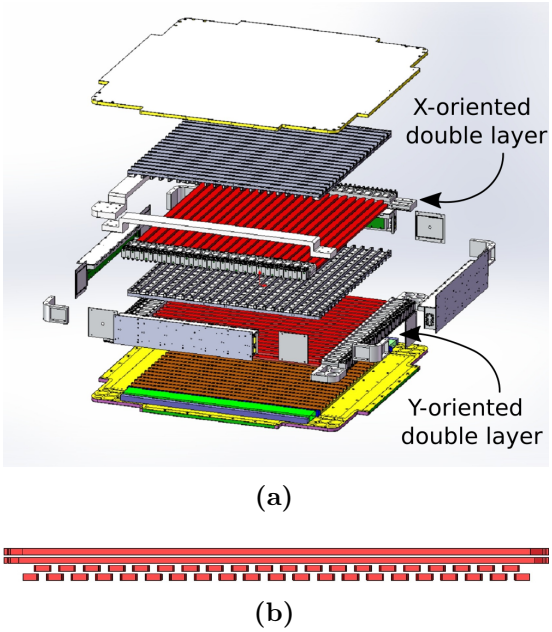

Figure 2.3: Detailed schema of the PSD sub-detector including (a) an exploded view of its X- and Y-oriented planes, along with (b) a cross-section of its four consecutive layers, arranged in two orthogonally interleaved planes [64].

1400 MIPs[2], "where a nominal value of an energy deposition by a particle with Z = 1 in a single PSD bar amounts to to approximately 2 MeV.

Every performance aspect was tested both via beam test campaigns at CERN as well as in orbit. The detection efficiency concerning charged particles interacting with a single PSD module amounts to $\geq 95\%$ while the collective PSD efficiency corresponds to $\geq 99.75\%$. Consequently, given its wide dynamic range and great detection efficiency, the PSD can provide detailed charge measurements from protons up to iron (Fe) and nickel (Ni) nuclei extracted from two years of flight data, as shown in Fig. 2.4. In order to obtain a significant reduction in detection inefficiencies from particles striking in-between the bars, all PSD layers were staggered within 8 mm of distance. An additional measure of background and noise reduction pertains to the trajectory reconstruction procedure, where consistent event information is requested between all sub-detectors, hence maximizing the probability of an accurate event reconstruction.

[2]Practically, relativistic particles with mean energy deposition rate (in matter) close to the minimum (determined by the Bethe-Bloch formula) are considered to be minimum ionizing particles or MIPs

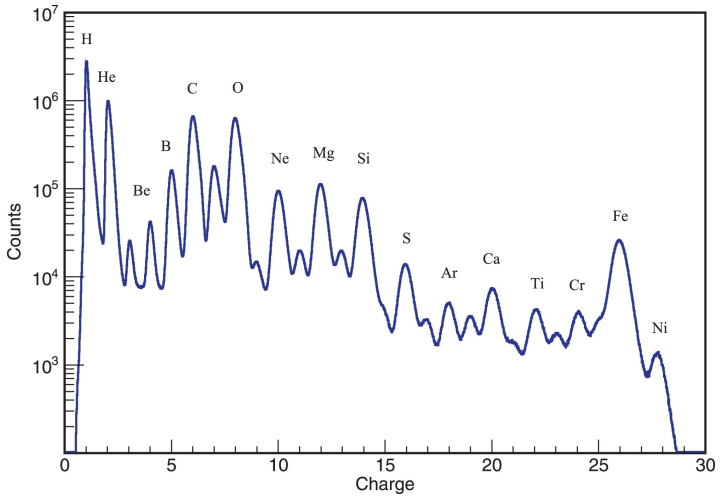

Figure 2.4: Analyzed PSD Charge spectrum from protons to nickel, concerning two years of DAMPE flight data. From [67].

2.2.2 Silicon-Tungsten tracKer (STK)

The Silicon-Tungsten tracKer (STK) [68] is situated beneath the PSD in order to identify the trajectory of impinging charged particles, while eliciting the production of electron-positron pairs in the case of incoming gamma-rays, as well as providing an additional charge measurement. The detector comprises six detection planes (Fig. 2.5), each one instrumented with two orthogonally interleaved layers of single-sided silicon micro-strip detectors (SSDs). Such a configuration allows for coherent measurements of X and Y coordinates, leading to a position-accurate hit of incoming particles.

In its entirety the STK consists of 192 ladders and 768 SSDs, with a single silicon layer including 16 ladders, each consisting of 4 SSDs (Fig. 2.6), manufactured by Hamamatsu Photonics [66]. Each SSD covers an area of 9.5 $\times$ 9.5 cm^2 with a pitch of 121 μm and 320 μm of thickness [63]. Additionally, three planes of tungsten (1 mm thickness) were instrumented in-between layers 2, 3 and 4, in order to assist the production of e^+e^- from gamma-rays. Finally, the STK strip-readout is done only for every other strip to regulate power consumption, electronics density and data transfer.

The STK is connected to a total of eight Tracker Readout Boards (TRB) (Fig. 2.5), providing: (a) the voltage supply, communication with the (b) data acquisition (DAQ) board and (c) the analog-to-digital (ADC) board. The detector is supported by seven aluminium honeycomb trays with the addition of two Carbon

Fiber Reinforced Polymer (CFRP) sheets encasing each tray, while its integrated thickness amounts to approximately one radiation length.

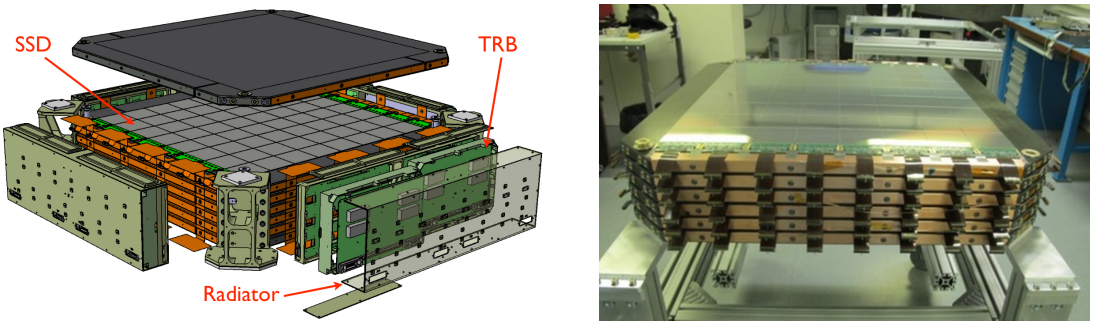

(a) (b)

Figure 2.5: The DAMPE STK, illustrated (a) in an exploded view including the various SSDs, TRB and radiator units [61], along with (b) a physical representation of the full sub-detector without its top tray installed.

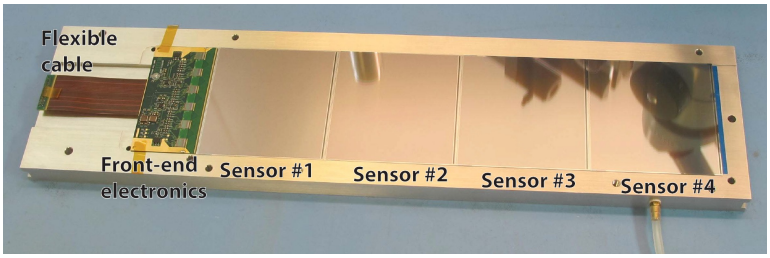

Figure 2.6: Single STK ladder comprising its 4 active sensors (silicon strip detectors) along with the front-end electronic board. From [61].

An impinging charged particle on the STK should interact with its active silicon layers, thus providing a signal in each plane which ultimately defines its track, with great precision. In contrast to charged particles and nuclei, gamma-rays (being neutral) do not interact with the SSDs. In that case, three thin tungsten layers promote the production of e^+e^- pairs, subsequently traced by consecutive silicon layers. A simple representation of the above-mentioned interactions can be viewed in Fig. 2.7.

Evaluating stability and performance aspects both at ground and on-orbit can assure an extended instrument lifetime. At ground, the STK response was tested along with the other sub-detectors, showing good charge measurement capabilities (seen in Fig. 2.8) and great stability during its operations. Furthermore, in order to account for possible geometrical inconsistencies regarding the position resolution of incoming particles, an alignment process is performed (first on ground and then on flight data). Its parameters are being updated every two weeks to ensure

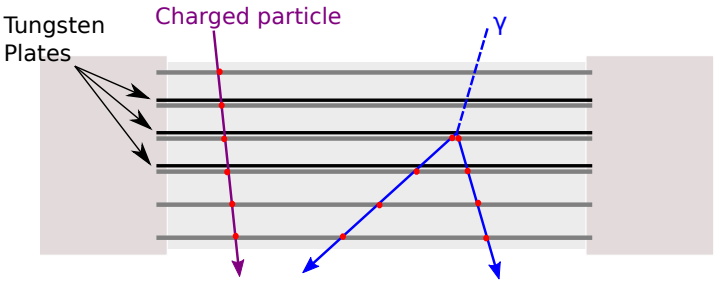

Figure 2.7: Simplified illustration of possible interactions considering charged particles and gamma-rays within the STK sub-detector. Interaction points are represented by red dots while -for the sake of simplicity- the double silicon layers are not shown. From [69].

overall robustness and optimal tracking resolution, with the latter varying only within a minimal percentage.

In space, the STK is mechanically stable while providing precise measurements during its operation [70], not exceeding a percentage of 0.3 % in noisy channels, as seen in Fig. 2.9. Additionally, Fig. 2.10 illustrates the temporal evolution of the STK mean noise and ladder temperature, while unveiling their correlation with a period of one year. Such temperature variations can be limited within 1 degree Celsius per day.

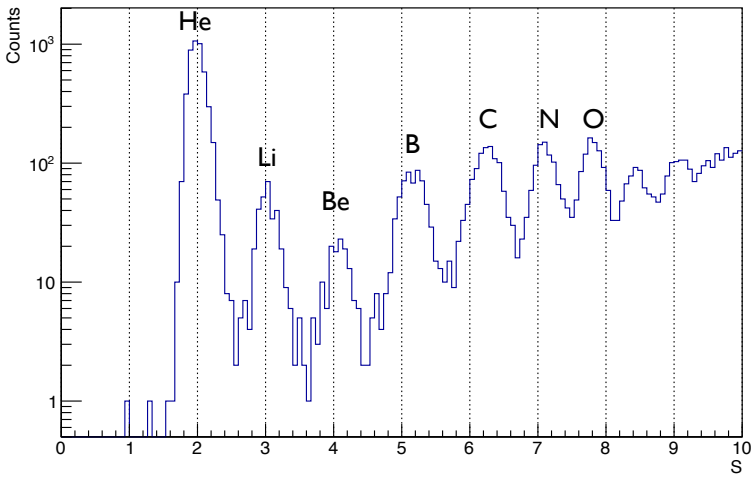

Figure 2.8: Charge signal extracted from the STK concerning nuclei with $Z > 1$. The spectrum originates from ions produced by a lead beam impinging on a target. From [61].

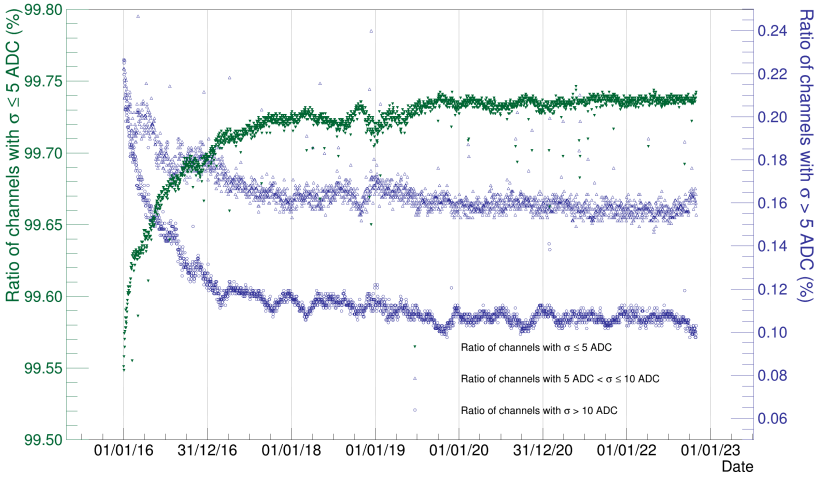

Figure 2.9: Evolution of STK noise with respect to the DAMPE livetime (until December 2022). Left- and right-side Y-axes correspond to a noise level lower (or greater) than 5 ADC, exhibiting a stable behavior. Figure corresponds to an updated version of [70].

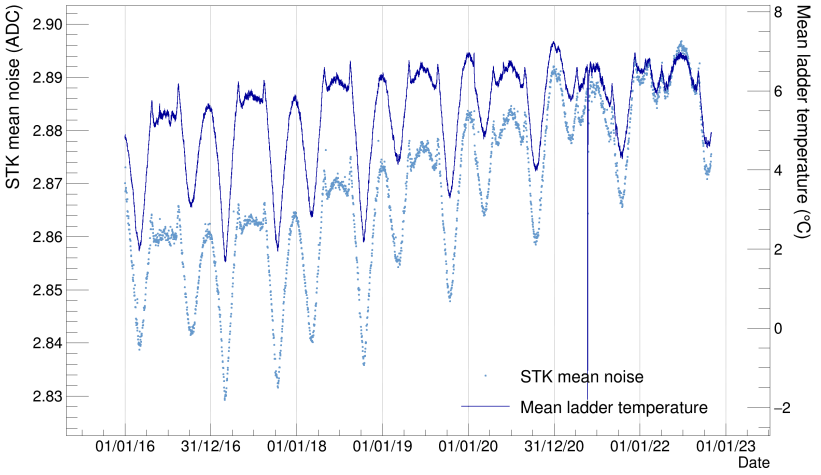

Figure 2.10: Correlation between STK noise and temperature with respect to the DAMPE livetime (until December 2022). Peak structures repeat with a period of one year. Figure corresponds to an updated version of [70].

2.2.3 Bismuth Germanium Oxide (BGO) calorimeter

The Bismuth Germanium Oxide (BGO) imaging calorimeter is situated at the core of DAMPE. At the time of writing this thesis, it corresponds to the deepest calorimeter in space, amounting to 32 X_0 and 1.6 λ_I (radiation and nuclear interaction lengths, respectively). It comprises 14 layers orthogonally interleaved in X and Y axes, while each layer consists of 22 BGO bars and each bar is readout by two PMTs (one per side). Each bar corresponds to $60 \times 2.5 \times 2.5$ cm^3, leading to a total active area of 60×60 cm^2.

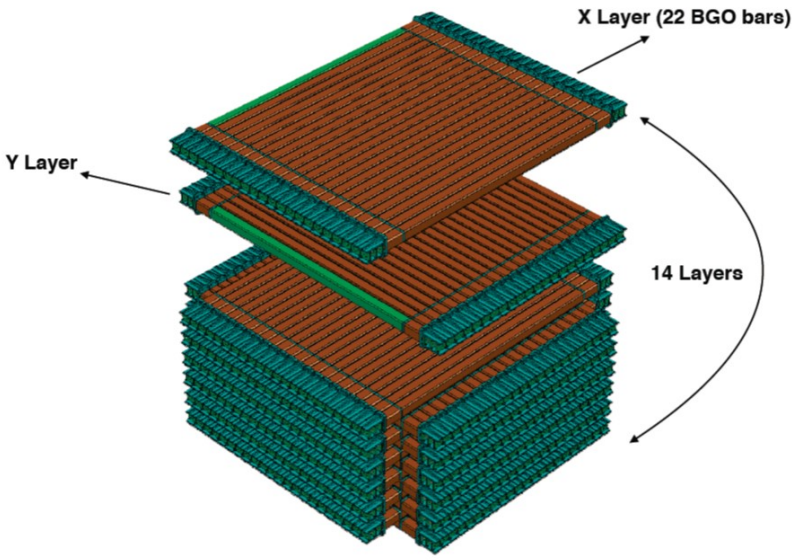

Figure 2.11: Structure of the BGO calorimeter. The schema focuses on the various X- and Y-oriented layers along with the segmented bar implementation. From [61].

Such a structure is optimally designed to provide a precise view of both longitudinal and lateral shower aspects. Its extended depth of 32 radiation lengths facilitates the containment of electromagnetic showers, although in the case of CR nuclei only a limited percentage of the hadronic shower is identified, thus unfolding methods (i.e., Bayesian approach [71]) are employed in order to provide an accurate reconstruction of the primary particle energy.

The DAMPE calorimeter serves a multitude of purposes. Impinging particles on the BGO give rise to electromagnetic or hadronic showers that lead to the emission of scintillation photons, consequently detected by the PMTs. Taking into account the cumulative deposited energy, precise measurements of primary CRs can be obtained. The BGO energy resolution has been evaluated both via beam test campaigns at CERN and in space [72]. The above-stated measurements are validated via Monte Carlo (MC) simulations, implemented through the official DAMPE software [73], based on the GEANT4 toolkit [74] (discussed later in this chapter). The energy resolution for electrons/positrons and gamma-rays is better than 1.2%, for energies higher than 100 GeV (Fig. 2.12b), while for protons and heavier nuclei it ranges from 25 to 35% up to 10 TeV (Fig. 2.12a).

Furthermore, the response to heavier nuclei (from helium to argon) has been evaluated via beam tests of primary ^{40}Ar particles at energies of 40 GeV/n and

75 GeV/n, in the facilities of CERN (Super Proton Synchrotron, SPS) [75]. In conjunction to beam test results, two different interaction models (corresponding to GEANT4 physics lists) were selected for the sake of comparison, namely QGSP_FTFP_BERT and FTFP_BERT. As seen in Fig. 2.13, beam test data and simulations appear to be in good agreement, illustrating an overall energy resolution of approximately 25% for carbon and 22% for oxygen nuclei.

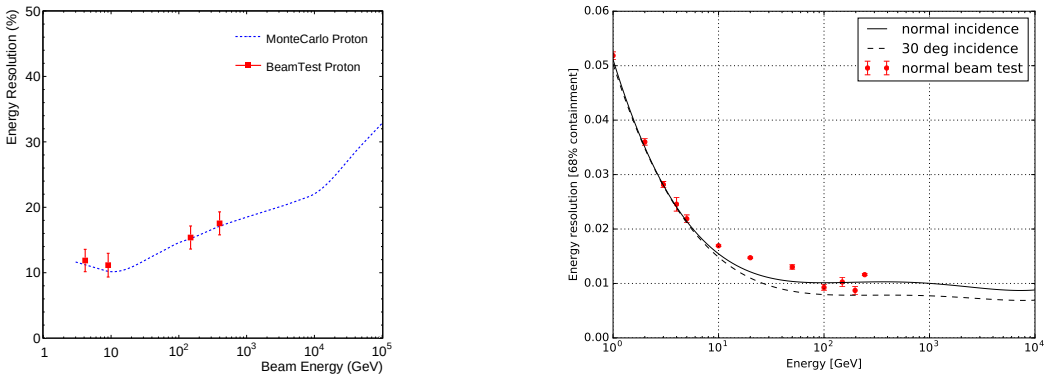

(a) **(b)**

Figure 2.12: Test beam results concerning the DAMPE energy resolution. In (a), the response in (on-axis) protons is shown with red points, while the blue line corresponds to MC simulations after spectral unfolding. In (b), the energy resolution for electrons and gamma-rays is illustrated (red points), with the addition of normal and 30 degree incidence curves. From [61].

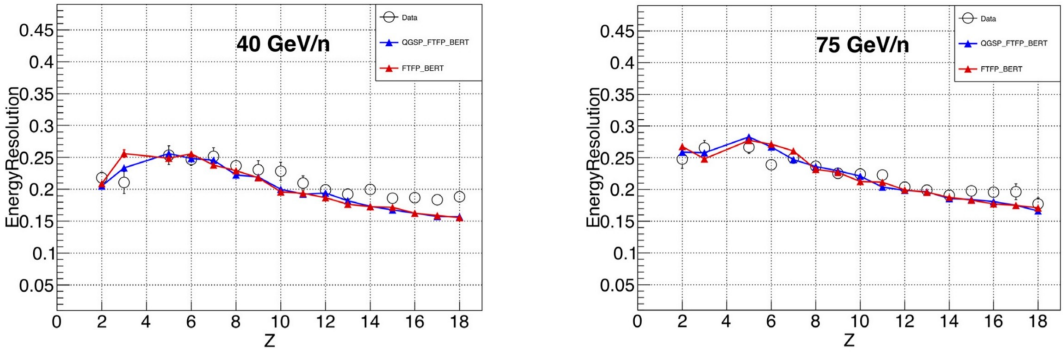

(a) **(b)**

Figure 2.13: Energy resolution with respect to the atomic number (Z) concerning particle beams of (a) 40 and (b) 75 GeV/n, represented by open black circles. MC simulations with two individual physics lists provided by GEANT4 are illustrated in blue and red triangles. From [75].

Additional calorimetric effects can emerge from the saturation of electronics regarding the BGO bar readout. A candidate event can deposit energies that could

possibly surpass the dynamic range of a given dynode and saturate the electronics (detailed description can be found in 3.3.3). In the case of electromagnetic showers, this issue can be effectively resolved by implementing a multi-dynode readout, thus avoiding saturation up to energies of 10 TeV. For highly energetic events pertaining to hadronic showers, additional methods are implemented in order to resolve saturation effects and accurately reconstruct their primary energies.

An important feature concerning the BGO calorimeter includes its particle identification capabilities. Electromagnetic and hadronic showers differ in their interactions with matter, which reflects on their shower evolution and topology inside the calorimeter. Therefore, such information can assist towards a precise understanding of the primary particle. Consequently, an accurate track reconstruction is necessary in order to correctly identify the impinging CR particle. Finally, the BGO calorimeter serves as a level-0 trigger for the DAMPE data acquisition system (DAQ), thus imposing a certain threshold concerning the acquired hit signals arriving at the trigger board.

2.2.4 NeUtron Detector (NUD)

The NeUtron Detector is situated at the bottom of the DAMPE payload. Its main objective is to provide an additional discrimination level between electromagnetic and hadronic showers initiated in a prior stage inside the BGO calorimeter, with primary energies higher than 100 GeV.

The NUD (illustrated in Fig. 2.14) consists of a single layer equipped with four boron-doped plastic scintillator units (Eljen technology, EJ45) of $30 \times 30 \times 1$ cm^3 each, with the inclusion of a single layer of aluminium wrapping aiming towards a greater reflection of photons. Each scintillator module is readout by a 10-dynode PMT, coupled to a wavelength-shifting fiber (WLSF) in order to maximize the photon detection efficiency and reduce possible light attenuation effects. Generally, a hadronic shower produced by a CR nucleus contains an order of magnitude more neutrons with respect to an electromagnetic shower initiated by electrons or gamma-rays. These neutrons will propagate downward from the BGO (being thermalized in the meanwhile) and reach the NUD, where they interact following the neutron-capture reaction:

$$n + {}^{10}\mathrm{B} \longrightarrow {}^{7}\mathrm{Li} + \alpha + \gamma \tag{2.1}$$

Light produced from the above-stated interaction propagates to the PMT and constitutes the main detector signal. Following a 1.6 μs interval after the initial BGO trigger, the NUD data acquisition is triggered, with a total duration of a few microseconds.

In Fig. 2.15, the NUD energy response to protons and electrons is shown, stemming from beam tests of 150 GeV electrons and 450 GeV protons, both depositing approximately the same amount of energy in the BGO [3]. Proton signals activate a significantly larger amount of channels with respect to electrons (100 to 2, respectively), with preliminary results showing a rejection power of 25 concerning electrons in the TeV energy range and a detection efficiency of 95% [76].

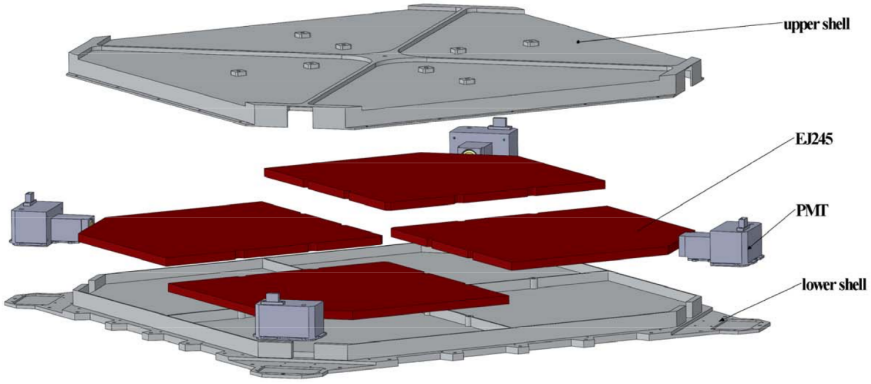

Figure 2.14: Exploded structure of the NUD detector. From [61].

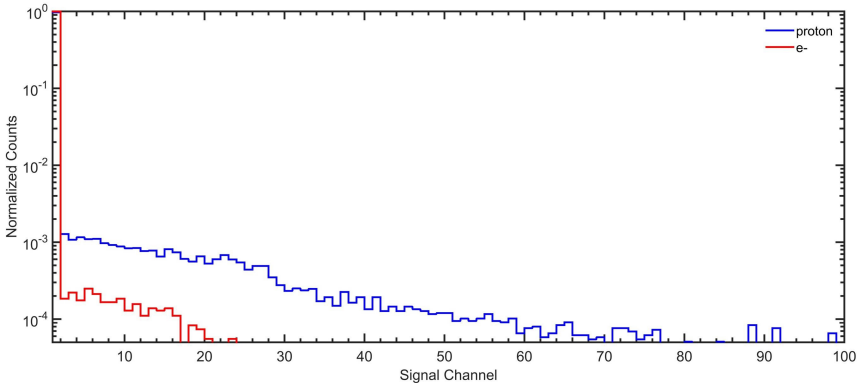

Figure 2.15: NUD response in beam test protons (in blue) and electrons (in red), corresponding to an energy deposit of approximately 150 GeV in the BGO calorimeter. The counts are normalized to unit area. From [61].

[3] As a rule of thumb, protons deposit 1/3 of their total energy in the calorimeter, which leads to a 450 GeV primary proton depositing an amount of energy similar to a 150 GeV electron.

2.3 Design parameters and performance

Following a detailed introduction to the various DAMPE sub-detectors, a summary of its main design parameters and scientific objectives is presented in Tab. 2.1. Main figures of merit include its projected energy range and resolution for CR gamma-rays/electrons and nuclei, along with its measured acceptance, calorimeter specifications and Field of View (FoV). As a consequence, DAMPE shows an increased exposure with respect to other current-generation experiments (as seen in Fig. 2.16), hence being able to collect more CR data in the same time interval and provide precise flux measurements at higher energies (with respect to prevailing CR experiments).

Table 2.1: Summary of performance parameters with DAMPE

Parameter	Value
Energy range (gamma-rays/electrons)	5 GeV - 10 TeV
Energy range (protons & nuclei)	50 GeV - 200 TeV
Energy resolution (gamma-rays/electrons)	$\leqq$ 1.5% at 800 GeV
Energy resolution (protons)	$\leqq$ 40% at 800 GeV
Geometric factor (electrons)	> 0.3 m^2
Calorimeter specifications	32 X_0, 1.6 λ_I
Field Of View (FoV)	$\sim$ 1.0 sr

2.4 Data acquisition and trigger logic

The DAMPE DAQ (illustrated in Fig. 2.17) [61, 77] creates a communication bridge between the payload computer and the detector, implements trigger decision logic, collects science and housekeeping data from all sub-detectors and sends them to ground. The system comprises two electronic modules, namely a Payload Data Process Unit (PDPU) and a Payload Management Unit (PMU). The PMU controls the instrument by decoding signals arriving from the onboard computer and sending them to the Front End Electronics (FEE) and PDPU.

The top and bottom four layers of the BGO calorimeter (out of 14 total layers) provide the level-0 trigger information, and if such a trigger is received, the digital pulse is sent to the PDPU. Afterwards, a global trigger signal is produced, following a 1 μs decision time interval from the decision board, thus initiating the acquisition of data. During data collection, the PDPU blocks further triggers

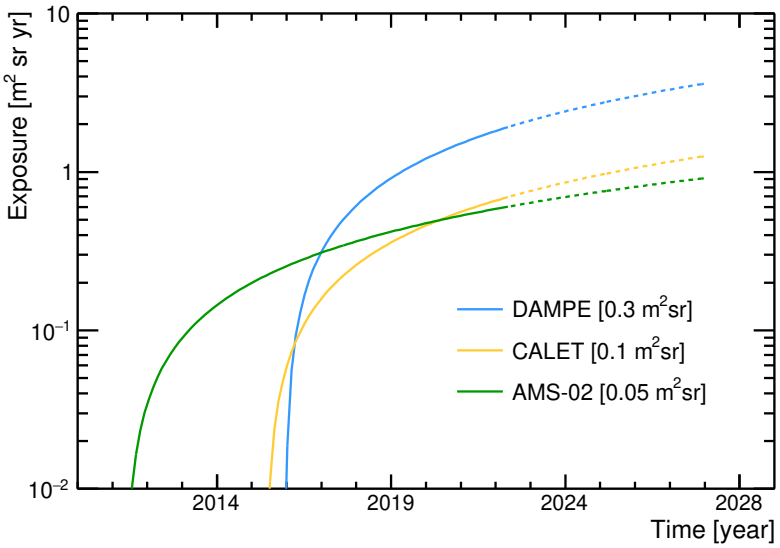

Figure 2.16: Exposure (calculated for CR electrons) of current CR experiments, commencing from their respective launch time. The geometric acceptance of each instrument is reported in brackets. Continuous lines correspond to past and current mission observations, while dashed lines represent possible future measurements.

which results in a dead time of 3 ms after each event. Four possible trigger requirements can be found in the DAMPE trigger logic schema (as seen in Fig. 2.18), with minimum ionizing particles (MIPs) as a reference point[4]:

- The Unbiased Trigger (UBT), requires signals in the first two BGO layers greater than 0.4 MIPs in each bar hit.
- The MIP Trigger (MIPT), is activated when a signal greater than 0.4 MIPs is registered in each hit bar concerning the first and penultimate two BGO layers.
- The Low Energy Trigger (LET), requires signals higher than 0.4 MIPs in the first two BGO layers and larger than 2 MIPs in the third and fourth, respectively.
- The High Energy Trigger (HET), requests an energy deposition greater than 10 MIPs in each one of the first three BGO layers and 2 MIPs for the fourth layer.

[4]One MIP corresponds to an energy deposition of $\sim$ 23 MeV, inside a BGO bar.

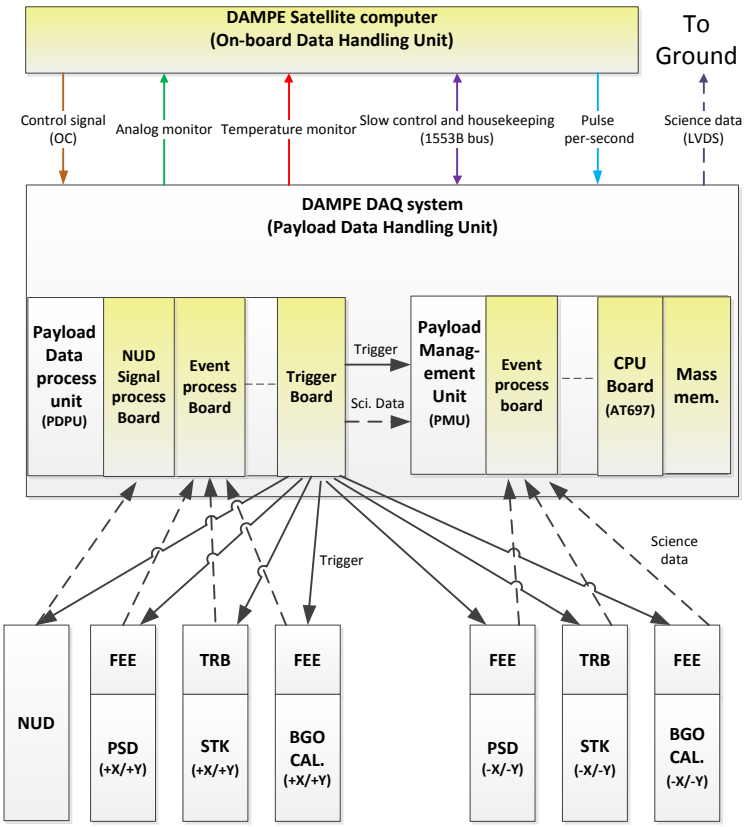

Figure 2.17: Data acquisition system of DAMPE. From [61].

Among the above-stated triggers, the UBT, MIPT and LET are pre-scaled[5]. Specifically, during DAMPE's orbit at low geographical latitudes ($\pm$ 20°) the pre-scale factors are set to 512/1, 4/1 and 8/1 respectively. At higher latitudes the UBT and LET pre-scale factors become 2028/1 and 64/1 respectively, while the MIPT is disabled. Global triggers amount to 70 Hz in flight (50 Hz for the HET), while all collected data (science, temperature and satellite status data) are saved in a mass memory of 16 GB, before being sent to ground with a specific timestamp (precise within 1 ms).

Subsequently, the entirety of satellite data is stored in data centers located in China, where they are converted to files appropriate for analysis (Fig. 2.19). From that point onward they are distributed to all institutions involved in the collaboration.

[5]meaning that a fraction of events which satisfy the trigger requirements are randomly discarded.

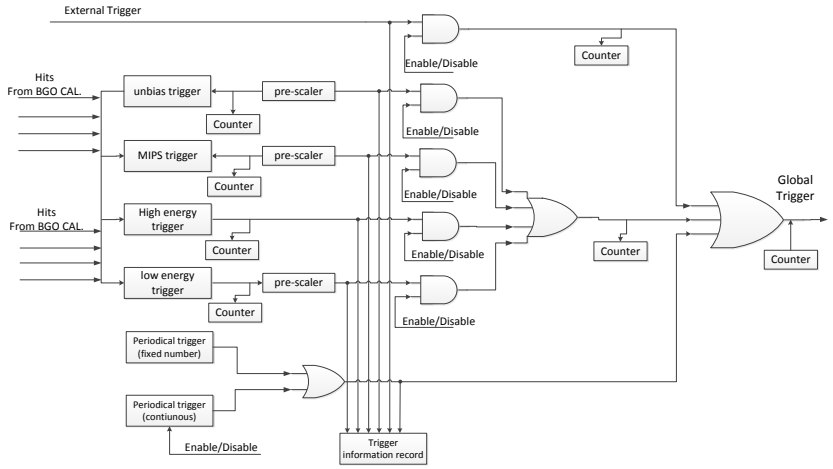

Figure 2.18: The trigger decision logic of DAMPE. From [61].

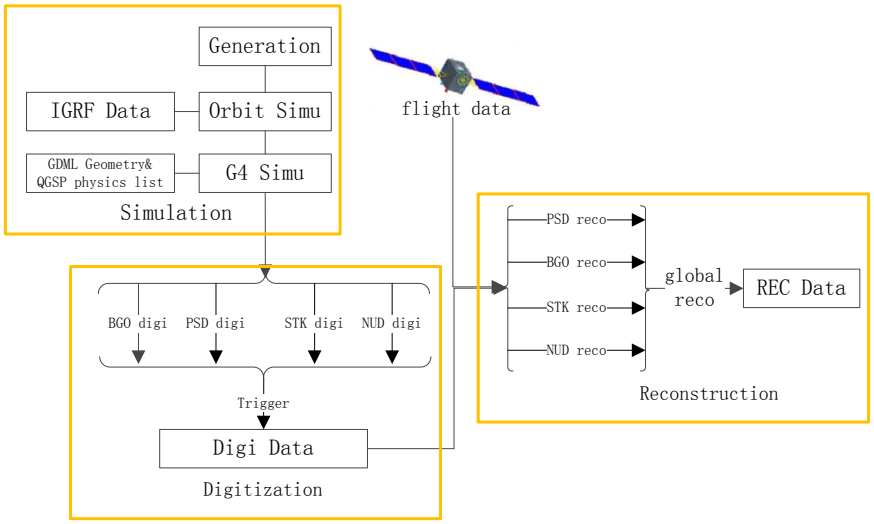

Figure 2.19: DAMPE data flow, containing flight and simulation data. From [61]

2.5 Simulation of data with DAMPE

Simulated data are indispensable for validation of any given physical experiment. Focusing on the case of Astroparticle Physics and CRs, great effort has been put towards the procurement of precise information regarding radiation propagating through various detectors. In that sense, simulations referred to as Monte Carlo (MC) from the homonym computational technique are utilized, being paramount not only in CRs but also in the majority of Particle Physics' experiments.

In DAMPE, the simulation toolkit of GEANT4 is utilized [74], interfaced with DmpSoftware [73], being the dedicated collaboration software package. The payload dimensions, materials and positioning of every detector are introduced

to the general GEANT4 toolkit as a Geometry Description Mark-up Language (GDML) file, originating from Computer Aided Design (CAD) [78] drawings of the detector. Thus, an optimal simulation accuracy can be attained given the detailed detector description.

On the other side, GEANT4 simulates particles in a wide energy range, generated within a half sphere of radius r = 1.38 m for electrons/protons and 1 m for heavier nuclei until iron, which envelopes the top half of the detector. The sampled distributions follow a power law spectrum of E^{-1} with particles of interest being electrons/gamma-rays and protons/heavier nuclei, starting from 1 GeV and reaching 1 PeV in many cases. Given the computationally expensive nature of such simulations, these samples are divided in various subsets, generally covering an order of magnitude in energy.

The interaction of particles with matter is described by two different hadronic interaction models: (a) the FTFP-BERT which includes the intra-nuclear model of Bertini [79] (BERT) taking effect below 5 GeV and the Fritiof model [80] with Reggeon cascade and Precompound (FTFP) above 4 GeV and (b) the QGSP-FTFP-BERT which adds the Quark-Gluon String model [81] with Precompound (QGSP) above 12 GeV. In the case of DAMPE, particles of energies up to 1 PeV could be detected, thus an additional interface has been implemented, between GEANT4 and the Cosmic Ray Monte Carlo (CRMC) package [82]. In that sense, models such as the EPOS-LHC [83] and Dual Parton model (DPMJET) [84] can be introduced within the simulations. Finally, the FLUKA [85] simulation toolkit is utilized (beside GEANT4) in the same energy, thus providing a complete and valuable comparison between the two simulation frameworks.

2.6 Selected Cosmic Ray results with DAMPE

2.6.1 Fine structure of the all-electron spectrum

The all–electron component (e^+e^-) comprises 1% of total CRs, with a spectrum well described by a single power–law, consistent with previous measurements. Initially, ground–based Imaging Atmospheric Cherenkov Telescopes (IACTs) HESS and VERITAS had shown hints of a spectral break in the $e^+ + e^-$ spectrum near the TeV range, with VERITAS extending its results up to 20 TeV [86]. In 2017, DAMPE [62] published results regarding the all–electron spectrum in the energy range of 25 GeV to 4.6 TeV with great precision and large acceptance

(from 530 days of data) (shown in Fig. 2.20), thus leading to the first direct detection of a spectral break at ≈ 1 TeV.

The aforementioned electrons experience energetic losses during propagation, which, in addition to the CR diffusion coefficient value (extracted by B/C measurements) leads to an estimation of their production origin, within approximately 100 pc (local neighborhood) [12].

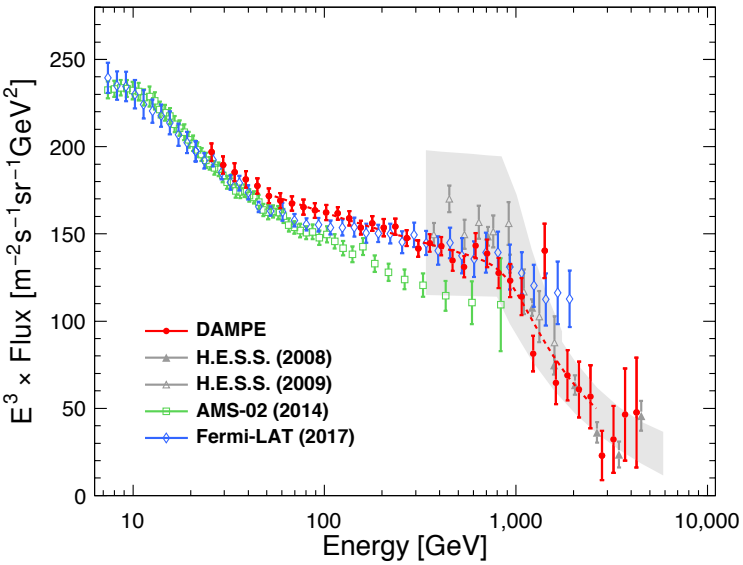

Figure 2.20: CR electron plus positron spectrum measured by DAMPE and compared to direct results of AMS-02 [87] and Fermi-LAT [88] along with indirect results from HESS [89, 90]. DAMPE, AMS-02 and Fermi-LAT points include statistical and systematic errors summed in quadrature, while the grey area represents HESS systematic errors (along with a $\sim 15\%$ energy scale uncertainty). From [62].

2.6.2 Protons and helium nuclei

Constituting the majority of CRs, protons [34] and helium nuclei [35] were thoroughly investigated by DAMPE. In the case of protons, a data sample of 30 months was analyzed in the energy range of 40 GeV to 100 TeV, leading to the detection of a spectral hardening around 500 GeV (consistent with previous observations) along with a novel softening featured approximately at 14 TeV (Fig. 2.21).

The aforementioned characteristics were precisely described by a smoothly-broken power-law (SBPL) model above the observed hardening, hence ruling-out the previously favored paradigm of a single power-law governing CR spectra up to PeV energies. Furthermore, DAMPE presented a detailed spectral measurement

of helium nuclei in the energy range of 70 GeV to 80 TeV, extracted from 54 months of flight data. In that sense, an analogous picture with the proton case was revealed; a hardening feature around 1 TeV in accordance with previous results, followed by a spectral softening around 34 TeV (seen in Fig. 2.22).

Combined with the proton results, the softening energy is consistent with a rigidity-dependence, although a mass-dependence cannot be ruled out. These novel observations necessitate a careful reconsideration (or update) of prevailing CR models, consequently aiding towards an extended understanding of the intricate details regarding the origin and acceleration mechanism of galactic CRs. Ongoing work includes a joint analysis of proton and helium nuclei (p+He), with the clear advantage of increased statistics, higher achieved energies, along with lower background contamination, hence allowing for direct comparison with results obtained by ground-based experiments.

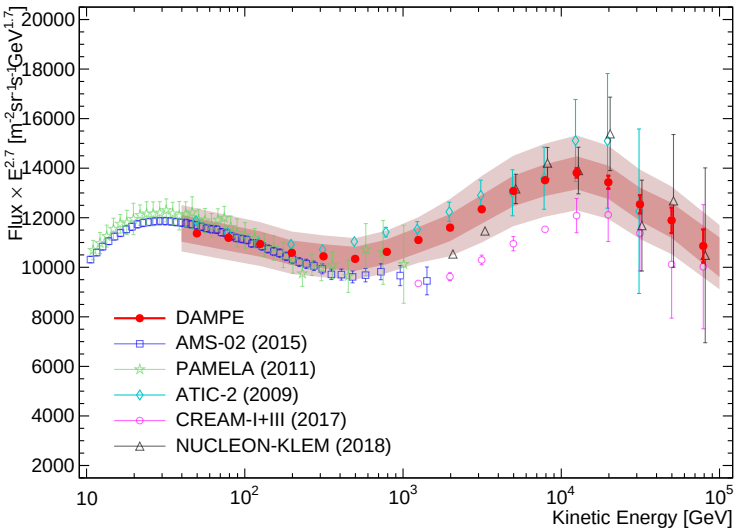

Figure 2.21: DAMPE proton spectrum from 40 GeV to 100 TeV. Statistical uncertainties are represented by error bars, while systematic errors from the analysis are illustrated with an inner darker band. The outer band corresponds to the total systematic uncertainties, including hadronic model errors. Results from AMS-02 [91], PAMELA [92], ATIC-2 [93], CREAM I+III [94] and NUCLEON KLEM [95] are compared to DAMPE data. Error bars for AMS-02 and PAMELA include statistical and systematic errors added in quadrature, ATIC, CREAM and NUCLEON errors correspond to statistical uncertainties. From [34].

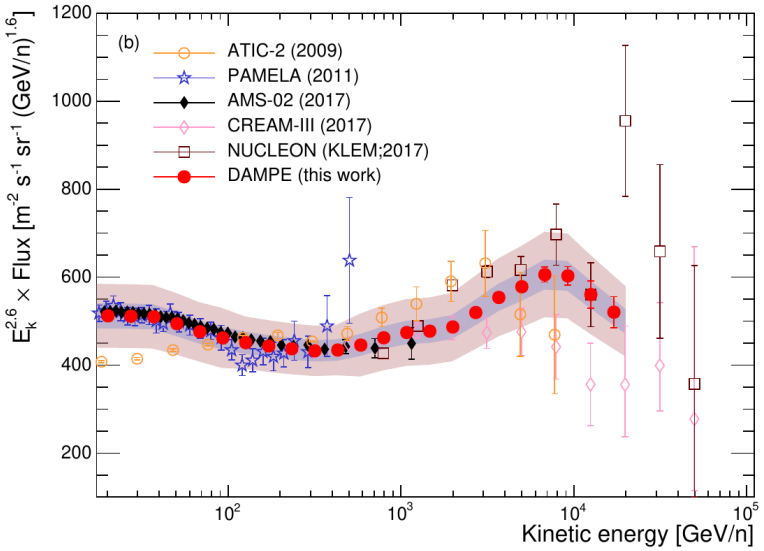

Figure 2.22: DAMPE helium spectrum from 70 GeV to 80 TeV. Statistical uncertainties are represented by error bars, while systematic errors from the analysis are illustrated with an inner darker band. The outer band corresponds to the total systematic uncertainties, including hadronic model errors, summed in quadrature. Results AMS-02 [96], ATIC [93], CREAM [94], PAMELA [92], AMS [31] and NUCLEON [97]. Error bars for AMS-02 and PAMELA include statistical and systematic errors added in quadrature, while statistical uncertainties are shown for other results. From [35].

2.7 Summary

This chapter provided an overview of the DAMPE space mission, focusing on its various sub-detectors, scientific objectives and recent CR results. In the following, a detailed view on the various analysis aspects considering the CR spectra of carbon and oxygen, will be presented. Additionally, important insights on flux ratios such as C/O, B/C and B/O, will be contributed, given their importance in clarifying aspects concerning the diffusion and propagation of CRs in the Galaxy.

Chapter 3

Analysis of Carbon and Oxygen nuclei

A general introduction to the DAMPE mission was presented in the previous chapter, showcasing its performance aspects and scientific objectives along with an overview of current measurements and results. These results extended in the multi TeV/n region with great precision, thus unveiling novel spectral features and as a consequence, leading to more open questions. From that point onward, DAMPE has the capability of expanding into the CNO region (also described as intermediate or medium mass nuclei) with precise measurements, where carbon and oxygen nuclei represent the most abundant nuclei, following the dominant contributions of proton and helium.

This work is devoted to the spectral measurement of carbon and oxygen nuclei from 10 GeV/n to approximately 25 and 10 TeV/n, respectively, for the first time with great precision. In addition to the aforementioned measurements, interesting insights will be provided on flux ratios such as: carbon-over-oxygen (C/O), boron-over-carbon (B/C) and boron-over-oxygen (B/O). As discussed previously, secondary-over-primary flux ratios (i.e., B/C, B/O) greatly assist towards a better understanding of the CR propagation mechanism. Carbon and oxygen are nuclei of primary origin, while given the secondary nature of boron resulting from spallation of heavier primaries with the Interstellar Medium, a concrete picture can be attained especially when such a quantity is precisely measured well inside the multi-TeV region.

Consequently, this chapter aims to highlight the complete analysis procedure concerning both carbon and oxygen nuclei with the addition of the flux ratios discussed above, hence leading to a more thorough picture pertaining to nuclei of the intermediate mass group.

3.1 Data samples and livetime

3.1.1 Flight data

The analyses of carbon and oxygen nuclei highlighted in this work contain 6 years (or 72 months) of DAMPE data, from January 1st, 2016 to December 31st, 2021. An average of 5.2 million events per day is acquired (as shown in Fig. 3.1), with a number of occasional and brief issues, halting its smooth data-taking. These can be summarized in:

1. 2016-02-22 to 2016-02-24: DAMPE operating in test mode. Pedestal measurements regarding the STK.
2. 2016-09-07 to 2016-09-08: DAC calibrations occupying a large part of the observation time.
3. 2017-12-29 to 2017-12-30: High voltage incident leading to data loss.
4. 2020-03-07 to 2020-03-08: Exceptionally high data rate, payload stuck in MIP calibration mode, operation schedule table not uploaded.
5. 2021-05-22 to 2021-05-25: Satellite battery fault leading to payload shut-down.
6. 2021-08-20: Lower tracking efficiency due to single Tracker Readout Board (TRB) reset.
7. 2021-08-23: Operation event list failed upload, data taking kept in MIP trigger mode.

Additionally, the monthly event count is presented in Fig. 3.2, this time subtracting the above-stated (anomalous) intervals. An overall consistency between the data yield of each month is evident, across the entirety of DAMPE's lifetime.

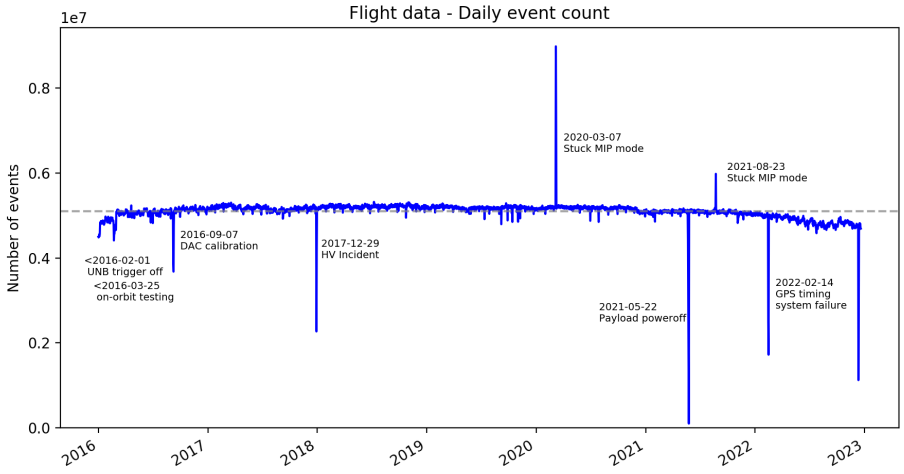

Figure 3.1: Daily event count for DAMPE, ranging from its initial data-taking period up to current acquisitions. Sharp vertical lines correspond to detector hindrances or calibrations, occurring rarely over the course of its lifetime.

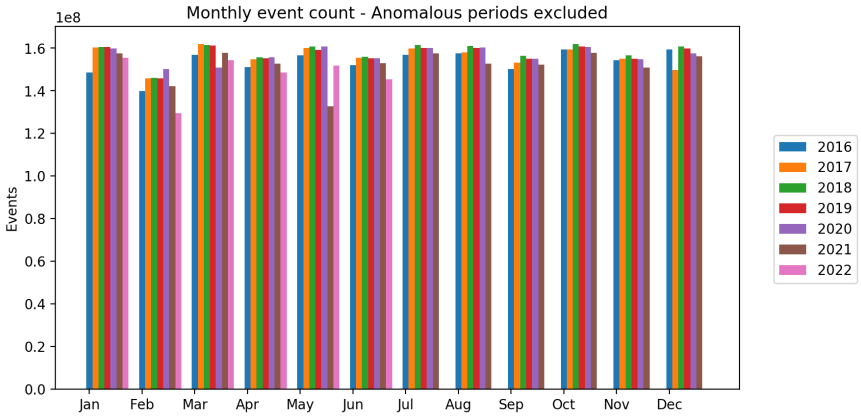

Figure 3.2: DAMPE event count with respect to the data acquisition time, in months.

Livetime

All of the above-stated intervals (except for item 6) are subtracted from the analysis dataset and will influence the calculated livetime. Its total value is affected by additional parameters, such as the dead time following a triggered event inside the detector, corresponding to 3.025 ms per event triggered. Moreover, as with every space detector in orbit, a given percentage of the operational interval is dedicated to calibrations of its various sub-detectors, a process that occupies approximately 1.5% of the total calculated livetime.

Furthermore, during its orbit, DAMPE encounters a region, commonly known as the South Atlantic Anomaly (SAA, as seen in Fig. 3.3), where the Earth's

magnetic field (specifically, the inner Van Allen belt) drops down to an altitude of 200 km, giving rise to a highly increased flux of low energy particles. Such kind of data are of no practical use for the analysis and are consequently excluded. Contributions stemming from the dead time due to data acquisition and detector passage from the SAA can be viewed in Figs. 3.4 and 3.5. The instrument livetime amounts to an average of about 18.15 hours per day (Fig. 3.6), while the total livetime (taking into account 6 years of flight data), corresponds to 1818 days or approximately $1.437 \cdot 10^8$ seconds.

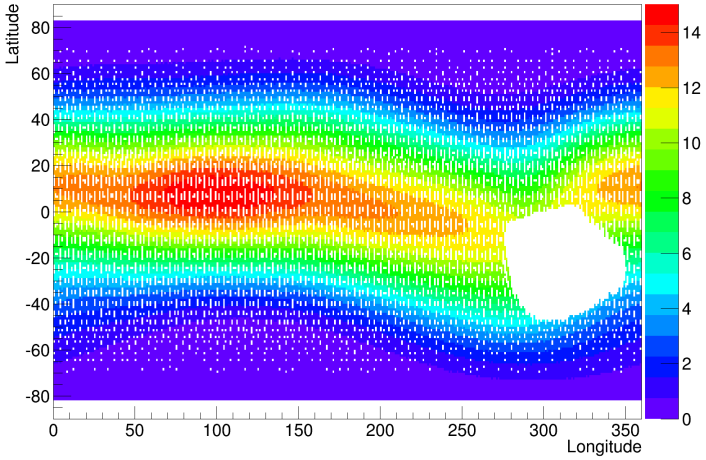

Figure 3.3: Latitude vs longitude representation with the various cutoff rigidities (in GV) illustrated in the full contour range. The white section corresponds to the South Atlantic Anomaly region.

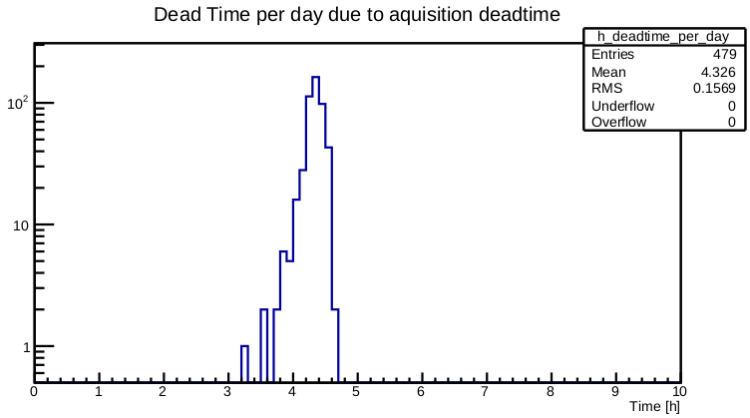

Figure 3.4: Daily contributions subtracted from the total livetime, corresponding to the dead time due to the detection of each event. From [69].

Figure 3.5: Daily contributions subtracted from the total livetime, due to the passage through the SAA region. From [69].

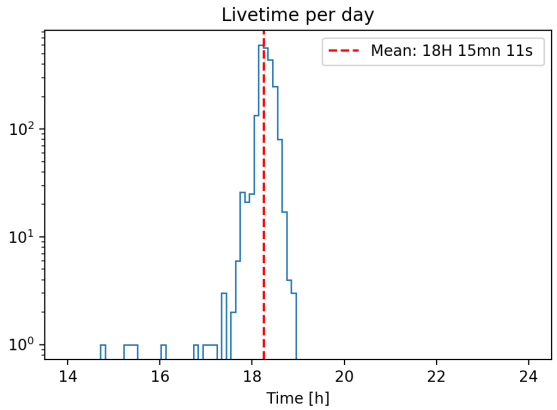

Figure 3.6: Daily livetime for DAMPE. Updated figure version from [69].

3.1.2 Monte Carlo simulated data

Studying the detector response is essential in achieving precise energy reconstruction of impinging events. Furthermore, evaluating the efficiency of the various selection cuts applied in the analysis as well as assessing the background percentage (arising from the above-mentioned selections), are fundamental aspects determined from MC simulations and compared to flight data. Additional detector effects can be corrected with the help of simulations, thus leading to a more optimized instrument operation.

The simulated events used in this analysis were based on GEANT4 (version 10.05p01) coupled to the DAMPE software, as discussed in the previous chapter. All events concerning carbon and oxygen nuclei were initially simulated with a power-law spectrum of E^{-1}. The large majority of events were produced with the FTFP_BERT physics list (from 100 GeV to 100 TeV of primary particle energy), while for energies greater than 100 TeV, the EPOS_LHC model is employed.

It should be noted that carbon and oxygen samples of similar event count,and energy intervals were also produced with FLUKA. The various energy ranges along with their respective physics list and number of events can be viewed in Tab. 3.1.

Table 3.1: List of simulated carbon and oxygen samples

Nucleus	Phys. list	Energy range [TeV]	Events [Millions]
Carbon	FTFP_BERT	0.1 - 1	100.15
	FTFP_BERT	1 - 10	106.97
	FTFP_BERT	10 - 100	109.88
	EPOS_LHC	100 - 500	13.28
Oxygen	FTFP_BERT	0.1 - 1	100.37
	FTFP_BERT	1 - 10	101.21
	FTFP_BERT	10 - 100	116.53
	EPOS_LHC	100 - 500	18.75

3.2 Selection cuts

The candidate carbon and oxygen events selected in this analysis should satisfy specific requirements regarding their quality. In that sense, both flight and simulated data are subjected to a series of selection cuts in order to ensure both an optimal event reconstruction as well as maintaining a consistent picture between different sub-detectors. The above-stated objectives are respected while keeping a low contamination percentage among neighboring nuclei.

3.2.1 Data pre-selections

Following an initial collection of analysis-ready data from the DAMPE repositories, a first layer of event skimming (or filtering) is applied. Such a procedure aids towards an effective removal of events not contained inside the BGO fiducial volume with the additional advantage of decreasing the file size. This skimming procedure is associated to the so-called "pre-selection" stage. In Fig. 3.7, an overview of events passing the skimming selection is presented, where each horizontal line corresponds to a different energy range. The implemented cuts concerning the skimming procedure are as follows:

- All events failing particle direction reconstruction are omitted. This can be evident by an event following an inconsistent track while propagating through the various subdetectors.
- Events depositing their maximum energy at the edge of the calorimeter concerning layers 1-2-3[1] are rejected. This cut prevents inconsistent energy reconstructions due to possible leakages, while ensuring a well-contained shower core within the calorimeter.
- Candidate event tracks should be found within 280 mm (either in X or Y directions) and [-46 mm, 448 mm] in Z coordinate, from the calorimetric center, thus allowing for events situated inside its fiducial volume.
- The maximum energy deposition in a single BGO layer should not surpass 35% of the total energy deposited, consequently limiting events entering from the detector's side.
- Events depositing energies lower than 20 GeV in the calorimeter are rejected in order to avoid interference from the geomagnetic rigidity cutoff [11].

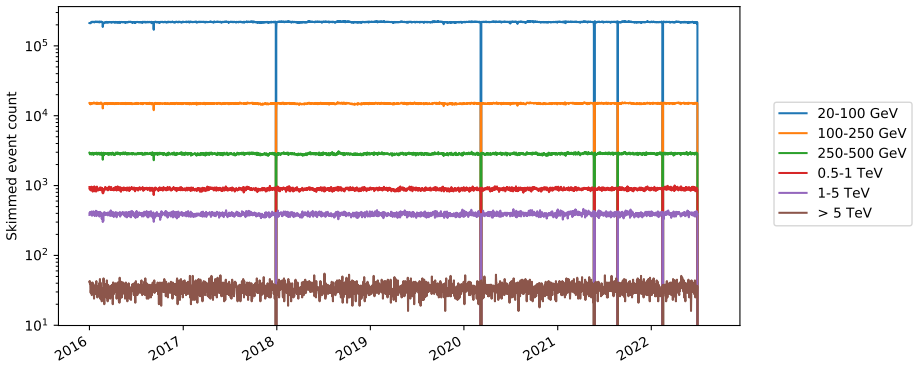

Figure 3.7: Daily counts of flight data passing the initial filtering (skimming) selections with respect to DAMPE's lifetime. The full dataset is divided in six energy ranges corresponding to an equal number of colored horizontal lines.

3.2.2 Analysis-specific selections

All events surviving the above-stated pre-selection stage provide a base of eligible flight and MC events. Afterwards, said events are subjected to a series of

[1] BGO layer numbering starts from zero.

analysis-specific cuts, oriented towards an optimal selection of carbon and oxygen candidate events, while maintaining a high overall acceptance and low background. In the following, a complete list of selection cuts and various corrections will be presented:

- Selected events should initially activate the High Energy Trigger (HET), as discussed in Chapter 2.
- An additional cut on the energy deposited inside the BGO calorimeter is imposed at 100 GeV, in order to avoid both the contribution from the geomagnetic cutoff as well as from solar energetic particles impinging on the detector [98].
- Events interacting with the PSD should reside within ± 400 mm (in both X and Y views) from its center, thus ensuring a well contained event.
- The STK track should have at least one cluster in X or Y plane of the first layer, thus assisting the logical propagation of particles.
- The χ^2/ndf of the candidate STK track is selected to be lower than 15, thus rejecting events with inconsistent tracking information.
- A zenith angle difference between STK and BGO tracks should be smaller than 25^o.
- The top STK interaction point should be within 200 mm when compared with XZ and YZ projections of the BGO track.
- Projections of the STK candidate track on the first and second BGO layers should lie within 60 mm from the BGO projected track.
- Candidate events should maintain the same track identity between XZ and YZ views.
- Finally, all initiated showers inside the calorimeter should evolve in accordance to the primary reconstructed track. In some cases particles interacting with the BGO bars can give rise to upward-oriented showers that can lead to erroneous information in STK and/or PSD signals. In that sense, the sum of energy deposited in the first and second BGO layers should be smaller than the sum of third and fourth layers ($E_{L0} + E_{L1} < E_{L2} + E_{L3}$).

In the following figures (Figs. 3.8 and 3.9), typical carbon and oxygen events derived from flight data (Jan. 2017) are presented. Both examples survived all selection cuts discussed above and regard two different deposited energies in the BGO calorimeter for the sake of completion.

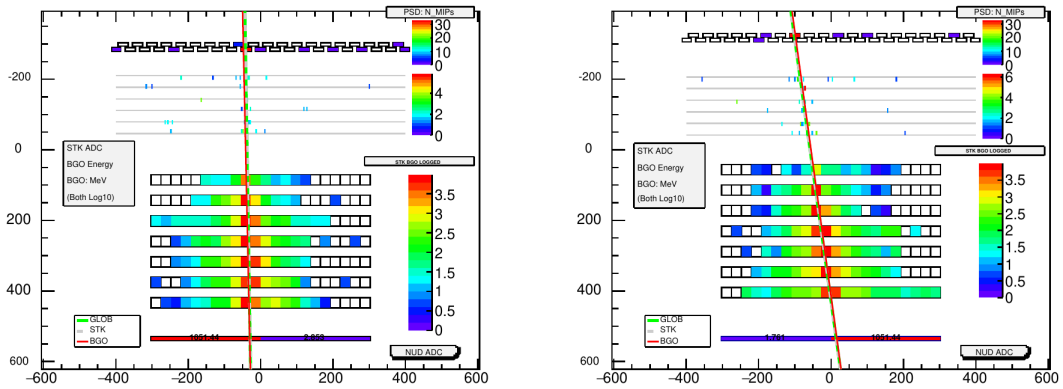

(a) Carbon event at $E_{BGO} = 165$ GeV

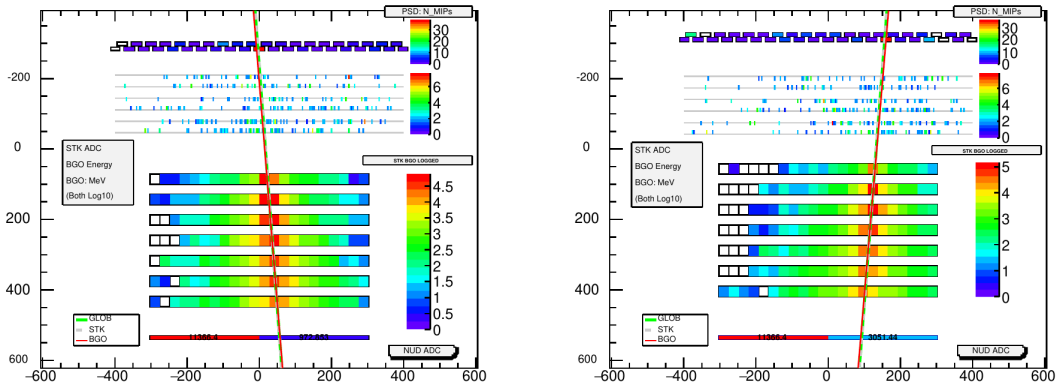

(b) Carbon event at $E_{BGO} = 1.4$ TeV

Figure 3.8: Events displays identified as carbon flight events (after selections) propagating through the various DAMPE sub-detectors. In both cases, left and right plots correspond to XZ and YZ views, respectively, while their reconstructed energies refer to incident particles of (a) 165 GeV and (b) 1.4 TeV, in BGO-deposited energy.

3.3 Reconstruction

3.3.1 PSD charge corrections

In order to define the charge measurement of a single PMT instrumented on a PSD bar, parameters such as the particle impact point and path length should be accurately measured. Due to ionization losses during the propagation of

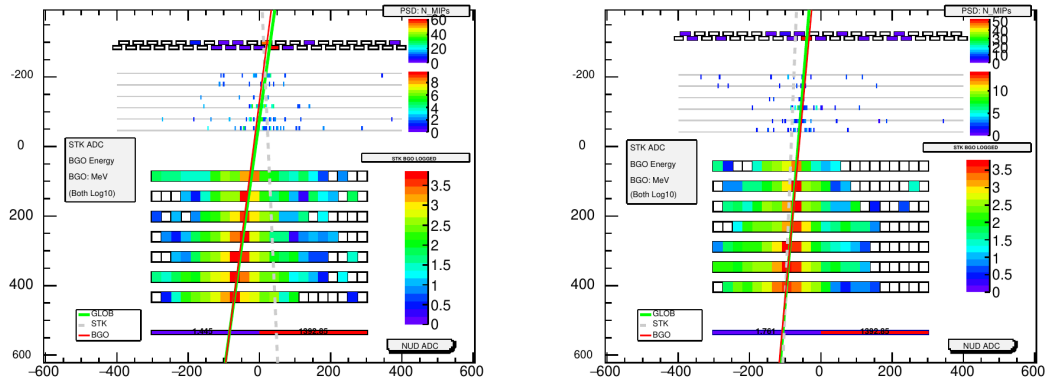

(a) Oxygen event at $E_{BGO} = 128$ GeV

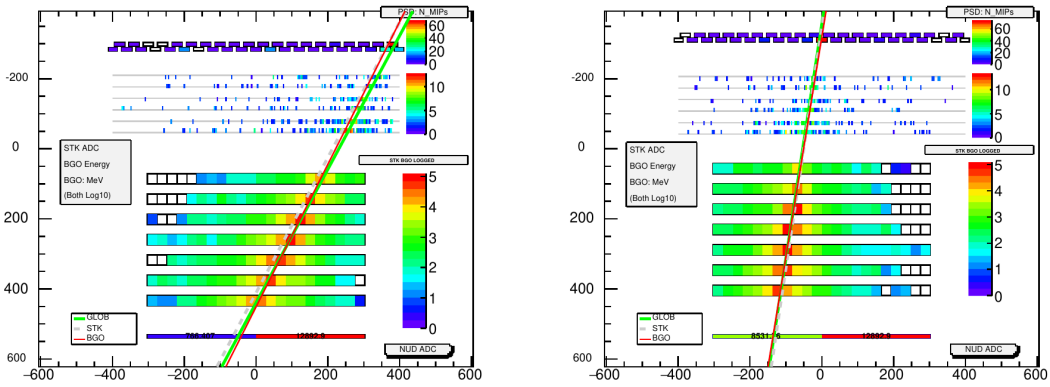

(b) Oxygen event at $E_{BGO} = 1.4$ TeV

Figure 3.9: Events displays concerning oxygen flight events (after selections), propagating through the various DAMPE sub-detectors. In both cases, left and right plots correspond to XZ and YZ views, respectively, while their reconstructed energies refer to incident particles of (a) 128 GeV and (b) 1.4 TeV, in BGO-deposited energy.

scintillating light towards a given PMT, attenuation effects can be evident. In that sense, and given the proportionality of deposited energy to charge squared ($\propto Z^2$), the real deposited energy can be corrected according to the impact position. Such a correction is conveniently named light attenuation correction and is broadly used to measure the real deposited energy in PSD bars per unit path length. A detailed view of the various corrections towards an optimized measurement of the absolute particle charge with the PSD is illustrated in [67].

In order to define a precise path length, an accurate description of the PSD bar geometry is needed. However, due to limited installation precision, vibrations during launching and weightlessness in space, a slight misalignment of the PSD geometric parameters can be detected. In that case, the aforementioned parame-

ters are precisely corrected with the help of proton "MIP" events passing through the PSD in its entirety.

Each PSD bar is divided uniformly in eleven segments and with the addition of strict selections regarding each PSD bar, three alignment parameters are eventually set, which ultimately define the path length. The corrected energy deposition can be derived from the path length multiplied to the most probable energy deposition per millimeter. A detailed look on the alignment method is presented in [99].

Additional corrections correspond to detector quenching effects. The response of a plastic scintillator to charged particles can be represented by a relation involving the scintillator light produced per unit path length ($\frac{dL}{dx}$) and the energy deposition per unit path length ($\frac{dE}{dx}$). taking into account the normalization factor S, the expected linear response function is as follows:

$$\frac{dL}{dx} = S\frac{dE}{dx} \tag{3.1}$$

In the case of DAMPE, the nuclei of interest reside in the energy range above a few GeV/n up to some tens of TeV/n. In this region the ionization energy loss is proportional to the square of the particle's electric charge (as mentioned before), meaning that the ionization density increases sharply with increasing charge. In such conditions, and for high ionization densities the scintillation efficiency is reduced, which gives rise to the so-called quenching effect. This effect is described by the Birks' formula [100]:

$$\frac{dL}{dx} = \frac{S\frac{dE}{dx}}{1 + kB\frac{dE}{dx}} \tag{3.2}$$

where kB corresponds to a quenching parameter extracted from the behavior of experimental data. In order to optimize the reproduction of DAMPE data, formula 3.2 is modified according to: the proportionality of deposited energy to charge squared ($E = aZ^2$, with a representing an average energy loss of 2 MeV/cm in the PSD bars) the apparent charge number (Z^*), a coefficient b correlating ADC values with energy deposition of proton MIPs, with the final addition of a linear term (cZ^*) in the denominator of the formula, as shown below:

$$Z^2 = \frac{Z^{*2}}{S/b + cZ^* - akBZ^{*2}} \tag{3.3}$$

Following the modifications discussed above, an equalization correction is also applied. This effect emerges from the slight mismatches between signal distributions produced by each PMT. In that case the contributions from each PMT are fitted with eq. 3.3, thus leading to an effective charge correction. The quenching and equalization corrections are performed at the same time after the light attenuation correction. Resulting from the above, a charge resolution of 0.17, 0.18, 0.21 and 0.2 has been achieved for boron, carbon, nitrogen and oxygen nuclei respectively.

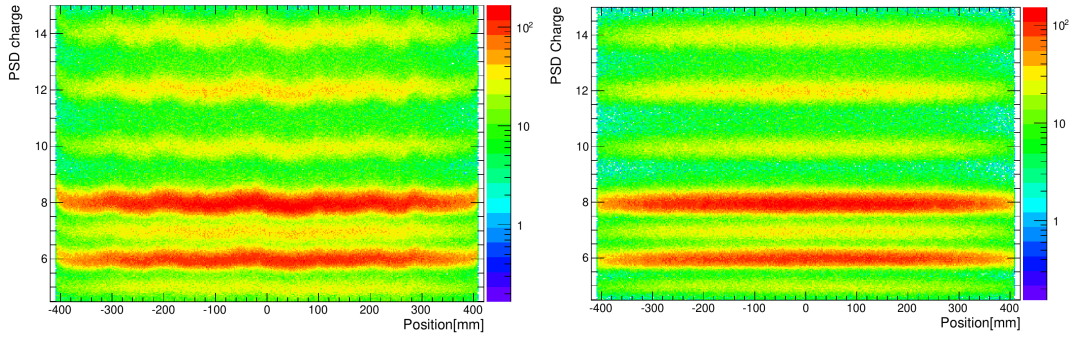

(a) **(b)**

Figure 3.10: PSD charge with respect to the hit position, for the 23rd scintillator bar of the first plane. In (a), the non-uniform effect ("wrinkles") provided by variable light reflection between scintillator and wrapping material is shown, while (b) correspond to the template-interpolation method used to correct for the aforementioned effect. From [101].

A final PSD correction pertains to nuclei heavier than protons and helium. Specifically, as seen in Fig. 3.10a, distinctive "wrinkles" in the PSD charge with respect to the hit position, are evident. This effect is introduced by possible installation non-uniformities of light reflection wrappings on the PSD bar. Consequently, an alteration on the reflection rate is expected, depending on the gap between the scintillator surface and wrapping material. In that case, a template-interpolation method was developed in order to address the variation of PSD signals with hit position.

The nucleus of choice in this template is oxygen, being one of the most abundant elements in the medium mass CR group. Following the aforementioned corrections, Fig. 3.10b illustrates the resulting PSD charge uniformity with

respect to the hit position, thus leading to more consistent measurements with greater resolution. A more detailed view on this correction can be found in [101].

3.3.2 STK eta correction

Apart from an accurate track definition, the STK provides additional measurements of the incoming particle charge. Important parameters towards an accurate charge measurement are the inclination angle and impact point, while an imprecise detection (i.e., charge spread in multiple silicon strips) might lead to possible signal losses. Consequently, an η_{STK} variable is introduced, in order to address this effect by distinguishing signals generated either on readout or floating strips of a given STK ladder. The η_{STK} variable is defined as:

$$\eta_{STK} = \frac{S_1}{S_1 + S_2} \tag{3.4}$$

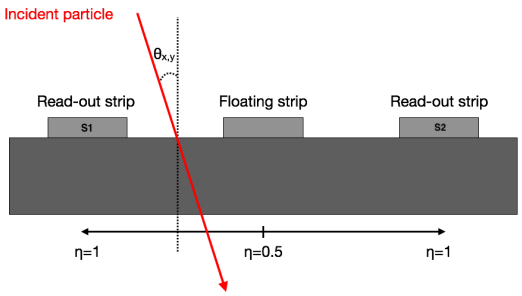

Figure 3.11: Cross-section of alternating read-out and floating strips on an STK ladder in the XY view, illustrating the correlation between η_{STK} and impact point of the particle. From [102].

where S_1 and S_2 correspond to signals of adjacent channels. As seen in Fig. 3.11, the η_{STK} value can receive values between 0.5 (similar signals between two neighboring readout strips) and 1 (cluster corresponding to a single strip).

The correction is briefly discussed here, while a more detailed version can be found in [102]. A selection of nucleonic candidates in both flight and simulated data regarding a given element (i.e., helium or carbon) are distributed in various bins containing the number of silicon strips, impact angle $\theta_{\chi,y}$ and η_{STK}. Each contribution is fitted with a Moyal distribution[2] [103] and its Most Probable

[2]This distribution describes the energy loss of a charged relativistic particle due to ionization of the medium, while providing an approximation for the Landau distribution.

Value (MPV) is extracted, for a given η bin. Combining bins of $\theta_{\chi,y}$ and number of strips, a bi-dimensional distribution of STK dependence on η_{STK} is produced and subsequently fitted with a quadratic function, as seen in the denominator of Eq. 3.5.

The nominator ($\Delta E_{\mathrm{N,1-\ strip}}$) corresponds to the target value of the cluster charge and is associated to the MPV of a given nucleus (N) regarding single-strip cluster signals. The correction parameters were applied to the STK charge of every ladder, resulting in a great reduction in energy losses. The correction parameter as well as the resulting energy are viewed in Eq. 3.5 and 3.6.

$$\text{Correction param. } (\eta_{STK}) = \frac{\Delta E_{\mathrm{N,1-\ strip}}}{a\eta_{STK}^2 + b\eta_{STK} + c} \tag{3.5}$$

$$\Delta E_{corr} = \Delta E \times \text{Correction param.}(\eta_{\mathrm{STK}}) \tag{3.6}$$

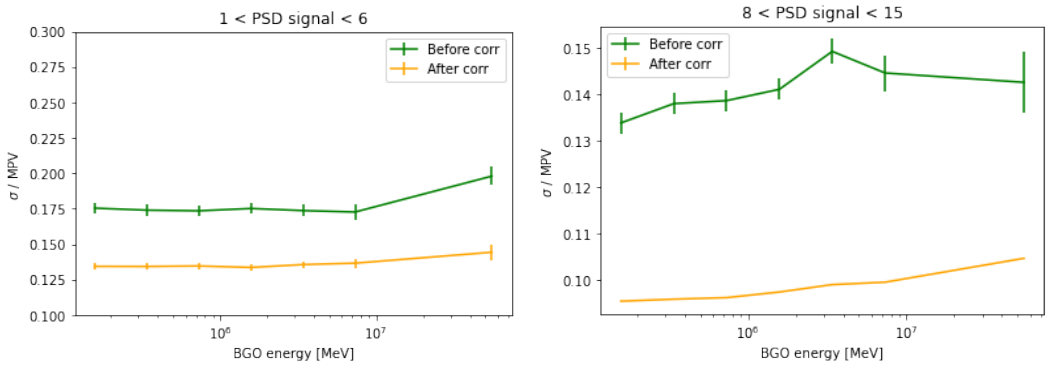

(a) **(b)**

Figure 3.12: Ratios of $\frac{\sigma}{MPV}$ with respect to the energy deposited in the BGO calorimeter. The two examples correspond to applied corrections in (a) protons and (b) helium nuclei, thus leading to an overall improvement in their respective peak positions. From [102].

3.3.3 BGO saturation correction

The DAMPE calorimeter is designed to operate in a wide range of deposited energies, with optimal resolution. At higher energies (greater than a few decades of TeV) there is a greater chance of saturating the low-gain channels of the electronic readout, which consequently leads to an underestimation of the measured energy.

As discussed in the previous chapter, each BGO bar is readout by one PMT per side, which (for the sake of simplicity) will be referred to as S0 and S1. Both PMTs are instrumented with different optical filters, with S1 having an attenuation factor of 5 with respect to S0. In order to cover a wider dynamic range, these two PMTs are readout by three sensitive dynodes (Dy2, Dy5, Dy8), corresponding to low, medium and high gain channels respectively (as seen in Fig. 3.13).

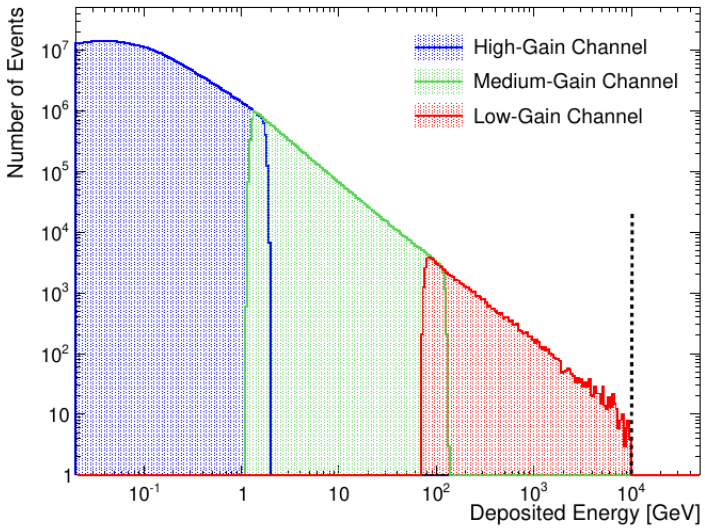

Figure 3.13: Energy deposition spectrum produced by flight data of a single PMT (S1) instrumented on a BGO bar. The various colored contributions correspond to high (blue), medium (green) and low (red) gain ranges, while the vertical black line represents the upper boundary of the measurement. From [104].

The saturation correction method depends on the combination of deposited energy in neighboring BGO crystals and longitudinal shower development, in order to accurately reconstruct the energy of saturated bars [104]. The first step pertains to the energy deposited in neighboring bars (left and right) of a saturated crystal, which is defined as follows:

$$\eta_{\mathrm{LR},j} = \frac{E_{\mathrm{Max},j}}{E_{\mathrm{Max},j} + E_{\mathrm{Left},j} + E_{\mathrm{Right},j}} \tag{3.7}$$

where $E_{\mathrm{Max},j}$ is the maximum energy deposit in the jth layer, $E_{\mathrm{Left},j}$ and ($E_{\mathrm{Right},j}$ correspond to the energy deposited in the neighboring left or right bars. Then, with $\eta_{\mathrm{LR},j}$, its possible to correct the deposited energy deposit as follows:

$$E_{\mathrm{Sat},j} = \frac{\eta_{\mathrm{LR},j}}{1-\eta_{\mathrm{LR},j}} \cdot (E_{\mathrm{Left},j} + E_{\mathrm{Right},j}) \tag{3.8}$$

Following the left-right correction, an initial estimation of the real deposited energy in the calorimeter is obtained. For a complete picture on the possible saturated bar an additional variable $\eta_{\mathrm{UD},j}$ is introduced, taking into account the deposited energy in the upper and lower BGO layers respectively:

$$\eta_{\mathrm{UD},j} = \frac{E_{\mathrm{Max},j}}{E_{\mathrm{Max},j} + E_{\mathrm{Left},j} + E_{\mathrm{Right},j} + E_{\mathrm{Up},j} + E_{\mathrm{Down},j}}. \tag{3.9}$$

with the further updated equation corresponding to:

$$E_{\mathrm{Sat},j} = \frac{\eta_{\mathrm{UD},j}}{1-\eta_{\mathrm{UD},j}} \times (E_{\mathrm{Left},j} + E_{\mathrm{Right},j} + E_{\mathrm{Up},j} + E_{\mathrm{Down},j}) \tag{3.10}$$

The correction procedure up to this point is thoroughly presented in [104], with an example on saturated bars being presented in Fig. 3.14. Specifically for this work an additional step is included in order to account for the case of adjacent saturated crystals within the same layer. These events can be rare but they are also addressed in order to provide a more complete picture.

The updated version of the correction includes a calculation of the η_{BGO} parameter regarding the ratio between minimum and maximum energy depositions in the left-right crystals (as seen in 3.11), thus leading to an estimation of the reconstructed energy in the second bar with a maximum energy deposition. In Fig. 3.15, the updated version of the saturation correction method is compared to its first iteration along with a case of no correction applied, for simulated events of highly energetic helium nuclei (10 TeV - 1 PeV). The ratio of corrected over simulated events is in good agreement with the method shown previously, while illustrating a clear increase in peak resolution. The same method is applied in the case of carbon and oxygen with analogous results.

$$\eta_{BGO} = \frac{\mathrm{Min}\,(E_L, E_R)}{\mathrm{Max}\,(E_L, E_R)} \tag{3.11}$$

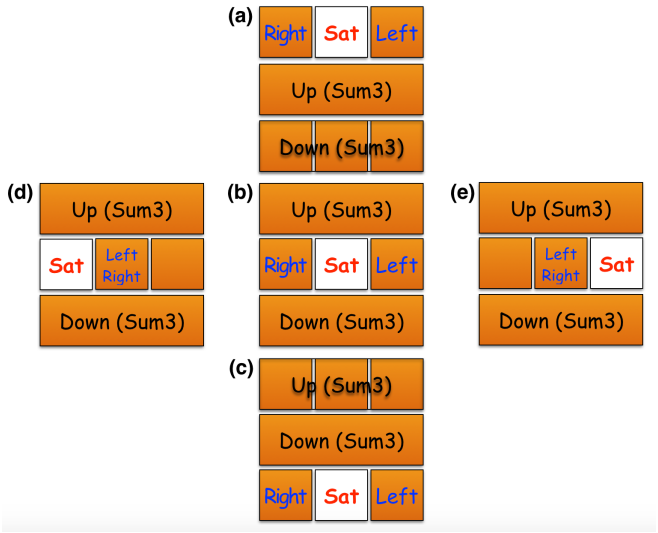

Figure 3.14: Schematic view of a possible classification concerning saturated events: at the (a) top layer (j = 1), (b) middle layers (j = 2-13), (c) bottom layer and for (d, e) saturated bars on the left and right edges, respectively. From [104].

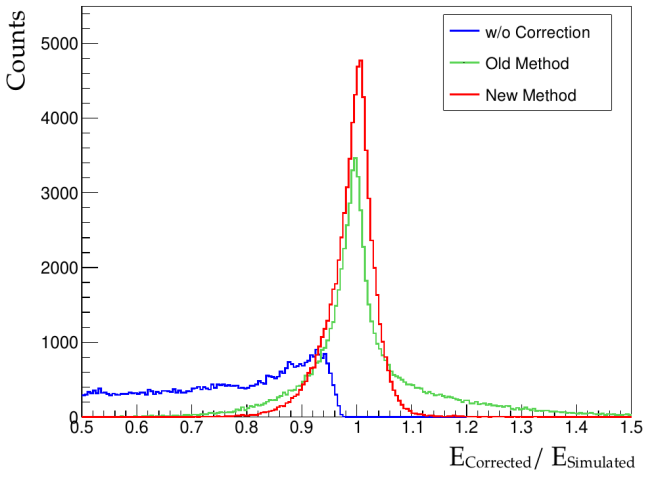

Figure 3.15: Reconstructed BGO energy events produced from MC simulations of helium nuclei in the energy range of 10 TeV - 1 PeV (primary energy). The various distributions correspond to the ratio between corrected and saturated events, where blue, green and red colors correspond to no corrections, the first saturation correction iteration and the updated saturation correction method, respectively.

3.4 Selection of Carbon and Oxygen events

Following the introduction of the various elements concerning selection cuts and corrections, a careful choice of carbon and oxygen events is performed. In order to achieve pure carbon and oxygen samples, a specific PSD and STK event selection procedure is adopted and presented in the following subsections.

3.4.1 PSD charge selection method

CR nuclei impinging on the PSD, can give rise to a multitude of interactions according to their incident energy and mass. When moving from lighter to heavier nuclei, the probability of nuclear fragmentation becomes more prominent, hence introducing a sizable charge distortion in the selected events. In order to address such an effect, a first-approximation solution would be to eliminate all candidate events suffering fragmentation in all four PSD layers. Unfortunately, this would significantly decrease the data size and even more at very high energies (multiple TeV), where the statistics are scarce by definition.

Thus, a more intricate method of determining the PSD charge is adopted in this analysis, following an event-by-event approach which aims at registering layer-consistent charge measurements, while avoiding all fragmented events in the process. The so-called progressing PSD charge method can be given by:

$$Q^{PSD} = \frac{\sum_i Q_i^{PSD}}{N_{Layers}} \tag{3.12}$$

where Q^{PSD} is the final PSD charge and Q_i^{PSD} corresponds to the charge value found in a given layer, with N_{Layers} signaling the number of consecutive PSD layers giving a non-zero charge. At the same time, a consistency check between signals in adjacent layers is requested:

$$\left|Q_i^{PSD} - Q_{i+1}^{PSD}\right| < 1 \tag{3.13}$$

which requires events registered in neighboring layers to be within one absolute charge value, thus eliminating possible inconsistencies arising mainly from fragmentation interactions or spurious events in the detector. In that sense, this method is following the path of a charged particle through the PSD, scanning the full sub-detector layer by layer. If non-zero signals are found in multiple layers then the average charge value is computed, under the assumption that all registered signals are found within one charge value of consecutive layers. If the aforementioned consistency check is not respected until a certain layer, then the charge obtained up to that point is saved.

In Fig. 3.16, a region including the nuclei of interest is presented (from boron to oxygen), when comparing registered events in Y and X PSD planes. The

distinctive contribution of all nuclei is made possible under the application of cuts discussed previously. Additionally, a general view of the total PSD charge with respect to the deposited BGO energy (acquired by the method introduced above) is illustrated in Fig. 3.17. All CR components are consistent in charge and well-separated, thus assisting in a more precise charge selection (to be discussed in the following section).

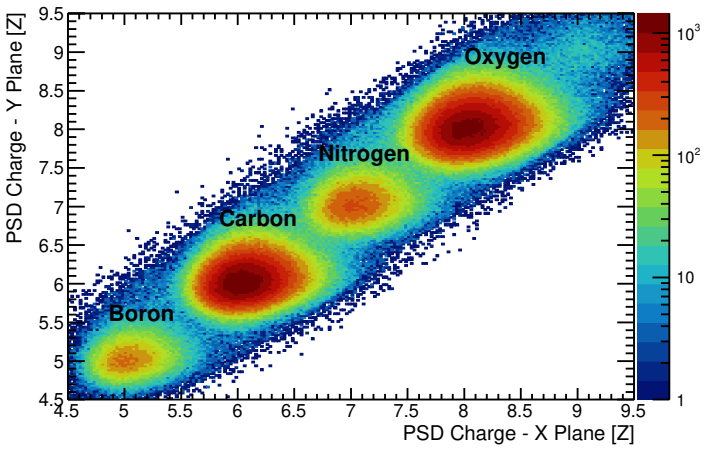

Figure 3.16: Comparison between accumulated charge distributions registered by the Y-oriented plane with respect to the X-oriented plane in the PSD, following the selection cut procedure discussed above. The various charge clusters refer to flight data of (from left to right): boron, carbon, nitrogen and oxygen contributions.

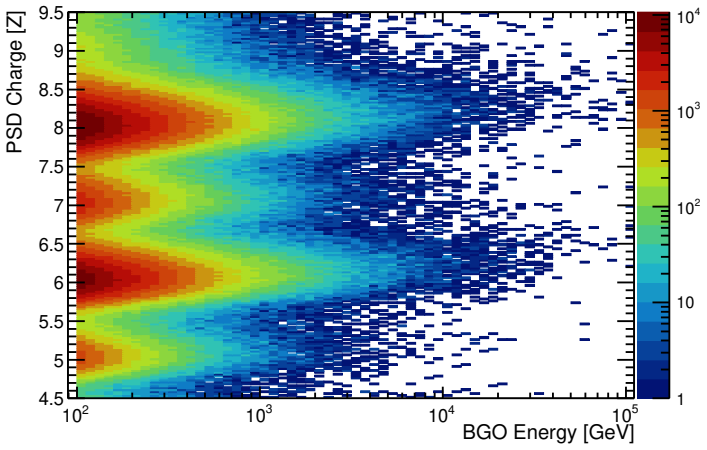

Figure 3.17: PSD charge spectrum with respect to the BGO energy regarding the full DAMPE dataset of six years (flight data), obtained with the PSD progressing charge method.

3.4.2 STK charge cut

The STK provides not only an accurate measurement of the incident particle's trajectory but also an overall charge spectrum of the various CR nuclei. For the case of carbon and oxygen, it is crucial to limit the contribution of lower mass primaries such as helium nuclei, which could add a small but measurable background specifically in higher BGO deposited energies.

The selected events should interact with the first STK layer, providing non-zero signals in either X or Y planes. In case a given event is successfully detected both in X and Y, then an average charge value is computed between the two measurements, in ADC (Analog-to-Digital-Converter) values. In Fig. 3.18, the spectrum of STK charge with respect to the PSD charge is illustrated, arising from selection cuts mentioned in previous sections, with clear contributions from protons to oxygen nuclei.

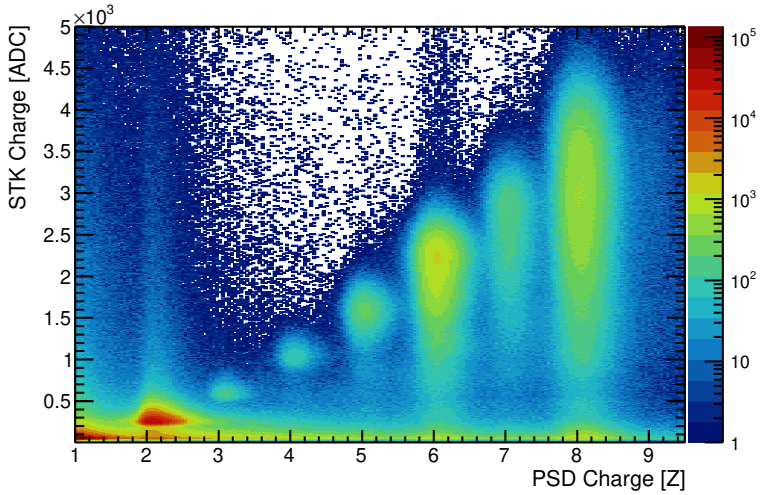

Figure 3.18: STK charge with respect to PSD charge, extracted from six years of DAMPE flight data. Contributions from protons to oxygen nuclei are clearly distinguished in this example.

In this analysis, events should pass a given cut, denoted by a fixed threshold in ADC values. This threshold is imposed around 900 ADC for events impinging in either X or Y planes of the first STK layer, in order to mitigate the contribution of lighter than beryllium nuclei and consequently, lower the overall background percentage. The result of the aforementioned cut is shown in Fig. 3.19, where contributions of protons, helium and lithium events are greatly suppressed, thus providing a more precise view on the nuclei of interest.

All of the aforementioned cuts are applied both in flight data and MC simulated events in order to ensure consistency throughout the analysis procedure.

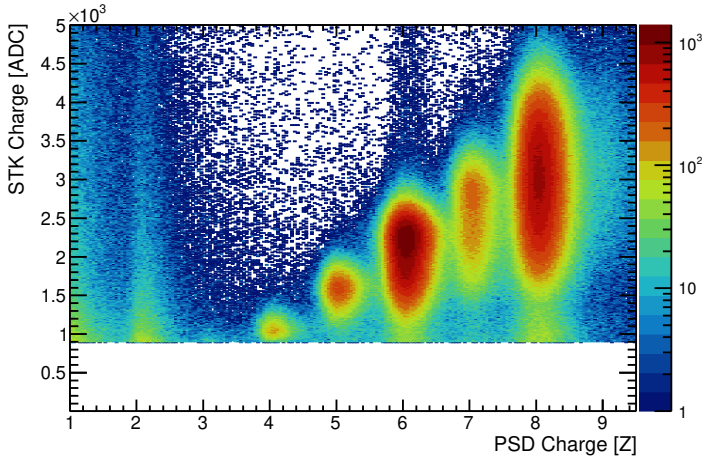

Figure 3.19: STK charge with respect to PSD charge, extracted from six years of DAMPE flight data. An analysis-specific cut is imposed around 900 ADC in order to significantly decrease the contribution of lower-than-beryllium masses. The nuclei of interest can be clearly distinguished in this example.

3.4.3 Selection of carbon and oxygen candidate events

Following a series of selection cuts and corrections in the various sub-detectors, a further step would be to carefully select carbon and oxygen candidates in the PSD according to their respective energy deposition in the BGO calorimeter. An integrated view of the full dataset concerning the PSD charge with respect the BGO energy deposit has been discussed in Fig. 3.17, representing the total flight data statistics used in this work.

In that case, the entire dataset is divided in various bins according to their energy deposition in the BGO calorimeter. This process is carried out for both flight and simulated data with their individual contributions being fit with a Landau-convoluted-with-Gaussian function (hereafter referred to as "Langaus") provided by the ROOT Data Analysis Framework [105], as seen in Fig. 3.20. It should be noted that both carbon and oxygen simulated data were reweighed from an initial E^{-1} distribution to a $E^{-2.6}$ in order to better approximate a more "realistic" scenario regarding the spectral index deriving from primary CRs.

Furthermore, the MPV and sigma parameters of all fitted distributions will be used in order to gauge the overall behavior of carbon and oxygen events in various energy ranges as well as delineating both upper and lower bounds for the

final charge selection. In the following, the various PSD charge spectra spanning over the full energy range will be presented, alongside their Langaus fit functions, regarding six years of DAMPE flight data.

Consequently, the MPV, Landau width and Gaussian sigma (the latter two, summed in quadrature) attributed to carbon and oxygen nuclei, are illustrated in Fig. 3.21. A deviation between the projected behavior of flight and simulated events is evident in these figures. Such an effect might arise from an incomplete method of simulating backscattered events, attributed to showers initiated deeper inside the BGO calorimeter. In that case, a correction on simulated data is performed in order to provide a more realistic representation of flight data. The aforementioned method is called "smearing correction" and can be summarized in eq. 3.14.

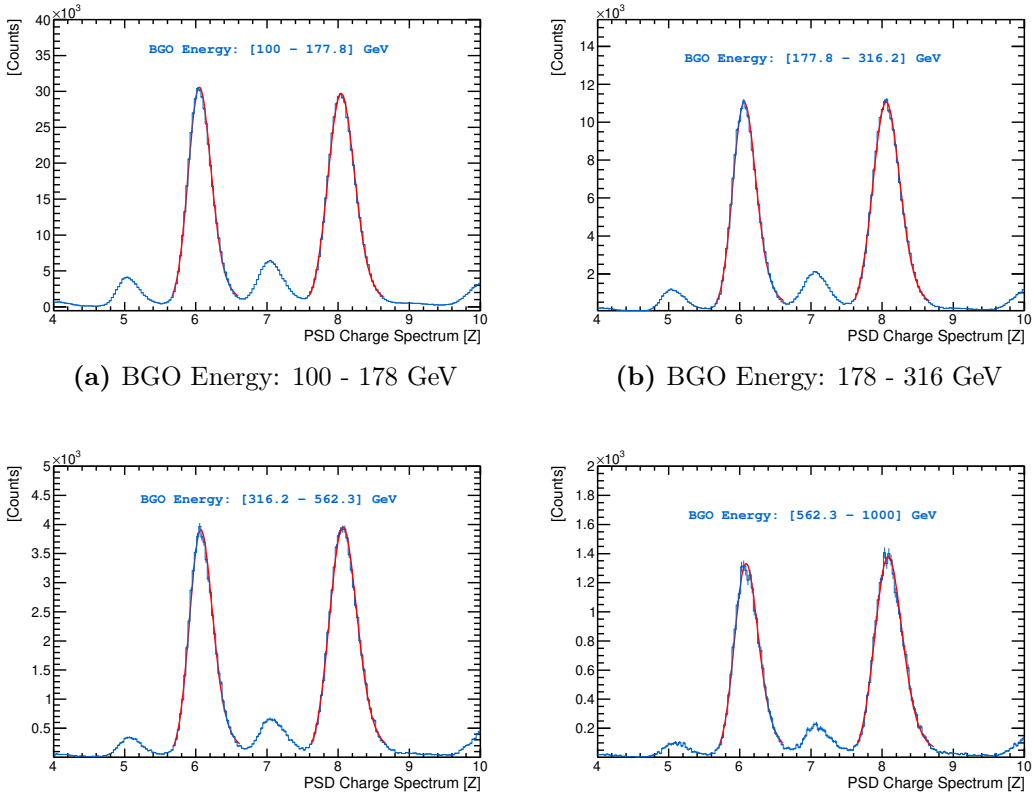

(a) BGO Energy: 100 - 178 GeV

(b) BGO Energy: 178 - 316 GeV

(c) BGO Energy: 316 - 562 GeV

(d) BGO Energy: 562 - 1000 GeV

Figure 3.20: PSD charge spectra concerning various bins of energy deposited in the BGO (from flight data).

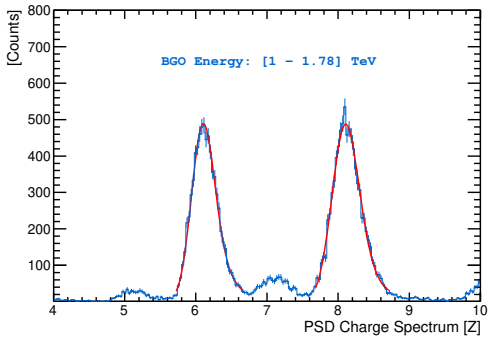

(e) BGO Energy: 1 - 1.78 TeV

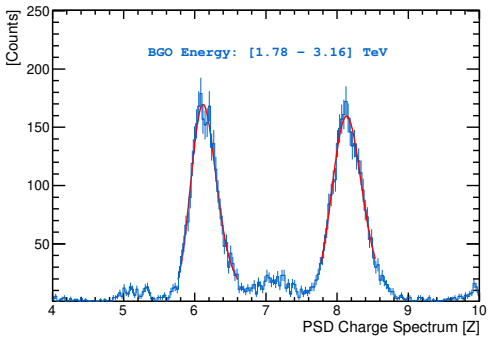

(f) BGO Energy: 1.78 - 3.16 TeV

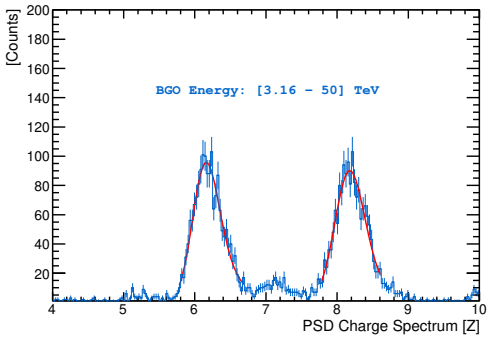

(g) BGO Energy: 3.16 - 50 TeV

Figure 3.20: (Continued) PSD charge spectra concerning various bins of energy deposited in the BGO (from flight data).

$$\Delta E'_{MC} = \left(\Delta E_{MC} - f_{MPV,MC}\left(\Delta E_{BGO}\right)\right) \frac{f_{\sigma,DATA}\left(\Delta E_{BGO}\right)}{f_{\sigma,MC}\left(\Delta E_{BGO}\right)} + f_{MPV,DATA}\left(\Delta E_{BGO}\right) \tag{3.14}$$

where $\Delta E'_{MC}$ corresponds to the simulated energy loss in the PSD for events with initial value ΔE_{MC}. The parameterized functions corresponding to MPV and sigma distributions for simulated (and flight data) are defined as $f_{MPV,MC(DATA)}\left(\Delta E_{BGO}\right)$ and $f_{\sigma,MC(DATA)}\left(\Delta E_{BGO}\right)$, respectively. Afterwards, simulated carbon and oxygen events (following the smearing correction), are re-fitted with the above-stated LanGaus functions, a sample of which is shown in the following (Fig. 3.22).

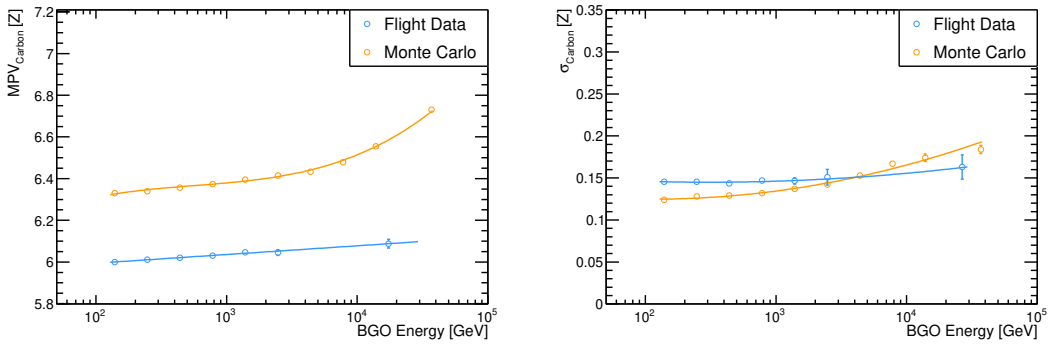

(a) Carbon MPV **(b)** Carbon Sigma

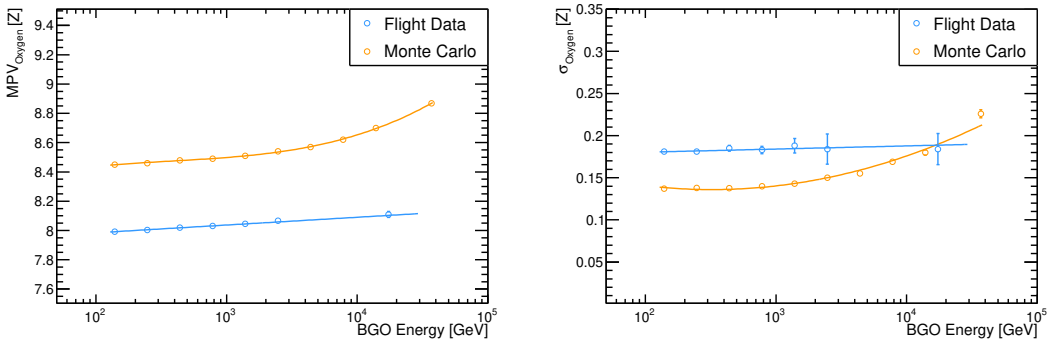

(c) Oxygen MPV **(d)** Oxygen Sigma

Figure 3.21: Behavior of carbon and oxygen (a) MPV and (b) sigma parameters (extracted from LanGaus fits), with respect to the energy deposited in the BGO calorimeter. Blue and yellow contributions correspond to flight and simulated data respectively.

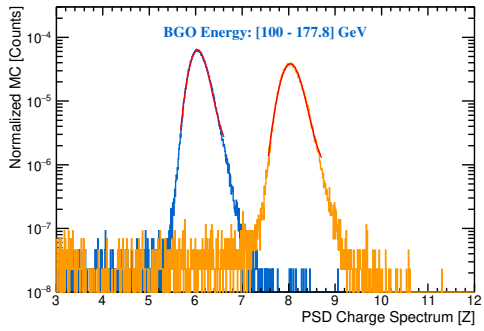

(a) 100 - 178 GeV

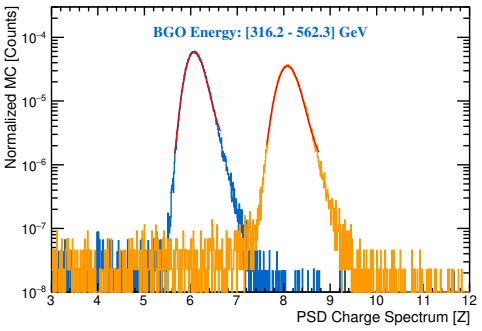

(b) 316 - 562 GeV

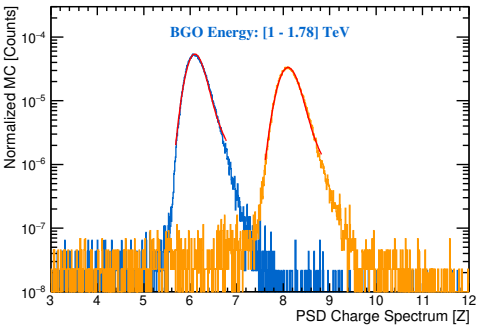

(c) 1 - 1.78 TeV

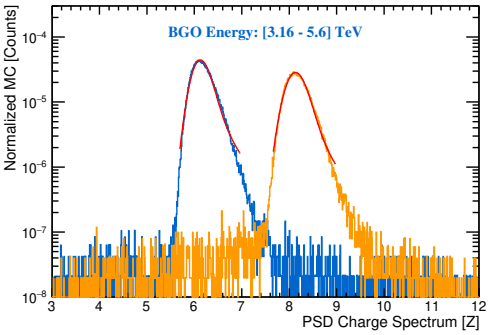

(d) 3.16 - 5.62 TeV

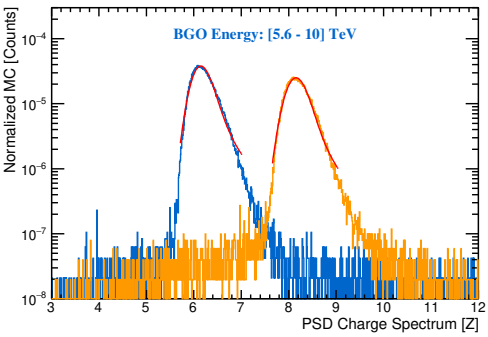

(e) 5.62 - 10 TeV

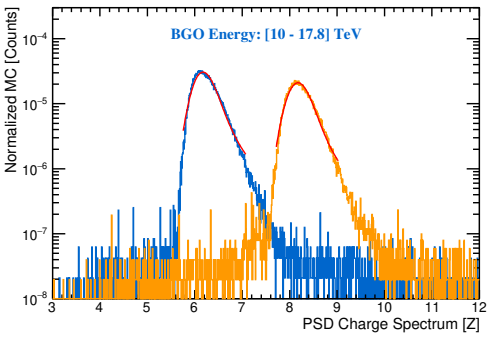

(f) 10 - 17.8 TeV

Figure 3.22: Corrected PSD charge spectra concerning MC carbon and oxygen simulated events in various bins of deposited energy in the BGO calorimeter.

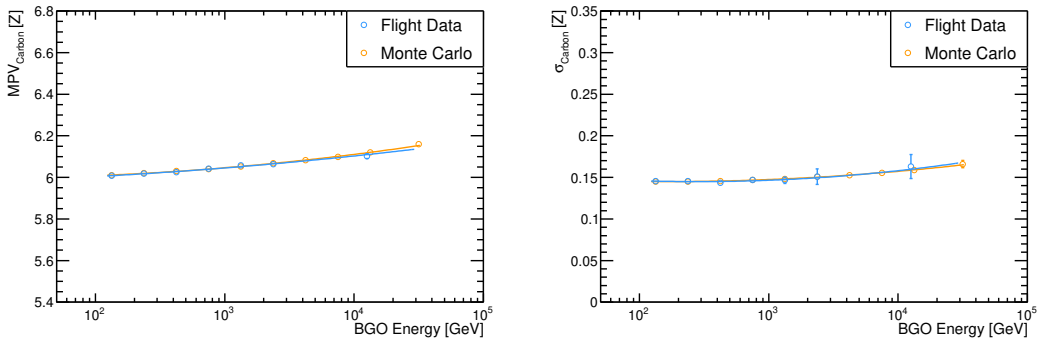

(a) Carbon MPV **(b)** Carbon Sigma

Figure 3.23: Corrected distributions of carbon (a) MPV and (b) sigma parameters, with respect to the energy deposited in the BGO calorimeter. Blue and yellow contributions correspond to flight and simulated data respectively.

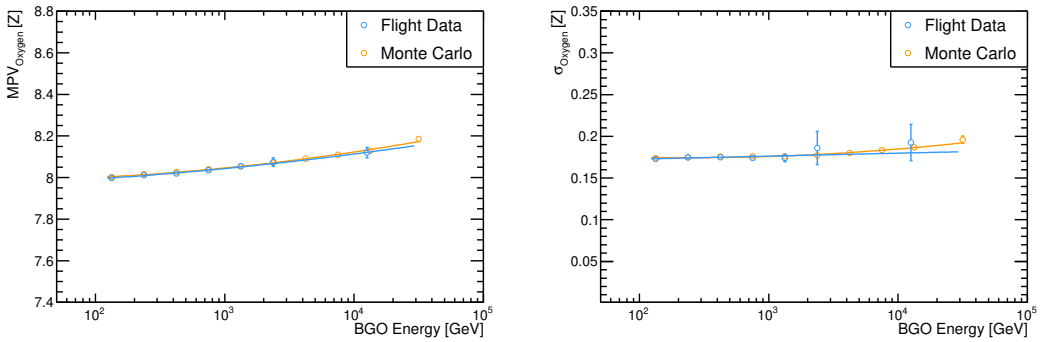

(a) Oxygen MPV **(b)** Oxygen Sigma

Figure 3.24: Corrected distributions of oxygen (a) MPV and (b) sigma parameters, with respect to the energy deposited in the BGO calorimeter. Blue and yellow contributions correspond to flight and simulated data respectively.

3.5 Background and charge selection

3.5.1 Background contamination studies

An optimal charge selection for carbon and oxygen nuclei, depends on the greater understanding of the background contamination introduced by neighboring (to carbon and oxygen) nuclei. In that case, flight and simulated data of beryllium, boron, carbon, nitrogen and oxygen nuclei are subjected to the entirety of selection cuts introduced in previous sections with the aim of comparing the two. The full list of MC simulated nuclei used towards the contamination estimation is presented in Tab. 3.2. As mentioned before, each simulated element is reweighed according to a power-law distribution pertaining to its projected spectral index, being $E^{-2.6}$ for primary and E^{-3} for secondary CRs, thus obtaining a more precise approximation of on-orbit data.

Table 3.2: List of simulated events used in the template fit for the optimal background estimation and charge definition.

Element	Isotope	Energy range [TeV]	Events [Millions]
Beryllium	^{7}Be, ^{9}Be	0.1 - 1	242
		1 - 10	20
		10 - 100	20
Boron	^{10}B, ^{11}B	0.1 - 1	85
		1 - 10	100
		10 - 100	105
Carbon	^{12}C	0.1 - 1	100
		1 - 10	107
		10 - 100	110
		100 - 500	13
Nitrogen	^{14}N, ^{15}N	0.1 - 1	129
		1 - 10	40
		10 - 100	81
		100 - 500	8
Oxygen	^{16}O	0.1 - 1	100
		1 - 10	101
		10 - 100	116
		100 - 500	19

Consequently, a unique model will be constructed, in order to accurately describe individual background contributions to the nuclei of interest. Depending on the aforementioned background percentage, such a method will provide an optimal determination of the charge selection bounds, taking into account the lowest possible contamination. The procedure concerning individual templates according to a given energy bin requires a careful inclusion of all MC simulated and flight PSD charge histograms. Then following the definition of the probability density function, a strict scaling (no bin fluctuations or data compensations are allowed) based on each individual MC template can be obtained, using RooFit.

In each BGO energy bin a constant PSD charge selection is imposed (defined by the above-stated MPV and sigma functions for carbon and oxygen), in order to compute the background contamination. The various templates according to the energy deposited in the calorimeter are shown in Fig. 3.25. The agreement between flight and simulated data is exceptional, with the general template fit providing a robust picture of the contamination percentage. The overall flight-over-simulated data ratio is quite stable with increasing energies, although an exception might be found in lighter-than-carbon nuclei where statistics are scarce, along with a general background reduction effect induced by the STK charge cut.

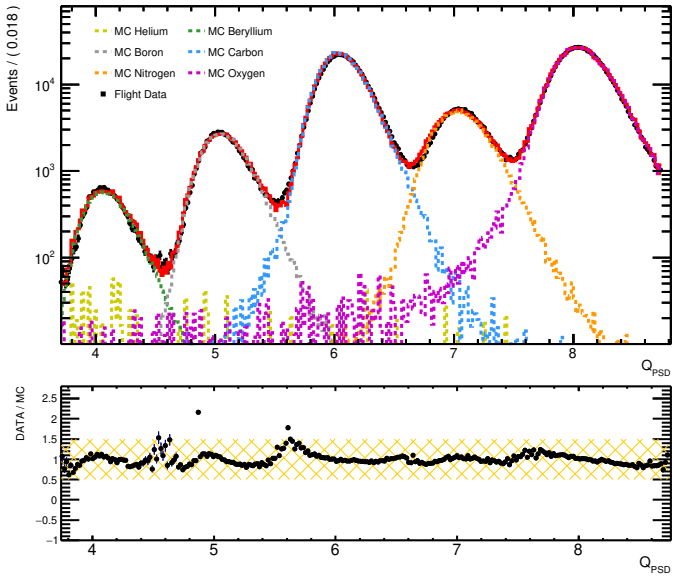

(a) BGO Energy: 100 - 178 GeV

Figure 3.25: PSD spectra concerning nuclei from beryllium to oxygen for the case of flight and simulated data in various energy bins (BGO energy). The various colored lines correspond to MC samples, black points refer to flight data, while the red continuous line represents the optimal template fit.

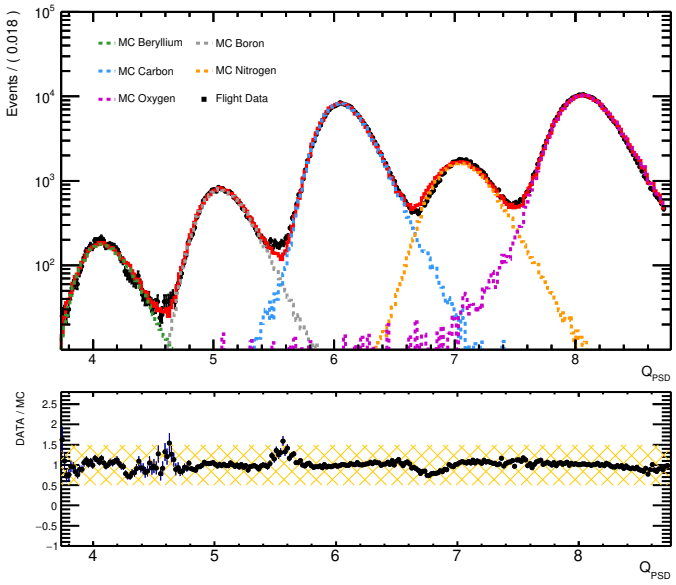

(b) BGO Energy: 178 - 316 GeV

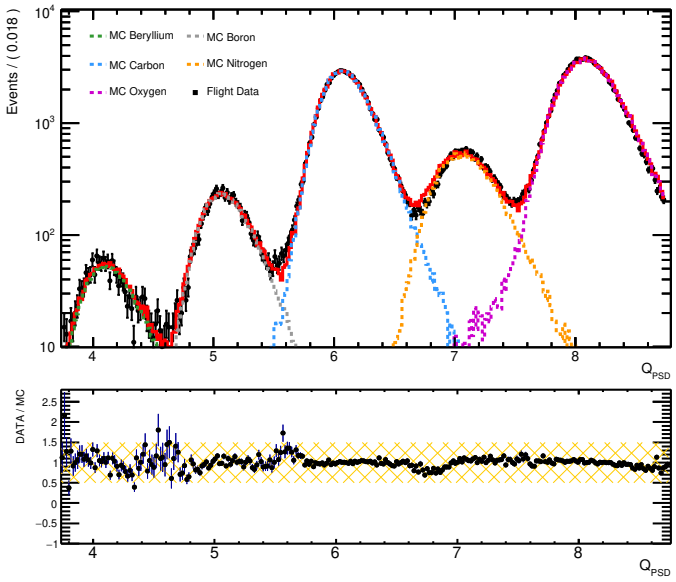

(c) BGO Energy: 316 - 562 GeV

Figure 3.25: (Continued) PSD spectra concerning nuclei from beryllium to oxygen for the case of flight and simulated data in various energy bins (BGO energy). The various colored lines correspond to MC samples used in this work, black points refer to flight data, while the red continuous line represents the optimal template fit.

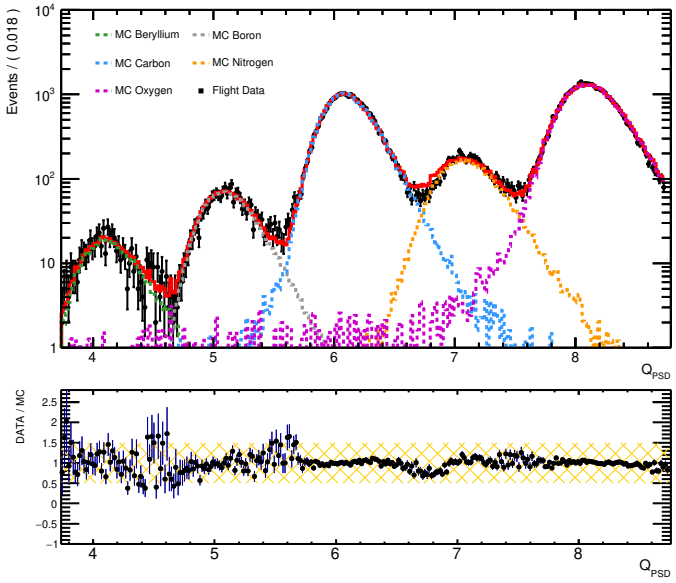

(d) BGO Energy: 562 GeV - 1 TeV

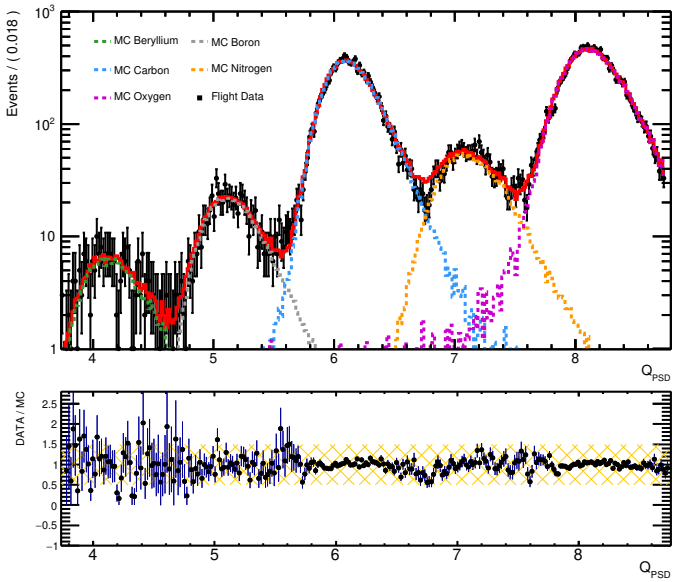

(e) BGO Energy: 1 - 1.78 TeV

Figure 3.25: (Continued) PSD spectra concerning nuclei from beryllium to oxygen for the case of flight and simulated data in various energy bins (BGO energy). The various colored lines correspond to MC samples used in this work, black points refer to flight data, while the red continuous line represents the optimal template fit.

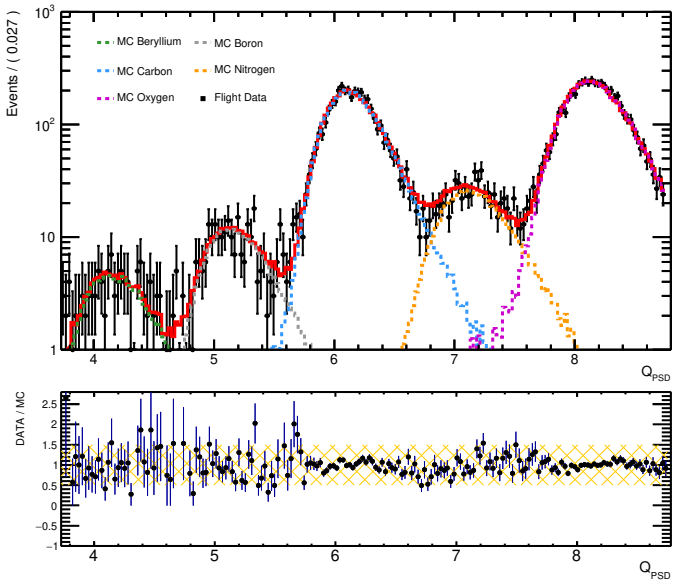

(f) BGO Energy: 1.78 - 3.16 TeV

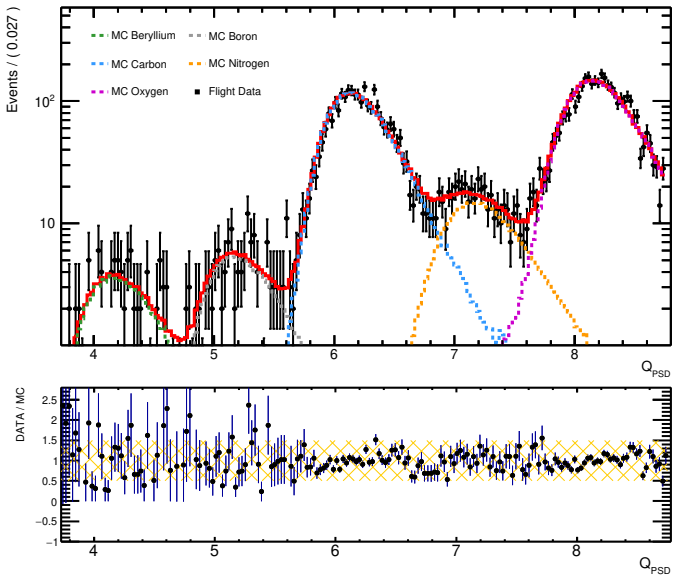

(g) BGO Energy: 3.16 - 50 TeV

Figure 3.25: (Continued) PSD spectra concerning nuclei from beryllium to oxygen for the case of flight and simulated data in various energy bins (BGO energy). The various colored lines correspond to MC samples used in this work, black points refer to flight data, while the red continuous line represents the optimal template fit.

3.5.2 Charge selection for carbon and oxygen

Following the configuration of the various template fits towards an accurate background estimation, the upper and lower limits concerning carbon and oxygen nuclei can be defined. These limits are imposed by the synergy of MPV and sigma functions delineated by the following functions (Eq. 3.15 and 3.16)

$$\text{MPV} - 1.4\,\sigma < \text{PSD Charge}_{Carbon} < \text{MPV} + 2.7\,\sigma \tag{3.15}$$

$$\text{MPV} - 1.2\,\sigma < \text{PSD Charge}_{Oxygen} < \text{MPV} + 3.5\,\sigma \tag{3.16}$$

Applying the charge selection limits as seen above, the total contamination fraction is computed for carbon and oxygen nuclei, as illustrated in Figs. 3.26 and 3.27. Evidently, the overall background percentage remains low, given the strict charge selection requirements. Specifically, the total background percentage for the case of carbon and oxygen spans from approximately 0.3 % to 1 % for the highest energy bins, thus maintaining a high sample purity in both cases. Ultimately, the complete picture regarding carbon and oxygen charge selections can be viewed in Fig. 3.28, where the PSD charge is shown with respect to the BGO energy, this time marked by dashed lines signaling the MPV along with upper and lower bounds delineated by the sigma values.

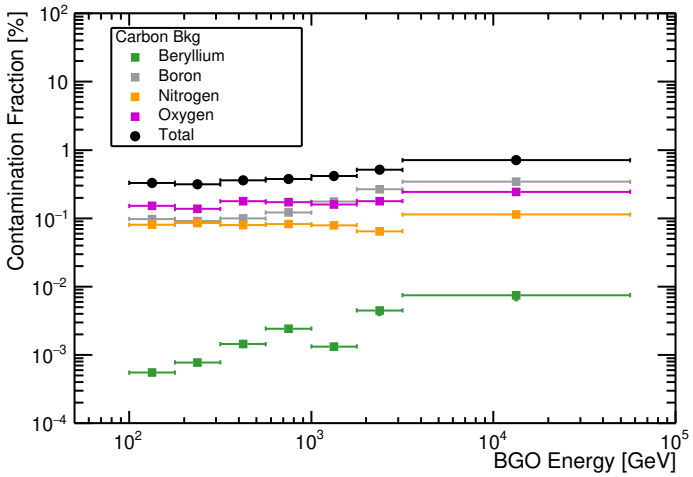

Figure 3.26: Overview of the various contamination fractions regarding the carbon analysis with respect to the energy deposited inside the BGO calorimeter.

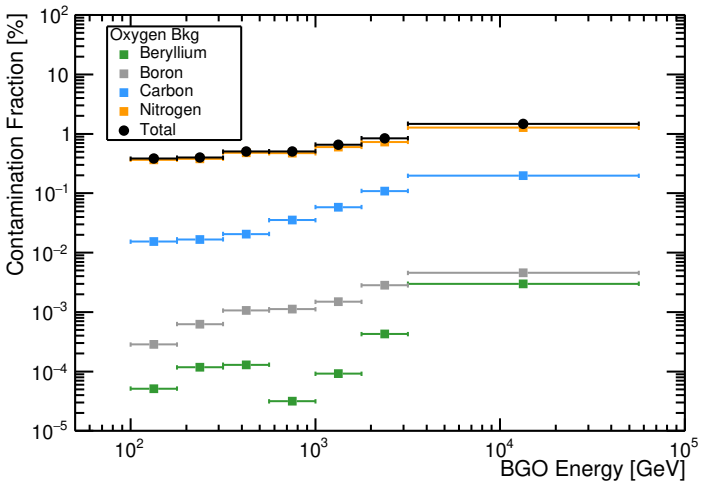

Figure 3.27: Overview of the various contamination fractions regarding oxygen nuclei with respect to the energy deposited inside the BGO calorimeter.

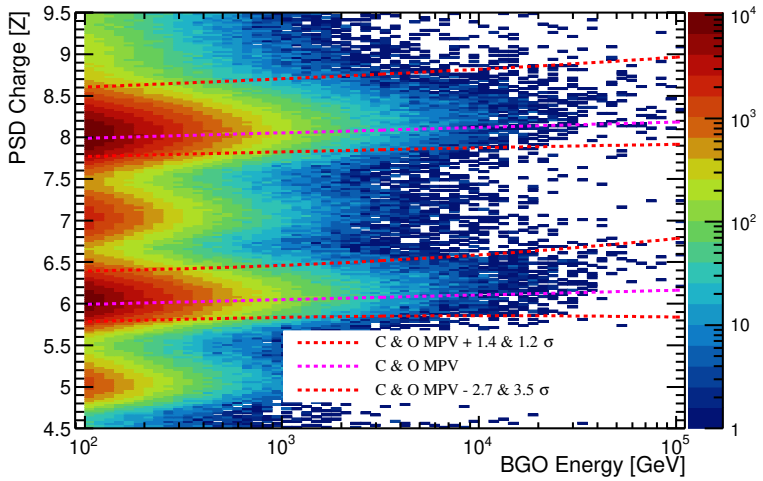

Figure 3.28: PSD charge spectrum with respect to BGO energy regarding the full DAMPE dataset. Red dashed lines correspond to upper and lower charge limits while magenta dashed lines denote the MPV behavior with increasing energies, for carbon and oxygen nuclei.

3.6 Efficiency validations with data

The spectral measurement of carbon and oxygen fluxes is affected (as all measurements) by statistic and systematic uncertainties. In this section, an overview of systematic uncertainties will be presented, pertaining to the various selection cuts applied throughout the analysis. The effect of a given cut is evaluated through a coherent efficiency estimation between flight and simulated data with any possible divergence being credited to the overall uncertainty percentage. For the case of MC simulated data, the contributions of all neighboring nuclei (ranging from beryllium to oxygen) were included in order to attain a more realistic comparison with on-orbit data.

For a specific selection cut under investigation, the aim is to gauge the number of surviving events as a function of the energy deposited inside the BGO calorimeter. An overview of efficiency validations with data will be presented in the following, focused on the systematic uncertainties arising from the HET request, as well as verifying PSD, STK and BGO selection cuts, for the case of carbon and oxygen nuclei.

3.6.1 High Energy Trigger efficiency

The four options implemented within the trigger logic of DAMPE were discussed in the previous chapter (Sec. 2.4). In order to evaluate the efficiency of the HET request, an additional trigger will be imposed. In that case, the efficiency validation will be provided from the ratio of events surviving both HET and LET requests over the number of events surviving the LET alone, as seen below:

$$\varepsilon_{\mathrm{HET}} = \frac{\mathrm{N}_{\mathrm{HET|LET}}}{\mathrm{N}_{\mathrm{LET}}} \tag{3.17}$$

Consequently, Fig. 3.29 illustrates the HET efficiency with respect to the energy deposited inside the BGO calorimeter, for carbon and oxygen analyses. Additional plots highlighting the agreement between flight and MC simulated data are shown, where an overall discrepancy of less than 0.5% is evident throughout the entire BGO energy range, within statistical uncertainties.

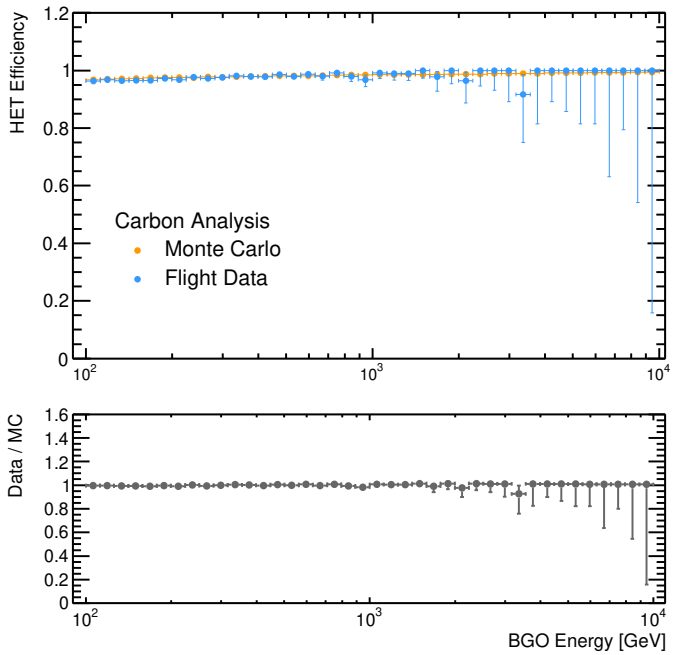

(a) Carbon

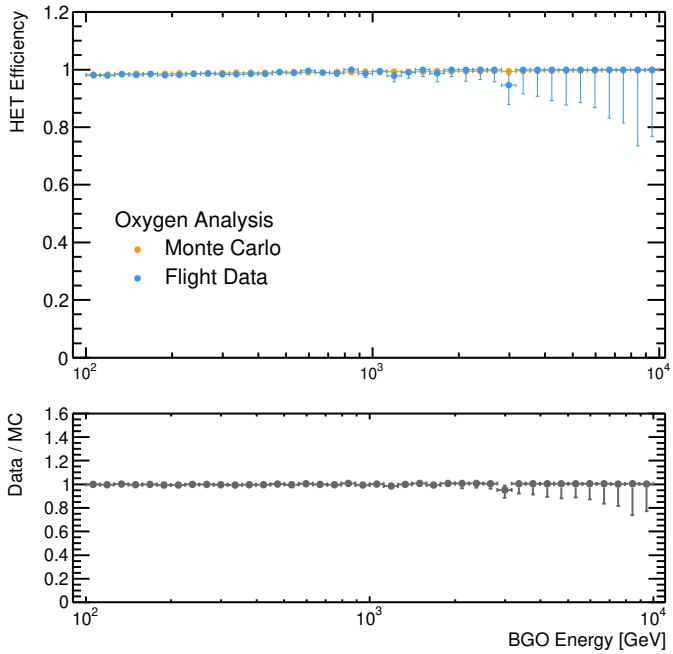

(b) Oxygen

Figure 3.29: High Energy Trigger efficiency validation with respect to the BGO energy deposition, regarding (a) carbon and (b) oxygen analyses. Flight and simulated data correspond to blue and yellow points respectively. The ratio of flight to MC simulated events is also illustrated, in order to highlight their overall agreement.

3.6.2 PSD event selection efficiency

In order to gauge the efficiency of the progressing PSD charge method discussed before, a wide charge window is imposed for carbon and oxygen data concerning the mean charge yield in Y and X PSD planes. Additional cuts in STK and BGO are also introduced, in order to accurately reproduce the list of selections used in the analysis. The general limits imposed on the PSD Y and X planes concerning the mean charge correspond to:

$$5.5 < \text{PSD Charge}_{X\&Y} < 6.7 \text{ (Carbon)} \tag{3.18}$$

$$7.5 < \text{PSD Charge}_{X\&Y} < 8.7 \text{ (Oxygen)} \tag{3.19}$$

while the PSD event selection efficiency is given by:

$$\varepsilon_{\text{PSD}} = \frac{\text{N}_{\text{PSD}_\text{X}|\text{PSD}_\text{Y}|\text{PSD}_\text{ProgCharge}|\text{STK}}}{\text{N}_{\text{PSD}_\text{X}|\text{PSD}_\text{Y}|\text{STK}}} \tag{3.20}$$

where $\text{N}_{\text{PSD}_\text{X}|\text{PSD}_\text{Y}|\text{PSD}_\text{ProgCharge}|\text{STK}}$ is the number of events passing selections including the cut corresponding to the progressing PSD charge method, while $\text{N}_{\text{PSD}_\text{X}|\text{PSD}_\text{Y}|\text{STK}}$ the event number including only the mean charge contributions in Y and X PSD plane along with the STK cut. The resulting efficiency measurements regarding the PSD charge selection method is shown in Fig. 3.30, where a good agreement between MC and flight data is achieved, with a divergence of less than 1% being evident in the entire BGO energy range, within statistical uncertainties.

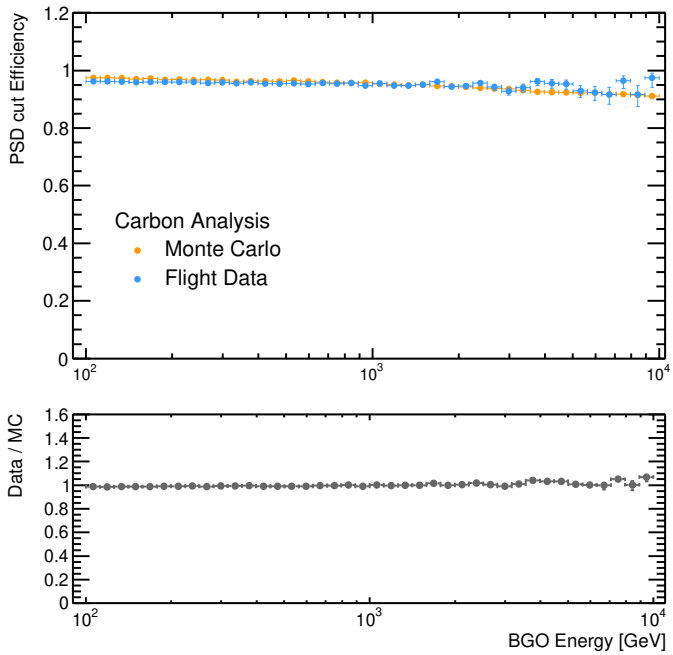

(a) Carbon

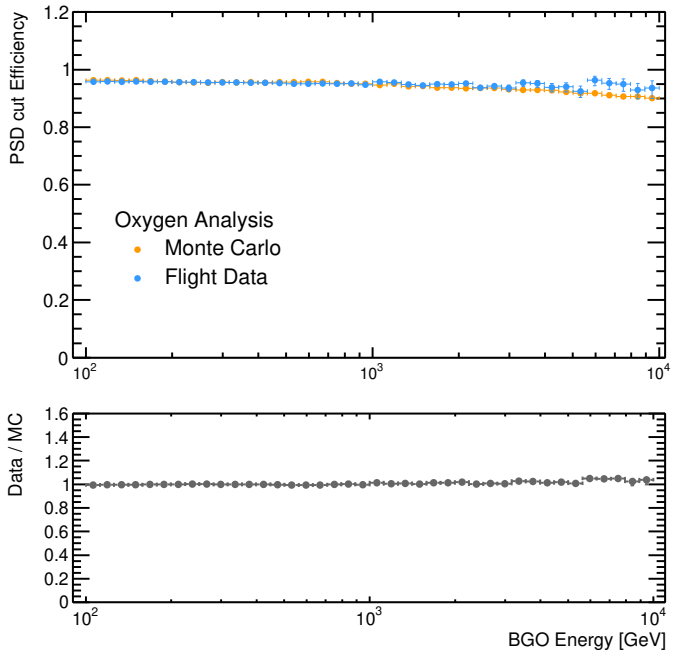

(b) Oxygen

Figure 3.30: PSD progressing window efficiency validation with respect to the BGO energy deposition, regarding (a) carbon and (b) oxygen analyses. Flight and simulated data correspond to blue and yellow points respectively. The ratio of flight to MC simulated events is also illustrated, in order to highlight their overall agreement.

3.6.3 STK layer efficiency

In order to define the efficiency concerning the selection cut of the first STK layer (both X_0 and Y_0 planes), an equivalent cut is imposed on both planes of the second STK layer around 900 ADC. The cut on the first STK layer is used throughout this work in order to remove unwanted events from nuclei with masses lighter than boron and beryllium, crucial in mitigating the background percentage for carbon and oxygen analyses. Consequently, the overall efficiency check is structured as follows:

$$\varepsilon_{\mathrm{STK_{FirstLayer}}} = \frac{\mathrm{N_{PSD|STK_{FirstLayer}|STK_{SecondLayer}}}}{\mathrm{N_{PSD|STK_{SecondLayer}}}} \tag{3.21}$$

with the corresponding results being shown in Fig. 3.31. A great overall agreement has been obtained for both carbon and oxygen, with the total divergence fluctuating less than 1% for the entire first layer, within statistical uncertainties.

3.6.4 BGO selection cut efficiency

The BGO selection cut concerning the sum of energy deposited in the first and second BGO layers being smaller than the sum of third and fourth layers ($E_{L1} + E_{L2} < E_{L3} + E_{L4}$) is important in alleviating the number of particles from upward-going showers in the calorimeter. A simple efficiency measurement is performed, as seen below:

$$\varepsilon_{\mathrm{BGO}} = \frac{\mathrm{N_{PSD|STK|BGO}}}{\mathrm{N_{PSD|STK}}} \tag{3.22}$$

where $\mathrm{N_{PSD|STK|BGO}}$ correspond to the number of events surviving PSD, STK and BGO cuts, with $\mathrm{N_{PSD|STK}}$ showing the total event yield without the aforementioned BGO cut. The resulting plots can be viewed in Fig. 3.32, where simulated and flight data are in excellent agreement apart from the very low energy range ($\sim$ 100 GeV), where a few % difference is evident due to a small inconsistency in simulating backscattered particles. From that point onward both flight and MC simulated data are in an excellent agreement, way below 1 %.

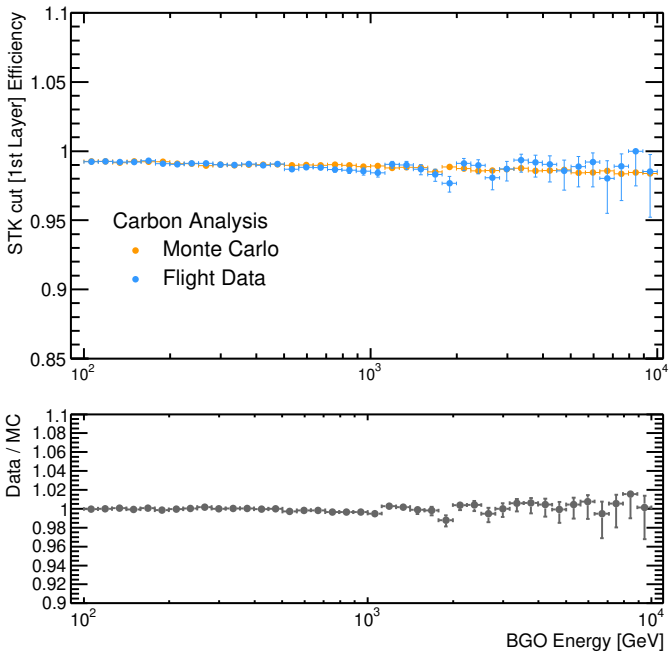

(a) Carbon

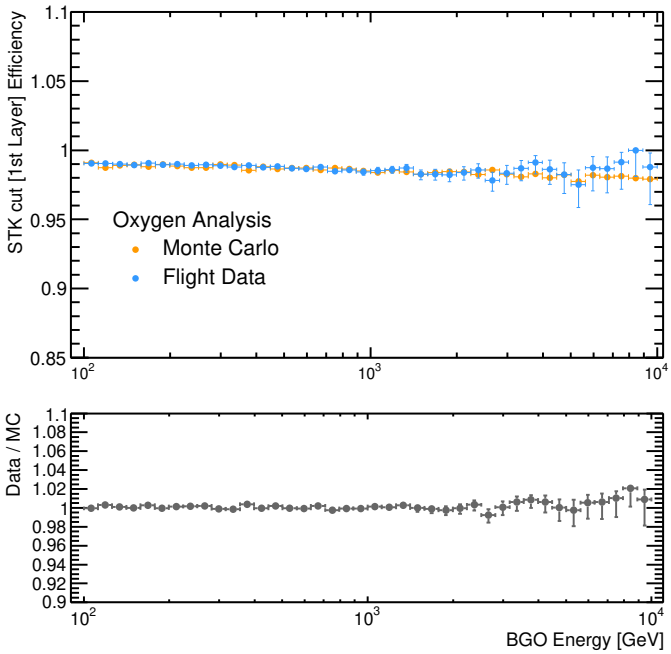

(b) Oxygen

Figure 3.31: STK (First layer) efficiency validation with respect to the BGO energy deposition, regarding (a) carbon and (b) oxygen analyses. Flight and simulated data correspond to blue and yellow points respectively. The ratio of flight to MC simulated events is also illustrated, in order to highlight their overall agreement.

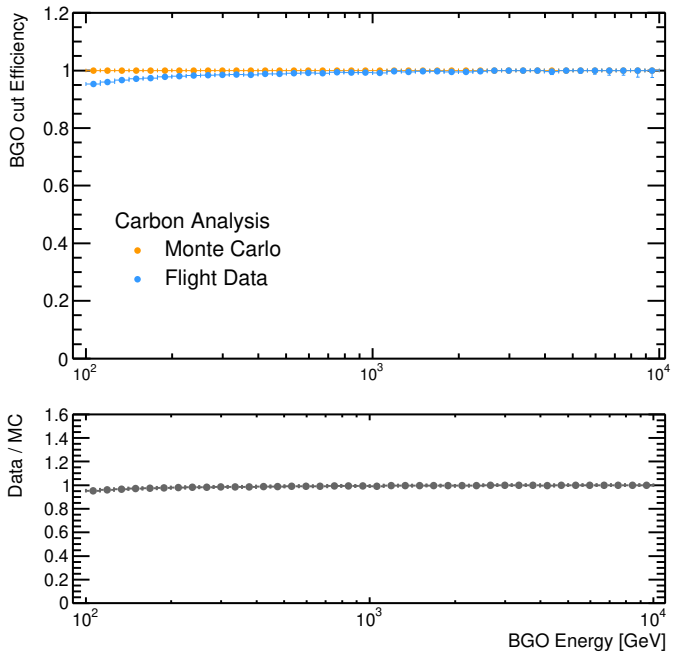

(a) Carbon

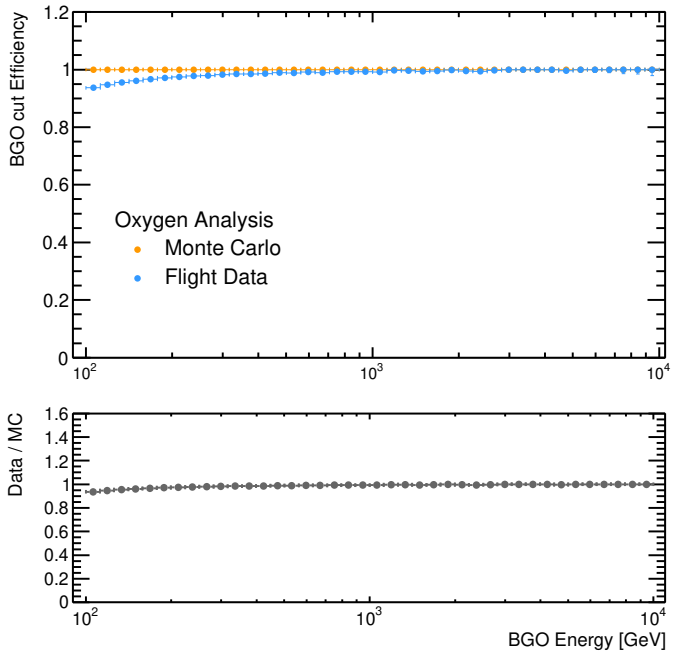

(b) Oxygen

Figure 3.32: BGO selection cut efficiency validation with respect to the BGO energy deposition, regarding (a) carbon and (b) oxygen analyses. Flight and simulated data correspond to blue and yellow points respectively. The ratio of flight to MC simulated events is also illustrated, in order to highlight their overall agreement.

3.7 Summary

In this Chapter, the complete analysis procedure concerning carbon and oxygen nuclei has been presented in detail. An introduction to the flight and simulated data was provided, along with a thorough list of analysis-specific selection cuts in order to attain pure samples of carbon and oxygen nuclei. A series of adjustments were performed in every sub-detector, which assisted in precisely reconstructing the incident energy of all candidate events. Furthermore, a detailed background measurement was carried out in order to gauge the contribution of neighboring (to carbon and oxygen) nuclei and consequently delineate the final limits concerning their respective charge selection. Finally, efficiency calculations for the majority analysis cuts were performed, in order to assess their accuracy and ensure a good agreement between flight and simulated data.

The following chapter focuses on the spectral measurements of carbon and oxygen nuclei, resulting from 6 years of DAMPE data. An additional part of this work pertains to flux ratios such as C/O, B/C and B/O, being essential in clarifying aspects of the CR diffusion and propagation mechanisms in the Galaxy.

Chapter 4

Carbon and Oxygen spectral measurements

The matters discussed in all previous sections culminate to the measurement of the carbon and oxygen fluxes. In addition to the carbon and oxygen spectra, flux ratios such as C/O and secondary-over-primary ratios like B/C and B/O will be an important part of this work, given their significance in clarifying various aspects of the CR propagation mechanism in the Galaxy.

4.1 Introduction

One of the main objectives referring to this work is the final flux measurement for carbon and oxygen nuclei. The measured quantity in this case is the differential flux $\Phi\left(E_i, E_i + \Delta E_i\right)$, given by the following formula:

$$\Delta\Phi\left(E_i, E_i + \Delta E_i\right) = \frac{\Delta \mathrm{N_i}}{\Delta \mathrm{E_i}\ \mathrm{A_{eff},}_i \Delta \mathrm{T}} \tag{4.1}$$

where $[E_i, E_i + \Delta E_i]$ corresponds to the i-th primary energy bin with a step of ΔE_i, while ΔN_i is the number of carbon or oxygen events surviving all selection cuts introduced in previous sections. $\mathrm{A_{eff},}_i$ is the effective acceptance which includes the geometric acceptance along with the efficiency of all applied cuts and finally, ΔT is the total instrument livetime, amounting to $1.4 \cdot 10^8$ seconds, for six years of DAMPE data.

4.2 Effective acceptance

As estimated in the previous section, the effective acceptance for the DAMPE instrument is measured according to the following equation:

$$A_{\mathrm{eff},i} = A_{\mathrm{gen}} \times \frac{N_{\mathrm{pass},i}}{N_{\mathrm{gen},i}} \tag{4.2}$$

where A_{gen} corresponds to a surface over which all MC simulation samples are generated (covering a half sphere of 1.0 m radius). $N_{\mathrm{gen},i}$ and $N_{\mathrm{pass},i}$ are the total number of events impinging on DAMPE and number of events surviving all selections imposed in the analysis.

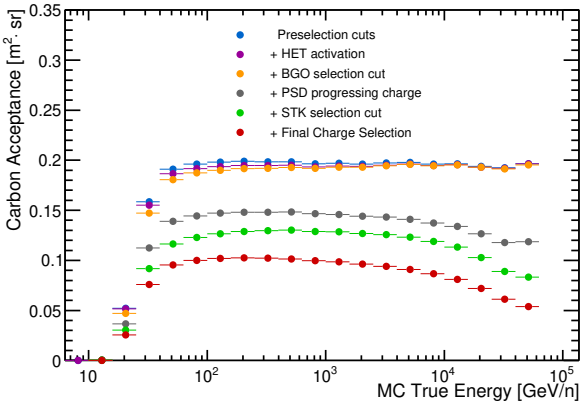

(a) Carbon

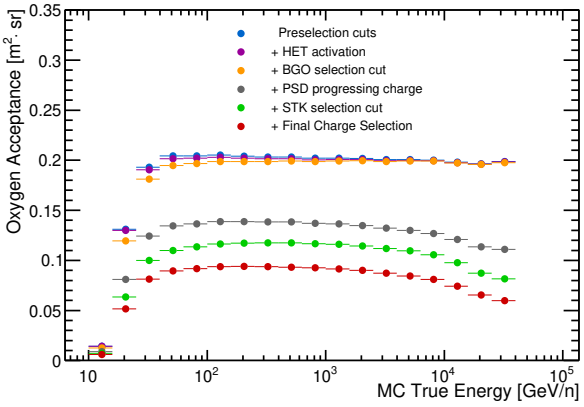

(b) Oxygen

Figure 4.1: Effective acceptance as a function of the primary energy per nucleon in the case of (a) carbon and (b) oxygen analyses. Each set of points corresponds to a given analysis cut leading to a sequence of added selections (from top to bottom), which amount to the final acceptance.

In Fig. 4.1, a summary of the various analyses selections is shown, where each set of analysis cuts is gradually added to the forthcoming (from top to bottom), thus leading to the calculation of the final acceptance for the case of carbon and oxygen nuclei. The sequence of added selections corresponds to:

- Pre-selections
- HET activation
- BGO selection cut ($E_{L1} + E_{L2} < E_{L3} + E_{L4}$)
- PSD progressing charge
- STK charge cut ($>$ 900 ADC)
- Charge selection cuts (upper and lower limits)

(in accordance with the background measurement), ultimately depicting the final acceptance. As a result, both carbon and oxygen acceptances show a stable trend with increasing energy, as well as a minor decline towards the highest energy bins. This is attributed mainly to strict charge selections in order to maintain the purity of carbon and oxygen data samples at increasingly higher energies.

4.3 Energy reconstruction

Despite the extended calorimetric depth of DAMPE (32 radiation lengths, 1.6 nuclear interaction length) and its excellent resolution, only a fraction of the energy corresponding to the primary particle can be contained within the BGO layers ($\sim$ 40% at 10 TeV). Focusing on hadronic showers, an additional level of uncertainty is introduced due to their inherent complexity which is accompanied by a shower initiation further down the calorimeter, when compared to electromagnetic showers.

These aspects necessitate the implementation of unfolding methods in order to obtain a precise spectrum regarding the impinging primary element of interest. Results presented in this work are based on an iterative Bayesian method [71], originating from a computational implementation developed by the Fermi-LAT collaboration [106, 107]. Initially, the number of observed events surviving the entirety of selection cuts (discussed in detail previously) is defined as follows:

$$N_{Observed,i} = \sum_j M_{ij} N_{True,j} \tag{4.3}$$

where $N_{Observed,i}$ corresponds to the number of observed events in the i-th bin of the energy deposited in the calorimeter. M_{ij} is the matrix element related to the detector response and $N_{True,j}$ is the number of events associated to incident particles in the j-th energy bin. The distribution of observed events with respect to the energy deposition in the calorimeter, for carbon and oxygen nuclei, is presented in Fig. 4.2, representing six years of DAMPE data. In order to calculate the response matrix mentioned above, an additional relation connecting both detected (BGO energy) and primary (true) energies is needed. In that case, the probability is estimated in the following:

$$\mathcal{P}\left(\mathrm{E_{BGO,i}} \mid \mathrm{E_{True,j}}\right) = \frac{\mathrm{n_{Observed,i}}|_{\mathrm{j}}}{\mathrm{N_{True,j}}} \tag{4.4}$$

where $\mathcal{P}\left(\mathrm{E_{BGO,i}} \mid \mathrm{E_{True,j}}\right)$ is the probability of a given event in the j-th bin of primary energy to be detected in the i-th bin of deposited energy, $n_{Observed,i}|_j$ being the number of events pertaining to the probability mentioned above, while $N_{True,j}$ refers to the number of carbon or oxygen nuclei with primary energy $E_{True,j}$.

The carbon and oxygen fluxes can be derived from the inversion of the response matrix discussed above, leading to the unfolding matrix calculation. This is defined by the probability distribution of an observed event with a given deposited energy inside the calorimeter, originating from an impinging carbon or oxygen nucleus of primary energy $E_{True,j}$, which translates to $\mathcal{P}\left(\mathrm{E_{True,i}} \mid \mathrm{E_{BGO,j}}\right)$. Thus, the general Bayesian method can be structured according to the following formula:

$$\mathcal{P}\left(E_{\mathrm{True},k} \mid E_{BGO}\right) = \frac{\mathcal{P}\left(E_{BGO} \mid E_{\mathrm{True},k}\right) \mathcal{P}\left(E_{\mathrm{True},k}\right)}{\sum_j \mathcal{P}\left(E_{BGO} \mid E_{\mathrm{True},j}\right) \mathcal{P}\left(E_{\mathrm{True},j}\right)} \tag{4.5}$$

where $E_{True,j}$ corresponds to the prior probability distribution, chosen as a power-law of index γ=2.7, consistent with the re-weighing of the MC simulated samples.

Consequently, the unfolding matrices obtained from the study of carbon and oxygen simulated data are illustrated in Fig. 4.3. The resulting distributions show good linearity between BGO deposited and true energy events, while the number of events extracted from the unfolding procedure are demonstrated in Fig. 4.4, following an average of five unfolding iterations needed for convergence. Finally, the majority of results corresponding to carbon and oxygen nuclei are produced in kinetic energy over nucleon (GeV/n), assuming pure contributions of ^{12}C and ^{16}O.

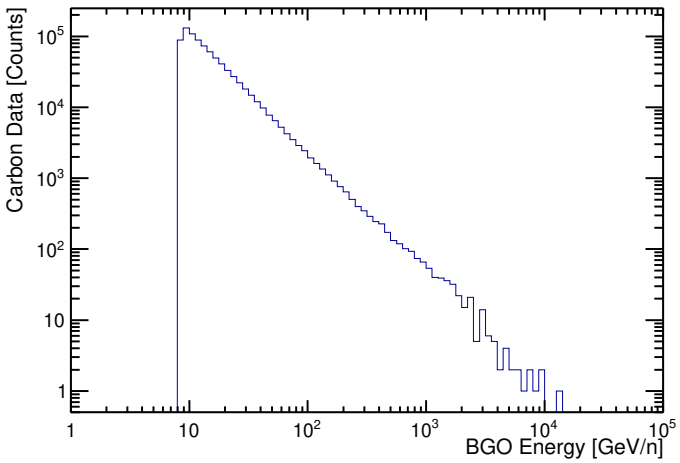

(a) Carbon

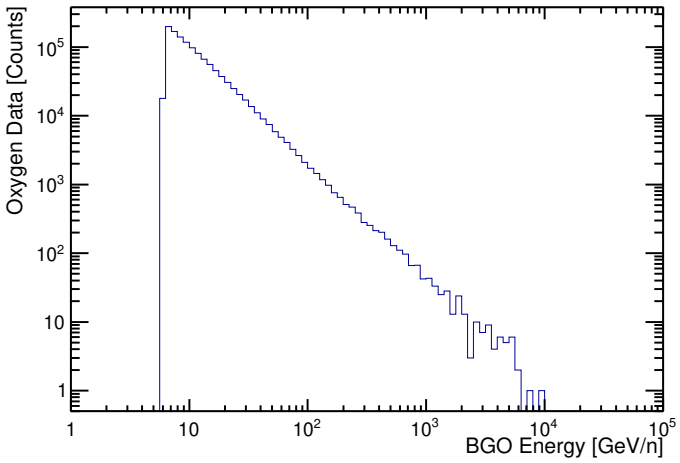

(b) Oxygen

Figure 4.2: Observed distributions of (a) carbon and (b) oxygen events with respect to the BGO energy. Both distributions correspond to events passing all selections cuts discussed in detail previously, with six years of DAMPE flight data.

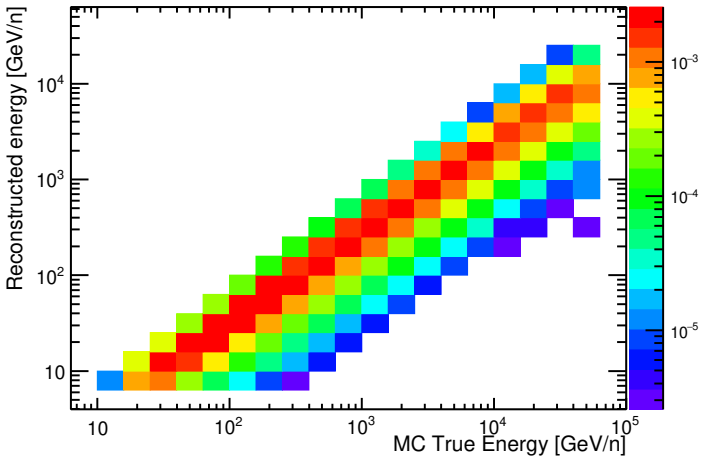

(a) Carbon

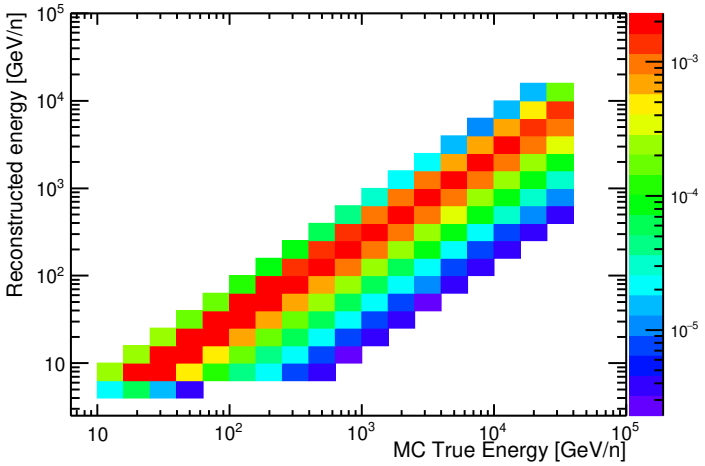

(b) Oxygen

Figure 4.3: Unfolding matrices for (a) carbon and (b) oxygen pertaining to the BGO energy with respect to the primary kinetic energy (extracted from the respective MC-generated samples). Both distributions correspond to events passing all selections cuts discussed in detail previously normalized to the total number of events per energy decade, from six years of DAMPE flight data.

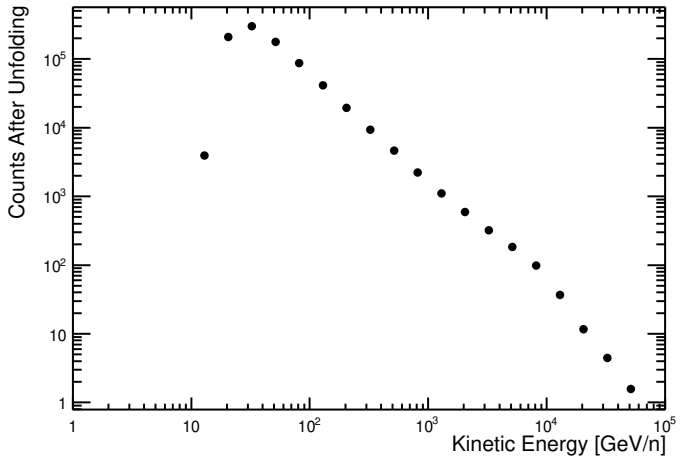

(a) Carbon

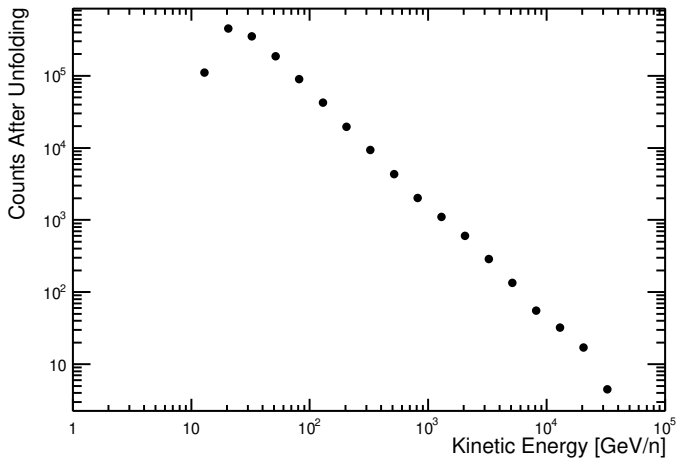

(b) Oxygen

Figure 4.4: Number of events after the unfolding procedure for (a) carbon and (b) oxygen, with respect to the primary kinetic energy per nucleon.

4.4 Uncertainty evaluation

Every analysis is affected by statistical and systematic uncertainties. In the following, both statistical and systematic uncertainties from the study of carbon and oxygen nuclei will be presented, along with an estimation on the selected hadronic interaction model.

4.4.1 Statistical uncertainties

An important source of uncertainty comes from the unfolding method when estimating the statistical error of each primary energy bin. In order to define the statistical uncertainties for carbon and oxygen fluxes, a Toy MC method is employed by generating simulated samples from Poisson distributions with mean values equal to the dataset of flight data, in order to evaluate possible fluctuations with respect to each BGO energy bin. Consequently, 10000 toy MC samples are produced according to the aforementioned count distributions (pertaining to the unfolding procedure). Said results are following Gaussian distributions, with their respective σ over μ ratio ($\frac{\sigma}{\mu}$) corresponding to the final statistical uncertainty used in each energy bin for the case of carbon and oxygen fluxes. These uncertainties will be illustrated in a further step, following the discussion on the analysis-specific systematic uncertainties.

4.4.2 Systematic uncertainties from the analysis

Systematic uncertainties from the background contamination, HET request and the various selection cuts in PSD, STK and BGO will be taken into account according to the efficiency estimations presented in the previous chapter. For each one of the aforementioned selection cuts, the respective difference between flight and simulated data is evaluated and finally added to the analysis-related systematic uncertainties. The individual systematic uncertainties correspond to ~ 1 % from the HET activation, 1.2 % from the background contamination, with 1.5 %, 2.5 % and 0.8 % for PSD, STK and BGO selection cuts respectively.

An additional source of systematic uncertainty can be derived from the unfolding method itself. Naturally, the use of a given unfolding method might result in a measurable systematic uncertainty. In order to evaluate its effect, the response matrix entries are sampled from a Poissonian distribution as before, while the prior is chosen as a power law with a variable index, extracted from a

uniform distribution. This distribution is selecting values between (-2.8, -2.4), being a range which includes the benchmark value of $\gamma = 2.6$ used throughout the analyses of carbon and oxygen nuclei. The resulting systematic uncertainty is quite low, around 1.1 % across the full energy range.

4.4.3 Hadronic model systematic uncertainties

A preliminary estimation of systematics due to the selected hadronic model will be discussed in the following, although this work is currently being finalized within the DAMPE collaboration. In that sense, the full analysis procedure was carried out, this time employing the FLUKA toolkit [85] to simulate carbon and oxygen nuclei from 100 GeV to 100 TeV. Following the exact same analysis procedure as presented in the previous chapter, the resulting fluxes are compared to the ones measured with GEANT4, resulting to a difference of less than 15% below energies of 100 GeV/n, followed by a variance of approximately 10% around 500 GeV/n and with a decreasing percentage up to the highest energies concerning both carbon and oxygen spectra. In this case, a 15 % systematic uncertainty up to energies of approximately 100 GeV/n is considered, followed by a 10 % continuous contribution up to the highest energies. It should be noted that such an estimate on the hadronic model uncertainty is rather conservative, but is preferred given its preliminary nature.

A further cross-check on the hadronic model systematics is performed in order to provide a more accurate estimate of said uncertainty (especially in lower energies), this time taking into account DAMPE results from data acquired during the various beam test campaigns at CERN (as presented in Chapter 2). In this work, ion data of 40 and 75 GeV/n from beam test campaigns were compared to similarly structured beams of carbon and oxygen, simulated with GEANT4. The same list of selection cuts was applied both for beam test and simulated data in order to ensure a coherent picture among the two. The resulting energy deposition ratio in the various BGO layers for both beam and simulated data in the aforementioned energies is presented in Fig. 4.5, where a good overall agreement is achieved, translating to an obtained mean BeamTest/Simulated data ratio of 0.977, which leads to an estimated uncertainty of approximately 3.8%, for carbon and oxygen data.

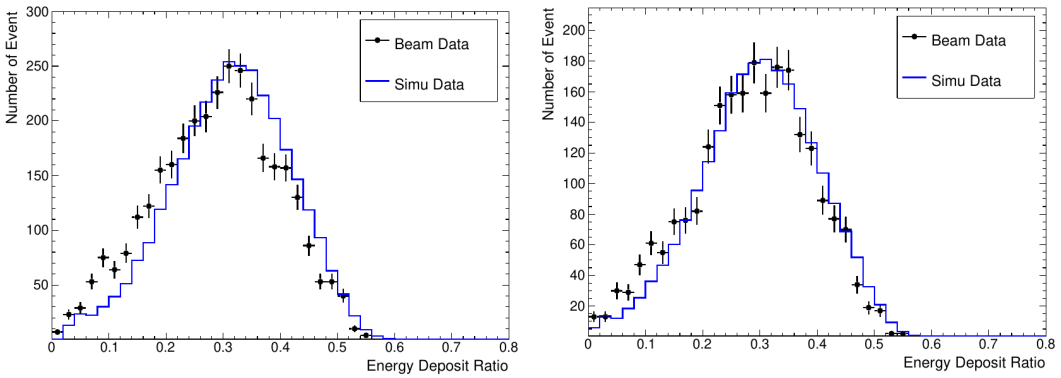

(a) Carbon - 40 GeV/n **(b)** Carbon - 75 GeV/n

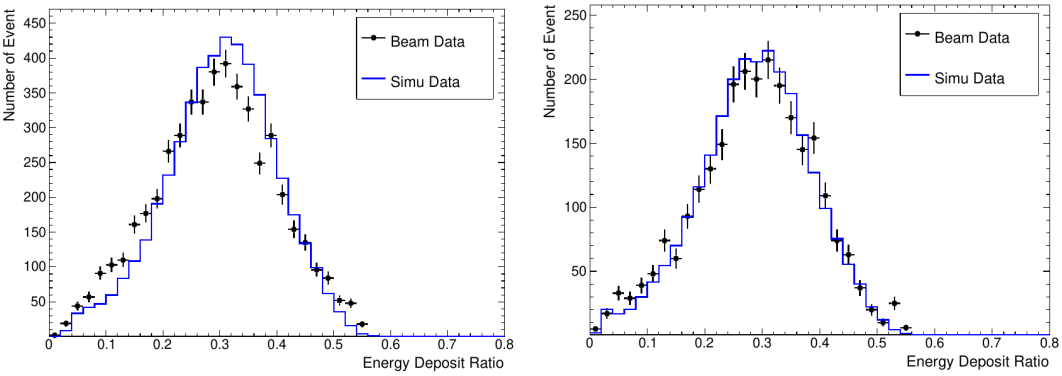

(c) Oxygen - 40 GeV/n **(d)** Oxygen - 75 GeV/n

Figure 4.5: Energy deposition ratio between BGO layers for (a,b) carbon and (c,d) oxygen nuclei concerning beam test (black points) and simulated (blue line) data of 40 and 75 GeV/n, respectively [75].

4.4.4 Collective list of uncertainties

The complete list of statistical and systematic uncertainties examined in this work, stemming from HE trigger, PSD, STK, BGO, background, unfolding and hadronic model selection, are shown in Fig. 4.6.

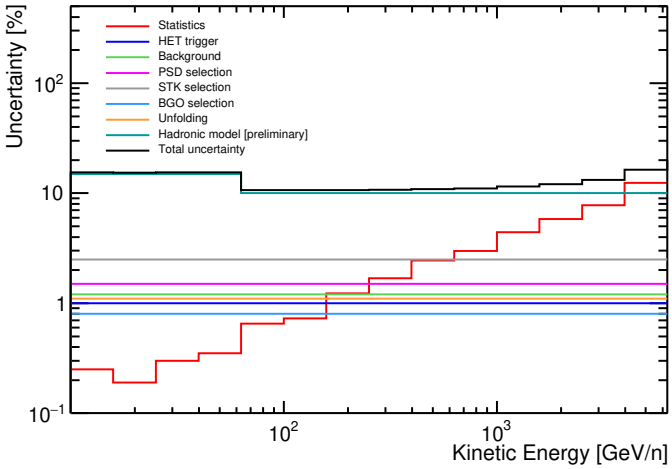

(a) Carbon

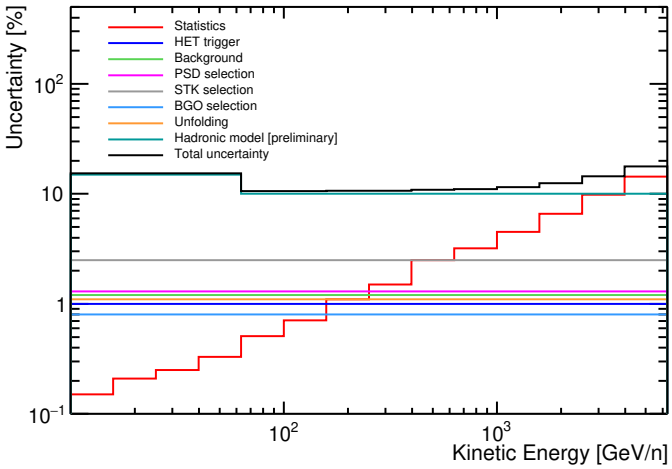

(b) Oxygen

Figure 4.6: Statistical and systematic uncertainties estimated from the analyses of (a) carbon and (b) oxygen nuclei, with respect to the kinetic energy per nucleon. Black lines corresponds to collective uncertainties (stat+sys) resulting from the analysis and hadronic model selection.

4.5 Carbon and Oxygen fluxes

Following a complete presentation of the analysis procedure, starting from data handling and selection of pure events all the way up to evaluating statistical and systematic uncertainties, the carbon and oxygen fluxes with respect to the kinetic energy per nucleon resulting from six years of DAMPE data, are demonstrated in Fig. 4.7.

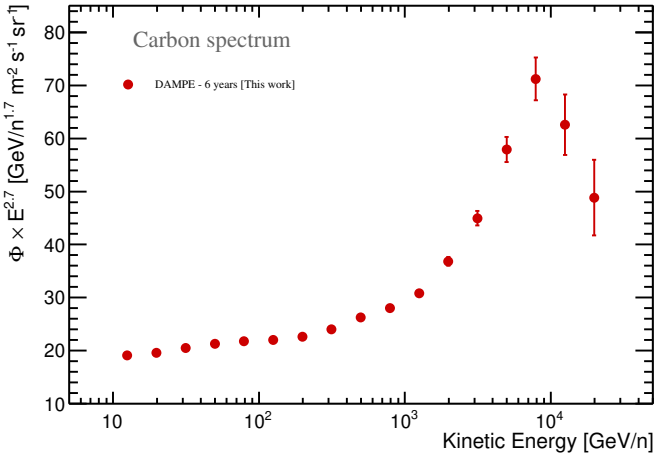

(a) Carbon

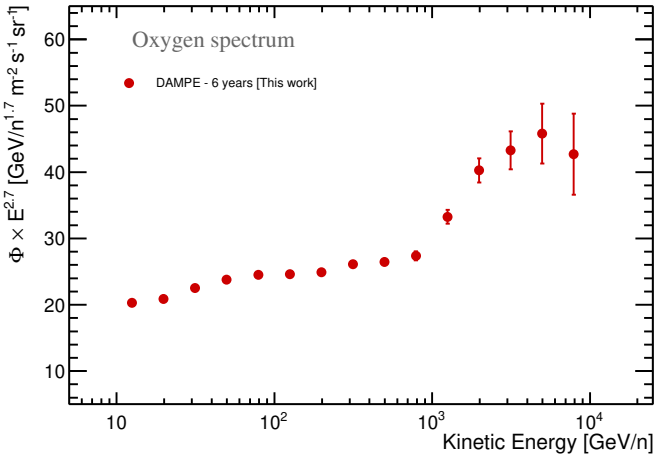

(b) Oxygen

Figure 4.7: Fluxes of CR (a) carbon and (b) oxygen with respect to the kinetic energy per nucleon, corresponding to six years of DAMPE data. Both fluxes are multiplied to $E^{2.7}$ while their respective error bars represent statistical uncertainties.

Both fluxes are multiplied by $E^{2.7}$ with their respective ranges starting from 10 GeV/n and reaching up to 25 TeV/n and 10 TeV/n, for carbon and oxygen respectively. The uncertainties shown in this figure correspond to statistical errors.

Furthermore, the DAMPE spectra are presented along with a current estimation of systematic uncertainties (stemming both from the analysis and the selected hadronic model), added in quadrature with the respective statistical errors, in Fig. 4.8.

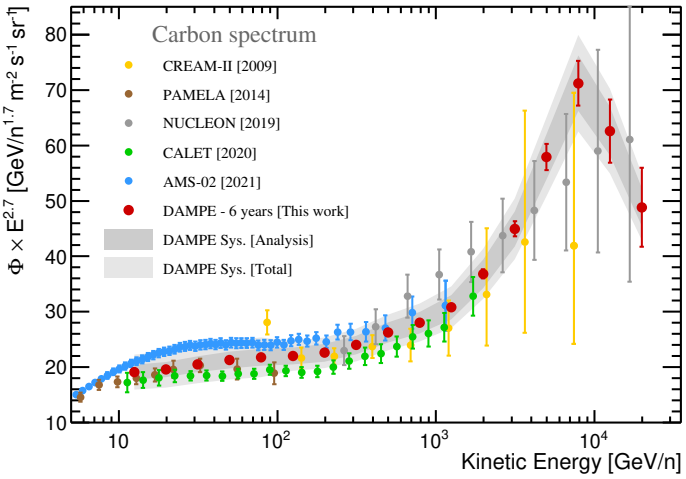

(a) Carbon

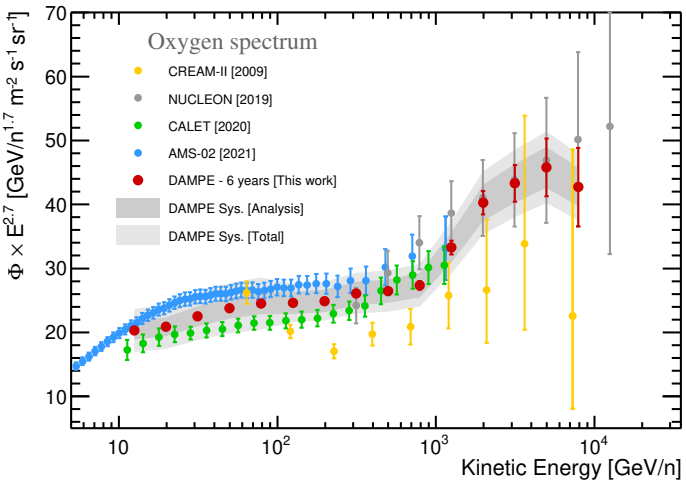

(b) Oxygen

Figure 4.8: Fluxes of CR (a) carbon and (b) oxygen with respect to the kinetic energy per nucleon, corresponding to six years of DAMPE data. Both fluxes are multiplied to $E^{2.7}$, red error bars represent statistical uncertainties while gray-shaded bands refer to systematic uncertainties from the analysis, as well as the total uncertainty estimated from the analysis and hadronic model selection, added in quadrature. The published works of CREAM [36], PAMELA (for carbon) [37], NUCLEON [38], CALET [39] and AMS-02 [40] experiments are shown for a detailed comparison.

This figure serves as a comparison between the work presented here and current results from other experiments. The published works of CREAM [36], PAMELA (pertaining to the carbon flux) [37], NUCLEON [38], CALET [39] and AMS-02 [40] experiments are shown in detail, while their displayed errors correspond to systematic and statistical uncertainties added in quadrature.

Focusing on the DAMPE spectra of carbon and oxygen, a hardening feature is evident at energies of approximately 300 - 500 GeV/n respectively, the shape of which is consistent with AMS-02 and CALET observations. Such a feature invalidates the conventional picture involving a universal injection spectrum at the sources and a single, featureless power-law spectrum extending up to PeV energies, as predicted by prevalent CR models. This feature can be explained either by a break in the overall spectrum of injected CRs in the ISM or due to possible features in the CR propagation mechanism [108] (i.e., break in the energy dependence of the CR diffusion coefficient). It should be noted that this feature is coherent with published DAMPE measurements of protons and helium nuclei in a similar energy range. Moreover, the DAMPE absolute fluxes below a few hundreds of GeV/n (in both cases) are consistently above CALET but slightly lower than AMS-02, although within the estimated uncertainties. In the same energy range, both fluxes calculated with FLUKA are closer to CALET results while at higher energies the difference is significantly smaller.

Extending the nucleonic CR spectra in the multi-TeV energy range with good precision is a major DAMPE objective. In this work, carbon and oxygen results are presented for the first time up to 25 and 10 TeV/n respectively, with increased statistics due to an exceptional detector exposure and low overall systematics. A strong hint for an additional spectral feature has been unveiled in both carbon and oxygen, manifested for the first time by a softening at energies of approximately 7.5 TeV/n or 90 TeV (or 15 TV), for the case of carbon. Said feature is more prominent in carbon data, while exhibiting an analogous decreasing trend for oxygen. Both results are in agreement with CR models foreseeing a rigidity-wise acceleration of particles at the sources, as well as with published DAMPE measurements of protons and helium nuclei in very similar energies. Given the novelty of such a feature, a broken power-law function was used to describe the softening for carbon, delineated by the following formula:

$$R\left(E_k\right) = \begin{cases} R_0 \left(E_k/E_b\right)^{-\gamma_1}, & E_k \leq E_b \\ R_0 \left(E_k/E_b\right)^{-\gamma_2}, & E_k > E_b \end{cases}, \tag{4.6}$$

where E_b corresponds to the break energy, with γ_1 and γ_2 referring to the spectral indices before and after the spectral break. As seen from Fig. 4.9, the softening feature can be represented accurately by a broken power-law, with a break energy of $R_b = 15.1 \pm 1.6$ TV or $E_b = 7.561 \pm 0.82$ TeV/n, consistent with recent DAMPE results of proton and helium and theoretical postulations placing such a feature at energies of ~ 15 TV.

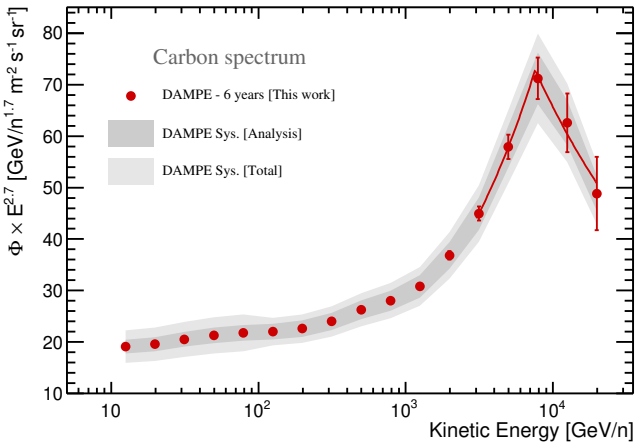

Figure 4.9: Broken power-law fit concerning the novel softening feature revealed by 6 years of DAMPE data. Red error bars represent statistical uncertainties while the gray band refers to statistical and systematic uncertainties (from the analysis procedure) added in quadrature. The break energy can be found at $R_b = 15.1 \pm 1.6$ TV or $E_b = 7.561 \pm 0.82$ TeV/n.

Moreover, the spectral difference before and after the softening is $|\Delta\gamma| \sim 0.9$ while the resulting normalized χ^2 being equal to 0.24. In order to gauge the significance of previous results, the carbon spectrum was fitted with a single power-law function, as seen below:

$$R\left(E_k\right) = R_0 \left(\frac{E_k}{\mathrm{GeV/n}}\right)^{-\gamma} \tag{4.7}$$

As a consequence, the single power-law paradigm is not sufficient to describe the softening in the carbon spectrum, given also its resulting χ^2 of 9.8. The

significance of the broken power-law fit describing the data is found at 5σ, referring to the softening at the energies presented above, thus signaling an insightful result in accordance with previously DAMPE published works for proton and helium nuclei. For the sake of completeness, the softening features for protons and helium were identified at energies of 13.6 and 34 TeV respectively, complimenting the latest results on carbon and oxygen fluxes. Finally, the values corresponding to both fluxes along with an overview of their statistical uncertainties can be viewed in Tables 4.1 and 4.2 respectively.

A further consistency check between carbon and oxygen nuclei pertains to their respective flux ratio, C/O, which is presented in Fig. 4.10. The collective results of CREAM, AMS-02 and CALET are illustrated alongside the DAMPE measurements and reveal a good agreement in a wide energy range, from 10 GeV/n until the onset of the TeV/n region, within the estimated uncertainties. An increasing trend can be detected in the multi TeV/n range, also hinted by CREAM measurements, although with considerably larger uncertainties.

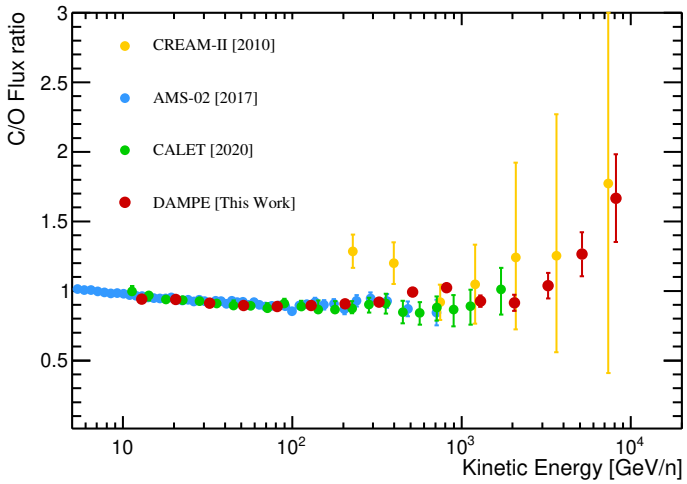

Figure 4.10: Flux ratio of C/O with respect to the kinetic energy per nucleon, corresponding to six years of DAMPE data. Red error bars represent statistical uncertainties. The published works of CREAM [36], CALET [39] and AMS-02 [40] are demonstrated for a detailed comparison.

Table 4.1: Carbon flux along with the respective statistical uncertainties.

Energy [GeV/n]	E_{min} [GeV/n]	E_{max} [GeV/n]	$\Phi_{Carbon} \pm \sigma_{stat}$ $[(GeV/n)^{-1}m^{-2}s^{-1}sr^{-1}]$
12.58	10.00	15.84	$(2.08 \pm 0.01)\ 10^{-2}$
19.95	15.84	25.11	$(6.10 \pm 0.16)\ 10^{-3}$
31.62	25.11	39.81	$(1.86 \pm 0.04)\ 10^{-3}$
50.11	39.81	63.09	$(5.50 \pm 0.17)\ 10^{-4}$
79.43	63.09	100.00	$(1.60 \pm 0.06)\ 10^{-4}$
125.89	100.00	158.48	$(4.78 \pm 0.03)\ 10^{-5}$
199.52	158.48	251.18	$(1.41 \pm 0.01)\ 10^{-5}$
316.22	251.18	398.10	$(4.34 \pm 0.05)\ 10^{-6}$
501.18	398.10	630.95	$(1.36 \pm 0.02)\ 10^{-6}$
794.32	630.95	1000.00	$(4.21 \pm 0.11)\ 10^{-7}$
1258.92	1000.00	1584.89	$(1.33 \pm 0.04)\ 10^{-7}$
1995.26	1584.89	2511.88	$(4.60 \pm 0.2)\ 10^{-8}$
3162.27	2511.88	3981.07	$(1.62 \pm 0.09)\ 10^{-8}$
5011.87	3981.07	6309.57	$(6.02 \pm 0.40)\ 10^{-9}$
7943.28	6309.57	10000.00	$(2.13 \pm 0.26)\ 10^{-9}$
12589.25	10000.00	15848.93	$(5.41 \pm 0.90)\ 10^{-10}$
19952.62	15848.93	25118.86	$(1.21 \pm 0.37)\ 10^{-10}$

Table 4.2: Oxygen flux along with the respective statistical uncertainties.

Energy [GeV/n]	E_{min} [GeV/n]	E_{max} [GeV/n]	$\Phi_{Oxygen} \pm \sigma_{stat}$ $[(GeV/n)^{-1}m^{-2}s^{-1}sr^{-1}]$
12.58	10.00	15.84	$(2.212 \pm 0.001)\ 10^{-2}$
19.95	15.84	25.11	$(6.56 \pm 0.01)\ 10^{-3}$
31.62	25.11	39.81	$(2.041 \pm 0.001)\ 10^{-3}$
50.11	39.81	63.09	$(6.21 \pm 0.01)\ 10^{-4}$
79.43	63.09	100.00	$(1.851 \pm 0.001)\ 10^{-4}$
125.89	100.00	158.48	$(5.35 \pm 0.02)\ 10^{-5}$
199.52	158.48	251.18	$(1.56 \pm 0.01)\ 10^{-5}$
316.22	251.18	398.10	$(4.72 \pm 0.05)\ 10^{-6}$
501.18	398.10	630.95	$(1.38 \pm 0.02)\ 10^{-6}$
794.32	630.95	1000.00	$(4.11 \pm 0.10)\ 10^{-7}$
1258.92	1000.00	1584.89	$(1.44 \pm 0.04)\ 10^{-7}$
1995.26	1584.89	2511.88	$(5.03 \pm 0.27)\ 10^{-8}$
3162.27	2511.88	3981.07	$(1.56 \pm 0.10)\ 10^{-8}$
5011.87	3981.07	6309.57	$(4.76 \pm 0.46)\ 10^{-9}$
7943.28	6309.57	10000.00	$(1.28 \pm 0.18)\ 10^{-9}$

4.6 B/C and B/O ratios

Moving on from the insightful results of carbon, oxygen fluxes and their related flux ratio (C/O), a complimentary part of this work is dedicated to secondary-over-primary ratios, such as B/C and B/O. Primary CRs such as carbon and oxygen are accelerated at astrophysical sources such as supernova remnants, while secondaries such as lithium, beryllium and boron are produced from the interactions of said primaries with the ISM during propagation [12, 109]. Consequently, flux ratios between secondary and primary nuclei can be valuable probes concerning the propagation mechanism of CRs in the Galaxy.

The spectra of primary CRs accelerated at the sources are expected to follow a power law $R^{-\gamma}$ according to the acceleration mechanism initially introduced by E. Fermi [24], with R corresponding to the rigidity and γ being the spectral index pertaining to the power-law. Following their propagation in the ISM, primary CRs should follow a softer spectrum $\propto R^{-(\gamma+\delta)}$, with δ corresponding to the slope of the rigidity dependence of the diffusion coefficient. On the other hand, secondary nuclei should follow a softer spectrum denoted by $\propto R^{-(\gamma+2\delta)}$, given their production from spallation of primaries with the ISM during transport. Consequently the flux ratio of secondary-to-primary CRs would be analogous to $R^{-\delta}$, naturally depending on the transport process, with important results from previous and current CR experiments.

In that sense, previously published measurements provided great insights on the evolution of B/C from a few GeV/n up to the TeV/n range, although with large uncertainties pertaining to higher energies. DAMPE can assist towards this direction with precise measurements of both B/C and B/O ratios with six years of data. The majority of event selections, statistic and systematic uncertainties emerging from the previously discussed carbon and oxygen analyses, are implemented in this work. For the case of boron, approximately 1.16×10^5 candidate events with $E_{BGO} > 80$ GeV were selected. The total contamination percentage (from contributions of neighboring elements) was estimated at $\sim 1-2\%$ for deposited energies lower than 1 TeV and 4.5% at 50 TeV, as seen in Fig. 4.11. Furthermore, the systematic uncertainty between flight data and MC associated to the HE trigger efficiency, is estimated around 2%, while the implementation of PSD and STK selection cuts results in uncertainties of 2% and 1%, respectively.

More importantly, this work has culminated to a very recent publication provided by the DAMPE collaboration [110], leading to precise flux ratio mea-

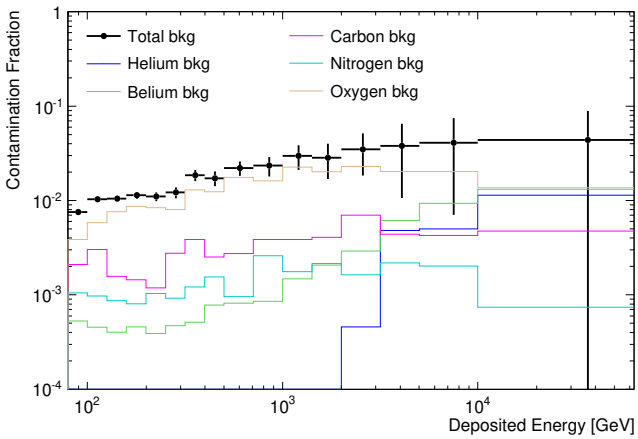

Figure 4.11: Contamination fraction from neighboring-to-boron nuclei with respect to the energy deposited in the BGO calorimeter, after all analysis selections. From [110].

surements in the energy range of 10 GeV/n to approximately 5.6 TeV/n. The DAMPE results on boron-over-carbon and boron-over-oxygen are shown in Fig. 4.12, along with a shaded band corresponding to the estimation of statistical and systematic uncertainties, summed in quadrature.

Pertaining to the novel DAMPE measurements, a good overall agreement with the majority of previous and current CR experiments is evident until energies of a few hundred GeV/n. DAMPE has shown the capacity of extending said measurements in the multi-TeV/n region with increased statistics and low systematic uncertainties. In that sense, a break in both B/C and B/O ratios is evident around the energy of 100 - 200 GeV/n, signaling, for the first time a change in the flux ratios. The fit on the data (represented by a red line) clearly shows a change (or break) in both spectra, well described by a broken power-law function, delineated by the formula defined in the previous section concerning the carbon softening. The break energies for both B/C and B/O fits are consistent to each other, approximately at $E_b \sim 100$ - 200 GeV/n. An additional uncertainty of the break energy associated with the energy measurement is about 2.2% as estimated from the geomagnetic cutoff of electrons and positrons [111]. The high-energy slopes of B/C and B/O above E_b are also consistent with each other, with the B/C energy slope being slightly softer than that of B/O. The difference may arise from the fact that a carbon spectrum can be softer than the oxygen spectrum below $\sim$ 100 GeV/n, due to a small contribution from the fragmentation of oxygen to carbon [108].

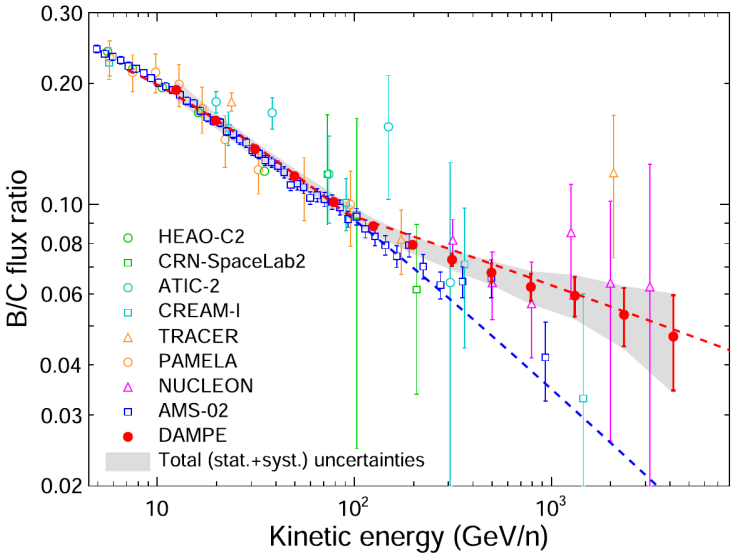

(a) Boron over carbon

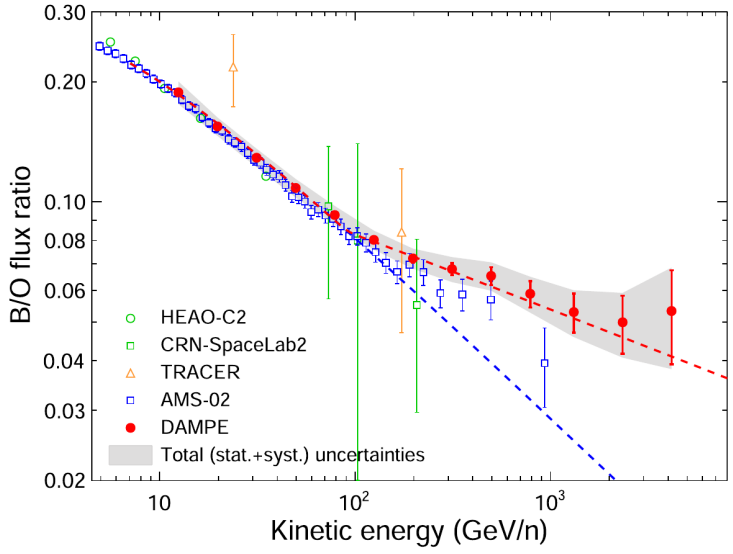

(b) Boron over oxygen

Figure 4.12: Flux ratios of (a) boron-over-carbon and (b) boron-over-oxygen with respect to the kinetic energy per nucleon, corresponding to six years of DAMPE data. Red error bars represent statistical uncertainties while gray bands refer to statistical and systematic uncertainties added in quadrature [110]. A broken power-law fit on the data is illustrated with a red line, diverging from the case of a single power-law as depicted by the blue dotted line. The published works of HEAO-C2 [57], CRN-SpaceLab2 [55], ATIC-2 [44], TRACER [59], CREAM-I [112], PAMELA [113], AMS-02 [53], NUCLEON [114] experiments are displayed for a detailed comparison.

The flux ratio results can be summarized in Tab. 4.3 along with their respective statistical and systematic uncertainties. Consequently, these results have great implications on the propagation mechanism of Galactic CRs. Interestingly, the slope parameter δ of the diffusion coefficient mentioned before, is predicted to be either 1/3 or 1/2 in the conventional turbulence theories [115, 116], a picture which is challenged by recent DAMPE findings. Numerous CR models can be tested based on these results, with the most favorable being a break in the diffusion coefficient. Another possible scenario would include a spectral break around rigidities of 200 GV coupled with predictions emerging from the Kraichnan theory of turbulence.

Then, at higher rigidities, a $R^{-0.2}$ dependence could be incompatible with the Kolmogorov theory of turbulence, although ameliorated when including the production of a small amount of secondaries in the sources. More complicated scenarios or even mixtures of various CR models could also lead to analogous spectral features in secondary-over-primary ratios, which could be probed further with future, precise measurements in higher energies. A more detailed look on the various analysis aspects referring to the flux ratios mentioned in this section is provided in [110].

Table 4.3: B/C and B/O ratios along with their statistical and systematic uncertainties. From [110].

Energy [GeV/n]	B/C Ratio $\pm \sigma_{stat} \pm \sigma_{sys}$	B/O Ratio $\pm \sigma_{stat} \pm \sigma_{sys}$
12.5	$0.193 \pm 0.002 \pm 0.011$	$0.188 \pm 0.003 \pm 0.012$
19.8	$0.162 \pm 0.001 \pm 0.007$	$0.155 \pm 0.001 \pm 0.008$
31.3	$0.137 \pm 0.001 \pm 0.006$	$0.129 \pm 0.001 \pm 0.007$
49.7	$0.118 \pm 0.001 \pm 0.005$	$0.108 \pm 0.001 \pm 0.006$
78.7	$0.102 \pm 0.001 \pm 0.004$	$0.093 \pm 0.001 \pm 0.005$
125	$0.088 \pm 0.001 \pm 0.004$	$0.080 \pm 0.001 \pm 0.004$
198	$0.079 \pm 0.002 \pm 0.004$	$0.072 \pm 0.002 \pm 0.004$
313	$0.073 \pm 0.003 \pm 0.003$	$0.068 \pm 0.002 \pm 0.004$
497	$0.068 \pm 0.004 \pm 0.003$	$0.065 \pm 0.003 \pm 0.004$
787	$0.062 \pm 0.005 \pm 0.003$	$0.059 \pm 0.004 \pm 0.004$
1315	$0.059 \pm 0.007 \pm 0.003$	$0.053 \pm 0.006 \pm 0.004$
2339	$0.053 \pm 0.009 \pm 0.004$	$0.050 \pm 0.008 \pm 0.004$
4160	$0.047 \pm 0.013 + 0.004$	$0.053 \pm 0.014 \pm 0.006$

4.7 Summary

In this Chapter, novel results concerning the analyses of intermediate mass nuclei with the DAMPE space mission have been presented. Specifically, the fluxes of carbon and oxygen nuclei were measured according to 6 years of DAMPE data, for the first time with increased statistics and low systematics, in a range of 10 GeV/n to 25 and 10 TeV/n, respectively.

Interesting features were detected in both spectra, with the first one being a hardening, evident at energies of approximately 300 - 500 GeV/n (for carbon and oxygen), the shape of which is consistent with observations from previous and current CR experiments. On to higher energies, new results have been presented in the multi-TeV/n region, where a strong hint of a spectral softening has been presented in carbon, at energies of approximately 7.5 TeV/n, or rigidity of 15.1TV with a significance of 5σ. This feature is consistent with a rigidity-dependent acceleration of particles at the sources and is more prominent in the case of carbon, while an analogous behavior might be expected from carbon, although more data will be needed.

The existence of said features invalidates the idea revolving around a universal injection spectrum at the sources and a single, featureless power-law spectrum extending up to PeV energies, as predicted by prevalent CR models. A feasible interpretation can be provided either by a break in the overall spectrum of injected CRs in the ISM or due to possible features in the CR propagation mechanism. Both results are in accordance with spectral features published in previous DAMPE works, such as helium nuclei and protons.

An additional consistency check is associated to the carbon-over-oxygen ratio, being in agreement with the majority of published results especially in lower energies, while extending in the TeV/n region with great accuracy. Additionally, a supplemental part of this work is dedicated to the measurement of secondary-over-primary ratios such as B/C and B/O (in the energy range of 10 GeV/n to approximately 5.6 TeV/n), being valuable probes in comprehending various aspects of the CR propagation mechanism in the Galaxy. Both B/C and B/O measurements are in excellent agreement with published results in energies up to few hundred GeV/n. Interestingly, above energies of 100 - 200 GeV/n a break is detected for the first time in both B/C and B/O ratios, with a subsequent extension to TeV/n energies. Following a selection of various spectral fits, it became evident that a broken power-law function accurately represents the data,

instead of a single power-law spectrum. These results have great implications on the propagation mechanism of Galactic CRs, with a variety of theoretical models being employed towards its precise interpretation. Favorable explanations could be attributed to a possible break in the diffusion coefficient, without excluding additional CR models, or even a mixture between some of them. In conclusion, the main point stemming from B/C and B/O data pertains to the dismissal of possible interpretations attributed to acceleration effects concerning the spectral hardening in CR protons [108], as shown by direct observations of space-borne experiments in recent years.

These results pave the way for a new generation of measurements, oriented towards higher energies with great accuracy and low systematic uncertainties. Hence, features such as the ones discussed above could be studied with even greater precision by future space-borne detectors, shedding light in open questions concerning the origin, acceleration and propagation mechanisms of CRs in the Universe. One of the prominent detectors proposed to address the majority of topics mentioned above is the High Energy cosmic-Radiation Detection (HERD) facility, the prospects of which will be presented in the following chapter.

Chapter 5

The HERD space mission

Highly–energetic particles were customarily detected only via indirect CR experiments, although with fundamental difficulties in making composition studies with small systematic uncertainties. On the other hand, direct CR experiments provide precise energy and charge measurements of incident particles with small systematics. However, due to rapidly decreasing CR fluxes with energy (and in conjunction with limited exposure), they are limited to statistically-meaningful observations in the 10 - 100 TeV range.

Forthcoming space–borne experiments should combine an increased geometric factor ($> m^2sr$), with extended mission duration ($\geq$10 yr), along with high discrimination power in separating different cosmic radiation components. Therefore, an overall enhancement in detector exposure can be attained, allowing for a deeper understanding of distinctive structures in CR spectra up to the highest achievable energies. In this context, the main objective would be to reach the "knee" in CRs with direct measurements and possibly distinguish the individual "knees" of consecutive elements, thus acquiring valuable information on the maximum energy attained by CR accelerators.

The High Energy cosmic-Radiation Detection (HERD) [117, 118] facility is designed to address the aforementioned requirements, as one of the prominent instruments to be installed on–board the China Space Station (CSS), illustrated in Fig. 5.1, with a projected duration of approximately 10 years. HERD will be capable of directly studying features in the spectra CR nuclei with optimal precision, up to the highest–achievable energies in space, while also providing insights on various topics concerning: gamma ray astronomy (energies larger than 100 MeV); the all-electron component and its fine structure up to tens of TeV, while searching for possible signatures of dark matter (DM) annihilation or

decay products, owing to its wide field–of–view (FoV). The HERD initiative is structured around an international collaboration involving researchers, institutes and universities from China, Italy, Switzerland and Spain contributing to this endeavor.

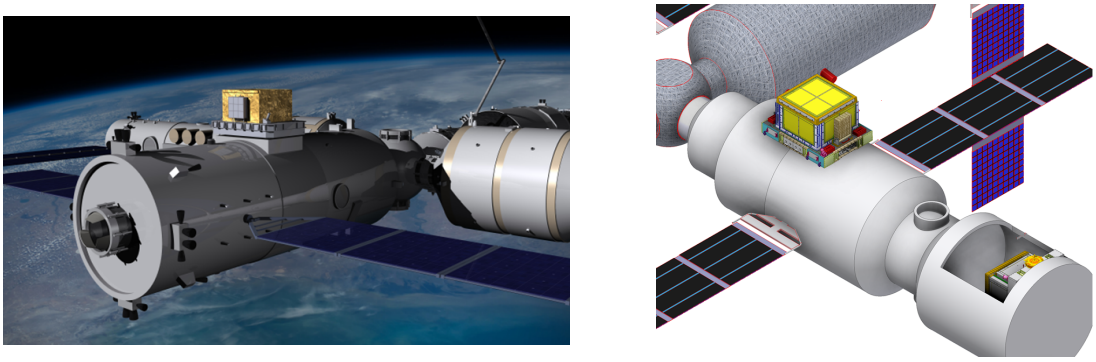

Figure 5.1: Schematic representations of the HERD payload on-board the Chinese Space Station.

5.1 Detector Description

HERD is designed around a segmented, 3−D imaging calorimeter (CALO). Such a design ensures detection of impinging radiation from both its top and 4 lateral sides, as well as precise energy measurements and separation of electrons/protons. A Fiber Tracker (FIT) is situated on all active sides around the calorimeter, in order to accurately determine tracks of incoming particles. A Plastic Scintillator Detector (PSD) is consequently enveloping the calorimeter and tracker, aiming to provide gamma–ray and charged particle triggers, together with an essential charge measurement. An additional measurement of the charge will be provided by the Silicon Charge Detector (SCD), covering all sub-detectors mentioned previously. Finally, in order to provide a calibration of the instrument response to nuclei in the TeV region, a Transition Radiation Detector (TRD) is placed on one of HERD's lateral faces.

Consequently, an order of magnitude increase in acceptance can be obtained by a novel design with advanced detector techniques fulfilling all physics requirements, while maintaining a manageable payload for a space mission. Furthermore, a dedicated analysis software is being developed for HERD [121], with the addition of a newly tested interface connecting high-energy hadronic event generators

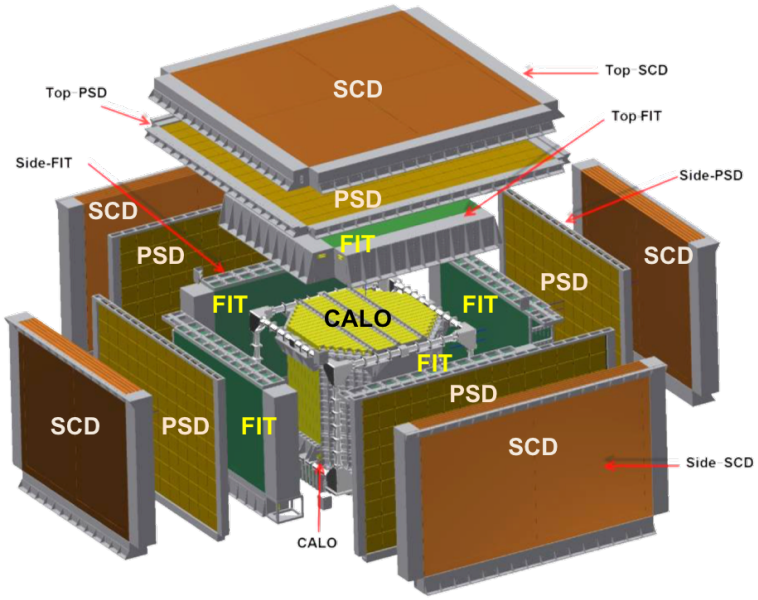

Figure 5.2: Graphical representation of HERD in an exploded view of the various sub-detectors, according to its baseline design. From [118–120].

implemented in CRMC [82], to the GEANT4 toolkit [122]. Such a tool offers a great opportunity of evaluating and optimizing high-energy hadronic models with the precise TeV–PeV data of current and future space-borne instruments.

HERD (as illustrated in Fig. 5.2) will be installed on-board the CSS around 2027, with an expected lifetime of $\geqq$ 10 years. The instrument will follow a Low–Earth Orbit (LEO) at an altitude of approximately 400 km, with an inclination angle of 42° and a maximum payload mass under 4 tons. Detailed specifications and primary scientific objectives of HERD can be found in Tab. 5.1, of the following section.

5.1.1 Calorimeter (CALO)

A 3−D imaging calorimeter (CALO) is situated at the center of HERD's payload [123]. The full detector in its current state comprises 7500 LYSO crystals of $3\times3\times3$ cm^3 cubes. Each crystal corresponds to a thickness of $\sim$2.6 X_0 (radiation length in LYSO is approximately 1.14 cm) and 1.4 Molière radii. Consequently, an integrated calorimeter of 55 X_0 and 3 λ_I (radiation and nuclear interaction lengths respectively) is constructed, being the largest and one of the most technically optimized calorimeters to be sent in space.

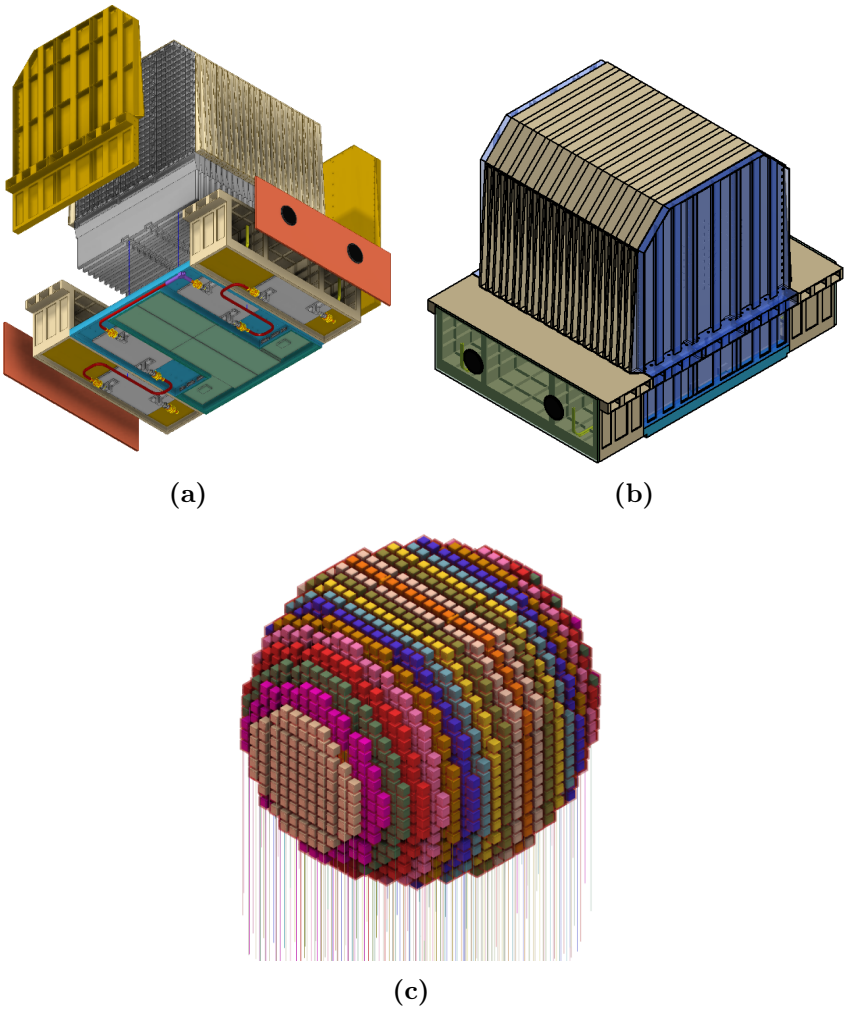

Figure 5.3: Schematic representations of the HERD calorimeter, where: (a) corresponds to the complete sub-detector layout including readout electronics, trigger and camera interfaces, (b) shows the support structure containing the core detector and (c) illustrates the spherical CALO design.

A small crystal in size is advantageous when detailed information regarding the shower development is needed, amounting to enhanced discrimination power between electromagnetic and hadronic shower topologies. Moreover, with an increased light yield, fast decay time and short nuclear interaction length, LYSO crystals are an exceptional choice for space–borne applications. Impinging particles on the CALO give rise to electromagnetic or hadronic showers that lead to the emission of scintillation photons. Said photons are accurately detected by a "dual-readout" system: the first part concerning Wavelength Shifting Fibers (WLSF) coupled to image Intensified scientific CMOS (IsCMOS) cameras, as in Fig. 5.4a, with the second including photodiodes (PD) connected to custom

front-end electronic chips (Fig. 5.4b). The readout redundancy provides a robust cross-calibration of the entire system and an important reduction of systematic uncertainties concerning energy measurements of TeV–PeV protons and nuclei.

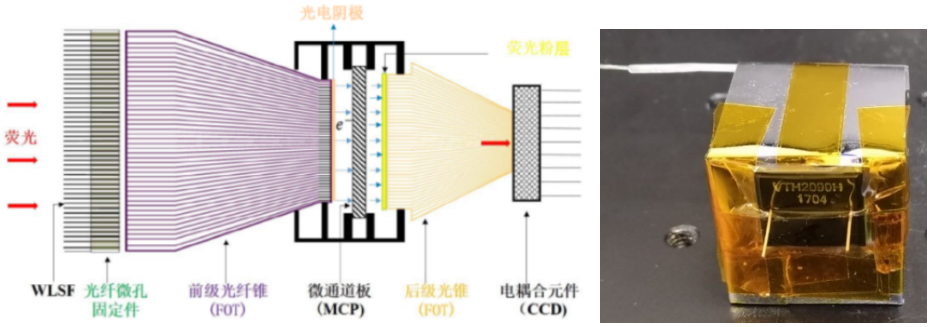

(a) (b)

Figure 5.4: CALO dual-readout system including: (a) an illustration of the CMOS camera coupled to wavelength-shifting fibers and (b) photodiode (PD) readout configuration under test.

5.1.2 Fiber Tracker (FIT)

The scintillating Fiber Tracker (FIT) [124] covers the CALO and serves as track reconstruction instrument for charged particles while inducing the conversion of gamma rays to electron/positron pairs. Various FIT performance aspects are evaluated focusing on its angular resolution, geometrical acceptance and conversion efficiency, while maintaining its mechanical robustness, in accordance with the space station requirements.

The current FIT design, comprises 5 tracking sectors, containing 7 tracking planes guaranteeing an equal number of independent measurements of the traversing particle interaction point. Subsequently, each plane includes two interleaved layers of modules measuring the two orthogonal spatial coordinates. Tracking planes on the top side are designed with 10 FIT modules on both X- and Y-oriented layers, while 6 and 10 FIT modules are installed on the X and Y layer respectively, regarding the side sector. Finally, a single module consists of a scintillating fiber mat and three silicon photomultiplier (SiPM) arrays. Tracking performance studies carried out at CERN SPS with the primary proton beam (400 GeV/c), led to an estimated measurement of the detector spatial resolution at 45 μm with a mean single hit detection efficiency at 99.6%. Further detector optimization and space qualification tests are ongoing with preliminary results confirming the mechanical robustness of the various FIT components.

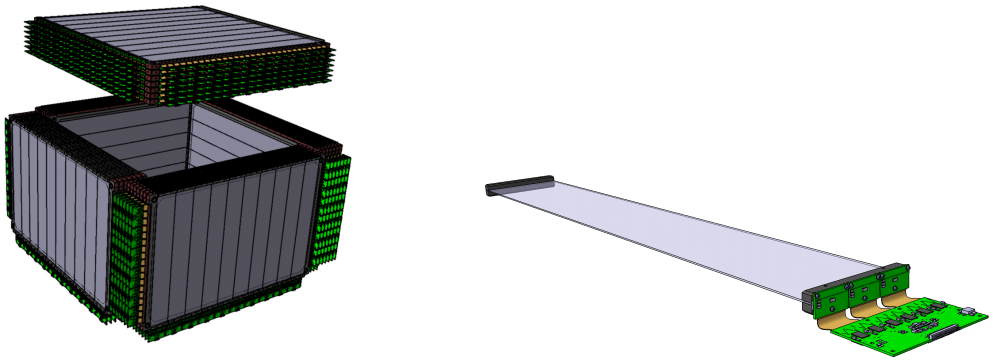

(a) (b)

Figure 5.5: Representation of the FIT detector (a) including 5 instrumented sides (4 lateral and 1 top sectors) along with (b) a single FIT module comprising a scintillating fiber mat and three SiPM arrays mounted on the front-end board. From [124].

5.1.3 Plastic Scintillator Detector (PSD)

The PSD [125, 126] envelops both CALO and FIT sub-detectors and will serve as anti–coincidence (discriminating incident photons from charged particles), while providing an essential charge measurement of incoming cosmic–ray nuclei in a range of $Z = 1 - 26$. A schematic view of the proposed PSD instrumentation is viewed in Fig. 5.6.

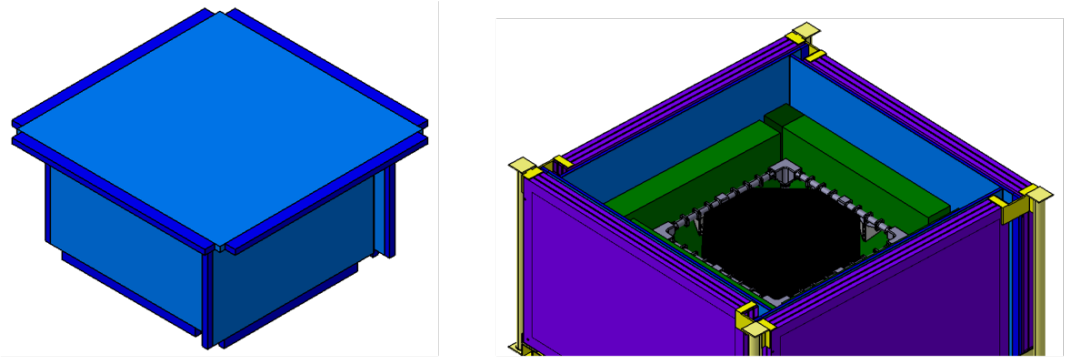

Figure 5.6: Schematic view of the PSD CAD model illustrating the positioning of the instrumented planes along with its interconnection amongst sub-detectors.

Thin and light materials (*i.e.,* organic scintillators) can be an optimal choice for this task with features such as low density and good radiation hardness, while being affordable and available in mass production. Silicon photomultipliers (SiPMs) will be the scintillator readout of choice, due to recent technological advancements exhibiting: fast signal detection; sensitivity to low light yields;

decreased power consumption and robustness. The PSD design should satisfy requirements such as: good energy resolution, high detection efficiency, broad dynamic range and high hermeticity.

Different layouts are currently under consideration concerning the scintillator geometry, each configuration presenting advantages and disadvantages, with the main trade-off related to the optimal number of readout channels versus back–scattering effects[1] [127]. Specifically, one scintillator geometry is based on long bars ($159\times3\times0.5$ cm^3 and $93.3\times3\times0.5$ cm^3 for horizontal and vertical bars respectively) as seen in Fig. 5.7, another on square tiles (10 cm/side and 0.5-1 cm thickness), illustrated in Fig. 5.8, while the last involves a solution compromising the advantages and disadvantages of the previous layouts.

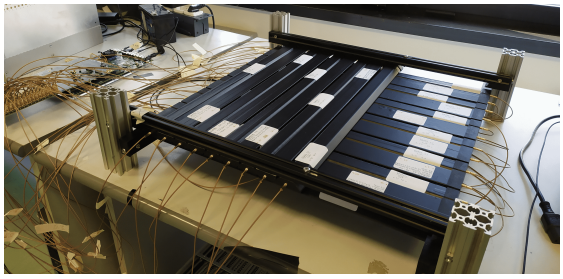

(a)

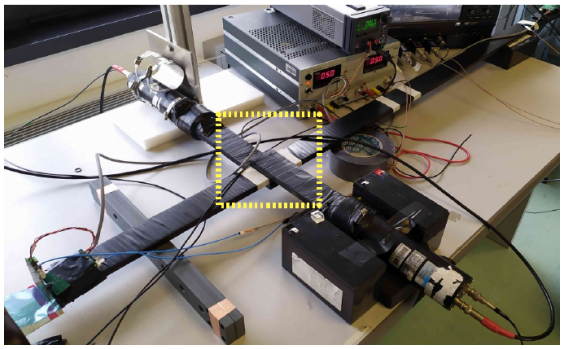

(b)

Figure 5.7: PSD bar configurations, where (a) corresponds to the prototype tested at CERN SPS and PS with varying particles in a wide range of energies. For (b), a 1.6 m PSD bar configuration is tested with CR muons. From [118, 125].

[1]A small fraction of secondaries emitted during electromagnetic showers in the calorimeter, will move backwards and eventually reach the PSD. Electron recoils produced via Compton scattering will also act as a veto for incident gammas, thus decreasing the photon detection efficiency, especially at higher energies ($>$ 10 GeV).

Current efforts concern the evaluation of various scintillator layouts and SiPM models. In particular, a novel geometry is being thoroughly tested, that involves a trapezoidal scintillator cross-section readout by multiple SiPMs of different active areas. Such a geometry increases the hermeticity of adjacent units and is favorable against the conventional, rectangular layout. The specific angle selected is 45° (extracted from MC simulations) providing the smallest possible fraction of events lost, in a wide range of impinging particle angles. The entirety of setups have been tested with CR muons, electrons from ^{90}Sr radioactive sources, along with particles from beam tests in a wide range of energies (few MeV - 400 GeV).

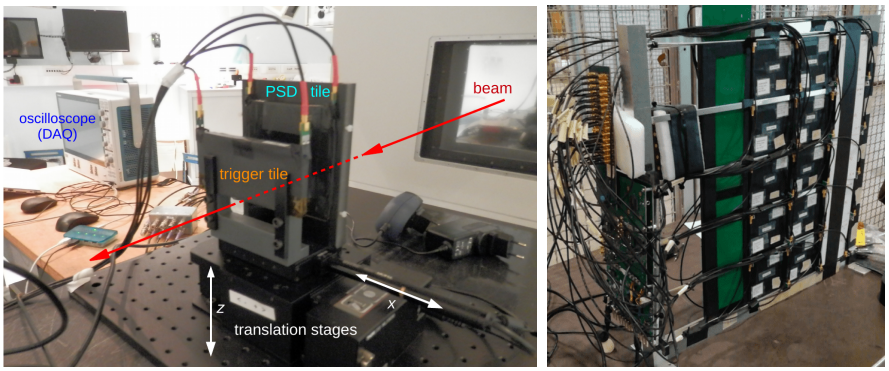

(a) **(b)**

Figure 5.8: PSD tile configurations concerning (a) a setup readout by 6 SiPMs with tests being carried out with proton/carbon beams of variable energies at CNAO (Pavia), (b) a prototype tested in CERN SPS and PS, made out of a single layer of 20 plastic tiles of different scintillator materials, in an array of 4×5 elements (of $10 \times 10 \times 0.5$ cm^3 dimensions each). An individual tile is readout by two PCB boards, each housing 3 SiPMs in OR-logic. From [118, 125].

5.1.4 Silicon Charge Detector (SCD)

The SCD installed above the PSD, will provide a precise charge measurement of incoming particles in a range of $Z = 1 - 26$. Five thin detector units are designed in the current configuration, one squared-shaped (1.6 x 1.6 m^2) placed on the top face of the instrument, and four (1.4 x 0.9 m^2) for the lateral sectors. Each detection module comprises 8 layers of 300 μm microstrip silicon detectors orthogonally interleaved onto low-density aluminum honeycombs, integrated to a total area of 60 m^2.

In that sense, a low level of CR nucleonic fragmentation can be achieved, leading to a decrease in systematic uncertainties while providing a vital charge

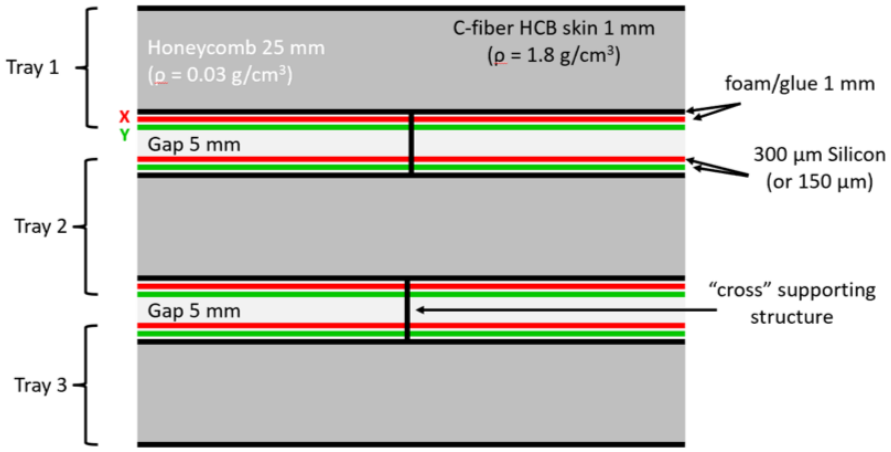

Figure 5.9: Paradigm of the proposed HERD SCD configuration. From [118].

measurement. Monte Carlo simulations have been carried out, regarding samples of various CR nuclei (from protons to iron) with energies from 10 GeV/n to 1 TeV/n (and isotropic incidence), leading to a combined charge resolution < 0.3 charge units for all samples. The aforementioned results will be verified at the CERN SPS ion beam line, thus quantifying the charge resolution of SCD prototypes.

5.1.5 Transition Radiation Detector (TRD)

Due to restricted means of ground-based calibration, an additional detector is needed to evaluate the CALO response to highly energetic hadronic showers. Therefore, a Transition Radiation Detector (TRD) is installed on one of the lateral sides of HERD, for proton calibration in the energy range of 1 - 10 TeV (Fig. 5.11). The X-ray photon flux from transition radiation depends on the Lorentz factor γ of the incident particle. In that sense, X-ray photons will be produced at $\gamma \sim 10^3$ and subsequently saturated at $\gamma \sim 10^4$, corresponding to the above-stated energy range of the impinging charged particle.

The TRD is conceived around a modular design (Fig. 5.10), involving a TR radiator and a Thick Gaseous Electron Multiplier (THGEM) comprising an effective area of 20 x 20 cm^2, with the addition of grid-like frames supporting the electronics readout.

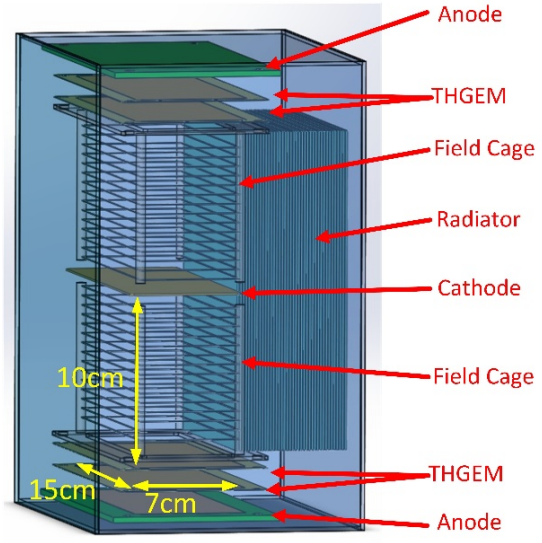

Figure 5.10: General configuration of the HERD TRD.

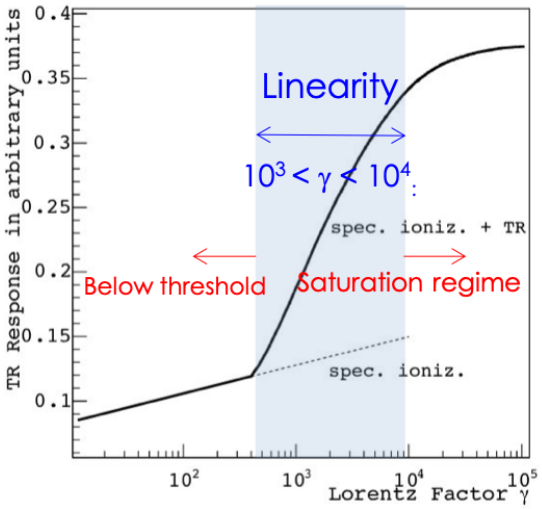

Figure 5.11: Transition radiation (TR) response with respect to the Lorentz factor, with a linearity region signaling the operational regime of the TRD. From [118, 126].

5.2 HERD design and performance aspects

All sub-detectors presented above constitute the complete and latest HERD design. Its main specifications and performance features are briefly summarized in Tab. 5.1. Main figures of merit include: energy range and resolution for CR gamma-rays/electrons and nuclei, projected acceptance for electrons/protons, calorimeter specifications and Field of View (FoV).

Furthermore, a comparison between the exposure of current CR experiments with the upcoming HERD mission, is illustrated in Fig. 2.16. In that sense, an order of magnitude increase in exposure can be obtained, by coupling a novel instrument design with state-of-the-art detection techniques and an increased mission lifetime.

Table 5.1: Main specifications and performance aspects of HERD

Parameter	Value
Energy range (e)	10 GeV − 100 TeV
Energy range (γ)	$>$ 0.1 GeV
Energy range (nuclei)	30 GeV − 3 PeV
Angular resolution (e/γ)	0.1° @ 10 GeV
Energy resolution (e)	1% @ 200 GeV
Energy resolution (p)	20% @ 100 GeV−PeV
e/p separation	10^{-6}
Geometric factor (e)	$>$ 3 m^2 sr @ 200 GeV
Geometric factor (p)	$>$ 2 m^2 sr @ 100 GeV
Payload mass	$\leqq$ 4000 kg
Field of view (FoV)	± 90°
Power	1900 W
Lifetime	$>$ 10 years

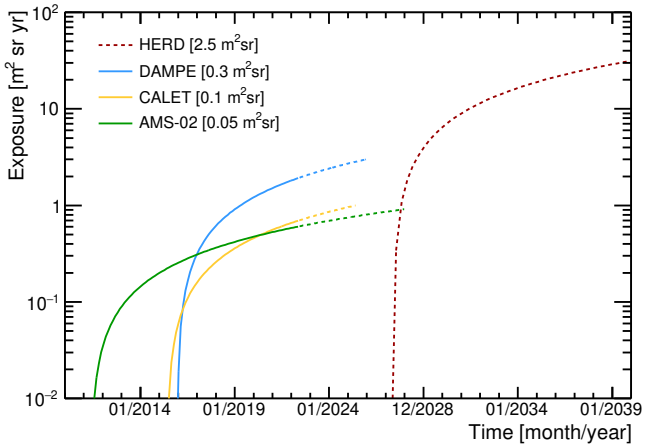

Figure 5.12: Overview of instrument exposures with respect to the time (calculated for the case of CR electrons), concerning various ongoing CR experiments (DAMPE, CALET, AMS-02) and the upcoming HERD mission. The geometric acceptance of each instrument is reported in brackets. Continuous lines correspond to past and current mission observations, while dashed lines correspond to future observations (starting from mid 2022). From [118].

5.3 Scientific objectives and expected results

5.3.1 Properties of CR nucleonic spectra

Spectral measurements of CR nuclei from protons to iron and up to the highest–achievable energies with great precision, are a major objective of HERD. Recent publications from direct CR experiments showcased intriguing features in the proton and helium spectra.

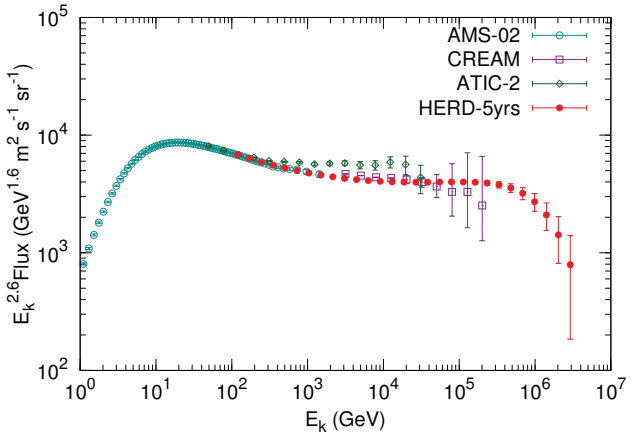

(a)

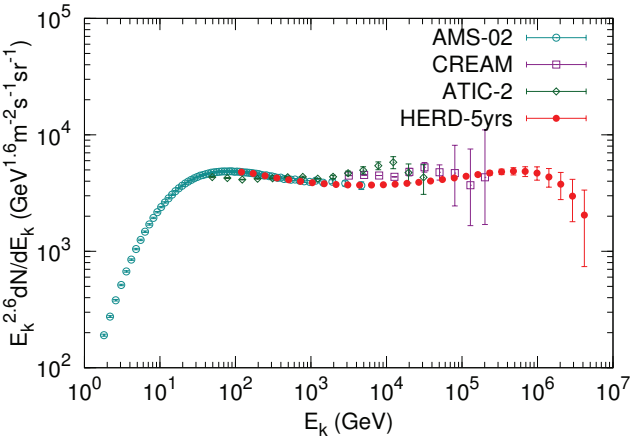

(b)

Figure 5.13: Possible expected spectral results for (a) protons and (b) helium nuclei, stemming from a 5-year exposure of HERD, compared to observations of AMS-02 [91, 96], CREAM [94] and ATIC [93]. HERD error bars correspond to statistical uncertainties. From [120].

In that case, HERD will be able to confirm these spectral features and extend current measurements, up to the highest achievable energies concerning space-borne instruments and direct CR observations. In such energetic regions ($\sim$ PeV),

pronounced features like the "knee" [128] in the all-particle spectrum of CRs could be directly probed via the so-called light component (protons and helium nuclei), as seen in Fig. 5.13a and 5.13b, from 5 years of HERD exposure. On the other hand, heavier elements being less abundant than protons in the ISM will have a minor contribution below the knee that could gradually increase, due to sources possibly accelerating particles rigidity– and not energy–wise. Furthermore, significant insights might arise when probing the individual CR "knees" of consecutive elements, even more so when studying the maximum energies reached by galactic accelerators.

Along with their origin and acceleration mechanism in the Universe, an important aspect of CRs pertains to their propagation in the Galaxy, a phenomenon customarily examined with secondary-to-primary flux ratios (*i.e.*, B/C, B/O). In that regard, nuclei such as lithium, beryllium and boron are considered to be of a secondary origin, produced by spallations of primary CRs with the Interstellar Medium during their propagation. Consequently, a major task to be addressed by HERD would be to extend current results, both on individual CR spectra as well as their respective secondary-to-primary ratios (along with searches of possible anisotropy hints), in the multi-TeV/n range (Fig. 5.14) where intriguing spectral features are postulated.

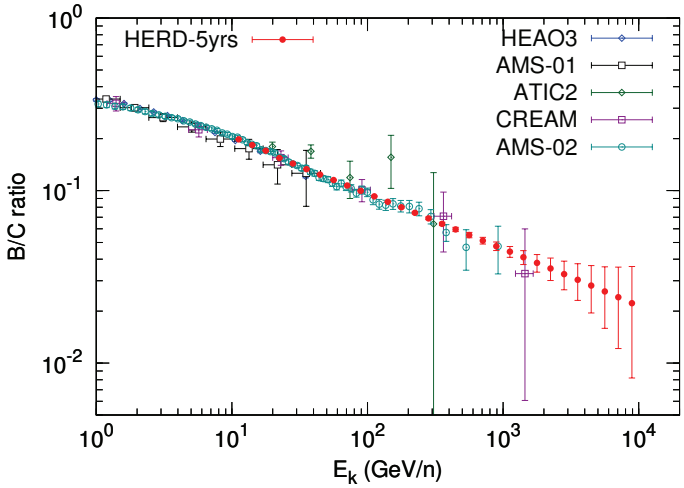

Figure 5.14: Expected measurements on the B/C ratio with 5 years of HERD exposure are shown (assuming a single power-law behavior), compared with HEAO3 [129], AMS–01 [130], ATIC–2 [131], CREAM [132] and AMS–02 [53] experimental results. HERD error bars correspond to statistical uncertainties. From [120].

5.3.2 The all-electron spectrum

Accounting for 1% of total CRs, electron and positrons can provide valuable insight on local sources, within the local neighborhood (a few hundred parsec). This feature is attributed mainly to large energy losses during particle acceleration/propagation, verified from the value of the diffusion coefficient (extracted from B/C results). The all-electron spectrum can be approximated by a single power-law consistent with recent observations [87, 88, 133]. In 2017, DAMPE published the first, direct evidence of a spectral break in the all-electron spectrum at $\sim$ 1 TeV with great precision [62], while extending the spectrum up to 5 TeV. These results were hinted by HESS [90], VERITAS [86] and validated by CALET [133], later on.

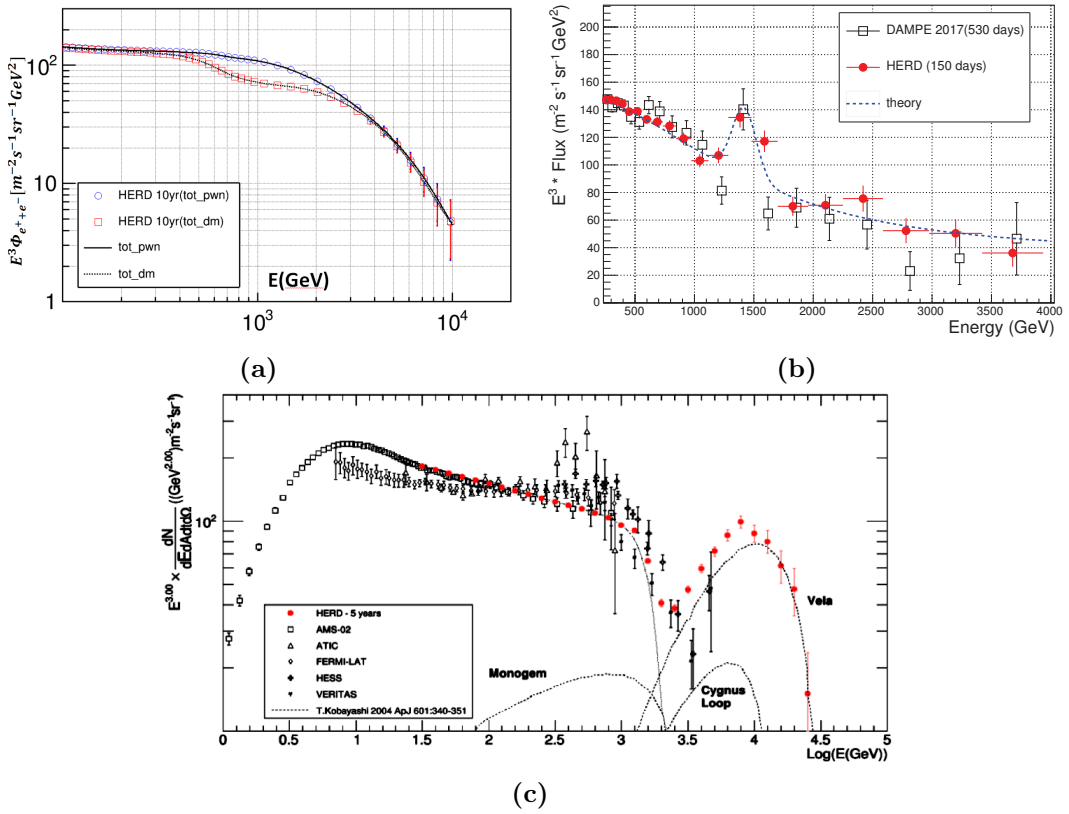

Figure 5.15: (a) Foreseen capabilities of HERD in distinguishing features in the all-electron spectrum within 1 year of observations. A soft spectrum connected to astrophysical origins, can be differentiated over a "bump-like" feature expected from DM. (b) Expected results on the search of a possible spectral feature approximately at 1.4 TeV, with 150 days of HERD exposure, in conjunction with the DAMPE contribution from 530 days of data-taking. HERD error bars correspond to statistical uncertainties. (c) Results on the e^+e^- extracted from 5 years of HERD exposure, signaling the expected contribution of nearby sources. From [120].

HERD will be capable of verifying such features accurately, while extending current measurements up to few tens of TeV due to its unprecedented acceptance. Such extension in energy could possibly reveal a dominant contribution from nearby electron sources (*i.e.*, Vela SNR) as illustrated in Fig. 5.15c, due to the connection of source contribution and radiation losses mentioned above. Additionally, HERD will be able to distinguish particles originating from astrophysical sources over possible dark matter (DM) annihilation products (illustrated in Fig. 5.15a), while also evaluating the existence of a possible spectral feature approximately at 1.4 TeV, as seen in the all-electron spectrum of DAMPE, illustrated in Fig. 5.15b. Furthermore, a measurable CR anisotropy could be detectable, provided that a nearby source contributes to the observed spectrum from a given direction. Taking into account the almost–isotropic contribution of electrons/positrons from DM annihilation (due to flat DM density distribution near the solar system), an observed anisotropy could demonstrate its astrophysical origin.

5.3.3 Prospects on Gamma-ray astrophysics

HERD will be providing insight on various topics associated to gamma–ray astrophysics [134], probing galactic and extra–galactic origins of diffuse gamma-ray emission while determining the nature of unidentified sources (owing to its wide FOV). Determining possible aspects of the γ-ray diffusion emission, can lead to enhanced understanding of CR intensities by tracing particle interactions of protons and electrons in the ISM.

Moreover, HERD could provide an intriguing perspective towards transient studies, focused on collective observations between space-borne and ground-based detectors, such as the Cherenkov Telescope Array (CTA), Advanced LIGO and Virgo experiments. Point-like sources can be probed by HERD (Fig. 5.16a), with a first approximation on the source differential sensitivity of the detector. Thus, preliminary results pointing away from (or to) the galactic plane, result to sensitivities of $\sim 10^{-6}$ MeV cm^{-2} s^{-1} (or $\sim 10^{-5}$ MeV cm^{-2} s^{-1}), obtained for energies of $\sim$1 GeV (or $\sim$ 10 GeV).

Complementary studies between space–borne and ground–based experiments are feasible for energies larger than 100 MeV, benefiting from the synergy between the above-stated detectors. That would lead to a simultaneous source coverage in a wide energy range with substantial overlap of spectral measurements. In

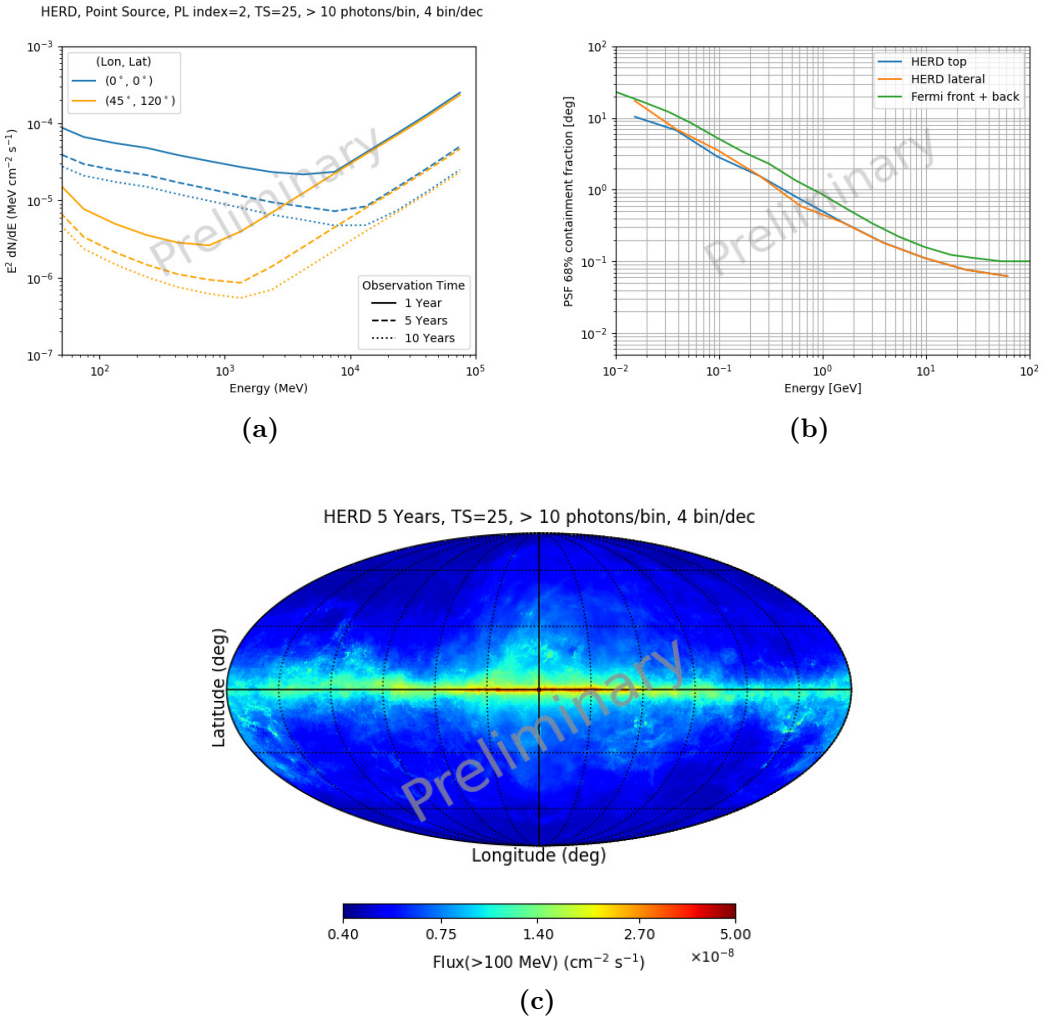

Figure 5.16: (a) Differential sensitivity of point-like sources for HERD, concerning sample galactic and extragalactic pointings at 1, 5 and 10 years. (b) Performance evaluation regarding a preliminary PSF calculation for the top and lateral sectors of HERD, compared with the Fermi-LAT average PSF. (c) HERD 5-year sky-map for gamma-rays above 100 MeV. From [134].

that regard, ongoing work on the expected full sky-map in gamma-rays (above 100 MeV) within 5 years of HERD exposure, is illustrated in Fig. 5.16c.

Furthermore, preliminary calculations concerning the Point Spread Function (PSF) of HERD (lateral and side faces) were carried out, based on simple performance estimations, compared with the average Fermi-LAT PSF (Fig. 5.16b). In that aspect, HERD will guarantee the continuation of gamma-ray observations, specifically after Fermi-LAT's future end-of-life with an additional extension to higher energies.

5.4 Summary

The HERD space mission has been illustrated in this chapter, starting from an overview of its novel design along with a brief introduction to its various sub-detectors. The main scientific objectives and performance parameters were also discussed, accompanied by the expected contributions of HERD in CR nuclei, electrons/positrons and gamma-rays.

In the following chapter, a deeper look in the HERD PSD will be provided, with the aim of evaluating various performance parameters in order to define the optimal geometry and overall configuration.

Chapter 6

R&D activities for the Plastic Scintillator Detector of HERD

In the previous chapter, a general overview of the HERD space mission highlighting its sub-detectors and main scientific objectives was presented. This chapter is dedicated to the study, design and optimization of the HERD PSD, a detector purposed as a mean of discriminating incident photons from charged particles, while being capable of identifying incoming cosmic–ray nuclei in a range of $Z = 1 - 26$.

This endeavor is a collaborative effort of various institutes from Italy and China, contributing towards the final determination of the optimal PSD layout. Main goal of this chapter is to illustrate the work focusing on the optimal PSD bar layout, starting from the study, configuration and test of prototypes involving different scintillator sizes and materials along with a variety of SiPMs covering all necessary requirements.

The majority of results presented throughout this chapter are associated to activities carried out in the National Laboratories of Gran Sasso (Laboratori Nazionali del Gran Sasso - LNGS) along with test beam campaigns taking place at CNAO, Pavia and in CERN SPS and PS facilities. A synopsis of the main PSD requirements and characteristics will be provided in the following, along with highlights from the various prototypes built, configured and thoroughly tested in the laboratory.

6.1 Introduction

The PSD design (as mentioned in the previous chapter) is conceived around the usage of scintillators readout by silicon photomultipliers (SiPM). A very brief introduction on the basic principles of scintillators and SiPMs, will be given in the following.

6.1.1 Scintillators

Plastic scintillators are traditionally used in nuclear and particle physics experiments to measure the charge of impinging charged particles, or as anticoincidence detectors, in the case of highly energetic gammas when used in conjunction with trackers and calorimeters. Their operation is based on the interaction of said (charged) particles with the active detector material which leads to the emission of scintillation light when excited. The produced light should propagate towards a sensitive photodetector, which converts it to an electrical signal.

Main advantages towards their selection include a low overall density, high efficiency, fast timing response, while being robust and relatively inexpensive as materials [135]. When a particle interacts with the scintillator its excited state typically lasts a few nanoseconds, with the emitted light being detected almost instantaneously by the photodetector. Given its high detection efficiency and timing capabilities, scintillators could also be useful when designing the trigger logic of a given experiment.

Additionally, plastic scintillators are highly versatile and can be customized to meet specific detection requisites. In that sense, they can follow different shapes and sizes to fit a wide range of geometries, making them suitable for use in space, where structural robustness is necessitated. Compared to other types of radiation detectors, plastic scintillators are relatively low cost. They can be manufactured using simple and inexpensive processes and along with their increased lifespan they constitute an interesting option towards the PSD realization.

6.1.2 Silicon Photomultipliers

Silicon photomultipliers (SiPMs), are solid-state photon detectors used in a variety of applications where high sensitivity, low noise, and fast response time are essential [136]. SiPMs are made from silicon wafers coated with a layer of

avalanche photodiodes (APDs) which operate in Geiger mode and connected in parallel, creating an array of many small APDs.

The operation principle of SiPMs is based on the concept of avalanche multiplication. When a photon interacts with the active silicon area, it generates an electron-hole pair. The electric field in the APD causes the electrons to accelerate and collide with other atoms, thus giving rise to multiple pairs. This process continues until a large number of electron-hole pairs are generated, ultimately producing a current pulse that is amplified and detected.

SiPMs have recently gained attention as a potential candidate for use in space-borne applications, due to their unique properties such as high gain, low power consumption, small size, and insensitivity to magnetic fields, thus being an improvement over traditional photomultiplier tubes (PMTs). Moreover they are compact, robust and relatively inexpensive sensors, all of them being crucial parameters especially when considering the limited power, size and weight budget of a space mission. The main performance characteristics of a SiPM are briefly presented in the following:

- *Photon detection efficiency (PDE).* The PDE is defined as the percentage of incident photons detected by the SiPM and is a product of the geometric fill factor, the quantum efficiency (QE) of the sensitive area and the avalanche initiation probability, as seen below:

$$\text{PDE} = \text{ Fill Factor } \times \text{QE}(\lambda) \times \text{ Avalanche Probability} \tag{6.1}$$

  where the Fill Factor (or FF) is given by the ratio of sensitive to total area, QE(λ) corresponds to the probability of an impinging photon (on the SiPM) to generate a charge carrier (electron-hole pair). Ultimately, the Avalanche Probability is defined as the probability that the aforementioned charge carrier will initiate a Geiger avalanche[1].

- *Gain.* The SiPM Gain corresponds to the number of charge carriers produced per incident photon and can be represented by the following equation:

[1]Also referred to as "impact ionization effect", corresponding to a charged carrier multiplication phenomenon, in which the number of drifting carriers is rapidly increasing, thus resembling an avalanche [136].

$$\mathrm{G} = \frac{C \cdot (V_{Bias} - V_{Breakdown})}{q_e} \tag{6.2}$$

where C is the pixel capacitance, $\mathrm{V_{Bias}} - \mathrm{V_{Breakdown}}$ corresponds to the overvoltage (in Volts) deriving from the reverse bias voltage (being the working SiPM voltage, denoted as $\mathrm{V_{Bias}}$) minus the breakdown voltage ($\mathrm{V_{Breakdown}}$), with q_e being the electron charge.

- *Dynamic range and linearity.* The dynamic range of a SiPM is defined as the ratio of the number of effective photons necessary to fire a single pixel, divided by the average number of photons necessary to fire 95 % of pixels. From the effective photon definition, one such photon suffices to fire a pixel in an unaltered SiPM. The dynamic range is a function of the total number of microcells, overvoltage and wavelength of incident photons. The SiPM linearity refers to the part of the dynamic range in which its output signal is directly proportional to the input light intensity over its dynamic range. In principle, linearity decreases with the increase of the number of photons in relation to the total number of available microcells.

- *Noise.* Primary source of noise in a SiPM is the number of dark counts, which arises due to thermal electrons generated in the active volume. The Dark Count Rate (DCR) is a function of active area, overvoltage and temperature. Each dark count is a result of a thermally generated electron that initiates an avalanche in the high field region. This effect takes place mostly in the single-electron regime, consequently the dark count probability is higher for single pixels fired.

  Another source of noise is the optical crosstalk, which can be produced from the excitation of neighboring pixels due to photon emission during an avalanche discharge in a given microcell. The crosstalk is a function of the overvoltage while also being affected by the fill factor.

  Finally, afterpulses can be an additional contribution to the overall SiPM noise, being an effect generated by trapped electrons produced in avalanches and released again after a delay of a few nanoseconds to several microseconds. If the time delay with respect to the preceding pulse is short, only pulses with small amplitude are generated. If the delay is larger than the pixel recovery time, a standard avalanche signal is triggered.

- *Temperature dependence.* The SiPM is dependent on possible temperature fluctuations, specifically affecting the photon detection efficiency, dark count rate and gain. For stable operations in the presence of significant temperature fluctuations, either a bias compensation or thermal regulation should be considered.

6.1.3 PSD design options

Main requirements concerning the PSD design, include: high detection efficiency, broad dynamic range and good energy resolution. In order to accomplish such objectives, a few different design layouts are currently under consideration, based primarily on the plastic scintillator geometry and number of readout channels. Consequently, the layouts under test involve: long scintillator bars as seen in Fig. 6.1, square tiles, as shown in Fig. 6.2, along with an intermediate solution between the aforementioned choices, including shorter (in length) but wider bars, serving as a compromise between the benefits and drawbacks of previous layouts. All configurations present advantages and disadvantages, related (among others) to the optimal number of readout channels versus back–splash (or back–scattering) effects. Ongoing tests and optimization efforts are carried out for the majority of layouts, aiming to define the best scintillator type and size, SiPM model and quantity to be instrumented, along with an overall verification of the PSD configuration, structural robustness and space readiness tests.

Figure 6.1: A selection of PSD bar prototypes of different sizes, readout by a collection of SiPMs. All configurations were realized in the Gran Sasso National Laboratories, in L'Aquila, Italy.

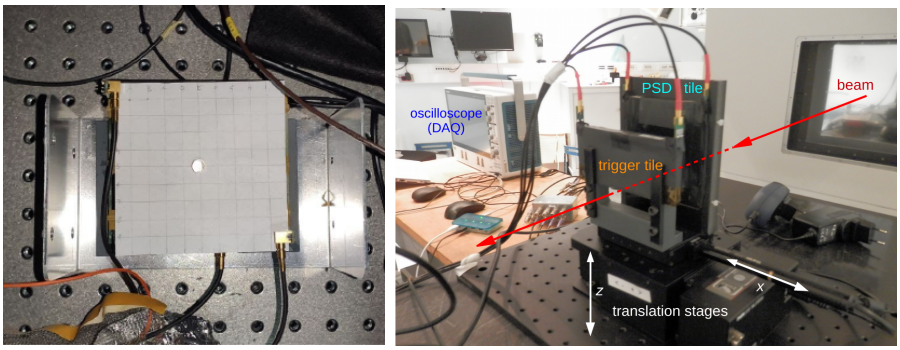

(a) (b)

Figure 6.2: Tile configurations under test representing measurements: (a) with a radioactive ^{90}Sr source placed on the tile center and (b) beam test activities in CNAO, Pavia. From [118, 125].

6.2 Characteristics of PSD bar configurations

The main characteristics and specifications of the various PSD configurations will be presented in this section. Initially, an overview of the scintillator bars and SiPMs under test are displayed in Tabs. 6.1 and 6.2.

A variety of SiPM models manufactured by AdvanSiD and Hamamatsu Photonics were examined in order to satisfy a high PDE, broad dynamic range, good linearity and optimal energy resolution. Specifically, SiPMs with various gains, microcell counts and peak sensitivity were tested, in conjunction to a number of plastic scintillators (Eljen technologies [65] and Saint-Gobain crystals [137]), although with similar characteristics in the majority of cases. Bars of different sizes and overall geometries (rectangular and trapezoidal) were tested in order to gauge possible effects arising from different scintillator materials, SiPMs and wrapping choices, eventually leading to the optimal PSD geometry.

From that point onward, a selection of tested bar prototypes will be discussed, consisting of different sizes, scintillator material and SiPM models. In that case, Tab. 6.3 is introduced in order to bring together all needed information concerning the prototypes under discussion. It is worth noting that all configurations (of the previously mentioned table) have a rectangular cross-section except for the last entry, which corresponds to a prototype of trapezoidal cross-section. In the following, the complete procedure concerning a PSD bar configuration, starting from their assembly, determination of each SiPM's working point, leading up to results coming from CR muons and electrons from a radioactive ^{90}Sr source, will be presented.

Table 6.1: SiPM model characteristics used for the PSD bar option

Parameter	AdvanSiD	Hamamatsu	
SiPM model	ASD-NUV3S	S13360-3025CS	S14160-3015PS
Effective area (mm)	3×3	3×3	3×3
Cell count	5520	14400	40000
Cell size (μm)	40	25	15
Cell fill factor (%)	60	47	49
Response range (nm)	350 - 900	270-900	290-900
Peak sensitivity (nm)	420	450	460
PDE (%)	43	25	32
Breakdown voltage (V)	$24 - 28$	50 ± 5	38 ± 3
Overvoltage (V)	$2 - 6$	5.0	4.0
Dark count rate	50-100 [kHz/mm^2]	200-1200 (kcps)	700-2100 (kcps)
Gain	3.6×10^6	7×10^5	3.6×10^5

Table 6.2: Plastic scintillator model characteristics used for the PSD bar option

Parameter	Saint-Gobain	Eljen Technology	
Scintillator Model	BC-404	EJ-200	EJ-204
Light Output (% Anthracene)	68	64	68
Rise Time (ns)	0.7	0.9	0.7
Decay Time (ns)	1.8	2.1	1.8
Pulse Width, FWHM, (ns)	2.2	2.5	2.2
Wavelength of Max Emission (nm)	408	425	408
Light Attenuation Length (cm)	160	380	160

Table 6.3: PSD bar configurations under test in GSSI and LNGS

Length · Width · Thickness [cm^3]	Scintillator	SiPMs per side	SiPM model
$50 \times 3 \times 1$	EJ-200	1	S13360-3025CS
$50 \times 3 \times 1$	EJ-200	1	ASD-NUV3S
$50 \times 6 \times 1$	EJ-200	2	S13360-3025CS
$75 \times 5 \times 1$	BC-404	2	S13360-3025CS
$150 \times 5 \times 1$	BC-404	2	ASD-NUV3S
$160 \times 3 \times 0.5$	EJ-204	2	S14160-3015PS

6.3 PSD bar preparation and calibration

A first step towards the construction of a PSD prototype pertains to the careful purification of the scintillator bar, accompanied by the application of consecutive reflective layers (i.e., Teflon, white paint, reflective tape) in order to boost the level of light reflectivity of the emitted scintillation photons and mitigate losses.

Furthermore, several layers of opaque wrapping are enveloping the bar under test in order to ensure minimization of light escaping the bar but more importantly, shielding it from external light, being an immense source of background as well as a major parameter concerning the plastic scintillator deterioration over time. In that stage, the SiPMs are ready to be optically coupled at both ends of the bar. A common approach for optical coupling is to use an optical grease or adhesive with a matching refractive index between the scintillator and SiPM. The grease or adhesive fills the small gaps between the scintillator and SiPM, thus reducing the amount of light that is lost due to reflection or refraction at the interface.

The SiPMs are carefully encased in 3-D printed, light-proof end-caps in order to avoid exterior light effects, consequently leading to a false signal. In conclusion, the objective is to maximize the amount of light detected by the SiPM, which can increase the sensitivity and accuracy of the PSD bar under test.

6.3.1 SiPM working point assessment

The main method in assessing the optimal working point of the SiPMs is based on the identification of a common gain among the various modules reading out the bar. Such a method alleviates the need of selecting a common bias voltage due to possible fluctuations in the exact breakdown region of each SiPM.

The general procedure can be summarized in the following steps, with the case of a $50 \times 3 \times 1$ cm^3 bar (EJ-200) readout by 1 Hamamatsu (S13360-3025CS) SiPM per side being used as a paradigm. Initially, a set of measurements concerning the DCR of each SiPM are carried out initially in a voltage range around the value proposed by the manufacturer. The charge distributions of photon equivalent peaks are then fitted with Landau-convoluted-with-Gaussian functions with the distance between consecutive peaks being used towards the gain estimation. Fig. 6.3 corresponds to gain measurements referring to both SiPMs used in the bar readout. Red lines correspond to linear fits of the data across the voltage range.

Evidently, both SiPMs show good gain linearity with increasing bias voltage. Taking into account the fit functions parameters, a common gain value can be

selected, thus leading to the final bias voltage determination. The gain can be calculated as follows:

$$G = \frac{\text{Distance between two consecutive p.e. peaks}}{\text{R} \cdot \text{A} \cdot \text{q}_\text{e}} \tag{6.3}$$

where the distance between two peaks is measured in (Volts · s), R corresponds to 50 Ω of resistance, A corresponds to the amplification provided from the readout Printed Circuit Board (PCB), being 30 for this case and finally q_e being the electron charge (1.6×10^{-19} Cb).

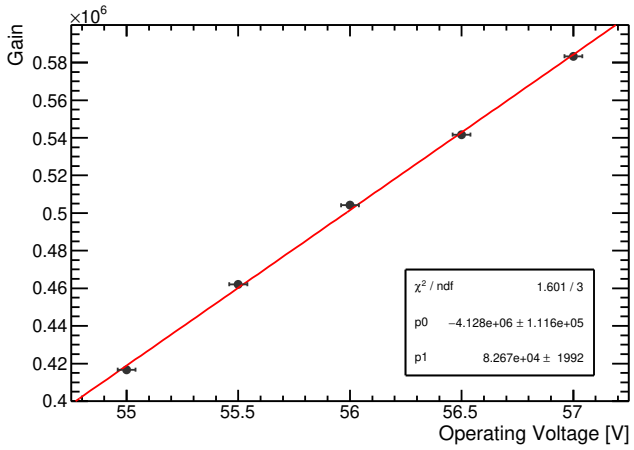

(a) Left SiPM

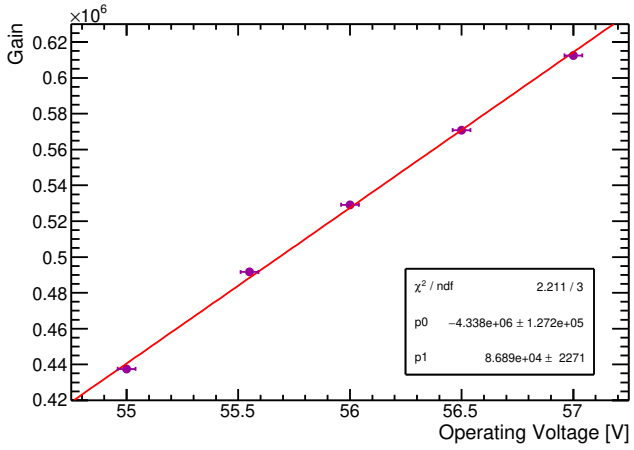

(b) Right SiPM

Figure 6.3: Gain measurements of (a) left and (b) right SiPMs coupled to the bar under test. Red lines correspond to linear fits on the data, while both legends are illustrating the fit parameters and χ^2/ndf.

Consequently, a common gain of G = 5.5×10^5 is selected for the bar readout of both sides, corresponding to bias voltages of 56.5 V and 56.25 V for left and right SiPMs respectively. Applying said voltages and acquiring an additional measurement of the dark count spectrum spectrum, leads to Fig. 6.4, where a consistency check between both sides is performed in order to calibrate the response of left- and right-side SiPMs. Such a procedure was implemented in the majority of bar configurations illustrated in Fig. 6.3. All charge distributions were registered slightly above the pedestal in order to preserve information only on primary photon equivalent peaks.

Furthermore, this particular SiPM model shows an exquisite dark count response, since only the first and second peaks are visible under the given bias voltage. Evidently, both dark count pulse spectra are in excellent agreement, while an additional fit of the single photon equivalent peak has been implemented in order to be used to evaluate the number of photons detected in the case of upcoming measurements.

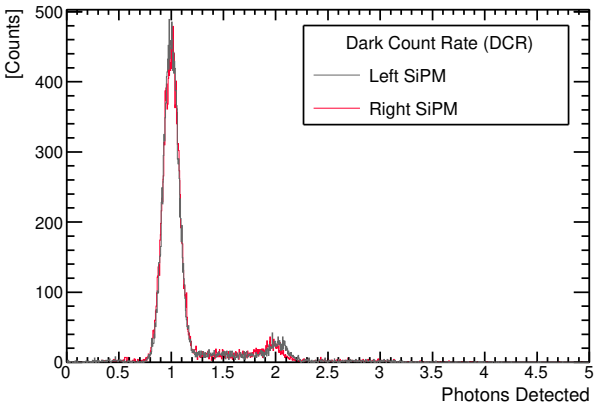

Figure 6.4: Dark count spectra regarding the SiPMs instrumented on the left and right side of the bar prototype under test. The collective gain corresponds to $G = 5.5 \times 10^5$.

6.4 Radiation source measurements

Following the determination of a common gain between left and right side SiPMs, the response of the aforementioned bar to low-energy electrons coming from a radioactive source, will be discussed in this section. The preferred radioactive source in this case is strontium (^{90}Sr), with a measured activity of 138 kBq emitted from a disk-like surface with a radius of 1 cm. A simple schematic view of the ^{90}Sr decay chain can be viewed in Fig. 6.5.

Strontium has a half-life of 28.8 years and decays to yttrium with a subsequent beta emission of 0.546 MeV. In a following step, yttrium, with a half-life of 64 hours should decay to stable zirconium with a concurrent beta emission of approximately 2.3 MeV. Therefore, two electrons with energies up to 2.3 MeV are expected to interact with the detector for each decaying ^{90}Sr nucleus.

In Fig. 6.6, the projected range of electrons inside a plastic scintillator material can be viewed, where two vertical dashed lines signal the maximum energies emitted in the case of strontium and ytrium beta decays. Electrons produced from strontium should have a range of approximately 0.5 mm, while the ones emitted from ytrium should reach an utmost range of 1 cm. Keeping into account the thickness of wrapping materials enveloping the bar, the low energy component with a projected range under a few mm will be absorbed. Consequently, only electrons coming from the decay channel of ytrium will be detected from all tested configurations.

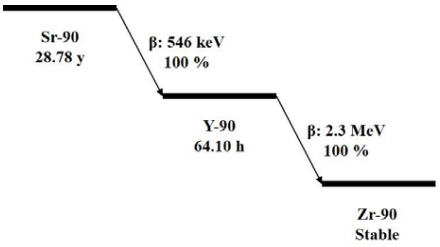

Figure 6.5: Schematic view of the ^{90}Sr decay chain.

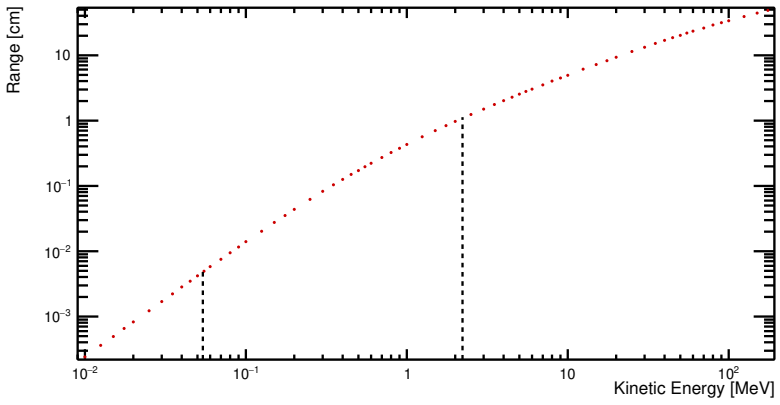

Figure 6.6: Range of electrons (in cm) inside a plastic scintillator, represented by red points. The two vertical (black) dashed lines correspond to the maximal energies emitted by the decay of ^{90}Sr and ^{90}Y around 0.546 MeV and 2.3 MeV, respectively. Data extracted from NIST [138].

Returning to the example of the PSD bar configuration discussed previously, a series of measurements were performed in various trigger positions in order to gauge its response to low energy electrons. A common gain of G = 5.5×10^5 is selected for the bar readout of both SiPMs, corresponding to bias voltages of 56.5 V and 56.25 V for left and right modules respectively. Moreover, a relatively high threshold of 5.5 p.e. was imposed for both SiPMs in order to avoid possible contributions from DCR and other noise-inducing effects. It should be noted that an event is registered when both SiPMs detect a given particle over the imposed threshold.

Fig. 6.7 provides a picture of the PSD bar under test referring to radioactive source measurements in different trigger positions. From top to bottom the source is placed at trigger positions of 10, 25 and 35 cm, when left and right ends correspond to 0 and 50 cm respectively. The selected source positions are symmetrical to the bar center (25 cm) in order to evaluate possible effects or peak asymmetries viewed from both SiPMs.

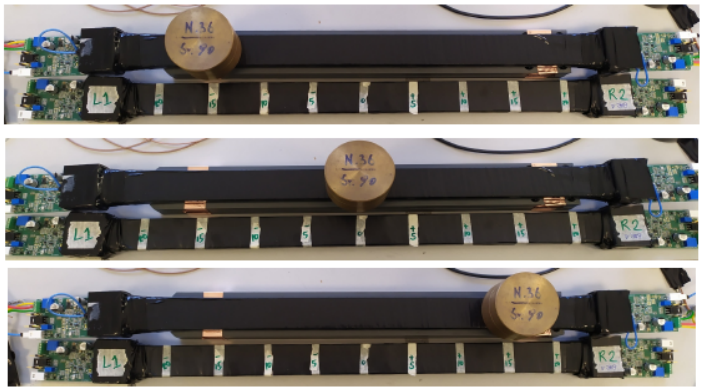

Figure 6.7: PSD bar configuration under test illustrating a strontium (^{90}Sr) source in different points across 50 × 3 × 1 cm^3 bar, readout by 1 SiPM/side. From [118].

Fig. 6.8 illustrates the acquired spectra for left and right SiPMs in black and red color, respectively. All spectra are normalized to the single p.e., thus providing the number of detected photons in each trigger position, viewed from both SiPMs. Moreover, LanGaus fits were applied to the data, in order to assess the MPV and sigma of the resulting photon equivalent distributions. Interestingly, in all source positions left and right SiPMs show very similar responses with an MPV of 35 - 37 photons detected when the source is placed close to a given SiPM and 22 - 24 photons when the same events are detected from the opposite side. As expected, at the bar center both sensors yield an MPV of 25 - 26 photons with similar

distribution widths (Landau). Finally, wider distributions of detected photons can be viewed when the source is closer to a bar end, while at the same time narrower distributions are formed in the opposite side, due to attenuation effects of propagating photons across the bar. This effect will be analyzed thoroughly in the following sections.

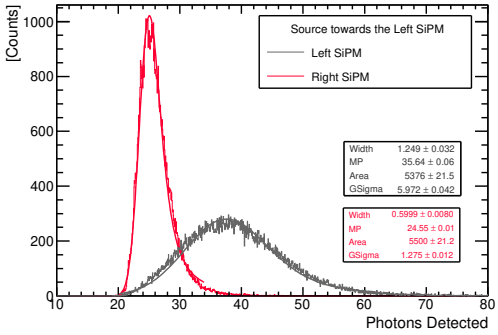

(a) Source towards the left end

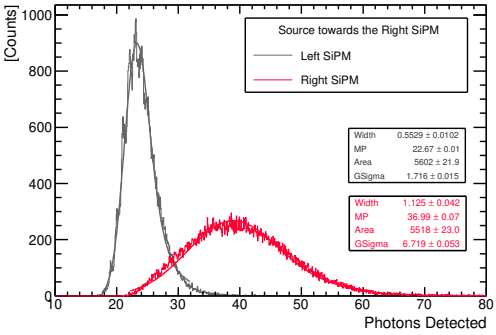

(b) Source at the bar center

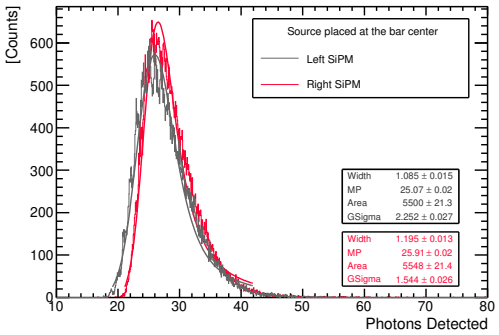

(c) Source towards the right end

Figure 6.8: Spectra of photons detected with respect to different trigger positions along a 50 cm bar, readout by 1 SiPM/side. Figures (a) and (c) correspond to ^{90}Sr source measurements in symmetric positions from the bar center (± 15 cm), towards left and right sides, respectively. In (b), the source is placed in the bar center. Black and red lines correspond to left and right SiPMs respectively, while both distributions are fitted with LanGaus functions.

6.5 CR muon measurements

A major part of this work revolves around the measurements of CR muons, in order to evaluate various performance parameters of the PSD configurations under test. Muons have a rest mass of 105.66 MeV/c^2, corresponding to approximately 207 times the mass of an electron and a lifetime of $\sim$ 2.2 microseconds. They mainly

originate from the decay of charged pions in the atmosphere and constitute the most abundant particle species near sea level with a flux of about 100 Hz/m^2 [13] and a wide range of energies (from hundreds of MeV to several GeV). The entirety of bar configurations presented or mentioned before has been thoroughly tested with muons as a means of evaluating various performance aspects, including a precise study on light attenuation effects along the bar. Pictures of the aforementioned configurations are presented in Fig. 6.9, pertaining to various scintillators types, sizes and geometries along with a different selection in SiPM readouts both in model and quantity.

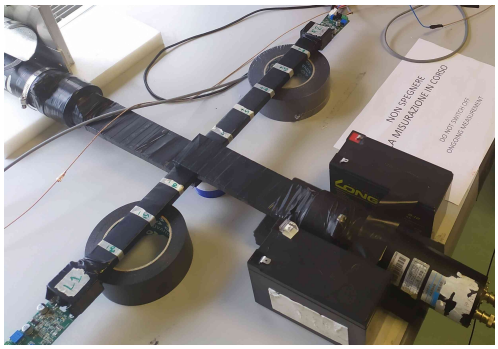

(a) 50 × 3 × 1 cm^3 bar

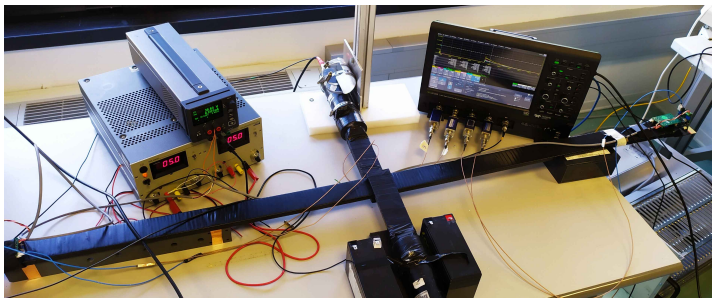

(b) 150 × 5 × 1 cm^3 bar

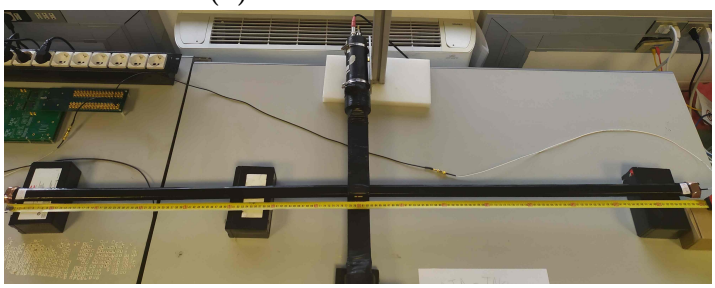

(c) 160 × 3 × 0.5 cm^3 bar

Figure 6.9: CR muon measurements with a collection of PSD bar configurations. These configurations differ in scintillator type, size and SiPM readout. Moreover, (a, b) correspond to bar geometries of rectangular cross section, while (c) pertains to a novel bar of trapezoidal cross-section.

As seen from the images above, all measurements were taken with an external trigger imposed by two scintillator bars and readout by single Hamamatsu PMTs. In order to maximize trigger performance, both scintillators are situated orthogonally to the bar under test, with one scintillator being placed above and the other below the bar, thus creating a scintillator "sandwich" (or a "cross"). Each trigger module has a width of 5 cm and thickness of 1 cm, with their respective length being dictated every time by the width of any evaluated PSD configuration.

Similarly to the case of radioactive source measurements, one of the PSD configurations will be selected to highlight the experimental procedure and its corresponding results. In this way, the core idea and results will be clear without risking possible repetitive overlaps.

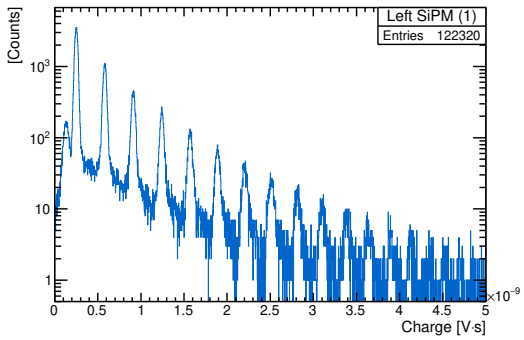

(a) Left SiPM (1) DCR

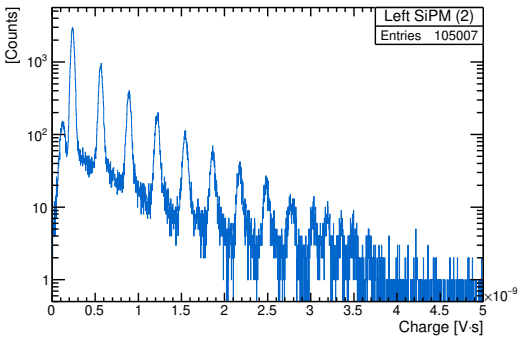

(b) Left SiPM (2) DCR

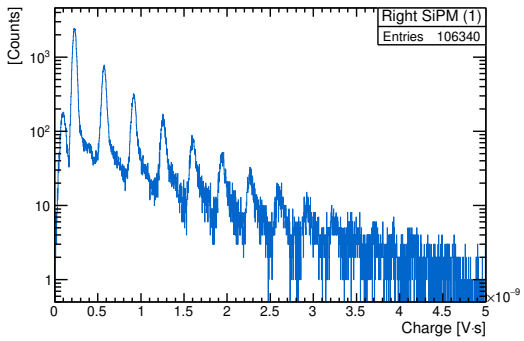

(c) Right SiPM (1) DCR

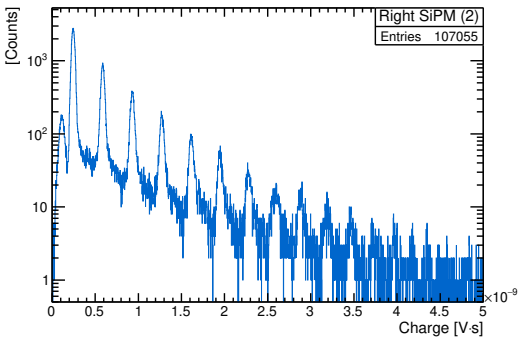

(d) Right SiPM (2) DCR

Figure 6.10: DCR spectra at approximately $V_{Bias} = 30$ V, and a common gain of $\sim 1.4 \cdot 10^6$, for the case of a BC-404 bar of $150 \times 5 \times 1$ cm^3 in dimension, readout by two ASD-NUV3S SiPMs per instrumented side.

All PSD bars, following an initial stage pertaining to the definition of a common SiPM working point, are subjected to measurements in symmetrical trigger positions with respect to the bar center. The selected PSD configuration in this case will be a BC-404 bar of $150 \times 5 \times 1$ cm^3 in dimension, readout by

two ASD-NUV3S SiPMs. All four SiPMs are calibrated according to a common gain of approximately $\sim 1.4 \cdot 10^6$, leading to a bias voltage of $V_{Bias} \sim 30$ V for all sensors. A final view on the DCR spectra concerning the four instrumented SiPMs is shown in Fig. 6.10, where every SiPM is adjusted to the voltage and gain discussed above.

Evidently, a comparison regarding the AdvanSiD and Hamamatsu SiPMs presented in this and previous sections respectively, can reveal a large divergence between their inherent noise spectra. This might be attributed to the difference in microcell size, being 40μm for AdvanSiD and 25μm for Hamamatsu, along with structural differences implemented by Hamamatsu in order to ensure a lower noise contribution.

The average muon count impinging on the scintillator-imposed surface corresponds to 0.4 - 0.6 Hz. When a muon traverses the configuration and is registered by the upper and lower PMTs in a time window of 100 ns, a trigger is produced for the four SiPMs coupled to the bar under test. Next step in that case will be to acquire a background measurement with the trigger configuration away from the bar, in order to verify the PSD bar random noise as seen in Fig. 6.11. Clearly, the only visible contribution after an hour-long acquisition corresponds to the pedestal, coming from every undetected trigger.

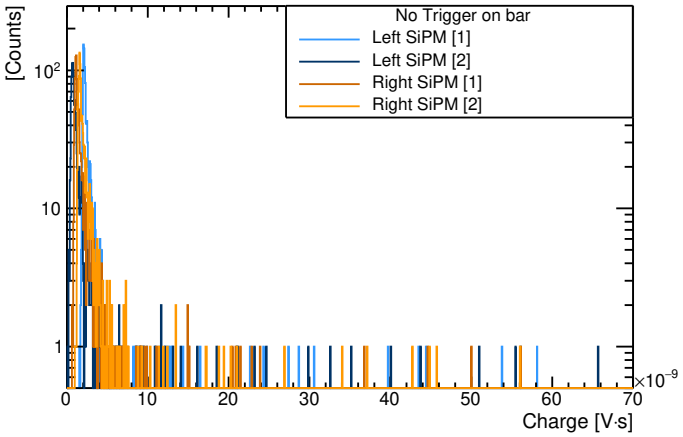

Figure 6.11: SiPM charge distributions illustrating the obtained pedestal when removing the trigger from the bar under test. All four modules (2 SiPMs/side) are calibrated to a common gain of approximately $\sim 1.4 \cdot 10^6$.

Thus, the following step is to acquire CR muon measurements in various positions along the bar, symmetrical to its center. In Fig. 6.12, charge distributions corresponding to CR muons in various trigger positions are illustrated. Left and

right SiPMs are colored in blue and yellow shades respectively, while the trigger positions are numbered from the left bar end (0 cm) towards the right (150 cm). All four SiPMs show a good response, evident also at the bar center (trigger position at 75 cm) where all SiPM contributions are in agreement.

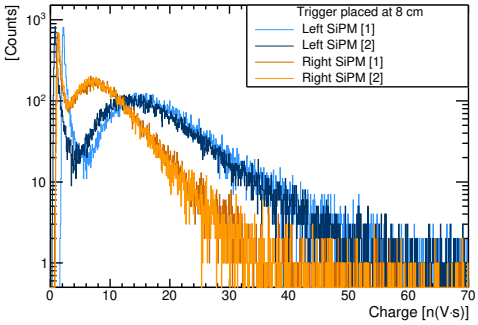

(a) Trigger at 8 cm

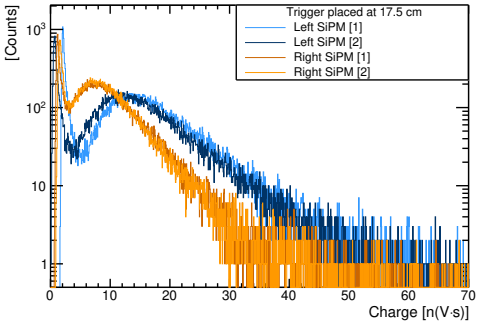

(b) Trigger at 17 cm

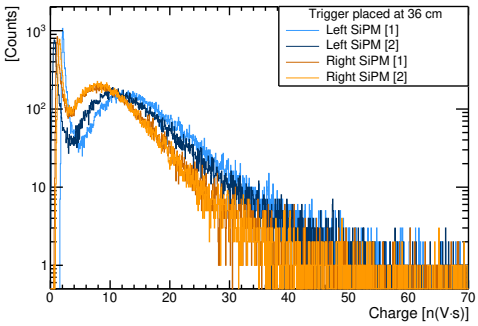

(c) Trigger at 36 cm

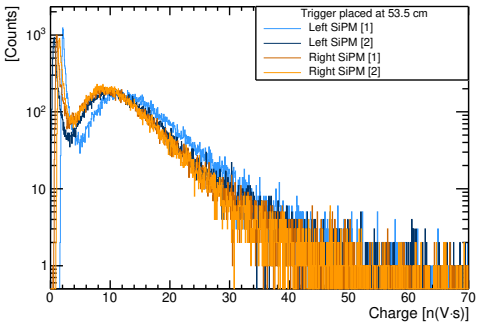

(d) Trigger at 53 cm

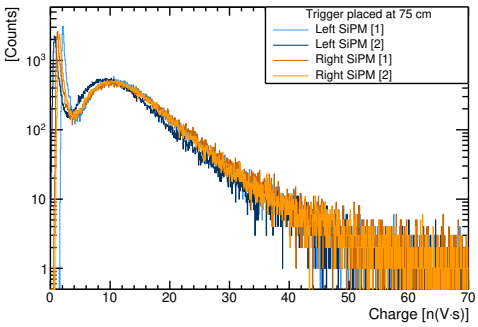

(e) Trigger at 75 cm

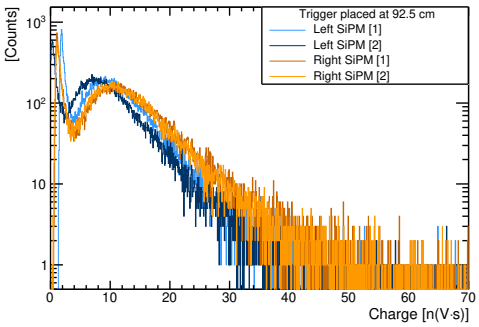

(f) Trigger at 92 cm

Figure 6.12: Charge distributions [in n(V·s)] of CR muons concerning a 150 cm bar readout by 2 SiPMs/side. The various figures correspond to charge measurements in different trigger positions, starting from the left (0 cm) towards the right (150 cm) bar end. Blue and orange colored distributions refer to left- and right-side SiPMs, respectively.

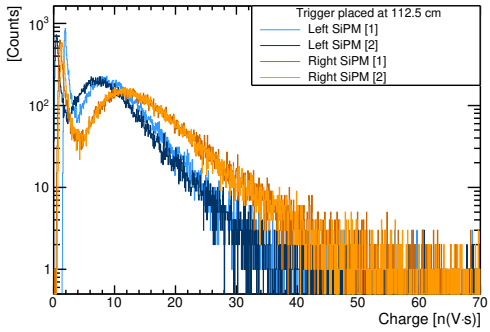

(g) Trigger at 112 cm

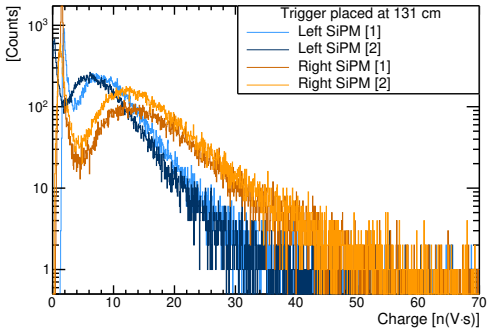

(h) Trigger at 131 cm

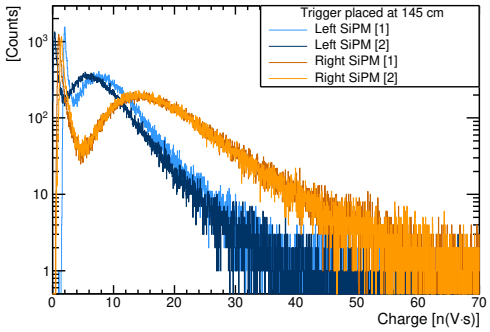

(i) Trigger at 145 cm

Figure 6.12: (Continued) Charge distributions [in n(V·s)] of CR muons concerning a 150 cm bar readout by 2 SiPMs/side. The various figures correspond to charge measurements in different trigger positions, starting from the left (0 cm) towards the right (150 cm) bar end. Blue and orange colored distributions refer to left- and right-side SiPMs, respectively.

The entirety of charge distributions corresponding to nine trigger positions are fitted with LanGaus functions, with the resulting MPV of each SiPM in every trigger position being presented in Fig. 6.13. Good agreement between left and right SiPMs is evident throughout the bar length, with a slight divergence between left side sensors attributed primarily to small gain differences due to voltage instabilities. The MPVs of each SiPM are normalized to unity and illustrate the behavior of light propagating across the 1.5 m bar. Final results on effective light attenuation length studies including all tested PSD configurations, will be summarized in the following section.

The single photon equivalent peak has been defined for every SiPM according to the procedure discussed previously and can be used to estimate the number of photons detected by each sensor, in various positions. In this case, each 1 n(V·s) of charge corresponds on average to 4.17 photons detected. Thus, when

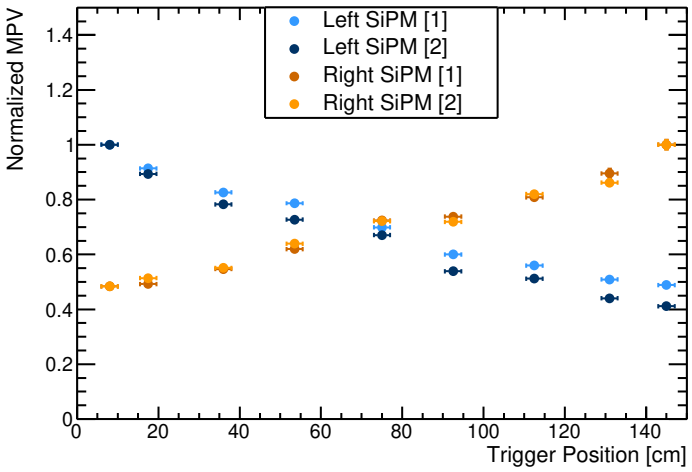

Figure 6.13: X-plot corresponding to MPV values (extracted from LanGaus fits) with respect to the trigger position of a 150 × 5 × 1 cm^3 readout by 2 SiPMs/side. All MPV values are normalized to unity.

the trigger is placed close to either left or right bar ends, an average of ∼ 60 photons is detected. When placing the trigger at the bar center, ∼ 42 photons are detected on average, corresponding to 70 % of the photons measured in either bar end. Finally, an average of ∼ 30 photons are detected from left- or right-side SiPMs when the trigger is situated on the opposite side, thus referring to a 50 % decrease.

6.6 Effective attenuation length measurements

Results on effective light attenuation studies including the example examined in the previous section as well as the rest of PSD configurations tested in the laboratory, will be presented in this section. As a general definition, the light attenuation length refers to the distance over which the scintillation light intensity emitted by the bar decreases by 1/e. Two distinct cases can be identified, the Bulk Attenuation Length (BAL) and the Technical Attenuation Length (TAL). The BAL describes the distance over which scintillation light is attenuated due to absorption and scattering in the bulk of the scintillator material, while the TAL is influenced by the overall geometry and construction of the scintillator detector, including its wrapping options, reflectors, etc. It should be noted that the light attenuation depends on the wavelength of emitted photons [139], especially since the wavelength spectrum of said photons is affected by their propagation towards

the given photodiode. Moreover, the quality of surface polishing influences the reflective properties [140] of the scintillator bar and could possibly alter the TAL value. In the case of long scintillator bars, both reflector type and wrapping method can affect the detector performance [141]. Consequently, a tight wrapping can ensure fewer reflections when photons propagate inside the bar. Additionally, the scintillator thickness and cross-section play an important role in light transport, since an increased bar cross-section can lead to an overall increase in the measured TAL [142]. Keeping these aspects into account, the general light attenuation formula [143] is defined as follows:

$$\mathrm{N(x)} = A_1 \cdot \mathrm{e}^{-\frac{\mathrm{x}}{\Lambda_\mathrm{S}}} + A_2 \cdot \mathrm{e}^{-\frac{\mathrm{x}}{\Lambda_\mathrm{L}}} + y_0 \simeq \mathrm{N}_0 \cdot \mathrm{e}^{-\frac{\mathrm{x}}{\Lambda_\mathrm{Eff}}} \tag{6.4}$$

where Λ_S and Λ_L correspond to short and long attenuation length components, A_1 and A_2 are the amplitudes and y_0 denotes the constant background. For the sake of simplicity, an "effective" light attenuation length (Λ_{Eff}) is approximated from the general equation, using a single exponential function which includes the collective effects of scintillator size, geometry, cross-section, wrapping material and SiPM readout, for the entirety of configurations listed previously. The process leading to the final measurement (thoroughly presented before) is summarized in the following:

1. CR muon measurements acquired in several trigger positions across the bar, symmetrical to its center.

2. Each charge spectrum from every SiPM is fitted with a Landau-convoluted-with-Gaussian function.

3. The Landau MPVs coming from all trigger positions are plotted with respect to the trigger position, normalized to unity.

4. Averaging the normalized MPV behavior with respect to the trigger position and fitting the resulting data with an exponential function, leads to a measurement of the effective light attenuation length.

In Fig. 6.14, collective results on the effective light attenuation from all PSD bar configurations illustrated in Fig. 6.9 are shown. These correspond to scintillator bars of different types and geometries along with a variety of readout SiPMs.

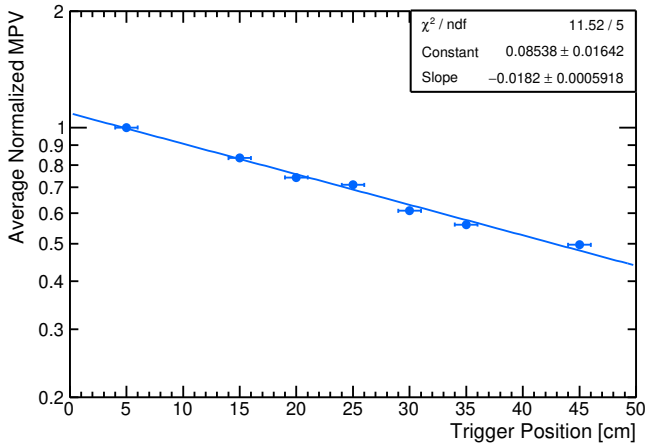

(a) $50 \times 3 \times 1$ cm^3 bar $\rightarrow \Lambda_{\text{Eff}} = 55 \pm 2$ cm

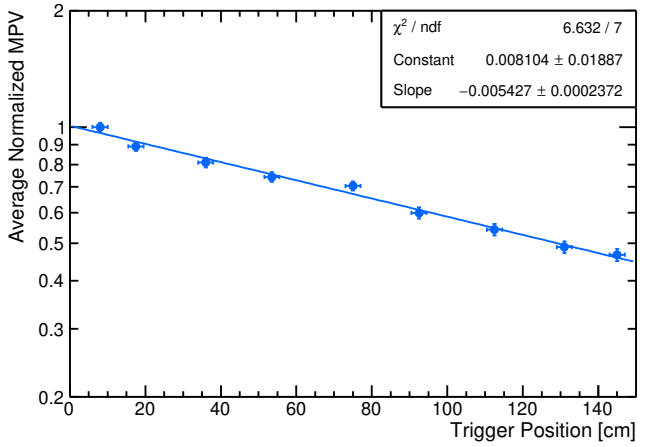

(b) $150 \times 5 \times 1$ cm^3 bar $\rightarrow \Lambda_{\text{Eff}} = 184 \pm 8$ cm

Figure 6.14: Normalized MPVs with respect to the bar trigger position, where (a) corresponds to a $50 \times 3 \times 1$ cm^3 bar readout by 1 SiPM/side, while (b) shows a $150 \times 5 \times 1$ cm^3 bar readout by 2 SiPMs/side. Both curves are fitted with exponential functions, resulting to effective attenuation lengths of (a) $\Lambda_{\text{Eff}} = 55 \pm 2$cm and (b) $\Lambda_{\text{Eff}} = 184 \pm 6$cm, respectively. Both configurations refer to bars of rectangular shape.

In Tab. 6.4, the effective attenuation length values determined from their respective exponential fit functions are presented, along with a general overview of all examined bar geometries, scintillator types and SiPM readouts. Moreover, the effective attenuation percentage from left-to-right bar ends is also shown, in order to highlight the light fraction that successfully propagates from one side to the other. As a general comment, the average percentage of all tested configurations is measured around ~ 50 % within uncertainties. All results are found to be compatible with the length of every tested bar ranging from 50 to

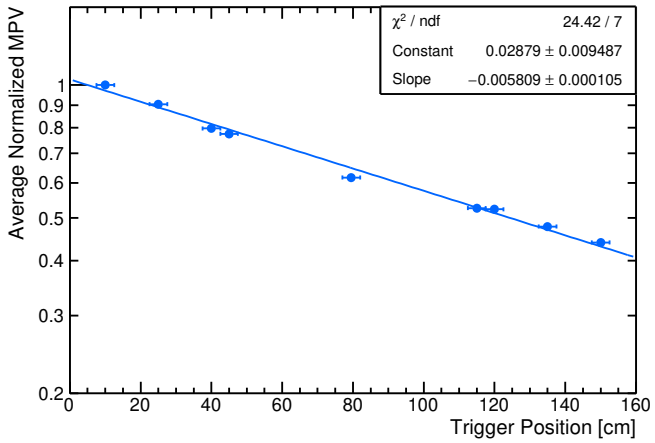

(c) 160 × 3 × 0.5 cm^3 bar → $\Lambda_{\text{Eff}} = 172 \pm 4$ cm

Figure 6.14: (Continued) Normalized MPVs with respect to the bar trigger position, where (c) illustrates a 160 × 3 × 0.5 cm^3 bar readout by 2 SiPMs/side. The data are fitted with an exponential function (its Y-axis plotted in logarithmic scale), resulting to an effective attenuation lengths of $\Lambda_{\text{Eff}} = 172 \pm 4$cm. It should be noted that this particular configuration corresponds to a bar of trapezoidal shape.

160 cm, thus showing a strong association of the effective light attenuation length with the bar geometry. Consequently, the entirety of PSD bar materials and overall configurations could be a viable option towards the PSD realization, with the final decision being a trade-off between readout channels and bar robustness in space conditions.

Table 6.4: Measurements overview for selected PSD bar configurations

Bar size [cm^3]	Scintillator	SiPM model	Λ_{Eff} [cm]	L-to-R end [%]
50 × 3 × 1	EJ-200	ASD-NUV3S	55 ± 2	50
150 × 5 × 1	BC-404	ASD-NUV3S	184 ± 8	49
160 × 3 × 0.5	EJ-204	S14160-3015PS	172 ± 4	44

Concerning the SiPM selection, impressive results have been acquired from both Hamamatsu models (S13 and S14 series) regarding their overall response to dark counts as well as their performance in low-energy electron and CR muon detection. Given the PSD design requirements, the S14160-3015PS model with 40000 microcells and low DCR should be an appropriate option in order to satisfy a large dynamic range and maintain good linearity. Furthermore, an additional SiPM model focusing on larger microcell size, fill factor and consequently larger PDE, should be a valuable addition to the scintillator readout. This can be

S13360-3025CS, given its good overall performance and low noise, as well as a possible, larger cell alternative which could combine an increased PDE with a decreased DCR. The proposed SiPM readout should include at least one module focusing on an increased dynamic range as well as one oriented towards a larger detection efficiency, on each instrumented side. This setup should satisfy an abundance in readout channels (aside from performance prerequisites) given its importance for a space mission.

6.7 Beam test campaigns at CERN

The optimal HERD layout is evaluated by a series of beam tests, with one of the latest being performed in two campaigns, taking place at CERN SPS (Fig. 6.15a) and PS (Fig. 6.15b) during the months of October/November 2021. Such an endeavor led to systematic performance tests of the individual sub-detector prototypes along with an integrated assessment of HERD as a whole. Each prototype was exposed to beams of electrons, muons, protons and pions in a range of 10 GeV to a few hundred GeV ($E_{Max} \sim 350$ GeV) with varying beam cross sections.

Two PSD layouts were tested in said campaigns, namely a PSD bar and tile prototype. The tile PSD prototype was based on a single layer of 20 scintillator tiles organized in an array of 4×5 elements (each one of $10\,cm \times 10\,cm \times 0.5\,cm$, in dimensions). The tiles, wrapped with a sheet of Tyvek, were read out by two PCB, each one embedding 3 SiPMs in *or-logic*. In the prototype, the two readout options for tiles were adopted. The total prototype dimension amounts to $57.8 \times 64.5 \times 25$ cm^3, with a common detection area of 0.25 m^2.

Concerning the bar prototype, a total of 19 trapezoidal-shaped scintillators (EJ-200 and BC-404) were arranged in two, orthogonally interleaved layers with various wrapping selections. The trapezoidal bar geometry increases the hermeticity of adjacent units and is favorable against the conventional, rectangular layout (as seen in Fig. 6.17). The specific angle selected is 45° (extracted from MC simulations) providing the smallest possible fraction of events lost, in a wide range of impinging particle angles. The individual bar dimensions are $50 \times 4 \times 1$ cm^3 (for horizontally-inclined bars) and $50 \times 3 \times 0.5$ cm^3 (for vertically-inclined bars). Regarding the prototype readout, single PCBs will be housing 2 MPPC S14160-3015PS per side in *or-logic* (with an *and-logic* regarding the full bar), covering all performance requisites (high dynamic range, good linearity, high

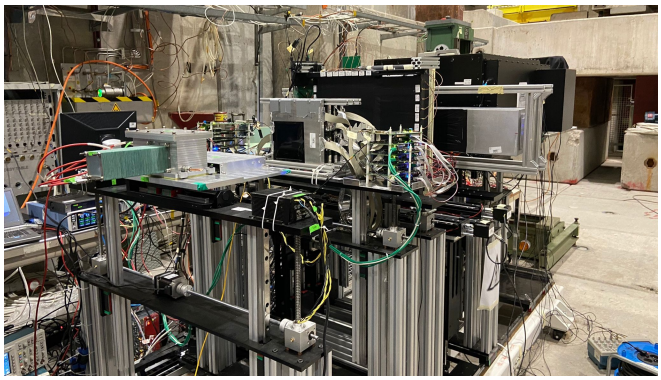

(a)

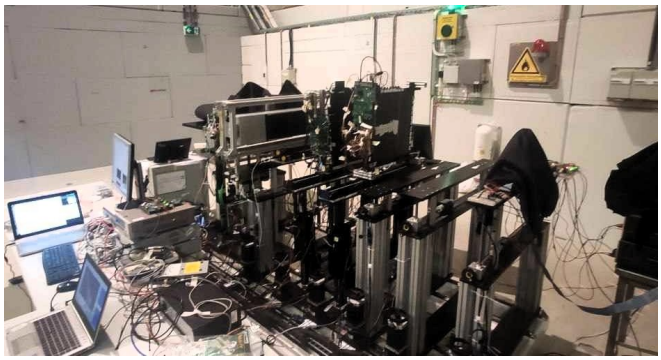

(b)

Figure 6.15: HERD sub-detector configurations at CERN (a) SPS and (b) PS beam test facilities, in Oct/Nov 2021. From [118, 125].

PDE, low DCR and crosstalk). The total prototype dimension amounts to 61.4 x 61.4 x 66.8 cm^3 with a common detection area of 0.25 m^2. Both tile and bar prototypes adopted the same read-out system, based on the CAEN Citiroc-based board DT5550W [144].

A few pictures illustrating the prototype configuration process are presented in Fig. 6.16. Following an initial purification and wrapping stage of individual bars, 2 PCBs housing 2 SiPMs each are coupled to the bar ends with an optical adhesive, in order to maximize efficiency and minimize photon losses. Afterwards, all SiPMs are shielded from external light with 3-D printed end caps of trapezoidal shape, which increase their robustness while assisting in the overall prototype hermeticity. Then, every bar is individually tested and calibrated in order to provide balanced charge response from side to side while being shielded from exterior light. In that sense, an important feature of this work was to verify the stability of each individual configuration by evaluating its core performance aspects. Some of the examined parameters were: light uniformity, photon yield

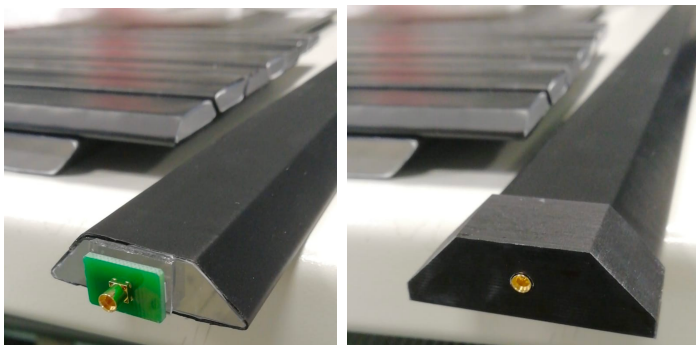

(a) (b)

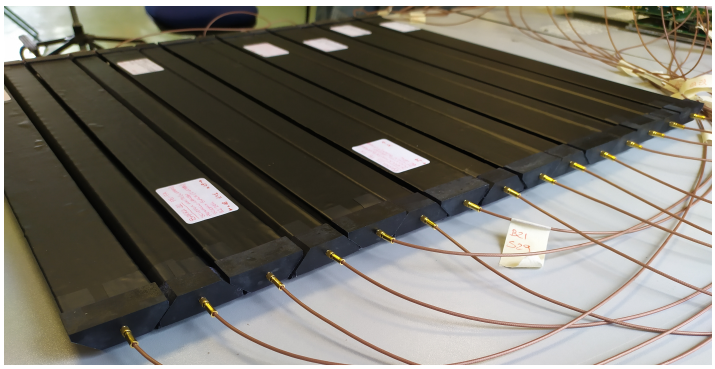

(c)

Figure 6.16: Selected pictures illustrating part of the process corresponding to the PSD bar assembly.

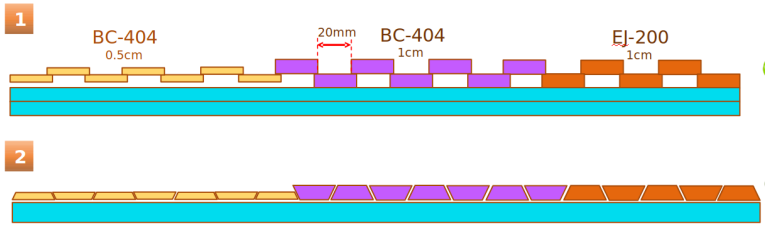

Figure 6.17: Schematic view representing a comparison between the conventional rectangular bar geometry (top) and the newly-introduced trapezoidal geometry (bottom).

and attenuation effects along the bar, taking into account inherent detector characteristics such as the PDE, optimal operational voltage selection, dark count rate (DCR) and cross-talk effects.

The full prototype mounted at the CERN SPS and PS facilities can be viewed in Fig. 6.18. For the sake of simplicity, the bar prototype was mapped out in order to assist in beam impact point identification due to its interleaved layout. In the following sub-sections, a selected sample of measurements will be presented,

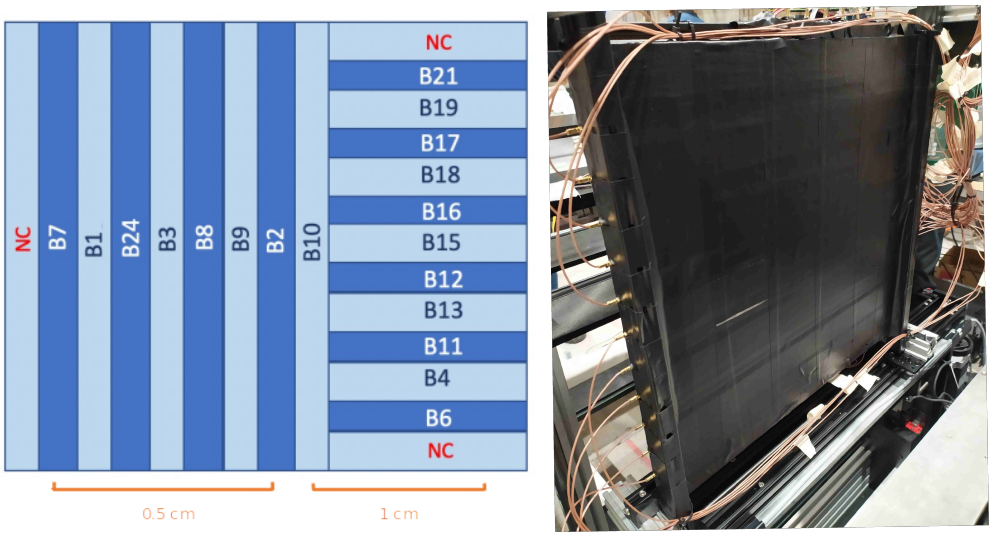

(a) (b)

Figure 6.18: (a) General prototype mapping where bars of $50 \times 4 \times 1$ cm^3 (horizontal) and $50 \times 3 \times 0.5$ cm^3 (vertical) are orthogonally arranged in a grid, readout by 2 SiPMs/side. (b) Final form of the PSD bar prototype, mounted at the CERN SPS and PSD facilities.

pertaining to measurements of protons and electrons at energies of 100 to 350 GeV in SPS, as well as pions (π^+ and π^-) at energies of 10 GeV in PS facilities.

For each set of measurements acquired, comparisons between different particle beams (electrons, protons, pions) have been performed, along with an evaluation of the overall configuration response with respect to the beam position. A complete map of hits corresponding to the various particle beams at SPS and PS campaigns is illustrated in Fig. 6.19, where different color codes represent the various particle beams impinging on the detector. Additional cross-checks between scintillator types and wrapping materials are obtained in order to figure out possible performance variances.

Finally, all charge distributions corresponding to horizontal and vertical bars were fitted with LanGaus functions (as discussed previously) and analyzed with respect to the beam position (also referred to as trigger position) in order to be compared with the rest of trapezoidal bars in the prototype, as well as with rectangular bars of the same size tested in laboratory conditions with CR muons.

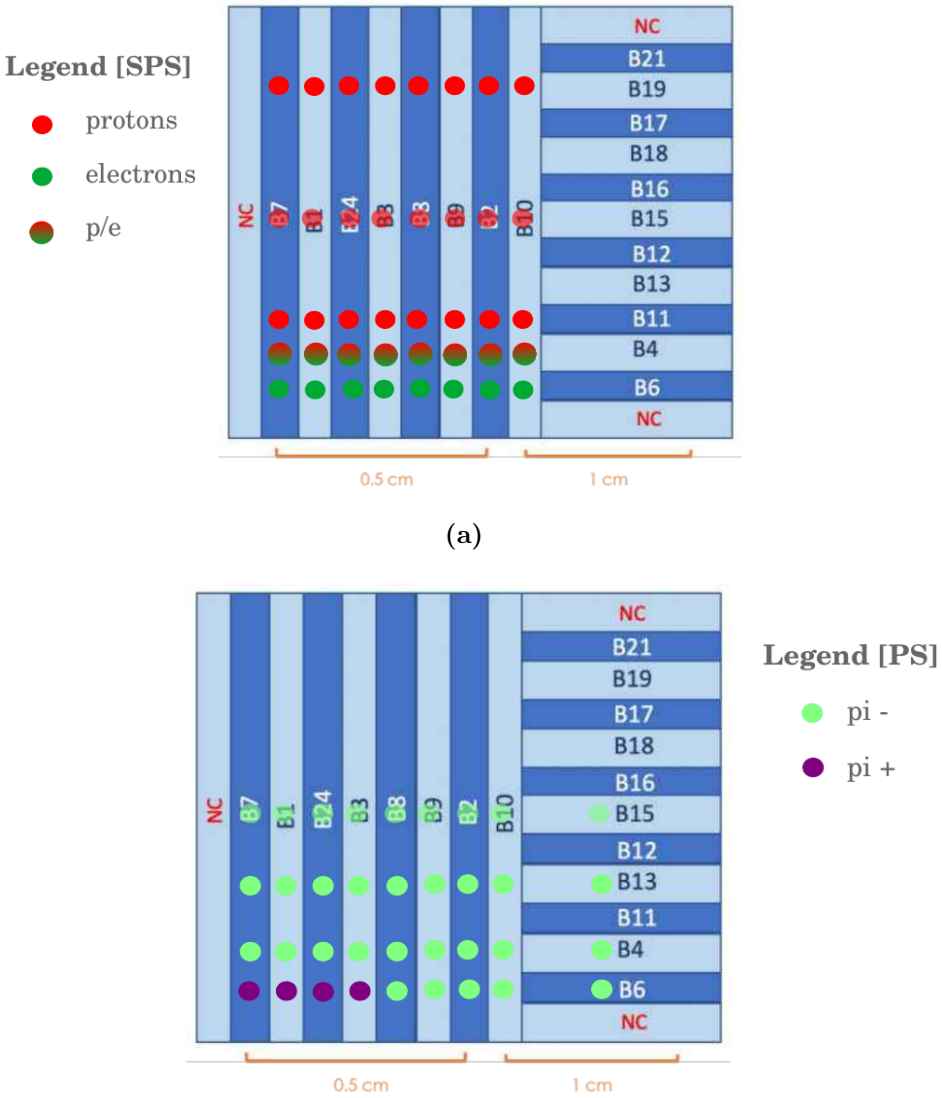

Figure 6.19: Beam positions corresponding to data acquisitions in CERN (a) SPS and (b) PS facilities. The various colors refer to impinging particles on a given trigger point, as dictated by the legends on each side. In the case of SPS data, overlapping measurements of protons and electrons are shown in a mixture of red and green colors.

6.7.1 CERN SPS and PS results

For the sake of simplicity, a single beam point will be adopted as reference. Said point corresponds to the exact beam position, derived by a hit intensity map built-in the CAEN DAQ board software. Consequently the beam was detected by both sides simultaneously, with the resulting signal distributions being evident in Fig. 6.20.

In Fig. 6.20, the results of protons, electrons and pions are presented, for the horizontal bar under test. Specifically, the bar refers to an EJ-204 scintillator of $50 \times 4 \times 1$ cm^3 in dimension, readout by 2 MPPC S14160-3015PS per side, with a bias voltage of approximately 42.75 V and a high gain (HG) value of 60, imposed by the readout board. Concerning the beam energies, the selected charge distributions shown correspond to protons of 350 GeV, electrons of 150-250 GeV and pions (π^-) of 10 GeV.

All sets of charge measurements present good overall consistency (as expected due to $Z = 1$ and MIP energies). For the case of electron spectra, two peaks can be evident towards 12 - 14·10^3 ADC, the first of which possibly signaling the concurrent detection of two electrons, while the second can be attributed to saturation effects of the readout electronics due to the high gain applied. It should be stressed that the selected high gain was significantly elevated in order to gauge possible differences in the spectra of singly-charged particle beams (protons, electrons and pions) and compare the responses of various bars, since no test on the dynamic range was intended in this configuration. As discussed in detail throughout the chapter, all charge contributions derived from the various beam positions are fitted with LanGaus functions in order to determine the behavior of light propagating through the bars. A complete analysis on vertical and horizontal bars has been performed, according to the collective results of proton, electron and pion beams. The results are shown in Fig. 6.21, where horizontal and vertical bars are distinguished in order to provide a clearer picture concerning the comparison between the two. All MPVs acquired from their respective fits are normalized to unity.

Exponential fits were applied to every curve, with an average value on the effective light attenuation length being measured for the case of horizontal and vertical bars, individually. These results are summarized in Fig. 6.22. Following the individual fits on the behavior of each bar with respect to the beam position, a mean value of all effective attenuation lengths for horizontal and vertical bars alike, amounts to $\Lambda_{\text{Eff}} = 45 \pm 3$ cm and $\Lambda_{\text{Eff}} = 43 \pm 5$ cm, respectively. Evidently,

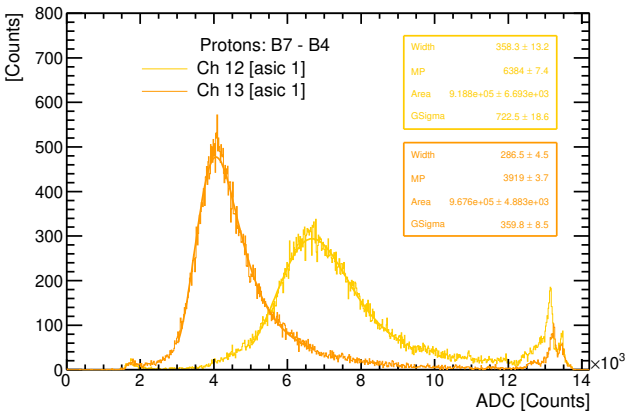

(a) Protons - horizontal bar (B4)

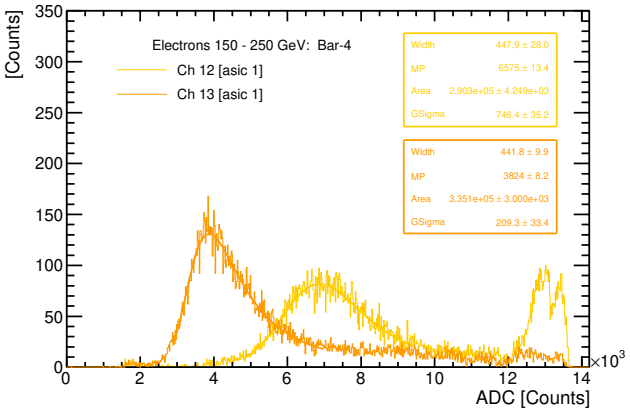

(b) Electrons - horizontal bar (B4)

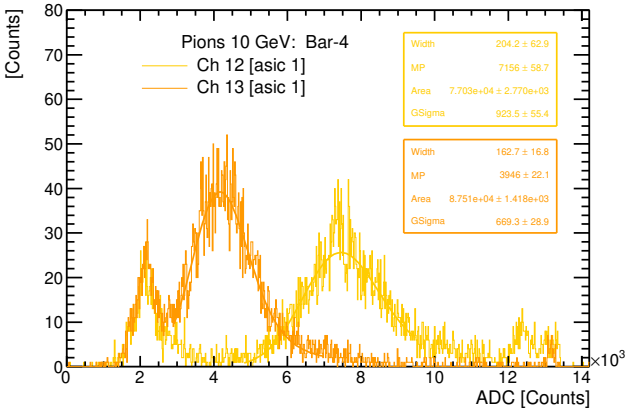

(c) Pions - horizontal bar (B4)

Figure 6.20: Charge spectra (in ADC) derived from the High Gain (HG) channel of the CAEN readout board, referring to measurements of (a) protons at 350 GeV, (b) electrons at 150 - 250 GeV and (c) pions at 10 GeV. The same bar is investigated for all three measurements, namely the B4 (horizontal) configuration, readout by 2 SiPMs/side with each SiPM side corresponding to yellow (upper SiPMs) and orange (lower SiPMs) colors respectively.

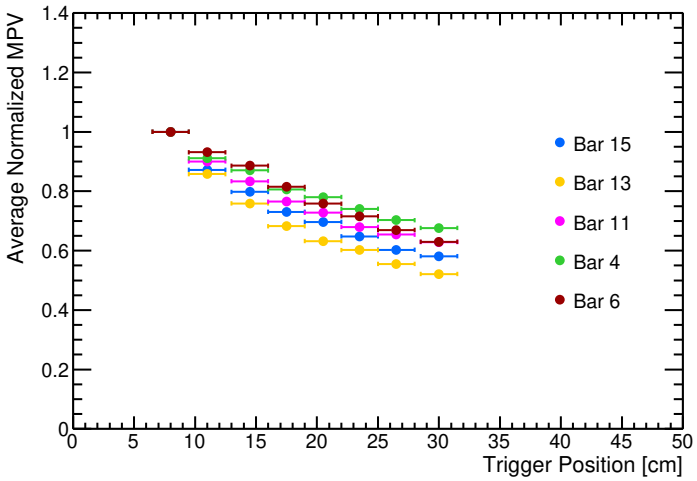

(a) Results on horizontal bars

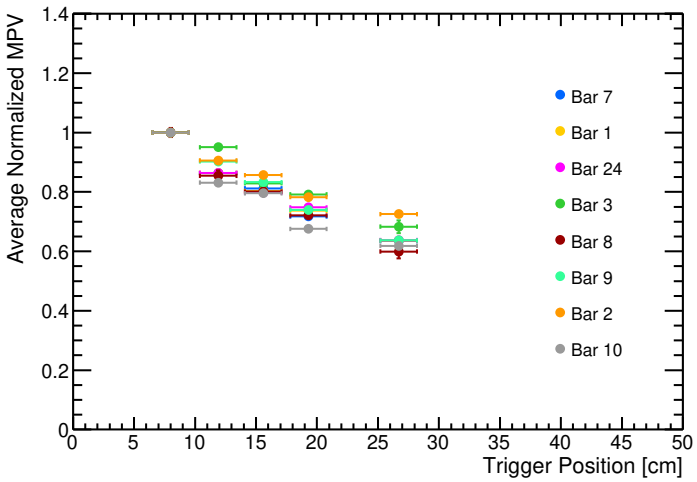

(b) Results on vertical bars

Figure 6.21: Normalized MPVs with respect to the beam (trigger) position for the case of (a) horizontal and (b) vertical bars concerning the PSD bar prototype. The shape of horizontal and vertical bars is: $50 \times 4 \times 1$ cm^3 and $50 \times 3 \times 0.5$ cm^3, respectively.

both horizontal and vertical bar geometries are in good agreement, with their effective attenuation length corresponding to the bar length.

All tested configurations are on par with an effective attenuation length close to the bar length under investigation, thus proving as viable options towards the PSD realization. Results stemming from both CERN test beam campaigns, prove the effectiveness of the novel trapezoidal geometry, both in the case of short (50 cm) and long (160 cm) bars, thus providing a compelling solution in addressing hermeticity issues.

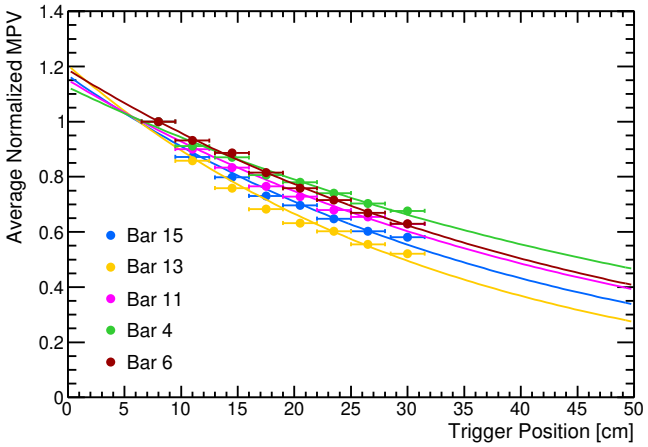

(a) Results on horizontal bars

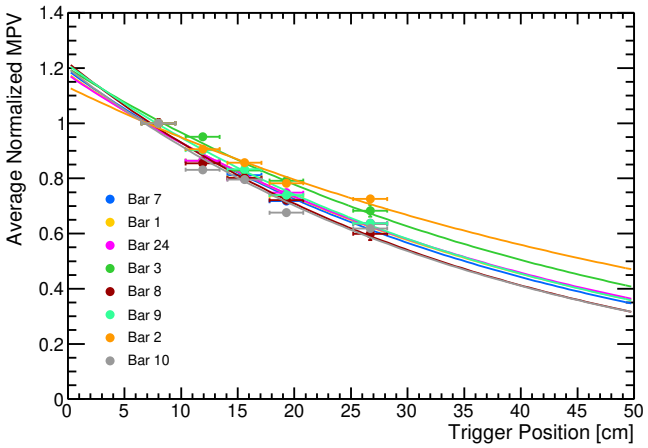

(b) Results on vertical bars

Figure 6.22: Normalized MPVs with respect to the beam (trigger) position for the case of (a) horizontal and (b) vertical bars concerning the PSD bar prototype. Colored lines correspond to exponential fits, extrapolated to the full length of each bar.

6.8 Summary

This work is associated to the study and optimization of the Plastic Scintillator Detector, being a sub-detector designed for the HERD space mission. Specifically, the examined layout concerned scintillator bars of various sizes and geometries, readout by a number of versatile SiPMs.

Main activities included the design, preparation and test regarding a multitude of bar configurations, thoroughly tested with CR muons and electrons from ^{90}Sr radioactive sources at INFN-LNGS, along with particle beams from accelerator tests at CERN SPS and PS facilities. All tested scintillator types yielded good

response under a variety of particles and energies, in conjunction to diverse SiPM models, covering a wide range of performance requirements. Part of this work pertained to the study of the effective light propagation across PSD bars, coupled with hermeticity studies that led to a novel instrumentation of trapezoidal PSD bars in various sizes. The attenuation effects were found to be low enough, since in each tested configuration at least 50 % of the emitted scintillation light was detected from one bar end to the other, thus displaying good overall performance.

Said measurements were verified by CR muons and low-energy electrons from radioactive sources, leading to precises photon measurements in a multitude of trigger positions along a variety of bars under test. The proposed PSD configuration should have a mechanically robust geometry to sustain launch vibrations and prolonged deterioration effects due to radiation damage. Moreover, the bar length, width and thickness should be adjusted accordingly, to fit all space mission requirements. The newly-introduced trapezoidal geometry should be considered towards the PSD realization since it ensures exceptional hermeticity between PSD bars and minimal event losses when charged radiation interacts with the detector under a given angle.

As for the SiPM readout, the majority of tests performed at LNGS and CERN have shown that a combination of small and large microcell SiPMs is necessary in order to achieve both a high PDE while maintaining good dynamic range and linearity. The selected sensors should be robust for use in space applications and exhibit the lowest possible percentage of noise effects (dark counts, cross-talk, afterpulses) in order to ensure high-quality measurements over an extended mission lifetime. Additionally, given the importance of module redundancy in space missions, every PSD bar side should be instrumented at least with a set of small/large microcell sensors, in order to ensure stable and efficient measurements in case of sensor damage, but also covering a large dynamic range without reductions in detection efficiency.

Conclusions

The work presented in this thesis pertained to the detection and study of Galactic Cosmic Rays with the DAMPE space mission and the future HERD project. In the first chapter, a general introduction to cosmic rays was provided, focusing mainly on highly-energetic particles originating in the Galaxy. A brief overview to the intricate acceleration and propagation mechanisms has be given, in order to shed light on the various aspects governing the final CR spectra of primary and secondary CRs arriving at Earth. These particles are subsequently detected by space- or ground-based detectors. A short introduction to past and current experiments is provided towards the end of the chapter, in order to highlight some of the main representatives of direct CR detection.

The DAMPE mission was illustrated in the second chapter, with a detailed look on its various sub-detectors, scientific objectives and recent CR results. The detector was launched on December 17th, 2015 and has been in smooth data acquisition ever since. The following two chapters (Chap. 3 and 4) were dedicated to precise spectral measurements of carbon and oxygen nuclei (being the main focus of this work), along with complimentary insights on their respective flux ratios i.e., C/O, B/C and B/O.

The complete analysis procedure concerning carbon and oxygen nuclei has been presented in Chapter 3. Six years of DAMPE flight data were analyzed in this work, coupled to a wide range of MC simulated carbon and oxygen samples (100 GeV - 500 TeV). Both flight and simulated data were subjected to a thorough list of analysis-specific selection cuts, in order to ensure the purity of all analyzed datasets. Furthermore, a detailed background measurement was carried out in order to gauge the contribution of neighboring (to carbon and oxygen) nuclei and consequently delineate the final limits concerning their respective charge selection. Finally, efficiency calculations and validations for the majority of analysis cuts were performed, in order to assess their accuracy and ensure a good agreement between flight and simulated data.

The fourth chapter focuses on the spectral measurement of carbon and oxygen nuclei from 10 GeV/n to 25 and 10 TeV/n, respectively, thus determining the core of this work. For both spectra, a hardening feature is evident at energies of approximately $300-500$ GeV/n, the shape of which is consistent with observations from previous and current CR experiments. This feature can be explained either by a break in the overall spectrum of injected CRs in the ISM or due to possible features in the CR propagation mechanism. Such features invalidate the conventional picture involving a universal injection spectrum at the sources and a single, featureless power-law spectrum extending up to PeV energies, as predicted by prevalent CR models.

Furthermore, a crucial DAMPE objective refers to the extension of such measurements at higher energies, with great accuracy and low systematics. In that case, new results have been presented in the multi-TeV/n region, where evidence of a spectral softening has been presented in carbon data, at an energy of approximately 7.5 TeV/n (or 90 TeV, or 15 TV). This result is prominent in the case of carbon, but could also be expected for the case of oxygen. This softening feature is consistent with a rigidity-dependent acceleration of particles at the sources and can be well described by a broken power-law spectrum, the significance of which is measured at 5σ. Moreover, this insightful result is in accordance with previous DAMPE published results for proton and helium nuclei, with softening features identified at energies of 13.6 and 34 TeV respectively, complimenting the latest results on carbon and oxygen fluxes.

A supplemental aspect of this work is associated to flux ratios such as carbon-over-oxygen (C/O) ratio, as well as secondary-over-primary ratios like boron-over-carbon (B/C) and boron-over-oxygen (B/O), being valuable probes concerning the diffusion and propagation mechanism of CRs in the Galaxy. Starting with C/O, an important consistency has been shown with the majority of published results especially in lower energies, while extending in the TeV/n region with great accuracy. Then for B/C and B/O flux ratios, new results have been published in the energy range of 10 GeV/n to approximately 5.6 TeV/n, showing an excellent agreement with published results in energies up to few hundred GeV/n. Interestingly, above energies of 100 - 200 GeV/n a break is detected for the first time in both flux ratios, which extends to TeV/n energies.

Following a selection of various spectral fits, it became evident that a broken power-law function accurately represents the flux ratio data, instead of a single power-law spectrum. These results have great implications on the propagation

mechanism of Galactic CRs, with a variety of theoretical models being employed towards its precise interpretation. Favorable explanations could be attributed to a possible break in the diffusion coefficient, without excluding additional CR models or even a mixture between some of them. In conclusion, the main point stemming from B/C and B/O data pertains to the dismissal of possible interpretations attributed to acceleration effects concerning the spectral hardening in CR protons [108], as shown by direct observations of space-borne experiments in recent years.

The entirety of results discussed above, pave the way for a new generation of measurements, oriented towards higher energies with great accuracy and low systematic uncertainties. Features such as the spectral softening found in carbon data can be discussed with even greater precision by future space-borne detectors, shedding light in open questions concerning the origin, acceleration and propagation mechanisms of CRs in the Universe. Taking into account the fruitful and long-standing experience of DAMPE in orbit, coupled with the experience gained from the various challenges that always accompany a space mission, a complementary part of this work is dedicated to the development and realization of a novel CR detector. Forthcoming space–borne experiments should combine an increased geometric factor (> 1 m^{2}sr), with extended mission duration (≥ 10 yr), along with high discrimination power in separating different cosmic radiation components. One of the prominent detectors proposed to address the majority of requirements mentioned above is the High Energy cosmic-Radiation Detection (HERD) facility, the prospects of which were presented in Chapters 5 and 6.

The main design parameters and scientific objectives of HERD are presented in the fifth chapter. HERD is expected to be installed on–board the China Space Station (CSS) around 2027, with a projected duration of approximately 10 years. One of its main goals is to provide accurate measurements of CR energy spectra up to the highest achievable energies in space ($\sim$ few PeV), thus probing the inherent characteristics of possible individual CR "knees" for the first time, directly. Moreover, scientific objectives revolving around gamma-ray astronomy and transient studies, along with indirect searches for dark matter are important towards the design of HERD. The payload is uniquely configured to accept particles from both its top and four lateral sides. Due to its novel design, an order of magnitude increase in geometric acceptance is foreseen, compared to current generation experiments.

The sixth (and last) chapter is dedicated to the study, design and optimization of the HERD PSD, a sub-detector purposed as a means of discriminating incident

photons from charged particles, while being capable of identifying incoming cosmic–ray nuclei in a range of $Z = 1 - 26$. Main goal of this work is to define the optimal PSD bar layout, starting from the study, configuration and test of bar prototypes involving different scintillator sizes and materials along with a variety of SiPMs covering all necessary requirements for a space mission. A multitude of bar configurations were thoroughly tested with CR muons and electrons from ^{90}Sr radioactive sources at INFN-LNGS, along with particle beams from accelerator tests at CERN SPS and PS facilities.

All tested scintillator types yielded good response under a variety of particles and energies, in conjunction to diverse SiPM models, covering a wide range of performance requirements. Part of this work pertained to the study of the effective light propagation across PSD bars, coupled with hermeticity studies that led to a novel instrumentation of trapezoidal PSD bars in various sizes. The attenuation effects were found to be low enough, since in each tested configuration at least 50 % of the emitted scintillation light, was detected from one bar end to the other, thus displaying good overall performance. The proposed PSD configuration should have a mechanically robust geometry to sustain vibrations from the launch and prolonged deterioration effects due to radiation damage. Consequently, the bar length, width and thickness should be adjusted accordingly, to fit the space mission requirements. Additionally, the newly-introduced trapezoidal geometry should be considered towards the PSD realization since it ensures exceptional hermeticity between PSD bars and minimal event losses when charged radiation interacts with the detector under a given angle.

As for the SiPM readout, the majority of tests performed at LNGS and CERN have shown that a combination of small and large microcell SiPMs is necessary in order to achieve both a high PDE while maintaining good dynamic range and linearity. The selected sensors should be robust for use in space applications and exhibit the lowest possible percentage of noise effects (dark counts, cross-talk, afterpulses) in order to ensure high-quality measurements over an extended mission lifetime. Additionally, given the importance of module redundancy in space missions, every PSD bar side should be instrumented at least with a set of small/large microcell sensors, in order to ensure stable and efficient measurements in case of sensor damage, but also covering a large dynamic range without reductions in detection efficiency.

References

[1] Henri Becquerel. "Sur les radiations émises par phosphorescence". In: *Comptes rendus de 1'Academie des Sciences, Paris* 122 (1896), pp. 420–421.

[2] Theodor Wulf. "On the radiation of high penetrating power that exists in the atmosphere". In: *Phys. Zeit* 1.152-157 (1909), p. 124.

[3] Domenico Pacini. "La radiazione penetrante alla superficie ed in seno alle acque". In: *Il Nuovo Cimento (1911-1923)* 3.1 (1912), pp. 93–100.

[4] Victor F Hess. "Observations in low level radiation during seven free balloon flights". In: *Phys. Zeit* 13.1084-1091 (1912), p. 24.

[5] Victor Hess. "On the observations of the penetrating radiation during seven balloon flights". In: *arXiv preprint arXiv:1808.02927* (2018).

[6] Janet Clay. "The nature of cosmic rays". In: *Proceedings of the Royal Society of London. Series A-Mathematical and Physical Sciences* 151.872 (1935), pp. 202–210.

[7] Arthur H Compton. "Cosmic rays as electrical particles". In: *Physical Review* 50.12 (1936), p. 1119.

[8] Luis Alvarez and Arthur H Compton. "A positively charged component of cosmic rays". In: *Physical Review* 43.10 (1933), p. 835.

[9] Thomas H Johnson. "The azimuthal asymmetry of the cosmic radiation". In: *Physical Review* 43.10 (1933), p. 834.

[10] Bruno Rossi. "Directional measurements on the cosmic rays near the geomagnetic equator". In: *Physical Review* 45.3 (1934), p. 212.

[11] Luca Baldini. *Space-Based Cosmic-Ray and Gamma-Ray Detectors: a Review.* 2014.

[12] Roberto Aloisio et al. "Selected Topics in Cosmic Ray Physics". In: *Multiple Messengers and Challenges in Astroparticle Physics.* Cham: Springer International Publishing, 2018, pp. 1–95. ISBN: 978-3-319-65425-6.

[13] Alessandro De Angelis and Mário Pimenta. *Introduction to particle and astroparticle physics: multimessenger astronomy and its particle physics foundations.* Springer, 2018.

[14] Claus Grupen. *Astroparticle physics.* Springer Science & Business Media, 2005.

[15] Carmelo Evoli. *The Cosmic-Ray Energy Spectrum.* 2020.

[16] W.D. Apel et al. "Energy spectra of elemental groups of cosmic rays: Update on the KASCADE unfolding analysis". In: *Astroparticle Physics* 31.2 (2009), pp. 86–91. ISSN: 0927-6505.

[17] Elena Amato. "The origin of galactic cosmic rays". In: *International Journal of Modern Physics D* 23.07 (2014), p. 1430013.

[18] R. L. Workman et al. "Review of Particle Physics". In: *PTEP* 2022 (2022), p. 083C01.

[19] Katia M. Ferrière. "The interstellar environment of our galaxy". In: *Rev. Mod. Phys.* 73 (4 2001), pp. 1031–1066.

[20] D.H. Perkins. *Particle Astrophysics, Second Edition*. Oxford Master Series in Physics. OUP Oxford, 2008. ISBN: 9780199545469.

[21] Malcolm S Longair. *High energy astrophysics*. Cambridge university press, 2011.

[22] Roger John Tayler. *The stars: their structure and evolution*. Cambridge University Press, 1994.

[23] E. E. Salpeter. "Nuclear Reactions in Stars Without Hydrogen." In: *The Astrophysical Journal* 115 (March 1952), pp. 326–328.

[24] Enrico Fermi. "On the Origin of the Cosmic Radiation". In: *Phys. Rev.* 75 (8 1949), pp. 1169–1174.

[25] Enrico Fermi. "Galactic Magnetic Fields and the Origin of Cosmic Radiation." In: *The Astrophysical Journal* 119 (1954), pp. 1–46.

[26] L O'C Drury. "An introduction to the theory of diffusive shock acceleration of energetic particles in tenuous plasmas". In: *Reports on Progress in Physics* 46.8 (1983), p. 973.

[27] TG Guzik et al. "The ATIC long duration balloon project". In: *Advances in Space Research* 33.10 (2004), pp. 1763–1770.

[28] HS Ahn et al. "The cosmic ray energetics and mass (CREAM) instrument". In: *Nuclear Instruments and Methods in Physics Research Section A: Accelerators, Spectrometers, Detectors and Associated Equipment* 579.3 (2007), pp. 1034–1053.

[29] O Adriani et al. "The PAMELA Mission: Heralding a new era in precision cosmic ray physics". In: *Physics Reports* 544.4 (2014), pp. 323–370.

[30] WB Atwood et al. "The large area telescope on the Fermi gamma-ray space telescope mission". In: *The Astrophysical Journal* 697.2 (2009), p. 1071.

[31] M Aguilar et al. "The Alpha Magnetic Spectrometer (AMS) on the International Space Station: Part I–results from the test flight on the space shuttle". In: *Physics Reports* 366.6 (2002), pp. 331–405.

[32] PS Marrocchesi, Calet Collaboration, et al. "CALET: A calorimeter-based orbital observatory for High Energy Astroparticle Physics". In: *Nuclear Instruments and Methods in Physics Research Section A: Accelerators, Spectrometers, Detectors and Associated Equipment* 692 (2012), pp. 240–245.

[33] Shoji Torii et al. "The CALorimetric Electron Telescope (CALET): high energy astroparticle physics observatory on the International Space Station". In: *Proceedings of Science, ICRC2015* 34 (2015), pp. id–581.

[34] Qea An et al. “Measurement of the cosmic ray proton spectrum from 40 GeV to 100 TeV with the DAMPE satellite”. In: *Science advances* 5.9 (2019), eaax3793.

[35] F. Alemanno et al. “Measurement of the Cosmic Ray Helium Energy Spectrum from 70 GeV to 80 TeV with the DAMPE Space Mission”. In: *Phys. Rev. Lett.* 126 (20 2021), p. 201102.

[36] H. S. Ahn et al. “ENERGY SPECTRA OF COSMIC-RAY NUCLEI AT HIGH ENERGIES”. In: *The Astrophysical Journal* 707.1 (2009), p. 593.

[37] O. Adriani et al. “MEASUREMENT OF BORON AND CARBON FLUXES IN COSMIC RAYS WITH THE PAMELA EXPERIMENT”. In: *The Astrophysical Journal* 791.2 (2014), p. 93.

[38] D. Karmanov et al. “Spectra of cosmic ray carbon and oxygen nuclei according to the NUCLEON experiment”. In: *Physics Letters B* 811 (2020), p. 135851. ISSN: 0370-2693.

[39] O. Adriani et al. “Direct Measurement of the Cosmic-Ray Carbon and Oxygen Spectra from 10 GeV/n to 2.2 TeV/n with the Calorimetric Electron Telescope on the International Space Station”. In: *Phys. Rev. Lett.* 125 (25 2020), p. 251102.

[40] M. Aguilar et al. “The Alpha Magnetic Spectrometer (AMS) on the international space station: Part II — Results from the first seven years”. In: *Physics Reports* 894 (2021). The Alpha Magnetic Spectrometer (AMS) on the International Space Station: Part II - Results from the First Seven Years, pp. 1–116. ISSN: 0370-1573.

[41] W. R. Webber and J. F. Ormes. “Cerenkov-scintillation counter measurements of nuclei heavier than helium in the primary cosmic radiation: 1. Charge composition and energy spectra between 200 Mev/nucleon and 5 bev/nucleon”. In: *Journal of Geophysical Research* 72 (1967), pp. 5957–5976.

[42] W. R. Webber and S. M. Yushak. “Comparative Energy Spectra of Z=3-8 Nuclei in the Energy Range 200 Mev/nuc to 3 Gev/nuc”. In: *International Cosmic Ray Conference* 12 (1979), p. 51.

[43] J. Buckley et al. “A new measurement of the flux of the light cosmic-ray nuclei at high energies”. In: *ApJ* 429 (1994), pp. 736–747.

[44] A. D. Panov et al. “Relative abundances of cosmic ray nuclei B-C-N-O in the energy region from 10 GeV/n to 300 GeV/n. Results from ATIC-2 (the science flight of ATIC)”. In: *International Cosmic Ray Conference*. Vol. 2. International Cosmic Ray Conference. 2008, pp. 3–6. arXiv: 0707.4415.

[45] V. K. Balasubrahmanyan et al. “The Multiply Charged Primary Cosmic Radiation at Solar Minimum 1965”. In: *Journal of Geophysical Research* 71 (1966), p. 1771.

[46] T. T. von Rosenvinge, J. F. Ormes, and W. R. Webber. “Measurements of Cosmic-Ray Li, Be and B Nuclei in the Energy Range 100 MeV/NUC to 22 BeV/NUC”. In: *Astrophysics and Space Science* 3 (1969), pp. 80–101.

[47] E. Juliusson. “Charge Composition and Energy Spectra of Cosmic-Ray Nuclei at Energies above 20 GeV Per Nucleon”. In: *ApJ* 191 (1974), pp. 331–348.

[48] C. D. Orth et al. "Abundances and spectra for cosmic-ray nuclei from lithium to iron for 2 to 150 GeV per nucleon". In: *ApJ* 226 (1978), pp. 1147–1161.

[49] Maehl, R. C. and Ormes, J. F. and Fisher, A. J. and Hagen, F. A. "Energy spectra of cosmic ray nuclei - Z of 4 to 26 and E of 0.3 to 2 GeV/amu". In: *Astrophysics and Space Science* 47 (1977), pp. 163–184.

[50] J. A. Lezniak and W. R. Webber. "The charge composition and energy spectra of cosmic-ray nuclei from 3000 MeV per nucleon to 50 GeV per nucleon". In: *ApJ* 223 (1978), pp. 676–696.

[51] J. H. Derrickson et al. "A measurement of the absolute energy spectra of galactic cosmic rays during the 1976-77 solar minimum". In: *International Journal of Radiation Applications and Instrumentation D Nuclear Tracks and Radiation Measurements* 20 (1992), pp. 415–421.

[52] M. Simon et al. "Energy spectra of cosmic-ray nuclei to above 100 GeV per nucleon". In: *ApJ* 239 (1980), pp. 712–724.

[53] M. Aguilar et al. "Precision Measurement of the Boron to Carbon Flux Ratio in Cosmic Rays from 1.9 GV to 2.6 TV with the Alpha Magnetic Spectrometer on the International Space Station". In: *Phys. Rev. Lett.* 117 (23 2016), p. 231102.

[54] H. S. Ahn et al. "Energy Spectra of Cosmic-ray Nuclei at High Energies". In: *ApJ* 707 (2009), pp. 593–603. arXiv: 0911.1889 [astro-ph.HE].

[55] D. Mueller et al. "Energy spectra and composition of primary cosmic rays". In: *ApJ* 374 (1991), pp. 356–365.

[56] N. Durgaprasad et al. "Chemical Composition of Relativistic Cosmic Rays Detected above the Atmosphere". In: *Physical Review D* 1 (1970), pp. 1021–1028.

[57] J. J. Engelmann et al. "Charge composition and energy spectra of cosmic-ray nuclei for elements from Be to NI - Results from HEAO-3-C2". In: *Astronomy and Astrophysics* 233 (1990), pp. 96–111.

[58] B. J. Teegarden, F. B. McDonald, and V. K. Balasubrahmanyan. "Spectra and charge composition of the low energy galactic cosmic radiation from Z=2 to 14". In: *International Cosmic Ray Conference* 1 (1970), p. 345.

[59] A. Obermeier et al. "Energy Spectra of Primary and Secondary Cosmic-Ray Nuclei Measured with TRACER". In: *ApJ* 742, 14 (2011), p. 14. arXiv: 1108.4838 [astro-ph.HE].

[60] David Maurin et al. "Cosmic-Ray Database Update: Ultra-High Energy, Ultra-Heavy, and Antinuclei Cosmic-Ray Data (CRDB v4.0)". In: *Universe* 6.8 (2020). ISSN: 2218-1997.

[61] J. Chang et al. "The DArk Matter Particle Explorer mission". In: *Astropart. Phys.* 95 (2017), pp. 6–24. arXiv: 1706.08453 [astro-ph.IM].

[62] G. Ambrosi et al. "Direct detection of a break in the teraelectronvolt cosmic-ray spectrum of electrons and positrons". In: *Nature* 552 (2017), pp. 63–66. arXiv: 1711.10981 [astro-ph.HE].

[63] A Tykhonov et al. "Internal alignment and position resolution of the silicon tracker of DAMPE determined with orbit data". In: *Nuclear Instruments and Methods in Physics Research Section A: Accelerators, Spectrometers, Detectors and Associated Equipment* 893 (2018), pp. 43–56.

[64] Yuhong Yu et al. "The plastic scintillator detector for DAMPE". In: *Astroparticle Physics* 94 (2017), pp. 1–10.

[65] Eljen Technology. *Plastic Scintillators*. https://eljentechnology.com/products/plastic-scintillators/ej-200-ej-204-ej-208-ej-212.

[66] *Hamamatsu Photonics*. https://www.hamamatsu.com/eu/en.html.

[67] Tiekuang Dong et al. "Charge measurement of cosmic ray nuclei with the plastic scintillator detector of DAMPE". In: *Astroparticle Physics* 105 (2019), pp. 31–36.

[68] Philipp Azzarello et al. "The DAMPE silicon–tungsten tracker". In: *Nuclear Instruments and Methods in Physics Research Section A: Accelerators, Spectrometers, Detectors and Associated Equipment* 831 (2016), pp. 378–384.

[69] D. Droz. "Electron Identification with Neural Networks and Measurement of the TeV Cosmic Electrons Flux with the DAMPE Experiment". PhD thesis. Geneva, Switzerland: University of Geneva, 2021.

[70] C. Perrina et al. "Performance of the DAMPE silicon-tungsten tracker during the first 5 years of in-orbit operations". In: *PoS* ICRC2021 (2021), p. 084.

[71] Giulio D'Agostini. "A multidimensional unfolding method based on Bayes' theorem". In: *Nuclear Instruments and Methods in Physics Research Section A: Accelerators, Spectrometers, Detectors and Associated Equipment* 362.2-3 (1995), pp. 487–498.

[72] H. T. Dai et al. "Response of the BGO Calorimeter to Cosmic-Ray Nuclei in the DAMPE Experiment on Orbit". In: *IEEE Transactions on Nuclear Science* 67.6 (2020), pp. 956–961.

[73] Chi Wang et al. "Offline software for the DAMPE experiment". In: *Chinese Physics C* 41.10 (2017), p. 106201.

[74] Sea Agostinelli et al. "GEANT4—a simulation toolkit". In: *Nuclear instruments and methods in physics research section A: Accelerators, Spectrometers, Detectors and Associated Equipment* 506.3 (2003), pp. 250–303.

[75] Yifeng Wei et al. "Performance of the DAMPE BGO calorimeter on the ion beam test". In: *Nuclear Instruments and Methods in Physics Research Section A: Accelerators, Spectrometers, Detectors and Associated Equipment* 922 (2019), pp. 177–184. ISSN: 0168-9002.

[76] Yong-Yi Huang et al. "Calibration and performance of the neutron detector onboard of the DAMPE mission". In: *Research in Astronomy and Astrophysics* 20.9 (2020), p. 153.

[77] Changqing Feng et al. "Design of the readout electronics for the Qualification Model of DAMPE BGO calorimeter". In: *arXiv preprint arXiv:1406.3886* (2014).

[78] Andrii Tykhonov. "Offline and CAD-GEANT4 software of the DAMPE mission". In: *XXVII International Symposium on Lepton Photon Interactions at High Energies*. Vol. 245. SISSA Medialab. 2016, p. 104.

[79] Aatos Heikkinen, Nikita Stepanov, and Johannes Peter Wellisch. "Bertini intra-nuclear cascade implementation in Geant4". In: *arXiv preprint nucl-th/0306008* (2003).

[80] Bo Andersson, G Gustafson, and Hong Pi. "The FRITIOF model for very high energy hadronic collisions". In: *Zeitschrift für Physik C Particles and Fields* 57.3 (1993), pp. 485–494.

[81] NN Kalmykov, SS Ostapchenko, and AI Pavlov. "Quark-gluon-string model and EAS simulation problems at ultra-high energies". In: *Nuclear Physics B-Proceedings Supplements* 52.3 (1997), pp. 17–28.

[82] C Baus, T Pierog, and R Ulrich. *Cosmic Ray Monte Carlo (CRMC)*. 2021.

[83] T Pierog et al. "EPOS LHC: Test of collective hadronization with data measured at the CERN Large Hadron Collider". In: *Physical Review C* 92.3 (2015), p. 034906.

[84] J Ranft. "Dual parton model at cosmic ray energies". In: *Physical Review D* 51.1 (1995), p. 64.

[85] Alfredo Ferrari et al. "FLUKA: a multi-particle transport code". In: *CERN Yellow report* 2005-10 (2005).

[86] A Archer et al. "Measurement of cosmic-ray electrons at TeV energies by VERITAS". In: *Physical Review D* 98.6 (2018), p. 062004.

[87] M Aguilar et al. "Precision Measurement of the $(e^+ + e^-)$ Flux in Primary Cosmic Rays from 0.5 GeV to 1 TeV with the Alpha Magnetic Spectrometer on the International Space Station". In: *Physical review letters* 113.22 (2014), p. 221102.

[88] S Abdollahi et al. "Cosmic-ray electron-positron spectrum from 7 GeV to 2 TeV with the Fermi Large Area Telescope". In: *Physical Review D* 95.8 (2017), p. 082007.

[89] F Aharonian et al. "Energy spectrum of cosmic-ray electrons at TeV energies". In: *Physical Review Letters* 101.26 (2008), p. 261104.

[90] F Aharonian et al. "Probing the ATIC peak in the cosmic-ray electron spectrum with HESS". In: *Astronomy & Astrophysics* 508.2 (2009), pp. 561–564.

[91] M Aguilar et al. "Precision measurement of the proton flux in primary cosmic rays from rigidity 1 GV to 1.8 TV with the Alpha Magnetic Spectrometer on the International Space Station". In: *Physical Review Letters* 114.17 (2015), p. 171103.

[92] O Adriani et al. "PAMELA measurements of cosmic-ray proton and helium spectra". In: *Science* 332.6025 (2011), pp. 69–72.

[93] AD Panov et al. "Energy spectra of abundant nuclei of primary cosmic rays from the data of ATIC-2 experiment: Final results". In: *Bulletin of the Russian Academy of Sciences: Physics* 73.5 (2009), pp. 564–567.

[94] Young Soo Yoon et al. "Proton and helium spectra from the CREAM-III flight". In: *The Astrophysical Journal* 839.1 (2017), p. 5.

[95] E Atkin et al. "New universal cosmic-ray knee near a magnetic rigidity of 10 TV with the NUCLEON space observatory". In: *JETP Letters* 108.1 (2018), pp. 5–12.

[96] M Aguilar et al. "Properties of cosmic helium isotopes measured by the Alpha Magnetic Spectrometer". In: *Physical review letters* 123.18 (2019), p. 181102.

[97] E Atkin et al. "First results of the cosmic ray NUCLEON experiment". In: *Journal of Cosmology and Astroparticle Physics* 2017.07 (2017), p. 020.

[98] L. Dorman. *Solar Neutrons and Related Phenomena*. Astrophysics and Space Science Library. Springer Netherlands, 2010. ISBN: 9789048137565.

[99] Peng-Xiong Ma et al. "A method for aligning the plastic scintillator detector on DAMPE". In: *Research in Astronomy and Astrophysics* 19.6 (2019), p. 082.

[100] J.B. Birks. "Scintillations from organic crystals: Specific fluorescence and relative response to different radiations". In: *Proceedings of the Physical Society. Section A* 64.10 (1951), pp. 874–877.

[101] PengXiong Ma et al. "Charge measurement of cosmic rays by Plastic Scintillantor Detector of DAMPE". In: *PoS* ICRC2021 (2021), p. 073.

[102] A. Ruina et al. "Charge Loss Correction in the Silicon-Tungsten Tracker-Converter for Proton-Helium Charge Identification in the DAMPE Detector". In: *PoS* ICRC2021 (2021), p. 083.

[103] J.E. Moyal. "XXX. Theory of ionization fluctuations". In: *The London, Edinburgh, and Dublin Philosophical Magazine and Journal of Science* 46.374 (1955), pp. 263–280.

[104] Chuan Yue et al. "Correction method for the readout saturation of the DAMPE calorimeter". In: *Nuclear Instruments and Methods in Physics Research Section A: Accelerators, Spectrometers, Detectors and Associated Equipment* (2020), p. 164645.

[105] Rene Brun and Fons Rademakers. "ROOT — An object oriented data analysis framework". In: *Nuclear Instruments and Methods in Physics Research Section A: Accelerators, Spectrometers, Detectors and Associated Equipment* 389.1 (1997). New Computing Techniques in Physics Research V, pp. 81–86. ISSN: 0168-9002.

[106] Francesco Loparco and Mario Nicola Mazziotta for the Star Collaboration. "Unfolding spectral analysis of the Fermi-LAT data". In: *arXiv: Instrumentation and Methods for Astrophysics* (2009).

[107] M. N. Mazziotta for the Star Collaboration. "A method to unfold the energy spectra of point like sources from the Fermi-LAT data". In: *arXiv: Instrumentation and Methods for Astrophysics* (2009).

[108] Carmelo Evoli, Roberto Aloisio, and Pasquale Blasi. "Galactic cosmic rays after the AMS-02 observations". In: *Phys. Rev. D* 99 (10 2019), p. 103023.

[109] Andrew W. Strong, Igor V. Moskalenko, and Vladimir S. Ptuskin. "Cosmic-Ray Propagation and Interactions in the Galaxy". In: *Annual Review of Nuclear and Particle Science* 57.1 (2007), pp. 285–327.

[110] DAMPE Collaboration. "Detection of spectral hardenings in cosmic-ray boron-to-carbon and boron-to-oxygen flux ratios with DAMPE". In: *Science Bulletin* 67.21 (2022), pp. 2162–2166. ISSN: 2095-9273.

[111] Jingjing Zang, Chuan Yue, and Xiang Li. "Measurement of absolute energy scale of ECAL of DAMPE with geomagnetic rigidity cutoff". In: *ICRC2017* (2017).

[112] H. S. Ahn et al. "Measurements of cosmic-ray secondary nuclei at high energies with the first flight of the CREAM balloon-borne experiment". In: *Astroparticle Physics* 30 (2008), pp. 133–141. arXiv: 0808.1718.

[113] PAMELA collaboration et al. "Ten years of PAMELA in space". In: *La Rivista del Nuovo Cimento* 40 (2017), pp. 473–522.

[114] V. Grebenyuk et al. "Secondary cosmic rays in the NUCLEON space experiment". In: *Advances in Space Research* 64.12 (2019). Advances in Cosmic-Ray Astrophysics and Related Areas, pp. 2559–2563. ISSN: 0273-1177.

[115] Kolmogorov A. N. "The local structure of turbulence in incompressible viscous fluid for very large Reynolds number". In: *Dokl. Akad. Nauk. SSSR* 30 (1941), pp. 301–303.

[116] Robert H. Kraichnan. "Inertial-Range Spectrum of Hydromagnetic Turbulence". In: *The Physics of Fluids* 8.7 (1965), pp. 1385–1387.

[117] S. N. Zhang et al. "The high energy cosmic-radiation detection (HERD) facility onboard China's Space Station". In: vol. 9144. SPIE, 2014, pp. 293–301.

[118] Dimitrios Kyratzis. "Overview of the HERD space mission". In: *Physica Scripta* 97.5 (2022), p. 054010.

[119] Dimitrios Kyratzis. "Latest advancements of the HERD space mission". In: *Nuclear Instruments and Methods in Physics Research Section A: Accelerators, Spectrometers, Detectors and Associated Equipment* 1048 (2023), p. 167970. ISSN: 0168-9002.

[120] Dimitrios Kyratzis. "HERD: The High Energy cosmic-Radiation Detector". In: *Nuovo Cimento C* 43.4-5 (2020), p. 117.

[121] Nicola Mori. "GGS: A Generic Geant4 Simulation package for small-and medium-sized particle detection experiments". In: *Nuclear Instruments and Methods in Physics Research Section A: Accelerators, Spectrometers, Detectors and Associated Equipment* 1002 (2021), p. 165298. ISSN: 0168-9002.

[122] Andrii Tykhonov, David Droz, Xin Wu, et al. "TeV–PeV hadronic simulations with DAMPE". In: *PoS* ICRC2019 (2019), p. 143.

[123] Lorenzo Pacini et al. "Design and expected performances of the large acceptance calorimeter for the HERD space mission." In: *PoS* ICRC2021 (2021), p. 066.

[124] Chiara Perrina et al. "FIT: the scintillating fiber tracker of the HERD space mission". In: *PoS* ICRC2021 (2021), p. 067.

[125] Dimitrios Kyratzis et al. "The Plastic Scintillator Detector of the HERD space mission". In: *PoS* ICRC2021 (2021), p. 054.

[126] Fabio Gargano. "The High Energy cosmic-Radiation Detection (HERD) facility on board the Chinese Space Station: hunting for high-energy cosmic rays". In: *PoS* ICRC2021 (2021), p. 026.

[127] AA Moiseev et al. "Observation and simulations of the backsplash effects in high-energy gamma-ray telescopes containing a massive calorimeter". In: *Astroparticle Physics* 22.3 (2004), pp. 275–283.

[128] G.V Kulikov and G. B. Khristiansen. "On the size spectrum of extensive air showers". In: *J. Exptl. Theoret. Phys.* 35 (1958), pp. 635–640.

[129] J. J. Engelmann et al. "Charge composition and energy spectra of cosmic-ray nuclei for elements from Be to Ni - Results from HEAO-3-C2." In: *Astronomy and Astrophysics* 233 (1990), pp. 96–111.

[130] M. Aguilar et al. "RELATIVE COMPOSITION AND ENERGY SPECTRA OF LIGHT NUCLEI IN COSMIC RAYS: RESULTS FROM AMS-01". In: *The Astrophysical Journal* 724.1 (2010), p. 329.

[131] A.D. Panov et al. "Relative abundances of cosmic ray nuclei B-C-N-O in the energy region from 10 GeV/n to 300 GeV/n. Results from ATIC-2 (the science flight of ATIC)". In: *PoS* ICRC2007 (2007).

[132] H.S. Ahn et al. "Measurements of cosmic-ray secondary nuclei at high energies with the first flight of the CREAM balloon-borne experiment". In: *Astroparticle Physics* 30.3 (2008), pp. 133–141. ISSN: 0927-6505.

[133] O Adriani et al. "Energy spectrum of cosmic-ray electron and positron from 10 GeV to 3 TeV observed with the calorimetric electron telescope on the international space station". In: *Physical review letters* 119.18 (2017), p. 181101.

[134] Luis Fariña et al. "Gamma-ray performance study of the HERD payload". In: *PoS* ICRC2021 (2021), p. 651.

[135] Glenn F. Knoll. *Radiation detection and measurement*. English. 4nd ed. Wiley New York, 2010, xix, 754 p. : ISBN: 0471815047.

[136] Hamamatsu Photonics. *Technical Guide To Silicon Photomultipliers*. https://hub.hamamatsu.com/us/en/technical-notes/mppc-sipms.html.

[137] Saint-Gobain crystals. *Plastic Scintillator properties*. https://www.crystals.saint-gobain.com/radiation-detection-scintillators/plastic-scintillators.

[138] National Institute of Standards and Technology (NIST). *Estar, Stopping power and range table for electrons*. https://physics.nist.gov/PhysRefData/Star/Text/ESTAR.html.

[139] V. Senchyshyn et al. "Accounting for self-absorption in calculation of light collection in plastic scintillators". In: *Nuclear Instruments and Methods in Physics Research Section A: Accelerators, Spectrometers, Detectors and Associated Equipment* 566.2 (2006), pp. 286–293. ISSN: 0168-9002.

[140] M Gierlik et al. "Light transport in long, plastic scintillators". In: *Nuclear Instruments and Methods in Physics Research Section A: Accelerators, Spectrometers, Detectors and Associated Equipment* 593.3 (2008), pp. 426–430.

[141] Ali Taheri and Reza Gholipour Peyvandi. "The impact of wrapping method and reflector type on the performance of rod plastic scintillators". In: *Measurement* 97 (2017), pp. 100–110.

[142] Mizuki Kurata et al. "Study of timing degradation and light attenuation in long plastic scintillation rods for time-of-flight counters in relativistic heavy ion experiments". In: *Nuclear Instruments and Methods in Physics Research Section A: Accelerators, Spectrometers, Detectors and Associated Equipment* 349.2-3 (1994), pp. 447–453.

[143] Łukasz Kapłon. "Technical attenuation length measurement of plastic scintillator strips for the total-body J-PET scanner". In: *IEEE Transactions on Nuclear Science* 67.10 (2020), pp. 2286–2289.

[144] *CAEN DAQ DT5550W Board*. https://www.caen.it/products/dt5550w/.